January 2015

Development of a Multi-Body Nonlinear Model for a Seat-Occupant System

Yousof Azizi
Purdue University

Graduate School Form 30
Updated 1/15/2015

PURDUE UNIVERSITY
GRADUATE SCHOOL
Thesis/Dissertation Acceptance

This is to certify that the thesis/dissertation prepared

By Yousof Azizi

Entitled

Development of a Multi-Body Nonlinear Model for a Seat-Occupant System

For the degree of Doctor of Philosophy

Is approved by the final examining committee:

Dr. Patricia Davies
Chair

Dr. Anil Bajaj
Co-chair

Dr. Eric Nauman

Dr. Amit Varma

To the best of my knowledge and as understood by the student in the Thesis/Dissertation Agreement, Publication Delay, and Certification Disclaimer (Graduate School Form 32), this thesis/dissertation adheres to the provisions of Purdue University's "Policy of Integrity in Research" and the use of copyright material.

Approved by Major Professor(s): Dr. Patricia Davies

Approved by: Dr. Ganesh Subbarayan 8/21/2015

Head of the Departmental Graduate Program Date

DEVELOPMENT OF A MULTI-BODY NONLINEAR MODEL FOR A SEAT-OCCUPANT SYSTEM

A Dissertation

Submitted to the Faculty

of

Purdue University

by

Yousof Azizi

In Partial Fulfillment of the

Requirements for the Degree

of

Doctor of Philosophy

December 2015

Purdue University

West Lafayette, Indiana

ACKNOWLEDGMENTS

I would like to sincerely thank my advisors Dr. Anil K. Bajaj and Dr. Patricia Davies for their guidance and patience throughout my study. Their continued guidance has greatly influenced my professional career. I was very fortunate to have the opportunity to work with such great scholars and teachers. I am really thankful to them and I will be in debt to them for the rest of my life. I also wish to thank Dr. Eric Nauman and Dr. Amit Varma for serving in my committee and providing helpful inputs during my preliminary defense and my final defense. I wish to thank the Herrick community and the members of my research group Udbhau, Vaidy, Yash and Gauri. I gratefully acknowledge the financial support for my research provided by the National Science Foundation, grant CMMI-0728101, as well as the teaching assistantship from School of Mechanical Engineering. I would also like to thank my parents, Mohammad and Parvin, Amoo Ali and my parent-in-law for their continued love and support. And finally, I sincerely thank my wife Parisa for her support in the past 6 years and sacrificing her professional career to be with me. Her presence greatly helped me through out my graduate studies. So thank you Parisa!

TABLE OF CONTENTS

Page

LIST OF TABLES

LIST OF FIGURES

Figure Page

Figure Page

Figure Page

Figure Page

Figure Page

ABSTRACT

Azizi, Yousof Ph.D., Purdue University, December 2015. Development of a Multi-Body Nonlinear Model for a Seat-Occupant System. Major Professors: Anil K. Bajaj and Patricia Davies, School of Mechanical Engineering.

A car seat is an important component of today's cars, which directly affects ride comfort experienced by occupants. Currently, the process of ride comfort evaluation is subjective. Alternatively, the ride comfort can be evaluated by a series of objective metrics in the dynamic response of the occupant. From previous studies it is well known that the dynamic behavior of a seat-occupant system is greatly affected by soft nonlinear viscoelastic materials used in the seat cushion. Therefore, in this research, especial attention was given to efficiently modeling the behavior of seat cushion. In the first part of this research, a phenomenological nonlinear viscoelastic foam model was proposed and its ability to capture uniaxial behavior of foam was investigated. The model is based on the assumption that the total stress can be decomposed into the sum of a nonlinear elastic component, modeled by a higher order polynomial of strain, and a nonlinear hereditary type viscoelastic component. System identification procedures were developed to estimate the model parameters using uniaxial cyclic compression data from experiments conducted at different rates on two types of low density polyurethane foams and three types of high density CONFOR foams. The performance of the proposed model was compared to that of other traditional continuum models. For each foam type, it was observed that lower order models are sufficient to describe the uniaxial behavior of the foam compressed at different rates. Although, the estimated model parameters were functions of the input strain rate. Alternatively, higher order comprehensive models, with strain independent parameters, were estimated as well. The estimated comprehensive model predicts foam responses under different compression rates. Also, a methodology was proposed to predict the

stress-response of a layered foam system using the estimated models of each foam in the layers. Next, the estimated foam model was incorporated into a single-degree of freedom foam-mass model which is also the simplest model of seat-occupant systems. The steady-state response of the system when it is subjected to harmonic base excitation was studied using the incremental harmonic balance method. The incremental harmonic balance method was used to reduce the time required to generate the steady-state response of the system. The incremental harmonic balance method was used to reduce the time required to generate the steady-state response of the system. Experiments are conducted on a single-degree of freedom foam-mass system subjected to harmonic base excitation. Initially, the simulated response predictions were found to deviate from the experimental results. The foam-mass model was then modified to incorporate rate dependency of foam parameters resulting in response predictions that were in good agreement with experimental results. In the second part of this research, the dynamic response of a seat-occupant system was examined through a more realistic planar multi-body seat-occupant model. A constraint Lagrangian formulation was used to derive the governing equations for the seat-occupant model. First, the governing equations were solved numerically to obtain the occupant transient response, the occupant's H-Point location and the interfacial pressure distribution. Variations in the H-Point location and the seat-occupant pressure distribution with changes in the seat-occupant parameters, including the seat geometry and the occupant's characteristics, were studied. The estimated pressure was also investigated experimentally and was found to match with the results obtained using the seat-occupant model. Next, the incremental harmonic balance method was modified and used to obtain the occupant's steady-state response when the seat-occupant system was subjected to harmonic base excitation at different frequencies. The system frequency response and mode shapes at different frequencies were also obtained and compared to the previously measured experimental frequency responses. Finally, variations in the estimated frequency response with changes in the seat-occupant parameters, including the seat geometry and the occupant characteristics, were studied.

1. INTRODUCTION

1.1 Motivation

A car is made of different electrical and mechanical components. These components have been redesigned and evolved over years which make current cars better in many aspects. However, comparing recent cars to their ancestors, it is observed that there are still several parts which have not been significantly modified or redesigned. One example is the car seat which has been left with minimum changes over years. Although, a well-designed car seat can be an essential component of a car. For example a comfortable seat can leave a good first impression on potential buyers. With growing demand for luxury cars and more comfortable economy cars, car manufacturers and OEM have become more interested in car seats in the recent years. This interest has motivated them to reconsider the seat design process.

In general the process of car seat design has two main objectives: (1) designing a seat with certain functionality, i.e. ergonomics, and (2) designing a car seat which provides comfort. Seat functionality is a function of the seat geometry and the occupant's position with respect to the seat. The latter includes identifying the occupant's H-Point location when it settles in the seat. Seating comfort can be divided into static comfort and dynamic comfort. Static seat comfort is an assessment of how comfortable the seat is in the absence of vibrational effects, mainly related to the correct amount of support given to various critical regions like lumbar, back and the pressure distribution at different interfaces between the seat and the passenger. Dynamic seat comfort is an assessment of seat comfort in the presence of structure borne vibration effects. Drivers in vehicles are subjected to whole body vibrations over a range of frequencies due to the variety of road conditions. These low frequency

Figure 1.1. Seat prototypes subjective testing. http://www.trucktrend.com.

whole body vibrations have different adverse effects on the occupants ranging from discomfort and dizziness to serious damages to lumbar and spine region in the long run. In order evaluate the design objectives in the process of design, it is important to develop objective tools which enable the designers to predict different metrics and measures, e.g. H-Point location, interfacial pressure distribution, vibration transmissibility, which are related to seat functionality and seat comfort. Also, such tools enable designers to gain some understandings of how different seat parts affect the seat occupant responses.

In practice, the current process of designing a car seat is mostly subjective. It involves multiple cycles of prototyping and then testing for prototype functionality and comfort, which is performed by a panel of judgment. For example, Figure 1.1 shows the process of blind comfort testing for a Ford Escape seat. Figure 1.2 shows how the pressure distribution is measured during the process of designing a Chevrolet Impala car seat. Based on the subjective inputs provided by the panel of judgment, the seat prototypes are improved over a period of time.

Figure 1.2. Measuring the pressure distribution between the seat prototype and the occupant. www.GM.com.

As described earlier, the current process of car seat design involves several cycles of prototyping and subjective testing, which makes the process expensive and lengthy. The process can significantly be accelerated and facilitated if an iterative pre-design cycle is added to the current design practice. This pre-design cycle relies on an accu-

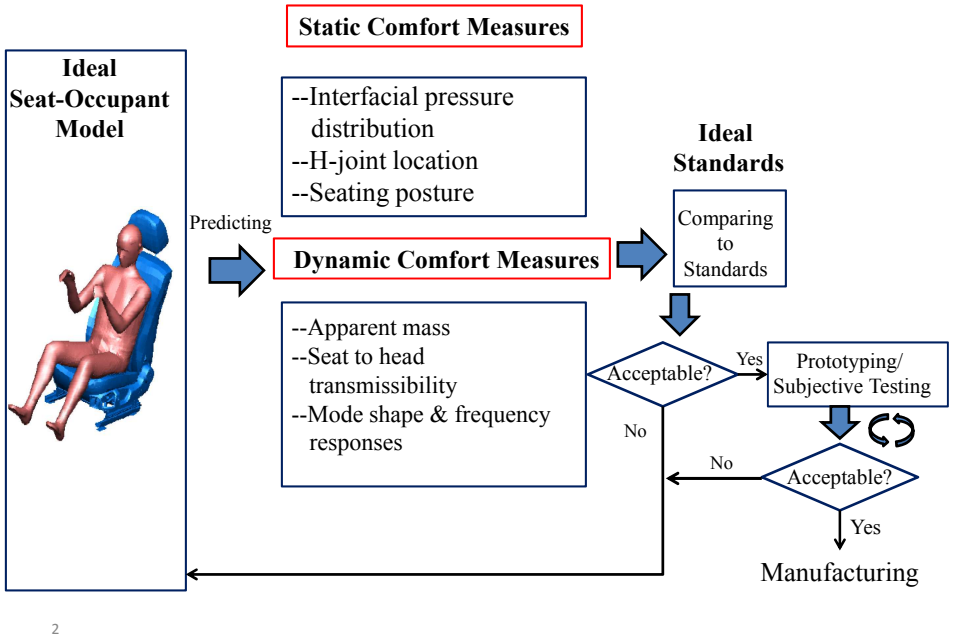

Figure 1.3. The proposed seat design cycle.

rate analytical seat-occupant model which can be used to predict the seat-occupant behavior, e.g. occupant's responses. The occupant responses can be used to predict a series of objective metrics which can be used to predict the seat functionality and the seat comfort before manufacturing any physical seat prototypes. These metrics are compared to ideal standards to predict the static and dynamics comfort perception. Based on the design objectives, the seat model is then modified to achieve the design goals. Then the physical prototypes are made based on the output of the pre-design cycle, which can undergo subjective testings. The proposed design cycle is illustrated in Figure 1.3.

As it is shown in Figure 1.3, the pre-design cycle relies on two main components: an accurate seat-occupant model which can be used to predict the seat comfort/functionality metrics and ideal standards used to predict the seat comfort/functionality based on the objective metrics. In the past years, several seat-occupant models have

been proposed and used to predict the dynamic responses of occupants. Although, most of the models have limited application range, e.g. just valid for one occupant with a certain body weight, and mostly are at system level. Also, there are some experimental studies which have led to the development of some standards such as *ISO* 2631.

1.2 Objectives

The main objective of this research is to develop subsystem level seat-occupant models which can be incorporated into the pre-design cycle shown in Figure 1.3. Such models enable designer to predict the comfort/functionality objective metrics more accurately and efficiently. Developing a subsystem level seat-occupant model consists of two main steps:

- Modeling the seat: a car seat is made of many components including the seat frame, suspension system, seat cover and seat cushion. The later is made of flexible polyurethane foam which is a nonlinear viscoelastic material. It is well known that occupant's dynamic response is greatly affected by the seat cushion mechanical behavior. Thus inclusion of foam's nonlinear viscoelastic behavior is important when a precise seat-occupant model is being developed.

- Modeling the occupant: a model is required to describe the mechanical behavior of the occupant in the system. Traditionally, the occupant is characterized using different models ranging from computationally costly finite element models to simple lumped models.

The overall goal of this research is to develop a seat-occupant model which helps us to understand the mechanical behavior of seat-occupant systems and to simplify seat design by eliminating the need for extensive prototyping. The model is built on the multi-body seat-occupant model which has been developed over years in our research group in Ray W. Herrick Laboratories. The model is shown in Figure 1.4. This

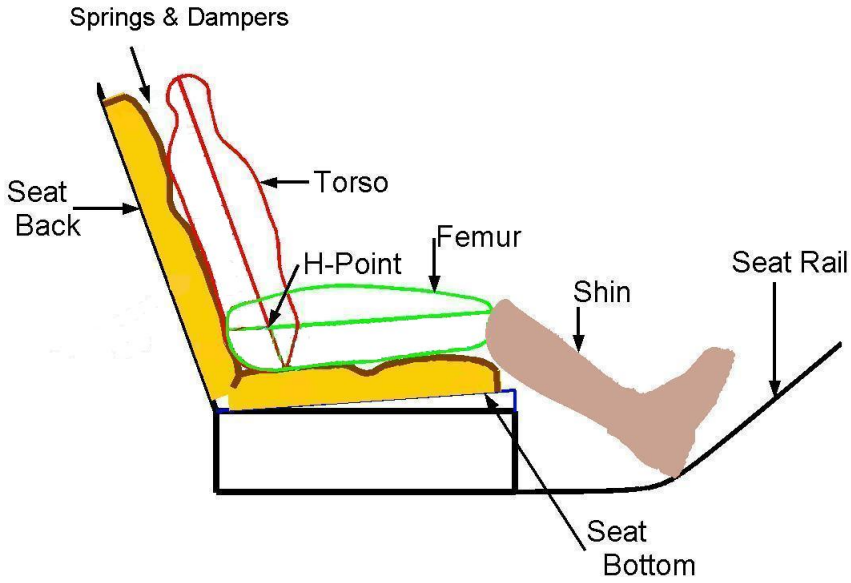

Figure 1.4. Ray W. Herrick Laboratories multibody seat-occupant model.

research this sea-occupant model is further modified by improving the seat-occupant model, which are summarized in the rest of this Chapter.

1.2.1 Developing Accurate Models for Car Seat

Most of the current foam models which describe the uniaxial mechanical behavior of polyurethane foams fall into two categories: the first group of models are simple models which have limited application ranges, e.g. different models are required to describe the foam behavior at different rates. The second group of models are effective but at the same time very complex to be incorporated into seat-occupant systems. The main goal of this research is to develop a simple nonlinear viscoelastic model which has a wider application range. The main objectives of this part of the research is:

- To use the quasi-static compression test data (slow tests) to develop and estimate phenomenological comprehensive foam models which have wider application range,
- To test the developed model on different types of polyurethane foams,
- To develop techniques for predicting the response of layered foam systems based on individual foam characteristics,
- To use the models, estimated using quasi-static compression test data, to predict the foam responses when subjected to harmonic excitations (fast test),
- To use data form impulse tests (very fast test) to develop a global nonlinear model.

1.2.2 Modifying the Seat-Occupant Model

The predesign cycle introduced before relies on a robust seat-occupant model which accurately predicts the comfort metrics. In this study, several components of the previously developed seat-occupant model is modified and the foam model developed in this research is incorporated into the seat model. The modified seat-occupant model enables us to accurately and efficiently predict the occupant dynamic responses and different measures used to evaluate seat functionality and metrics. The main objectives of this part of the research is:

- To fine tune the previously developed seat occupant model
- To incorporate more robust foam models in the seat-occupant model
- To modify the model which characterizes the interfacial behaviors
- To predict the occupant transient response and to evaluate the metrics used to evaluate static comfort

- To predict the occupant steady-state response when it the system is subjected to harmonic base excitation and to evaluate the metrics used to evaluate dynamic comfort
- To develop a robust computation technique which can be used to efficiently compute the steady-state responses of a large system of nonlinear differential equations subjected to harmonic inputs

1.3 Organization

The thesis is organized as follows. An overview of literature and prior work related to polyurethane foam modeling and seat-occupant modeling are given in Chapter 2. In Chapter 3, the quasi-static behavior of polyurethane foam under large strain compression is described. This is followed by the development of a phenomenological nonlinear viscoelastic model which describes the uniaxial behavior of polyurethane foams. Next, the model identification and model parameter estimation procedures are introduced and the results of fitting the model to the experimental data are presented. The utility of the proposed foam model is tested on 5 different types of foams including low density polyurethane foams and high density CONFOR foams. Next methodology for estimating the mechanical behavior of layered foam is presented. In Chapter 3, the estimated foam models are used to study the mechanical behavior of a single degree of freedom foam-mass system. This system is also the simplest model for a seat-occupant system. Then the incremental harmonic balance method is used to compute the system steady-state responses of the single degree of freedom foam-mass system. Then response predictions is then compared to experimental results. Chapter 4 covers the description of the multibody seat-occupant model which is used in this research to estimate the dynamic behavior of the seat-occupant system. In Chapter 5, the multibody seat-occupant model is used to predict the transient response of the seat-occupant system. The system governing equation derived in Chapter 5 is solved numerically to compute the transient responses of the seat-occupant system.

Also the effects of variation in different subsystem parameters on the occupant response are also studied. Chapter 6 focuses on predicting the steady-state response of the seat-occupant system subjected to harmonic base excitation. An improved incremental harmonic balance method is adopted to solve the governing equations of the seat-occupant model and the steady-state responses of the occupant are computed for different base excitation levels and frequencies. The final chapter is Chapter 7, which gives a summary of the results, conclusions drawn from this research and recommendations for future work.

2. LITERATURE REVIEW

In this chapter first different techniques and modeling approaches used to describe the mechanical behavior of polyurethane foams are reviewed. In the first part, different microstructural models, continuum modes and phenomenological models of polyurethane foams are presented. In the second part of this chapter, different studies for modeling seat-occupant systems are reviewed. Several modeling techniques including lumped parameter models, multibody models, finite element models and some experimental models are reviewed. At the end of this chapter, some of the common standards used for predicting comfort perception of occupants are given as well.

2.1 Polyurethane Foam Modeling

Flexible polyurethane foam is used in a wide range of engineering and industrial applications including seating, cushioning, sports and medical equipment, and vibration and sound isolation. To utilize this material effectively, it is important to have a good understanding of its mechanical behavior. This can be accomplished by developing an effective mathematical model which characterizes the nonlinear and viscoelastic behavior of foam. References by Gibson and Ashby [1], Widdle [2], and Deshmukh [3] contain an extensive review of cellular solids modeling. The work done on study of cellular solids is vast and so a detailed discussion is not given here. This chapter only gives a brief overview of some notable concepts ans previous studies.

The first section contains discussion of the microstructure based models of foam previously developed followed by a description of continuum based models of foam and rubber. The third section is focused on the work that has been done related phenomenological modeling of polyurethane foams.

2.1.1 Microstructural Models

One of the main techniques commonly used to characterize the mechanical behavior of cellular solids is based on developing models at the microstructure level. For example, polyurethane foam is composed of a network of small units called cells, see Figure 2.1. In general, foams can be divided into two categories: open cell foam and closed cell foam. For open-cell foams, the cell faces are absent which allows the movement of air between cells and outside of the foam as foam is subjected to compression and decompression. In the case of closed-cell foams, the cell faces are usually, completely or partially, closed. In general, foam's mechanical behavior is a function of the material used to manufacture the foam, cell's geometry and foam's relative density. In order to develop effective microstructural models especial attention needs to be paid to modeling the cells.

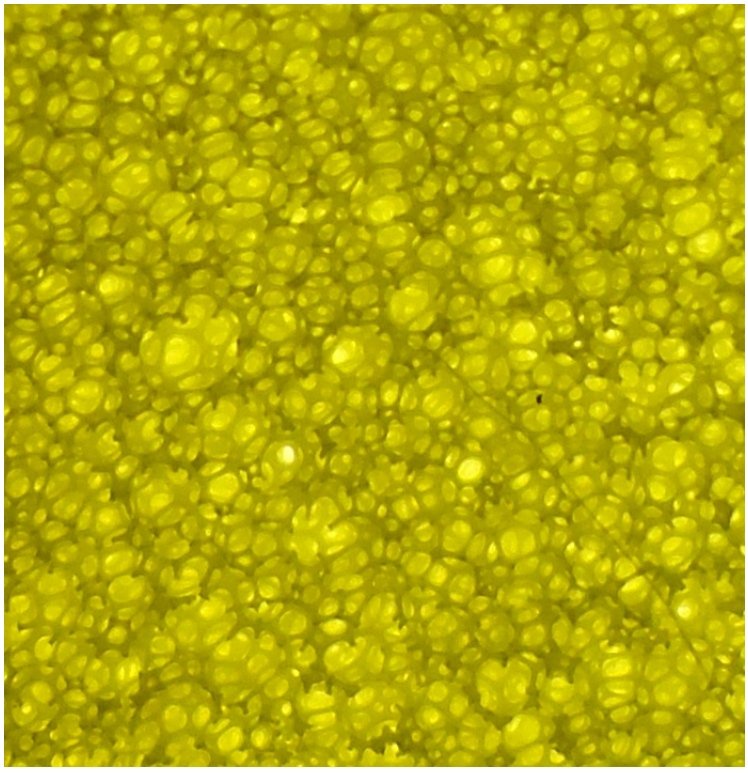

Figure 2.1. Foam sample microstructure [3].

One of the most successful studies in modeling the uniaxial compressive behavior of foam using the material microstructure is the work by Gibson and Ashby [1]. In this model, the foam cells are modeled by cubic elements. Also the foam struts are modeled by Euler-Bernoulli beams which are assumed to be responsible for the foam collapse. Using this model, Gibson and Ashby could describe the foam behavior in the three deformation regions known as linear, collapse and densification regions. Based on this model, Warren and Kraynik [4] proposed a microstructural model in which the fundamental unit was a tetrahedral joint. Using this model, they found the linear elastic properties of foam materials. This model was modified later in [5] by assuming the tetrahedral joint behaves as a pin joint. The new model can describe the foam behavior under small and large input strains.

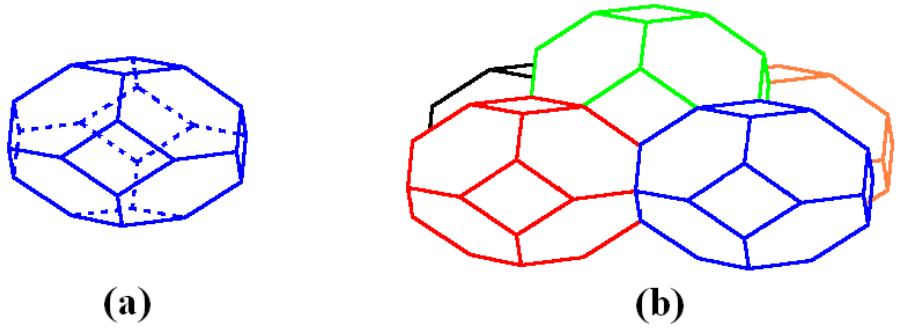

Figure 2.2. Cellular structure of foam represented by (a) One, and (b) five tetrakaidecahedrons elements [2].

Later, Warren and Kraynik [6] further modified the model by assuming that the fundamental element to be a tetrakaidecahedral cell, see Figure 2.2. In the new model, the struts are allowed to bend, stretch and twist. Zhu *et al.* [7] extended th model to consider large strain compression in the foam. Their model can describe the foam behavior in the first two regions of the stress-strain response of foam, namely linear and collapse regions. However, the proposed model failed to effectively describe the third region of the stress-stain response. Later, Zhu and Mills incorporated viscoelasticity in the model by measuring the creep properties of foam. Widdle [2]

developed a microstructural model for polyurethane foams. Although the model was linear and purely elastic, the model describes the mechanical behavior of foam under compression and shear.

Alternatively, in some studies, Voronoi tessellations are used to model foam microstructure. Voronoi tessellations are made of an irregular array of Voronoi cells which are similar to the irregular microstructure found in foamed materials. Silva, Hayes and Gibson [8] used this modeling technique to describe the foam behavior. In their model the cells, made of linear material, are in general hexagonal. Using the finite element analysis of the proposed microstructure, the estimated the linear elastic coefficient of the foam material. Silva *et al.* [8] studied how imperfections in the veronoi structures affects the mechanical behavior of foam when the structure is made of linear material and the input is small. Van der Burg *et al.* [9] proposed a model based on the work found in [8] to describe the 3D behavior of foam material and by estimating the equivalent linear elastic coefficient in different directions. Later, Shulmeister *et al.* [10] extended the work of Van der Burg *et al.* [9] by incorporating material nonlinearity in as well as large deformations of a Voronoi structure in the model. Also see [7, 11–13]. Also see [14]. Most of the models reviewed in this section only described the elastic behavior of the foam material. *et al.* [15] and Huang *et al.* [16] studied the time dependent creep properties of foam by Voronoi structures. For other microstructural models see [2, 3].

2.1.2 Continuum Models

Microstructural models may give a picture of the foam behavior at microstructure level. However, most of the current microstructural models have limited application range and sometimes neglect the viscoelastic properties of foam. Another approach to model the mechanical behavior of foam is to use a continuum description of the material. Unlike the microstructure based models, in the case of cellular solids like

polyurethane foam, the continuum based model is able to account for the elastic as well as viscoelastic nature of the material.

Viscoelastic materials show a time-dependence in their response and they are sometimes referred to as materials with memory. For linear viscoelastic materials, this characteristic can be represented through a hereditary integral model [17]. Another way of representing the viscoelastic behavior is through the use of the fractional derivative models as presented by Bagley and Torvik [18]. These may work well for linear viscoelastic materials, but generalization of them to include non-linear material behavior has not been explored. For hereditary models, a simple extension to model nonlinear viscoelastic behavior could be to convolve the kernel with a nonlinear function of strain as shown by Bloch *et al.* [19]. This approach was also used by Banks *et al.* [20] and Banks [21] when modeling the behavior of carbon black and silicon filled elastomers. They convolved the hereditary kernel with a polynomial function of strain. Banks *et al.* [20] developed a model for a carbon filled elastomer that is the sum of a linear function of strain and a nonlinear viscoelastic model to describe the stress strain relationship. The work was further extended in [22] where general nonlinear constitutive models for both quasi-static and dynamic deformations of a viscoelastic rod under tension were developed. Bergstrom and Boyce [23] developed a model that characterizes the nonlinear time-dependent uniaxial behavior of foam. This "micromechanism inspired" model is based on the assumption that the foam material can be replaced by two networks acting in parallel. One network represents the elastic, short time, response while the other network captures the time dependent, long time, response. The results of fitting this model to slow compression tests ($0.0002\ /s - 0.001\ /s$) were satisfactory. Suvorova *et al.* [24] used the Robotnov model to study nonlinear and time-dependent uniaxial behavior of foam. They showed that the same model with the same set of parameters can be used to describe the uniaxial behavior of foam under various types of loading. However, in their studies they excluded the effect of strain rate and the model only works for small strains.

In the past years, extensive research has also been conducted on modeling the mechanical behavior of foam under fast compression tests (e.g. strain rates greater than $100/s$). Yang and Shim [25] studied the constitutive modeling of finite deformation in elastomeric polyurethane foam under high compression rates. They used visco-hyperelastic material models where the static response is defined by a compressible hyperelastic model derived for a special strain energy potential function, and the strain rate sensitive viscoelasticity is characterized by using a nonlinear Maxwell relaxation model. They demonstrated that a model with seven parameters, estimated by using a least squares fit to the experimental data, is sufficient to describe the uniaxial behavior of foam under strain rates ranging from 100 $/s$ to 1000 $/s$. Some other similar attempts to model high strain-rate responses of foam are presented in [26, 27].

In general, the continuum mechanics modeling approach has been used extensively in deformation studies of rubber. For extensive review of modeling techniques refer to [3].

2.1.3 Phenomenological Models

The third class of models are the phenomenological models. In general, a phenomenological model is developed based on a known constitutive model structure and by refining the model structure according to the empirical behavior of the material, i.e. its responses in a series of standard tests such as quasi-static compression tests. One example of such studies is by White *et al.* [28] where it is assumed that the total foam compressive force in the foam is the sum of a nonlinear elastic and a linear viscoelastic contribution [29, 30]. In these studies, modeling the elastic behavior of cellular solids is purely phenomenological [28, 31] where a constitutive model in the form of a polynomial of strain is proposed based on fits of the model to experimental data. The viscoelastic contribution was modeled with a hereditary integral and was a linear function of strain. In order to account for rate dependency of polyurethane foam, Puri [32] used the linear hereditary type viscoelastic model which is a function

of strain rate. Deng, Bajaj and Davies [31] also assumed an additive decomposition of the total stress in the form of a sum of elastic and viscoelastic components, although fractional derivative models were used to account for the viscoelastic force contribution. Also see [21, 33].

In rest of this chapter, different techniques commonly used to model the mechanical behavior of a seat-occupant system are reviewed.

2.2 Seat-Occupant Modeling

A seat-occupant system is composed of different components and parts. An ideal seat-occupant model must be at subsystem level and must consist of different subsystem level models for its components. There are different modeling methods which can me utilized to describe the dynamic behavior of a seat-occupant system. For example, the occupant can be modeled using one, two or three dimensional models, e.g. corresponding to vertical, fore-and-aft, and lateral motion of the occupant. Seat-occupant models are generally categorized into different classes as:

- lumped parameter models;
- finite element models;
- multi-body models;
- experimental models.

In this section different seat-occupants models and related studies are reviewed.

2.2.1 Lumped Parameter Models

In general, lumped parameter models are the simplest models of the seat-occupant systems and they are used as an initial/trial model before developing more complicated multi-dimension models. They are often used to develop models for measuring simple quantities like seat to head transmissibility, apparent mass and etc [34]. Here,

the seated human body is modeled as several masses interconnected by springs and dampers with varying degree of complexity. These models are easy to analyze and validate with experiments. Most of the lumped parameter models are usually linear. One exception is the model proposed by Pang *et al.* [35] where the interconnecting springs and dampers are nonlinear. Also, most of the lumped parameter models are one dimensional which enables them to be simple but yet effective in estimating important dynamic parameters such as seat-to-occupant vibration transmissibility. One exception is the work by Rakheja *et al.* [36]. They developed a two dimensional seat-occupant model which has 4 degrees of freedom.

Wei and Griffin [37] have developed one dimensional models with 1 and 2 degrees of freedom. In order to estimate the model parameters, such as spring and damper coefficients, they fitted the proposed model to the data from tests conducted on 60 human subjects [38]. In the experiments the seat back was removed and the seat bottom was rigid and the system, including the occupant, was subjected to low frequency random excitations. It was observed that at lower frequencies the model with 2 degrees of freedom performs the best. Later, the experimental data was used by Rosen and Arcan [39] to estimate and validate their 3D seat-occupant model. The proposed model was complex and it had total of 35 degrees of freedom. Especially, the car seat is represented by a model with 26 degrees-of-freedom. In the model, the occupant tissues and the seat cushion were represented by linear viscoelastic materials and the parameters of the viscoelastic materials were estimated using data from experiments conducted on actual soft tissues.

Qassem *et al.* [40] studied the vibration transmissiblity to the occupant from the seat back and the seat bottom as well as occupant's hands when it is in contact with the steering wheel. They also developed a model with 26 degrees-of-freedom to predict the system transfer functions, also see [41]. The system parameters were taken from some other similar studies by Mizrahi and Susak [42], Nigam and Malik [43] and Patil *et al.* [44]. They also verified their model by conducting experiments on

different human subjects when they are subjected to low frequency and high frequency vibrations.

Smith [45] conducted low frequency harmonic base excitation tests on different seated subjects and measured the mechanical impedance curves. Based on the observations in the experimentally measured curves, he proposed a seat-occupant model with 5 degrees of freedom. The mass values are realistic and were obtained based on the mass values of the human subjects. The spring and damper coefficients were obtained based on the resonance frequencies of the system which were experimentally measured. This work was later modified in [46]. The modified model incorporates the nonlinear behavior of the body. Th modified model gives a better predictions for the resonance frequencies of the system.

For more detailed review of lumped parameter model refer to [47–49].

2.2.2 Finite Element Models

Finite Element models (FE) are traditionally used for modeling impact and injury in automotive systems during a crash. In the recent finite element analysis has become a practical tool for analyzing and modeling seats and seat-occupant system. Finite element models are commonly used for static comfort evaluation, i.e. predicting seat-bottom interface pressure distribution, contact forces, and H-point prediction. Recently, new FE models have also been developed which can be used to predict the dynamic response of the seated occupants and thus can be used for dynamic comfort evaluation. These models are capable of predicting different metrics such as the seat to head transmissibility and spinal loads [50, 51]. However, finite element models have many degrees of freedom and thus consequently their computation time is significant. Also, these models are usually dependent on commercial FEA software packages which makes it difficult to modify and to study different design factors like different models of foam. Therefore, these models are suitable for verifying the final seat design, but they are too costly to be used during the design process. Some

examples of FEA models developed for studying seat-occupant systems can be found in [47, 52–57]. Some of the common FE softwares commonly used in industry are ALASKA, PAM-CRASH MADYMO, CASIMIR and ROBBY.

2.2.3 Multi-Body Models

Multibody seat-occupant models are made of rigid bodies interconnected by pin joints, springs and dashpots. In general, multibody models have several degrees of freedom and they are in nature nonlinear due to geometric nonlinearity. These models are more realistic when they are compared to lumped parameter models and they can be used to predict the model shapes of the occupant. Compared to finite element models, multibody models are simple and more efficient. They can be incorporated into the predesign cycle discussed earlier. However, despite these advantages, multibody models have not widely been used in seat-occupant modeling.

There are some examples of seat-occupant models which incorporate multibody models for occupants in the literature. Matsumoto *et al.* [58] developed two models with 4 and 5 degrees of freedom. Experimental studies demonstrated that there is a dominant peak at arround 5 Hz in the frequency response of the seat-occupant system. Using the proposed multibody model, Matsumoto *et al.* could predict this resonant frequency. Toshimora *et al.* [59] developed a two dimensional multibody model with 10 degrees of freedom. It was shown that, similar to the previous example, the proposed model can predict the system lower resonant frequency. However, the model fails to predict the system higher resonant frequencies.

Cho and Yoon [60,61] developed multibody model with 9 degrees of freedom. The model consists of three rigid bodies which are interconnected by elastic elements. The occupant is connected to the seat by linear springs and dashpots. They also conducted experiments on subjects and measured the vibration transmissibility in the vertical and horizontal directions. The data was then used to estimate the model parameters. See also [62].

Teng *et al*. proposed a three dimensional seat-occupant model with 48 degrees of freedom. The occupant physical properties is similar to Hybrid III dummy used in crash tests [63]. Using the model, they predicted the vibration transmissibilities in different directions. They also verified the predicted transmissibilities by experimental data from tests conducted on actual dummy by Panjabi *et al*. [64]. Also, their predictions are in agreement which the experimental results presented in [65] and ISO 5982 [66]. The models reviewed above are mostly at system level. Also, the seat cushion is replaced by a few numbers of springs and dashpots. Such models may not be used to precisely predict the interfacial pressure distribution which is an important static comfort metric. Also in most of these models, the occupant is attached to the seat by springs and dampers and thus the occupant's bodies can't slide along the seat. Therefore, the occupant settling point may not be predicted.

Verver *et al*. [52] proposed a finite-element-multibody seat-occupant model. The seat model is realistic and it includes the most important parts of a car seat including the head restraint. Also in order to estimate the parameters of the seat cushion, they conducted compression tests on the seat foam and used the results to estimate the foam parameters. Also see [67].

Ippili, Bajaj and Davies [68] used a 5 DOF multibody model to study the seat-occupant behavior subjected to vertical base excitation. They also incorporated a nonlinear viscoelastic foam model in their multi-body seat occupant model to account for seat behavior. Similar models can be found in [32, 47, 69, 70]. Although, these multi-body seat-occupant models are effective and simple, compared to FE models, they are still complex due to geometric nonlinearity imposed on the model which is already nonlinear due to the foam characteristics. Therefore, the mathematical equations which govern the multi-body seat-occupant models are usually complex. Solving such complex equations demands a powerful computation technique which is the third component of the seat-occupant model. Using a fast and robust computation technique can also enable us to explore the seat-occupant model faster and to undergo more number of iterations while designing a seat. Joshi [47] studied the steady state

behavior of a 2D seat-occupant system, similar to the one explained at the end of the previous paragraph, subjected to sinusoidal base excitation. She used direct numerical integration of the governing equations to determine the steady state response of the system. It was observed that direct integration is computationally costly, particularly when the system takes a long time to reach the steady state (also see [32, 68]).

2.2.4 Experimental Models

In the literature, there are a few examples of experimental studies which have used to derive comfort metrics from subjective tests. These studies usually involve performing experiments on existing seat prototypes. The experiments involve several human subjects, e.g. panel of judges, and based on their subjective perception of comfort, some comfort metrics are derived. Although these studies can't directly be used to design a car seat, e.g. difficult to determine the influence of subsystem on the seat-occupant response, they are frequently used to develop comfort standards. In this section a couple of these studies are reviewed. For some other examples of the experimental models refer to [71–75].

Basri and Griffin [76] studied the discomfort arising from whole-body vertical vibration when sitting on a rigid seat. Different seat prototypes with a back rest (inclined at $0^0, \cdots, 60^o$) and without a backrest were considered. 12 subjects judged the discomfort to vertical harmonic vibration at frequencies from $1 - 20\ Hz$ and magnitude from 0.2 to 2 $ms^{-2}\ r.m.s.$. The discomfort perception was studied relative to the discomfort produced by 8 Hz vibration at 0.4 $ms^{-2}\ r.m.s.$.

Ebe and Griffin [77] proposed that car seat comfort is a function of both static and dynamic factors. They studied the relationship between the characteristic of a seat cushion with the seat static comfort. They tested four different automobile cushion and the subjective comfort judgments were correlated with sample stiffness. For each cushion pair, comfort score is defined based on their relative comfort. They

also studied the importance of static comfort compared to dynamic comfort when the human subject is subjected to whole-body vibration.

Dupuis and Zerllet [78] studied the comfort perception reported by 352 truck drivers exposed to whole-body vibration during 3 years period. The drivers were questioned about the level of discomfort or annoyance when they were subjected to random vibration with frequency ranging from 2 to 20 Hz and acceleration ranging from 0.2 to 1.5 ms^{-2} $r.m.s.$. They also used available X-rays showing different parts of the spines to study possible damages. Also see [79].

These experimental studies have led to the development of several standards. Today, these standards are widely used to evaluate ride comfort and safety. Some of the most well known standards for measurement and evaluation of human exposure to whole-body vibration are:

1. ISO 2631-1 (1997): Mechanical vibration and shock evaluation of human exposed to whole-body vibration,
2. BS 6841 (1987): Guide to measurement and evaluation of human exposure ti whole-body mechanical vibration and repeated shock,
3. ISO 5008 (2002): for agricultural wheeled tractors and field machinery,
4. ISO 10056 (2001): for railway vehicles,
5. EN 13059 (2001): for industrial trucks,
6. EN 1032, ISO/DIS 5982, ISO 10326, ISO 7096, EN 13490, etc.

2.3 Objective Metrics for Dynamic Comfort Evaluation

One common factor that affects the seat occupant comfort is the vibration transmitted to the occupant. Therefore, whole-body vibration of the occupant is an important factor which affects the dynamic comfort as well as annoyance. Traditionally,

the whole-body vibration of human body, as well as dynamic comfort, is evaluated in terms of metrics which are defined based on the biodynamic response of the occupant. In this section some of the widely used comfort metrics are reviewed.

1. Mechanical Impedance (MI): According to ISO/DIS 5982, the Mechanical Impedance is a complex ratio of applied periodic excitation force $F(f)$ at frequency f to the resulting vibration velocity $V(f)$ measured at the same point and in same direction as the applied force. The Mechanical Impedance is given by

$$MI(f) = \frac{F(f)}{V(f)}. \tag{2.1}$$

   Mechanical Impedance is also known as driving point Mechanical Impedance (DPMI) and it gives information about external force necessary to produce the specific response in the system.

2. Transmissibility: Transmissibility is a complex ratio of response motion of different points on the occupant, e.g. head, back, chest, etc., to the forced vibration motion at the seat-body interface. Usually for the seat comfort evaluation, displacement, velocity or acceleration of the occupant's head is used to define the Seat-To-Head Transmissibility (STHT). Therefore, Seat-To-Head-Transmissibility is given by

$$STHT(f) = \frac{X_h(f)}{X_s(f)}, \tag{2.2}$$

   or,

$$STHT(f) = \frac{V_h(f)}{V_s(f)}, \tag{2.3}$$

   or,

$$STHT(f) = \frac{V_h(f)}{V_s(f)}. \tag{2.4}$$

   Here, X, V and A represent displacement, velocity and acceleration. Also subscript $_h$ and $_s$ represent head and seat, respectively. It is a ratio which signifies the extent to which the input vibration to the body is transmitted to parts of body.

3. Apparent Mass: Apparent Mass (AM) is defined in ISO/DIS 5982 as a complex ratio of applied periodic excitation force $F(f)$ at frequency f to the resulting vibration acceleration $A(f)$ at the same frequency, measured at the same point and in the same direction as the applied force. Apparent Mass is given by

$$AM(f) = \frac{F(f)}{A(f)}. \tag{2.5}$$

The apparent mass usually is measured at seat and occupant interfaces and represents a force applied to a body that accelerates the body by an amount proportional to the force indirect proportional to body mass as a constant of proportionality.

4. Absorbed Power [48]: Human body is made from elastic tissues and thus energy flow takes place through it. This flow of energy is a parameter that characterizes the interaction between human body and its surroundings. This flow of energy is known as absorbed power. Absorbed power by human body depends on various parameters. One of them is human body type. For same vibration, obsessed people get more absorbed power than muscular people. A seat having larger contact area with body produces lower absorbed power. It measures the rate at which the vibratory input is used. In time domain, the absorbed power can be written as

$$AP = \frac{a}{T}\int_0^T F(\tau)V(\tau)d\tau. \tag{2.6}$$

In addition to the objective metrics reviewed before, there are many other measures which are commonly used in practice to evaluate the ride comfort. Some of these metrics are directly related to the structure borne vibration transmitted to the occupant. For example, weighted Root Mean Square Acceleration of the transmitted vibration is a common objective metric used for comfort evaluation. Another important metric is the frequency of the whole-body vibration. For example, Table 2.1 gives some information about the reaction of a human subjected to whole-body vibration at different frequencies, ranging from 1 Hz to 20 Hz.

Table 2.1. Reaction of human body to whole-body vibration. Results are reported here using data reported in [79].

Headache	4-9
Speech disturbance	13-20
Jaw resonance	6-8
Pharynx disturbance	12-16
Respiration complaints	4-8
Chest pain	5-7
Back pain	8-12
Abdominal pain	5-7
Constant urge to urinate and defecate	10-18
Increase muscle tension	13-20

2.4 Chapter Summary

In this Chapter different categories of seat-occupant models were reviewed and different examples of models from each category were given. It was observed that lumped parameter models are easy to analyze and validate with experiments; however, they are usually restricted to only one-dimensional analysis, which makes it difficult to relate them to actual seat-occupant systems. It was also observed that finite element models have large degrees of freedom and consequently the computation time necessary to predict response is much larger than for the other two types of models. Therefore, the finite element models may be suitable for verifying the close-to-final seat design, but they can be too costly and difficult to use during the design process. Finally it was observed that multi-body models are in general more complex than lumped parameter models while they are simpler than finite element models. Due to their geometry, these models are naturally nonlinear. However, it is easy to relate these models to physical seat-occupant systems, e.g. to observe mode shapes of the occupant's dynamic responses.

3. POLYURETHANE FOAM QUASI-STATIC BEHAVIOR

Flexible polyurethane foam is used in a wide range of engineering and industrial applications including seating, cushioning, sports and medical equipments, and vibration and sound isolation. To utilize this material effectively, it is important to have a good understanding of its mechanical behavior. This can be accomplished by developing mathematical models which characterize the nonlinear and viscoelastic behavior of foam.

To date, various models with different complexities have been proposed and investigated to capture the foam response under various mechanical loading conditions. These models can generally be categorized into three groups:

- microstructural models,
- continuum models,
- phenomenological models.

As reviewed before, models in the first category are in general complex and mostly used to describe the behavior of foam in linear regions. Most of the models in this category also neglect viscoelastic behavior of the foam. Models in the second category fall into two groups: models which are simple, although they are less effective in modeling the behavior of foam under large strain compression, and models which are complex and effective in modeling the behavior of foam under large strains including compression and shear. Phenomenological models in the third category are built on the simple continuum models. The structure of these models are modified to increase their capabilities in describing the foam behavior.

In this chapter, a model of uniaxial compressive behavior of polyurethane foam is developed. The model is an extension of previously explored traditional foam

models which are often used to describe the uniaxial behavior of polyurethane foam under large compressions. A system identification technique is developed to estimate the parameters of the nonlinear viscoelastic model from experimental data. The experimental data was acquired during a series of cyclic uniaxial compression tests conducted at different compression rates [80]. The performance of the proposed model is also compared to the performance of some other traditional foam models.

In the previous studies, it was observed that when the traditional foam models were fitted to compression test data at different rates, models with different parameters were required. Here, it was initially observed that low-order proposed models were sufficient to model the behavior in individual tests and the model predictions were more accurate compared to previously explored models. It was also shown that the estimated parameter values are simple functions of the compression rates used in experiments. However, by using a higher-order model, it is possible to capture the response accurately for tests at different strain rates by using a model without requiring the parameters to be dependent on strain rate. The model utility in describing polyurethane foam behavior is tested on 4 types of foams including low density car seat foam and high density CONFOR foam. Also, a new methodology is developed to study mechanics of a layered foam system when it is compressed at constant rates. Using the identified comprehensive models, estimated for individual foams in each layer, the strain rate in each layer is computed. It is observed that the strains and strain rates in different layers are different from the input strain and strain rate. Also the stress-time, or stress-strain, responses of the layered system are also predicted and compared to the experimental measurements.

This chapter is composed of three main sections: the first part of this chapter focuses on low density foams, the second part focuses on high density CONFOR foams and finally the last part of this chapter focuses on characterizing the mechanical behavior of layered foam systems. This chapter is organized as follows: experiments conducted to examine the response of polyurethane foam samples in uniaxial compression are described below. This is followed by the development of the new model

along with a short review of the previous models. Next, a identification procedure is introduced and the results of fitting the model to the experimental data are presented. Finally, two successful approaches to modifying the models to address the problem of identified parameters being dependent on strain-rate are developed by: (1) increasing the order of the viscoelastic model to construct a comprehensive model, (2) using low-order models but making the viscoelastic model parameters functions of strain rate. With either approach, it is shown that models can predict responses in all tests. Next, the proposed foam model performance is tested by fitting the model to the experimental data from conducting compression tests on high density CONFOR foams. Also, comprehensive higher order models and comprehensive strain rate dependent models are estimated for CONFOR foams. Then, a method is proposed to predict the mechanical responses of a layered foam system. Then the foam models estimated for individual layers along with the proposed methodology are used to predict the layered foam stress-time (stress-strain) responses and results are compared to the experimental data. The chapter ends with a summary of the research findings.

3.1 Uniaxial Compression Test

In order to study the mechanical behavior of flexible polyurethane foam, uniaxial compression experiments were performed on foam blocks using a MTS 858 Mini Bionix testing machine shown in Fig. 3.1(a). The machine consists of a hydraulic actuator mounted on the cross-head on the machine which drives the upper compression plate following a predetermined path profile in the vertical direction. The displacement of the actuator is measured by a built-in linear variable differential transformer unit (LVDT). A load cell having a maximum capacity of 25 kN is mounted at the base of the machine where the lower stationary compression plate rests. The machine is equipped with a built-in data acquisition system with the anti-aliasing filter cut-off frequency set to 50 Hz and the signals are sampled at the rate of 128 Hz. During the experiment, is was observed that the data acquired by the MTS machine was noisy.

The noise could have been from the hydraulic power pack near the MTS machine and also from the quantization errors in the data acquisition system which was configured to measure much larger forces. To reduce the noise, the acquired data was digitally filtered with a low-pass filter with a cut-off frequency of 5 Hz and was then down sampled by a factor of 10 samples per second.

In this study, uniaxial tests were performed on a 3-inch foam cube (76.2 $mm \times$ 76.2 $mm \times 76.2$ mm). This type of foam is used in car seats and the foam tested has a relative density = 0.027. As foam exhibits time-dependent viscoelastic behavior, the foam sample was left unloaded for at least two days before each test to ensure that the foam block completely recovered [28]. Then, the foam cube was placed on the lower plate of the MTS machine while the actuator followed the path (displacement cycle) depicted in Fig. 3.1(b), compressing the foam sample by 66% (i.e. to 34% of its initial length). The actuator was programmed to move down at a constant rate. To study multi-time scale behavior, tests were conducted at input nominal strain rates ranging from $88 \times 10^{-4}/s$ to $53 \times 10^{-5}/s$ ($T = 150$ s to $T = 2470$ s). Table 3.1 shows the different rates used in each case.

Table 3.1. Compression test conducted at various rates.

Test	T_1	T_2	T_3
Compression Rate ($seconds^{-1}$)	88×10^{-4}	45×10^{-4}	21×10^{-4}
Test	T_4	T_5	T_6
Compression Rate ($seconds^{-1}$)	11×10^{-4}	80×10^{-5}	53×10^{-5}

The stress is calculated by dividing force by the area of the face of the foam block that is in contact with the top plate and the strain is calculated by dividing the displacement of the top plate face from its original uncompressed position at the start of the experiment divided by the height of the foam. The resulting stress versus time and stress versus strain results are shown in Fig. 3.2.

(a)

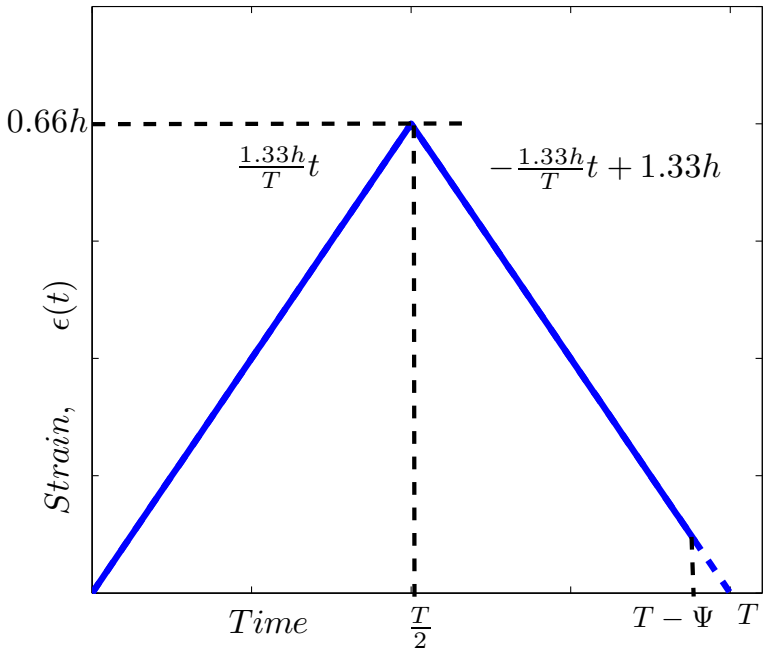

(b)

Figure 3.1. The experimental setup for compression tests on a cubic $76.2mm \times 76.2mm \times 76.2mm$ foam sample and the displacement path profile of the top plate during the compression tests. The top plate looses contact at time $t = T - \Psi$ with the top of the foam. The downward direction is taken to be the positive direction.

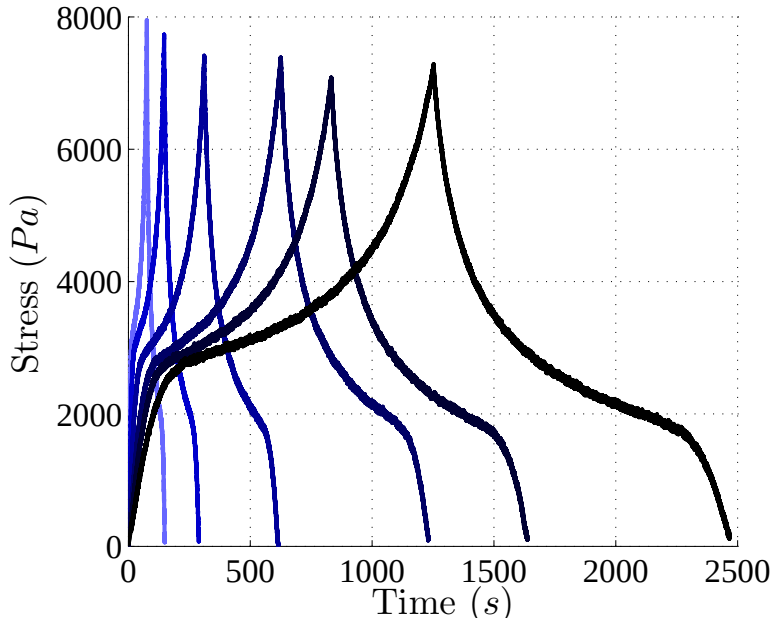

(a)

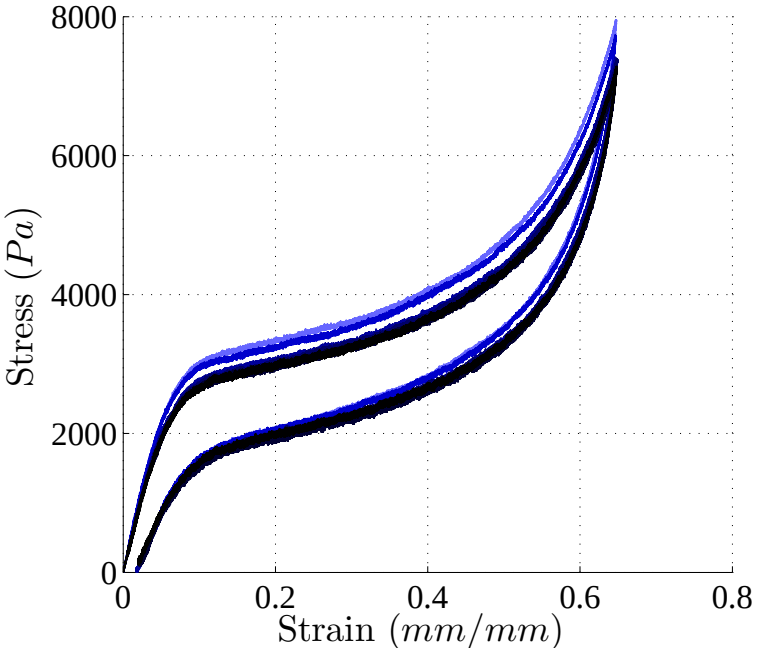

(b)

Figure 3.2. Results of six compression tests of different durations. (a) Stress versus time, and (b) the same data plotted against strain. Light to dark blue indicates decreasing strain rate from $0.0088/s$ to $0.00053/s$.

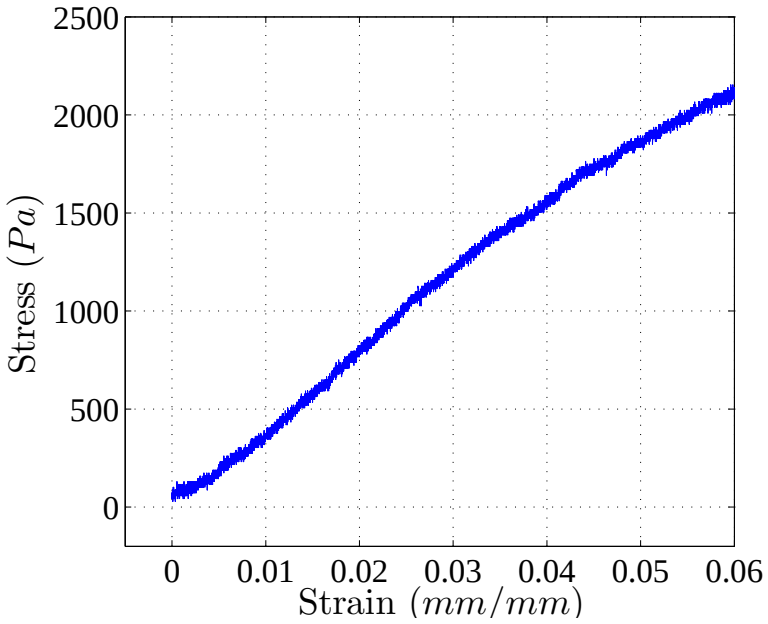

Figure 3.3. Response of the foam block during the initial small strain part of the compression test.

On closer examination of the response at the beginning of the loading cycle (see Fig. 3.3), it is observed that the stress-strain curve is not linear in this low strain region. This can be perhaps explained by noting some local effects in the beginning of compression cycle, e.g. imperfect contact of the compression plate with slightly inclined foam surface, and local buckling of the polyurethane cells exposed on the surface after cutting. In order to remove the effect of this local behavior due to imperfections, the initial part of stress response is linearized by extrapolating the linear portion of the stress strain curve, as illustrated Fig. 3.4(a). Then, the nonlinear initial portion is replaced by the straight line and $t = t_0$ is set to be the time reference, as shown in Fig. 3.4(b). Note that the time duration of the initial nonlinear response is very small (less than 1%) compared to the overall time of test.

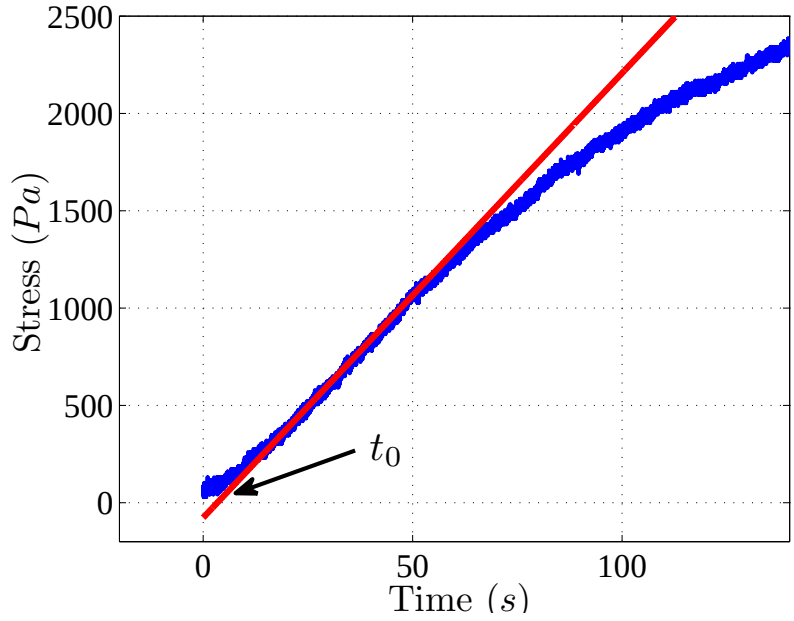

(a)

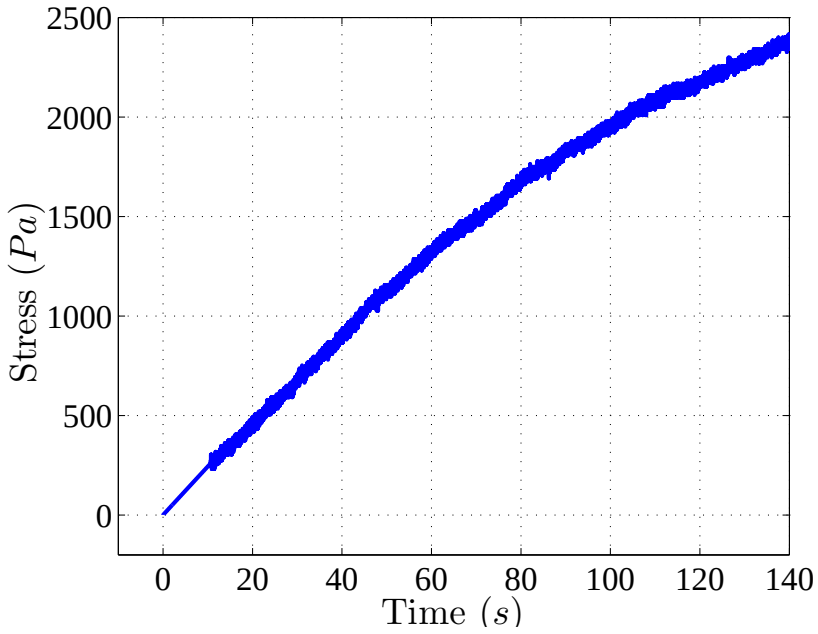

(b)

Figure 3.4. An illustration of linearizing of the initial response in the compression test data. (a) Red line is tangent to the linear section of stress-strain curve observed shortly after the contact is initiated; t_0 is the intersection of red line with zero stress. (b) Adjusted data.

3.2 Mathematical Modeling of Flexible Polyurethane Foam

In order to describe the mechanical behavior of polyurethane foam, mathematical models need to be developed. Over years, many models have been proposed. One example of such models is the continuum hereditary type model which has been reviewed in many publications and has been incorporated in different CAE commercial softwares such as ABAQUS.

In this model, the total measured stress can be decomposed into a nonlinear elastic stress term and a viscoelastic stress term as:

$$\sigma = \sigma_e + \sigma_v, \tag{3.1}$$

where, σ_e and σ_v represent the nonlinear elastic component and the viscoelastic component, respectively. Traditionally, the elastic component σ_e is modeled by Ogden's model for hyperelastic materials. For the case of uniaxial compression and assuming zero lateral strain (zero Poisson's ratio), Ogden's model becomes:

$$\sigma_e = \frac{1}{\epsilon + 1} \sum_{i=1}^{I} \mu_i [(\epsilon + 1)^{\delta_i} - 1], \tag{3.2}$$

where, ϵ is the strain and μ_i, δ_i are the system parameters. For uniaxial tests, the assumption of zero Poisson's ratio is reasonable, as shown in the research conducted by Widdle, Bajaj and Davies [81]. In this study, the elastic component σ_e expressed by Ogden's model, is replaced by a higher order polynomial in strain to facilitate the parameter estimation procedures that are given in Appendix A. Later, the estimated polynomial can be utilized to estimate the Ogden's model parameters following the method developed by Widdle [2] and also used by Deshmukh [3]. Therefore, the elastic term is defined as,

$$\sigma_e = \frac{1}{\epsilon + 1} \sum_{i=1}^{I} \mu_i [(\epsilon + 1)^{\delta_i} - 1] \approx \sum_{i=1}^{N} k_i \epsilon^i, \tag{3.3}$$

where k_i and ϵ are the elastic component parameters and input strain, respectively. The viscoelastic term is modeled using a hereditary type model as

$$\sigma_v = \int_0^t \sum_{j=1}^{M_1} a_j e^{-\alpha_j (t-\tau)} \sigma_e(\tau) d\tau, \tag{3.4}$$

where σ_e is the elastic component and a_j and α_j are the viscoelastic component parameters. The elastic component as well as the viscoelastic parameters can be estimated by fitting Equation (3.1) to the experimental data. The estimation procedure will be explained later in this chapter. The result of fitting the model when $N = 10$ and $M_1 = 1$ to T_1 test data is shown in Figure 3.5(a). The estimation error, i.e. difference between the actual response and the predicted response, is also shown in Figure 3.5(b).

As it is shown, the response prediction matches the measured response in the beginning, in the middle and at the end of the response. It is hypothesized that the estimation error can be modeled by another hereditary type viscoelastic component which is defined by convolving a relaxation kernel with the input strain rate. Note that, for different tests, the input strain rates are constant and the output of the hypothesized additional viscoelastic component is the step response of the second viscoelastic component. Also note that the error term shown in Figure 3.5(b) looks like the step response of a first order dynamic system. In the next section, the foam model given by Equation (3.4) is modified by adding the additional term described above and the performance of the new model is investigated.

3.3 Proposed Model for Flexible Polyurethane Foam

It is assumed that the stress response, σ, of the foam can be decomposed as,

$$\sigma = \sigma_e + \sigma_v = \sigma_e + \sigma_{v1} + \sigma_{v2}, \tag{3.5}$$

where, σ_e and σ_v represent the nonlinear elastic component and the viscoelastic component, respectively. The elastic component σ_e is modeled by a higher order polynomial as described earlier using Equation (3.3). Note that the estimated polynomial can be utilized to estimate the Ogden's model parameters following the method developed by Widdle [2] and also used by Deshmukh [3].

The viscoelastic terms in Equation (3.5) are convolutions of relaxation kernels with functions of strain and/or strain rate (hereditary-type viscoelastic models). Here, σ_v

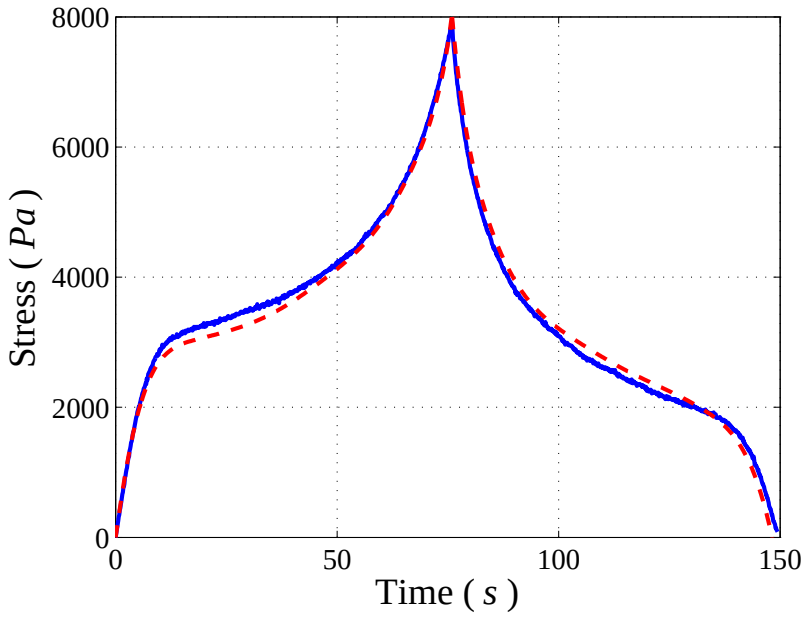

(a)

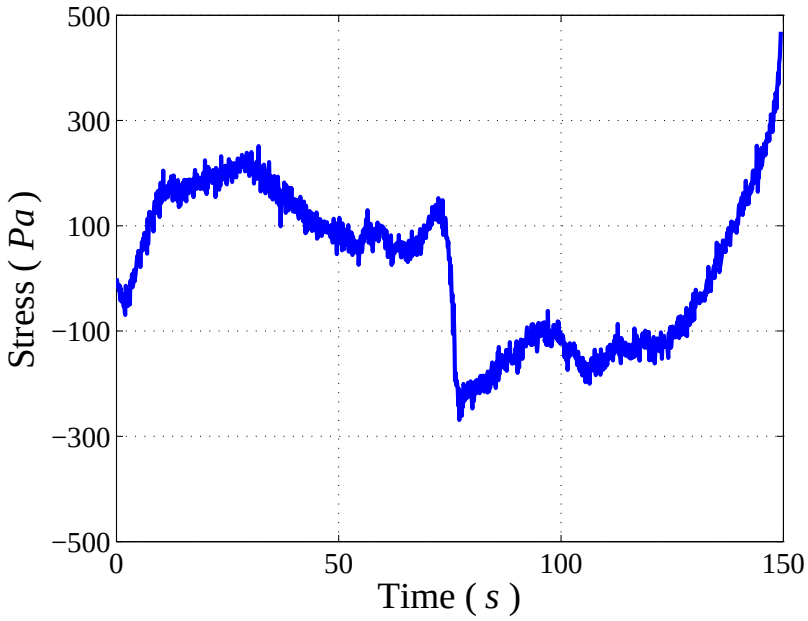

(b)

Figure 3.5. Result of fitting the foam model given by Equation (3.1) to T_1 test data. $N = 10$ and $M_1 = 1$. (a) Blue curve is the experimental data and red curve is the predicted curve based on estimated parameters, (b) difference between experimental data and prediction.

is decomposed into a sum of two viscoelastic terms (σ_{v1} and σ_{v2}): the first viscoelastic term, σ_{v1}, is defined as a convolution of a relaxation kernel and the nonlinear elastic stress component σ_e. The second viscoelastic term, σ_{v2}, is defined as a convolution of a relaxation kernel with strain rate. Thus, the three stress components are in general of the form:

$$\sigma_e = \frac{1}{\epsilon(t)+1}\sum_{i=1}^{I}\mu_i[(\epsilon(t)+1)^{\delta_i}-1] \approx \sum_{i=1}^{N} k_i\epsilon^i(t), \tag{3.6}$$

$$\sigma_{v1} = \int_0^t \sum_{j=1}^{M_1} a_j e^{-\alpha_j(t-\tau)} \sum_{i=1}^{N_2} l_i\epsilon^i(\tau)d\tau, \tag{3.7}$$

$$\sigma_{v2} = \int_0^t \sum_{l=1}^{M_2} b_l e^{-\beta_l(t-\tau)}\dot{\epsilon}(\tau)d\tau. \tag{3.8}$$

Here, k_i, l_i, a_j, b_l, α_j and β_l are elastic and viscoelastic component parameters which are identified by fitting Equation (3.5) to experimental data.

The model described above is comprehensive and can be reduced to the four viscoelastic models studied before [2, 3, 28, 29, 31, 32]. If the first viscoelastic term is set to zero ($\sigma_{v1} = 0$), $\sigma = \sigma_e + \sigma_{v2}$, this is the model explored by Puri in [32] and is referred to as Model 1 throughout this paper. In Model 2, the second viscoelastic term is set to zero ($\sigma_{v2} = 0$) and the nonlinear function inside the first viscoelastic term is replaced by a linear term ($N_2 = 1$ so that $\sigma = \sigma_e + \sigma_{v1L}$); this model was previously studied by Widdle in [2]. If the total stress is defined as a sum of elastic stress σ_e and just the first viscoelastic term σ_{v1} involving convolution with elastic stress σ_e, $N_2 = N$ and $l_i = k_i$, this model is referred to as Model 3 which was studied in the previous section. Finally, if the total stress is defined as a sum of the elastic stress σ_e and both viscoelastic terms σ_{v1} and σ_{v2}, with $N_2 = N$ and $l_i = k_i$, the resulting model is referred to as Model 4. Model 4 is the most comprehensive model derived here and includes the other three models as special cases. These four models are summarized in Tab. 3.2.

In the following section, procedures for estimating the parameters of Model 4, given the values for N, M_1, M_2, and the stress-strain test data, are described. In order to evaluate and demonstrate robustness of the estimation procedure, its ability

to estimate a simulated response with known parameters is studied as well. This parameter estimation method is used to determine the orders of different terms (values of N, M_1, and M_2) necessary to reasonably capture the experimental responses.

Table 3.2. Different nonlinear viscoelastic models of foam.

	Model Description
Model 1	$\sigma = \sigma_e + \sigma_{v2} = \sum_{i=1}^{N} k_i \epsilon^i(t) + \int_0^t \sum_{l=1}^{M_2} b_l e^{-\beta_l (t-\tau)} \dot{\epsilon}(\tau) d\tau$
Model 2	$\sigma = \sigma_e + \sigma_{v1L} = \sum_{i=1}^{N} k_i \epsilon^i(t) + \int_0^t \sum_{j=1}^{M_1} a_j e^{-\alpha_j (t-\tau)} k_L \epsilon(\tau) d\tau$
Model 3	$\sigma = \sigma_e + \sigma_{v1} = \sum_{i=1}^{N} k_i \epsilon^i(t) + \int_0^t \sum_{j=1}^{M_1} a_j e^{-\alpha_j (t-\tau)} \sum_{i=1}^{N} k_i \epsilon^i(\tau) d\tau$
Model 4	$\sigma = \sigma_e + \sigma_{v1} + \sigma_{v2} = \sum_{i=1}^{N} k_i \epsilon^i(t) + \int_0^t \sum_{j=1}^{M_1} a_j e^{-\alpha_j (t-\tau)} \sum_{i=1}^{N} k_i \epsilon^i(\tau) d\tau + \int_0^t \sum_{l=1}^{M_2} b_l e^{-\beta_l (t-\tau)} \dot{\epsilon}(\tau) d\tau$

3.4 Parameter Estimation Procedures

The proposed parameter estimation method for Model 4 is an iterative procedure that consists of two main loops: an inner loop, and an outer loop. The inner loop is used to estimate the parameters of the elastic stress component (k_i) and of the first viscoelastic component (a_j and α_j), i.e. parameters of the first two term in Model 4, while the outer loop estimates of the parameters of the second viscoelastic term (b_j and β_j), i.e. parameters of the third term in Model 4.

3.4.1 Derivation of the Parameter Estimation Equation

The first step is to transform the differential equation form of the model into a discrete-time model by using an impulse invariant mapping of the hereditary kernels [82, 83]. Consider the second viscoelastic term σ_{v2}:

$$\sigma_{v2}(t) = \sum_{l=1}^{M_2} b_l e^{-\beta_l t} * \dot{\epsilon}(t), \tag{3.9}$$

where $(*)$ represents convolution. The impulse response of this system relating $\dot{\epsilon}(t)$ to $\sigma_{v2}(t)$ can be expressed as,

$$g(t) = \sum_{l=1}^{M_2} b_l e^{-\beta_l t}. \tag{3.10}$$

Sampling the impulse response at the sampling frequency f_s (Hz), yields:

$$g(n\Delta) = g_n = \Delta \sum_{l=1}^{M_2} b_l e^{-\beta_l n\Delta}, \tag{3.11}$$

where Δ is the sampling interval in seconds which is the inverse of sampling frequency (f_s). Taking z-transform of Equation (3.11) gives,

$$G(z) = \Delta \sum_{l=1}^{M_2} \frac{b_l}{1 - e^{-\beta_l \Delta} z^{-1}}. \tag{3.12}$$

This can be rewritten as,

$$G(z) = 1 + \frac{F_0 + F_1 z^{-1} + \cdots + F_{M_2-1} z^{-(M_2-1)}}{1 + E_1 z^{-1} + \cdots + E_{M_2} z^{-M_2}}. \tag{3.13}$$

If u_n is the input to this filter and v_n is the output, then the difference equation can be written as:

$$v_n = -E_1 v_{n-1} - \cdots - E_{M_2} v_{n-M_2} + F_0 u_n + \cdots + F_{M_2-1} u_{n-M_2+1}. \tag{3.14}$$

Here, $u_n = \dot{\epsilon}(n\Delta)$ and $v_n = \sigma_{v2}(n\Delta)$. This is an $ARMA$ filter. Note that, the above equation can also be written in terms of a system relating $\epsilon(n\Delta)$ to $\sigma_{v2}(n\Delta)$. However, if $\dot{\epsilon}(n\Delta)$ is used, i.e. Equation (3.14), a digital differentiator needs to be designed to generate this signal from recorded $\epsilon(n\Delta)$. For example, the program $firpm$ in $Matlab$ can be used to design this differentiator. In this work, $\epsilon(t)$ are simple ramps and thus estimating $\dot{\epsilon}(t)$ at $t = n\Delta$ is straight forward. Finally, given the input u_n (or $\dot{\epsilon}(n\Delta)$) and the output v_n (or $\sigma_{v2}(n\Delta)$), Equation (3.14) can be used to develop a system of equations:

$$\begin{bmatrix} v_{M_2+1} \\ \vdots \\ v_{n_{end}} \end{bmatrix} = \begin{bmatrix} v_{M_2} & \cdots & v_1 & u_{M_2+1} & \cdots & u_2 \\ & & \ddots & & & \\ v_{n_{end}-1} & \cdots & v_{n_{end}-M_2} & u_{n_{end}} & \cdots & u_{n_{end}-M_2+1} \end{bmatrix} \begin{bmatrix} E_1 \\ \vdots \\ E_{M_2} \\ F_0 \\ \vdots \\ F_{M_2-1}. \end{bmatrix}. \tag{3.15}$$

This system of equations can be solved to obtain the unknowns E_l and F_l. Then, the partial fraction decomposition of Equation (3.13) is used to identify b_l and β_l in Equation (3.12).

Following the same procedure for the first two terms of Model 4, which are the terms also present in Model 3:

$$\sigma_{m3}(t) \equiv \sigma_e(t) + \sigma_{v1}(t) = \sigma_e(t) + \sum_{j=1}^{M_1} a_j e^{-\alpha_j t} * \sigma_e(t) = \sigma_e(t) * \{\delta(t) + \sum_{j=1}^{M_1} a_j e^{-\alpha_j t}\}. \tag{3.16}$$

The impulse response of this system relating $\sigma_e(t)$ to $\sigma_{m3}(t)$ can be expressed as,

$$h(t) = \delta(t) + \sum_{j=1}^{M_1} a_j e^{-\alpha_j t}, \tag{3.17}$$

where $\delta(t)$ represents unit impulse function. Sampling the impulse response at sampling frequency f_s (Hz), yields:

$$h(n\Delta) = h_n = \Delta[\delta_n + \sum_{j=1}^{M_1} a_j e^{-\alpha_j n\Delta}], \tag{3.18}$$

where Δ is the sampling interval in seconds which is the inverse of sampling frequency (f_s), $\delta_n = 1$ for $n = 0$ and $\delta_n = 0$ if $n \neq 0$. Taking z-transform of Equation (3.18) gives,

$$H(z) = \Delta[1 + \sum_{j=1}^{M_1} \frac{a_j}{1 - e^{-\alpha_j \Delta} z^{-1}}]. \tag{3.19}$$

This can be rewritten as,

$$\begin{aligned} H(z) &= 1 + \frac{B_0 + B_1 z^{-1} + \cdots + B_{M_1-1} z^{-(M_1-1)}}{1 + A_1 z^{-1} + \cdots + A_{M_1} z^{-M_1}} \\ &= \frac{(1 + B_0) + (B_1 + A_1) z^{-1} + \cdots + a_{M_1} z^{-M_1}}{1 + A_1 z^{-1} + \cdots + A_{M_1} z^{-M_1}}. \end{aligned} \tag{3.20}$$

This can be further simplified as,

$$H(z) = \frac{D_0 + D_1 z^{-1} + \cdots + D_{M_1} z^{-M_1}}{1 + C_1 z^{-1} + \cdots + C_{M_1} z^{-M_1}}. \tag{3.21}$$

If x_n is the input to this filter and y_n is the output, then the difference equation can be written as,

$$y_n = -C_1 y_{n-1} - \cdots - C_{M_1} y_{n-M_1} + D_0 x_n + \cdots + D_{M_1} x_{n-M_1}. \tag{3.22}$$

Here, $x_n = \sigma_e(n\Delta)$ and $y_n = \sigma_{m3}(n\Delta)$. Note that this is a (M_1, M_1) $NARMAX$ filter. If $\sigma_e(n\Delta)$ and $\sigma_{m3}(n\Delta)$ are known, Equation (3.22) can be used to develop the following set of equations:

$$\begin{bmatrix} y_{M_1+1} \\ y_{M_1+2} \\ \vdots \\ y_{n_{end}} \end{bmatrix} = \begin{bmatrix} y_{M_1} & \cdots & y_1 & x_{M_1+1} & \cdots & x_1 \\ & & \ddots & & & \\ y_{n_{end}-1} & \cdots & y_{n_{end}-M_1} & x_{n_{end}} & \cdots & x_{n_{end}-M_1} \end{bmatrix} \begin{bmatrix} C_1 \\ \vdots \\ C_{M_1} \\ D_0 \\ \vdots \\ D_{M_1}. \end{bmatrix}, \tag{3.23}$$

where n_{end} is the last sample. The system of equations can be solved to identify C_j and D_j (or A_j and B_j).

Recall that $\sigma_e(n\Delta) = \sum_{i=1}^{N} k_i \epsilon^i(n\Delta)$. Using this, Equation (3.22) can be expanded and reorganized as follows:

$$\begin{aligned} \rho_n &\equiv y_n + C_1 y_{n-1} + \cdots + C_{M_1} y_{n-M_1} \\ &= k_1(D_0\epsilon_n + \cdots + D_{M_1}\epsilon_{n-M_1}) + \cdots + k_N(D_0\epsilon_n^N + \cdots + D_{M_1}\epsilon_{n-M_1}^N). \end{aligned} \tag{3.24}$$

If C_j and D_j are known along with ϵ_n and $y_n = \sigma_{m3}(n\Delta)$, then Equation (3.24) can be used to construct the following system of equations:

$$\begin{bmatrix} \rho_{M_1+1} \\ \vdots \\ \rho_{n_{end}} \end{bmatrix} = \begin{bmatrix} D_0\epsilon_{M_1+1} + \cdots + D_{M_1}\epsilon_1 & \cdots & D_0\epsilon_{M_1+1}^N + \cdots + D_{M_1}^N\epsilon_1 \\ & \ddots & \\ D_0\epsilon_{n_{end}} + \cdots + D_{M_1}\epsilon_{n_{end}-M_1} & \cdots & D_0\epsilon_{n_{end}}^N + \cdots + D_{M_1}^N\epsilon_{n_{end}-M_1} \end{bmatrix} [C_1, \cdots, C_{M_1}, D_0, \cdots, D_{M_1}]^T. \tag{3.25}$$

Finally, the linear regression can be used to estimate the polynomial coefficients k_i.

3.4.2 Iterative Double-Loop Estimation Procedure

There are 3 sets of terms that need to be estimated: parameters of the first viscoelastic term (C_j and D_j), the elastic parameters k_i, and parameters of the second viscoelastic term (E_l and F_l). In the outer loop the parameters E_l and F_l are estimated. In the inner loop, the current estimates of the k_i are first used to construct $\sigma_e(n\Delta)$ and the C_j and D_j are estimated. These estimates are then used to update estimates of the polynomial coefficients k_i. The step by step procedure is as follows:

- Step 0. Form initial estimates for k_i by fitting a N^{th} order polynomial to the average of loading and unloading stress-strain curves. Also, initially assume $\sigma_{v2} = 0$.
- Step 1. Outer loop begins. Subtract σ_{v2} from total stress σ and call it σ_{m3} ($\sigma_{m3} = \sigma - \sigma_{v2}$).

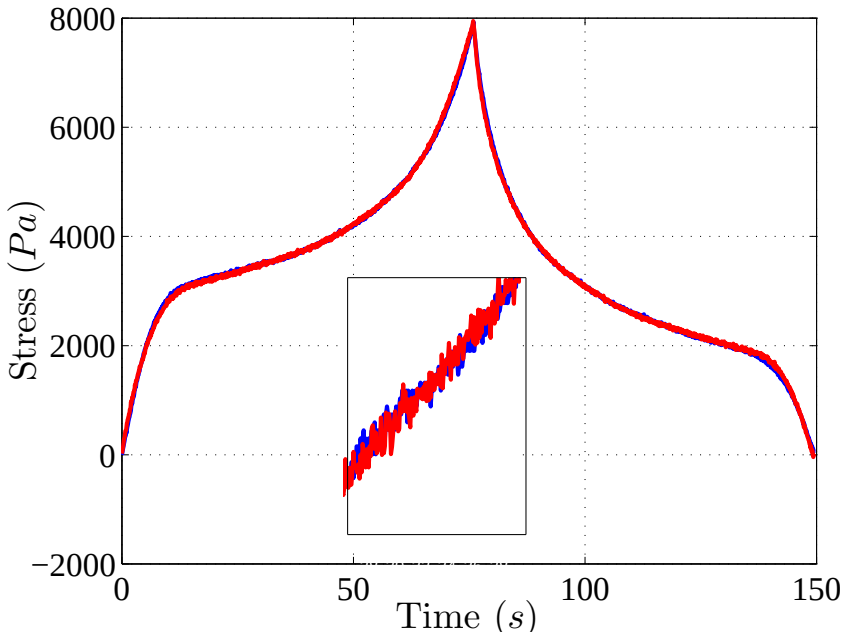

Figure 3.6. Simulated T_1 compression test (strain rate equals $88 \times 10^{-4}\ s^{-1}$) using a model with $N = 10$ and $M_1 = M_2 = 1$. Blue: experiment; Red: simulation.

- Step 2. Inner loop begins.

  a. Estimate the C_j and D_j from Equation (3.23).

  b. Estimate the k_i using Equation (3.25) given C_j and D_j estimated in Step 2a. σ_e is updated.

  c. Steps 2a and 2b are repeated until convergence is achieved (end of inner loop).

- Step 3. Continuing with the outer loop, define $\sigma_{v2} = \sigma - \sigma_{v1} - \sigma_e$ where σ_{v1} and σ_e are estimated in the inner loop.

- Step 4. Estimate E_l and F_l using Equation (3.15).

- Step 5. Repeat step 1 to Step 4 until convergence is achieved (i.e. its parameters) which ends the estimation procedures.

Given the estimated parameters C_j and D_j, the partial fraction decomposition of Equation (3.20) is used to identify parameters of the first viscoelastic term a_j and α_j in Equation (3.19). Similarly, given the estimated parameters E_l and F_l, the partial fraction decomposition of Equation (3.13) is used to identify parameters of the second viscoelastic term b_j and β_j in Equation (3.12).

Above procedures are used to estimate the elastic and viscoelastic parameters of all 6 compression tests. The procedures described above are used to investigate the performance of the parameter estimation algorithm. Six data sets are simulated using Equation (3.5) and the actual estimated parameters from the experiments. The simulated tests are similar to the experimental compression tests with identical input strain rates. In order to simulate the noise present in experimental data, Gaussian distributed random noise is added to the simulated noise-free responses. The mean of the noise signal is zero and the standard deviation is set to be 16% of the average of the response throughout the test. This noise level was chosen because it is similar to the noise levels in the experimental response data. An example of experimental and simulated responses are shown in Fig. 3.6. The estimated parameters for 100 different noise realizations are normalized by their true known values and are presented in Figs. 3.7-3.9 for all 6 tests. These results show that the algorithm is capable of estimating the known system parameters with small error.

3.5 Results

The parameter estimation algorithm is used to estimate the parameters of the foam Model 4 by fitting this model to uniaxial compression tests shown in Fig. 3.2. Compression tests were conducted by compressing a cubic sample of foam to 34% of its original height at the following compression rates: $88 \times 10^{-4}/s$, $45 \times 10^{-4}/s$, $21 \times 10^{-4}/s$, $11 \times 10^{-4}/s$, $80 \times 10^{-5}/s$ and $53 \times 10^{-5}/s$. These six tests are identified as, test T_1,$\cdots$, and T_6, respectively, as shown in Table 3.1.

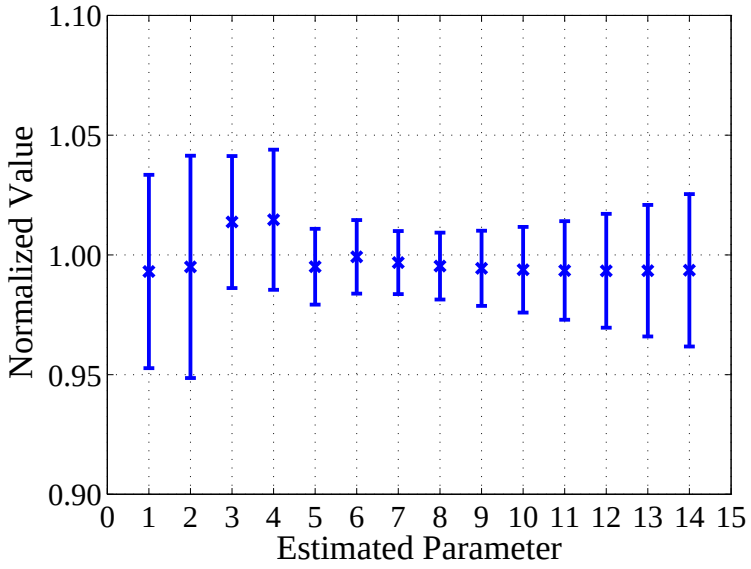

(a)

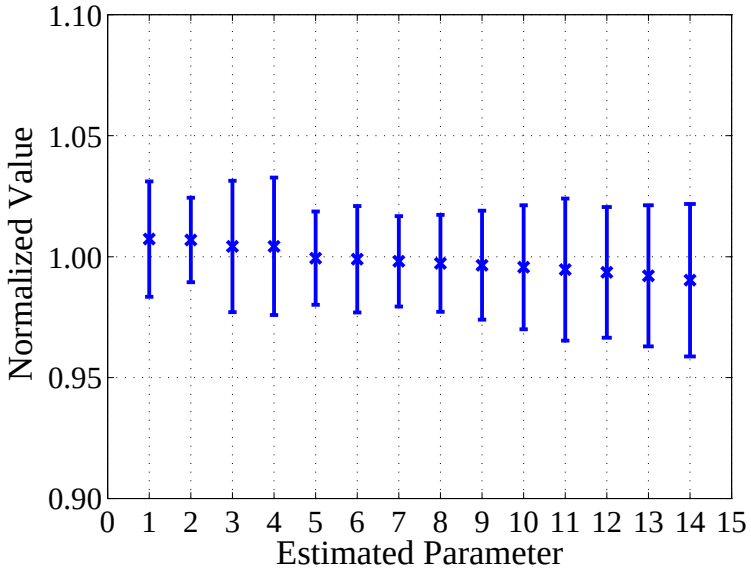

(b)

Figure 3.7. Normalized estimated parameters for 100 noise realizations; x-axis represents the fourteen parameters in the order a, α, b, β, $k_1, \cdots$, and k_{10}: (a) simulated 150 s compression test, and (b) simulated 290 s compression test. The cross represents mean value of the estimated parameters and the bars indicate the standard deviation of the estimates.

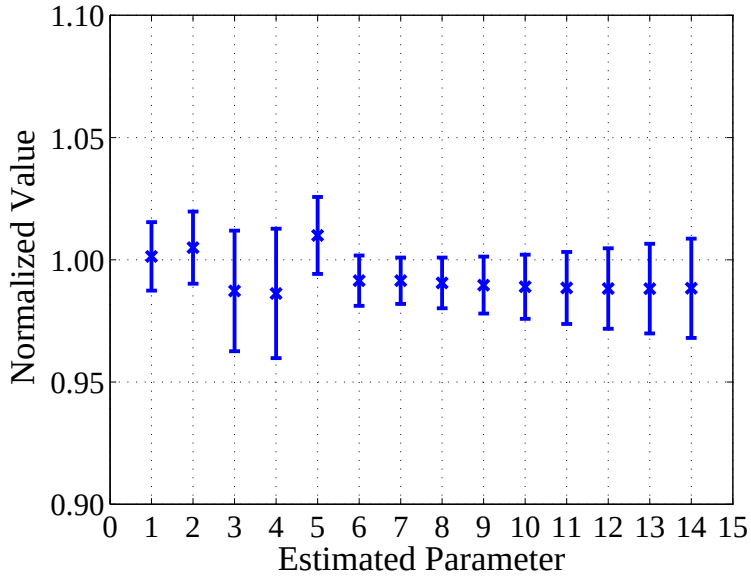

(a)

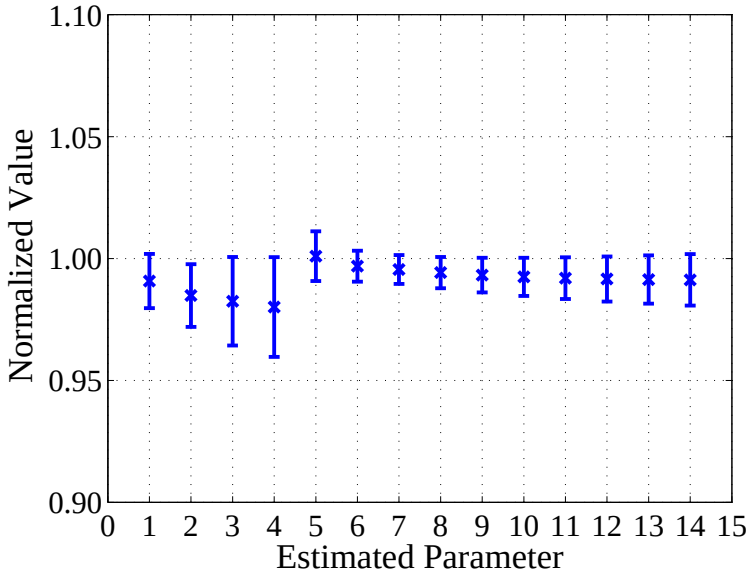

(b)

Figure 3.8. Normalized estimated parameters for 100 noise realizations; x-axis represents the fourteen parameters in the order a, α, b, β, k_1, $\cdots$, and k_{10}: (a) simulated 631 s compression test, and (b) simulated 1233 s compression test. The cross represents mean value of the estimated parameters and the bars indicate the standard deviation of the estimates.

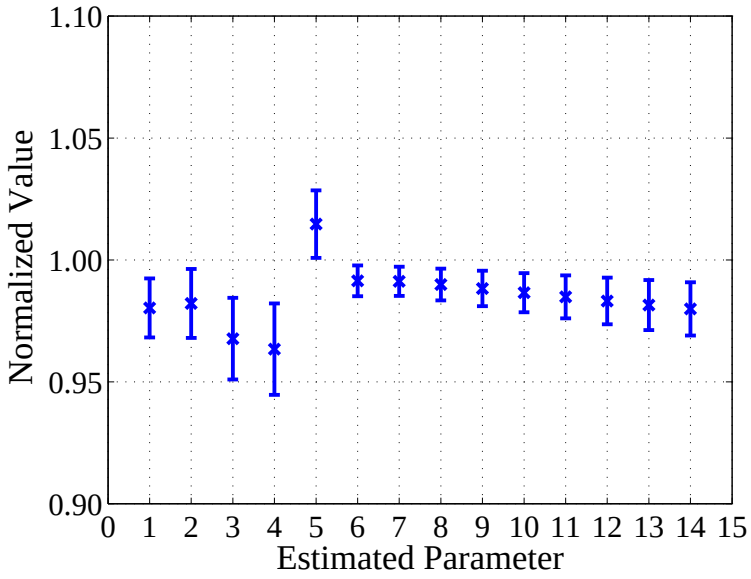

(a)

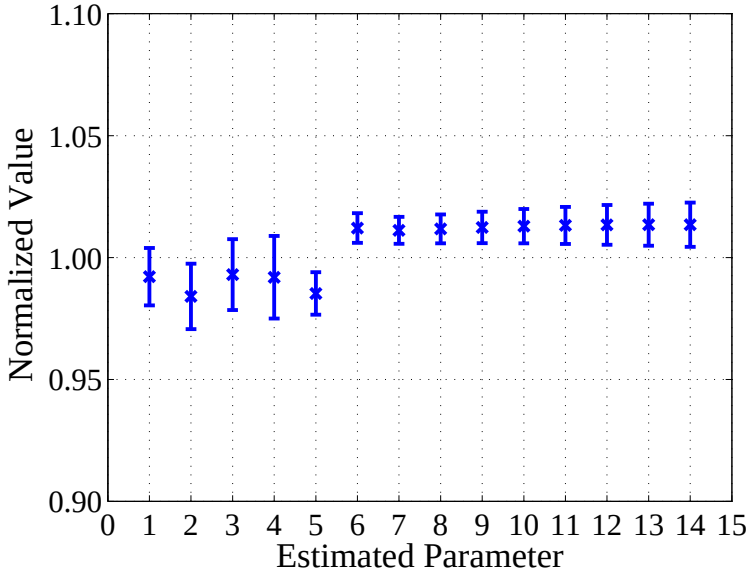

(b)

Figure 3.9. Normalized estimated parameters for 100 noise realizations; x-axis represents the fourteen parameters in the order a, α, b, β, $k_1, \cdots$, and k_{10}: (a) simulated 1233 s compression test, and (b) simulated 1650 s compression test. The cross represents mean value of the estimated parameters and the bars indicate the standard deviation of the estimates.

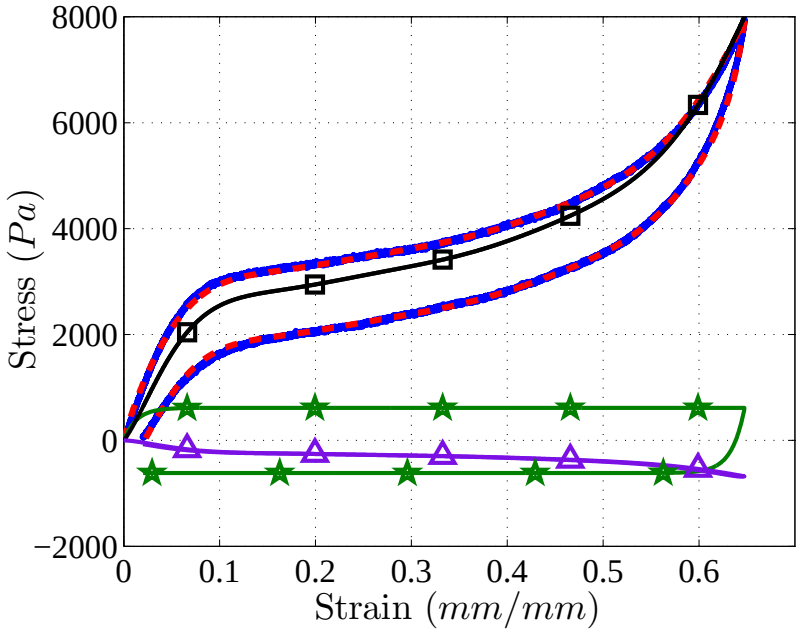

(a)

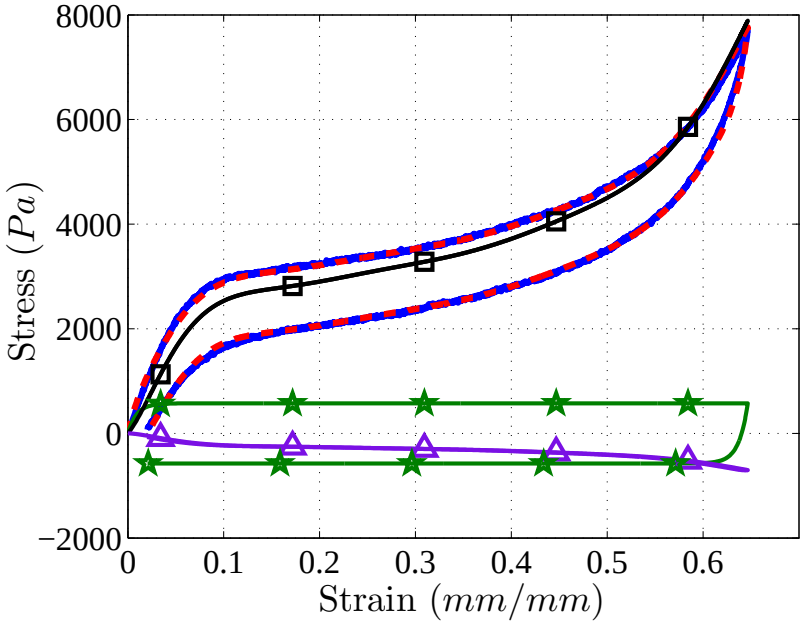

(b)

Figure 3.10. Response prediction resulting from fitting Model 4 ($N = 10$ and $M_1 = M_2 = 1$) to data from tests: (a) T_1, and (b) T_2. Solid blue: experimental data; dashed red: predicted response; black (square): elastic component σ_e; purple (triangle): first viscoelastic component σ_{v1}; and green (star): second viscoelastic component σ_{v2}.

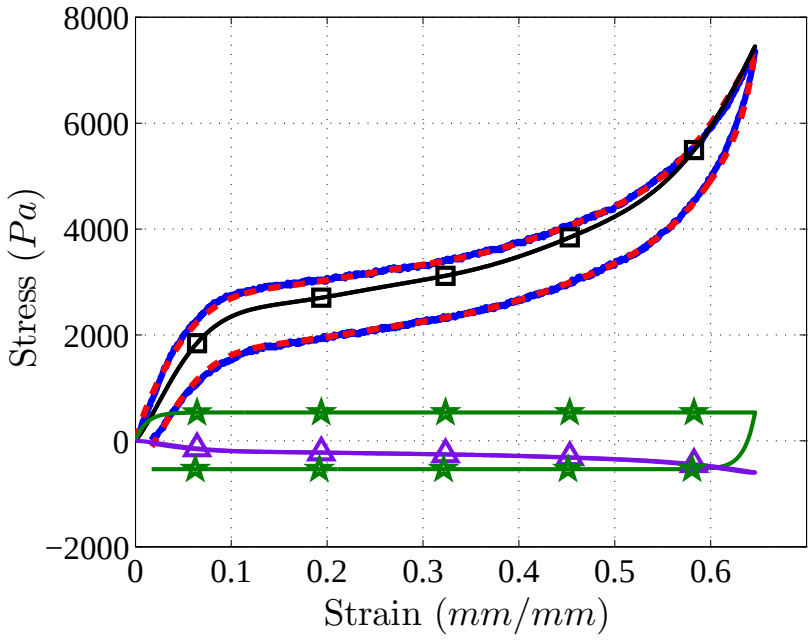

(a)

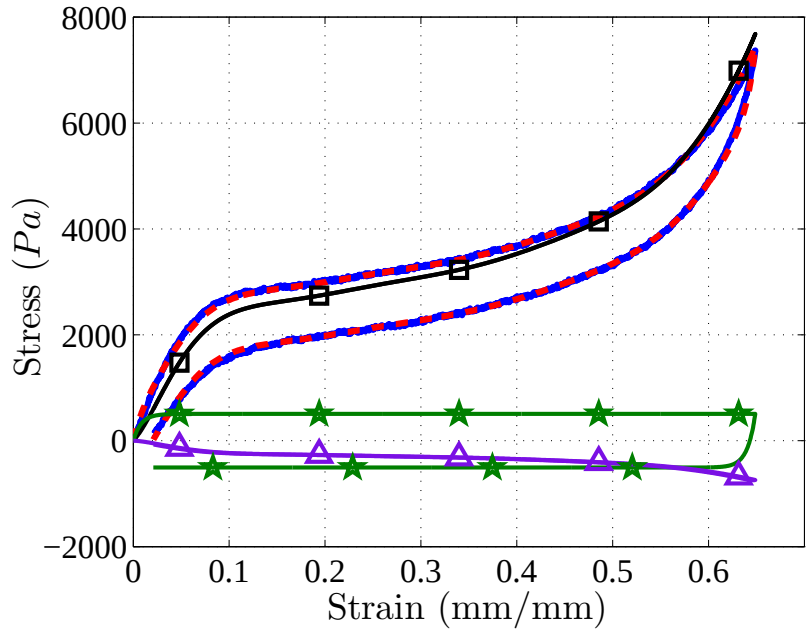

(b)

Figure 3.11. Response prediction resulting from fitting Model 4 ($N = 10$ and $M_1 = M_2 = 1$) to data from tests: (a) T_3 and (d) T_3. Solid blue: experimental data; dashed red: predicted response; black (square): elastic component σ_e; purple (triangle): first viscoelastic component σ_{v1}; and green (star): second viscoelastic component σ_{v2}.

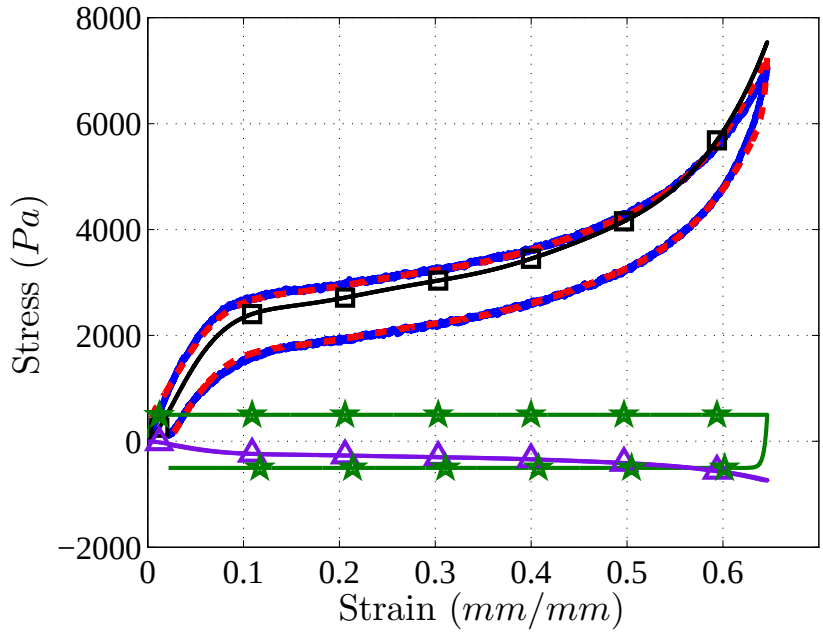

(a)

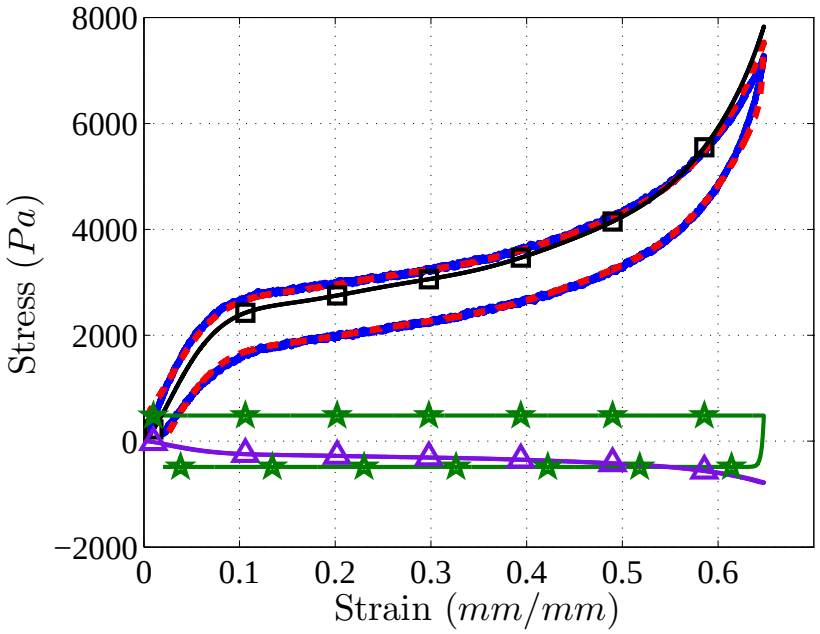

(b)

Figure 3.12. Response prediction resulting from fitting Model 4 ($N = 10$ and $M_1 = M_2 = 1$) to data from tests: (a) T_5 and (b) T_6. Solid blue: experimental data; dashed red: predicted response; black (square): elastic component σ_e; purple (triangle): first viscoelastic component σ_{v1}; and green (star): second viscoelastic component σ_{v2}.

Table 3.3. Estimates of the viscoelastic parameters in Model 4. Estimates were calculated using data from the first four tests (T_1, T_2, T_3, and T_4). To obtain similar prediction accuracy in the longer duration tests, more viscoelastic terms are needed (see Table 3.5). $\pm$ represents the standard deviation of the estimates given in Figs. 3.8 and 3.9.

	α_1	β_1	a_1	b_1
T_1	1.48±0.06	0.55±0.02	-0.103±0.004	38810±970
T_2	0.96±0.01	0.38±0.01	-0.083±0.002	49750±1500
T_3	0.542±0.008	0.267±0.005	-0.0451±0.0005	65523±1310
T_4	0.319±0.003	0.166±0.002	-0.0281±0.0003	78939 ±790

The parameter estimation procedure explained above is iterative and used to iteratively estimate the system parameters for all 6 tests (T_1,$\cdots$, and T_6). The estimated responses and the estimated components, i.e. σ_e, σ_{v1}, σ_{v2}, are shown in Figs. 3.10 to 3.12, respectively. For each of the six tests, the number of terms in the elastic and viscoelastic parts of the model were chosen to be: $N = 10$ (a 10^{th} order polynomial describes the elastic behavior), $M_1 = 1$ and $M_2 = 1$. The corresponding estimated parameters are reported in the Tables 3.3 and 3.4.

The estimated parameters vary during the iterative process. Convergence of the parameters as a function of iterations for a typical set of test data is illustrated in Figs. 3.13 and 3.14. It is assumed that the parameter estimates have converged when

Table 3.4. Estimated elastic parameters for Model 4 for T_1 where $N = 10,\ M_1 = 1,\ M_2 = 1.$ $\pm$ represents the standard deviation of the estimates given in Figs. 3.8 and 3.9.

$k_1 \times 10^4$ (N/m^2)	$k_2 \times 10^5$ (N/m^2)	$k_3 \times 10^7$ (N/m^2)	$k_4 \times 10^8$ (N/m^2)	$k_5 \times 10^8$ (N/m^2)
2.51±0.05	5.59±0.12	-1.24±0.03	1.07±0.03	-5.25±0.16
$k_6 \times 10^9$ (N/m^2)	$k_7 \times 10^9$ (N/m^2)	$k_8 \times 10^9$ (N/m^2)	$k_9 \times 10^9$ (N/m^2)	$k_{10} \times 10^8$ (N/m^2)
1.57±0.05	-2.97±0.11	3.44±0.14	-2.23±0.10	6.20±0.28

the variation in the past 5 iterations is less than 0.01% of the current estimates. The assumption is important as temporary convergence, e.g. see estimated β_1 after 10 iterations in Figure 3.14(b), can occur and can lead to false estimations.

As shown in Figs. 3.10(a)-3.11(b), the response predictions from the estimated models (Model 4: $N = 10$, $M_1 = 1$ and $M_2 = 1$) closely match the measured response data with $R^2 = 0.999$. Here the R^2 value is computed by first computing the mean of the actual response as,

$$\mu_S = \frac{1}{n}\sum_{i=1}^{n} S_i, \tag{3.26}$$

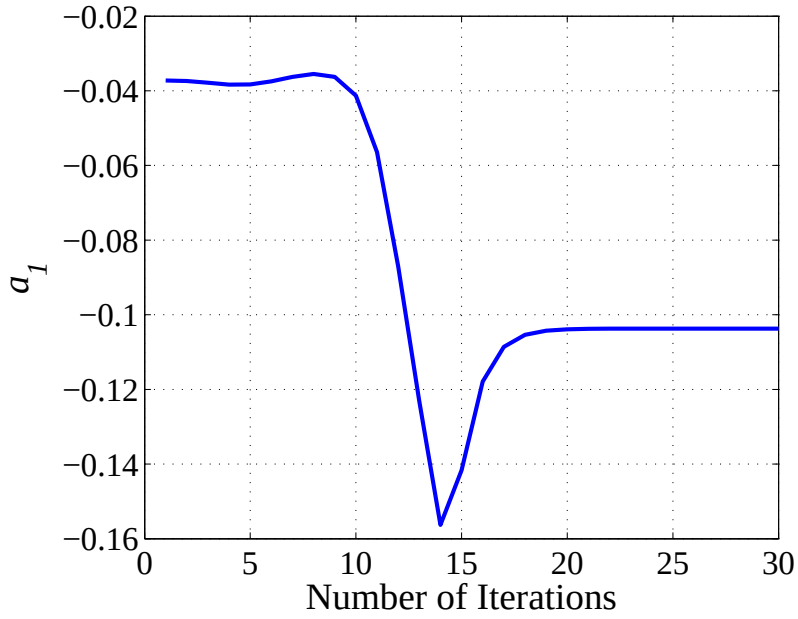

(a)

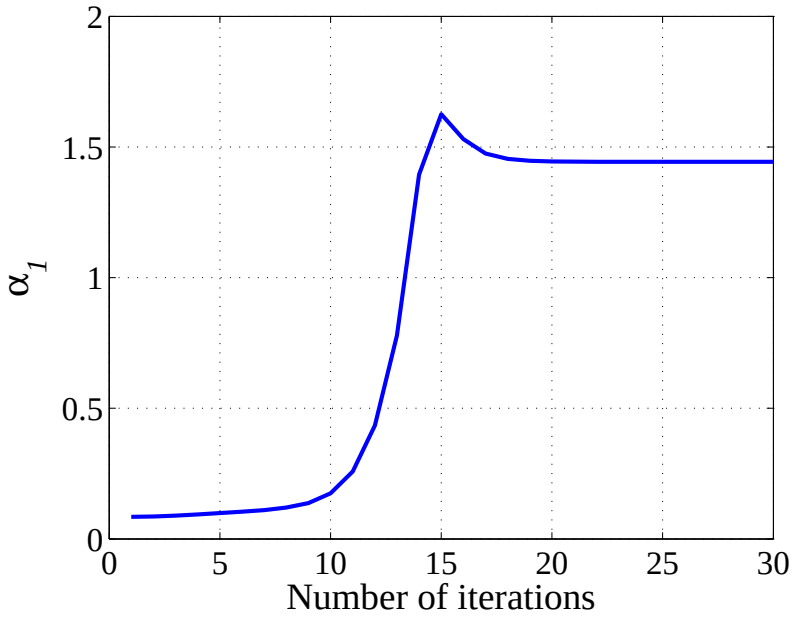

(b)

Figure 3.13. Convergence of the estimated parameters of the first viscoelastic term (a_1 and α_1) during internal loop for a typical data set.

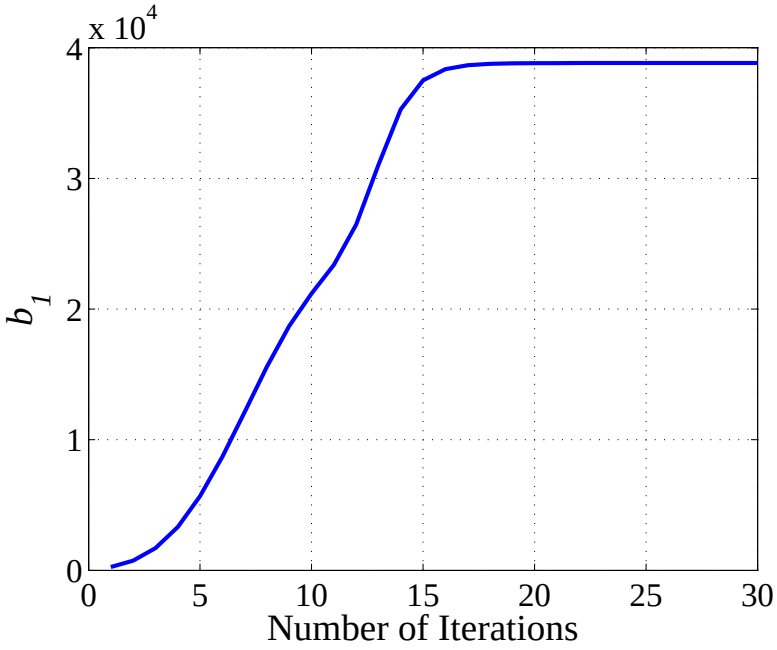

(a)

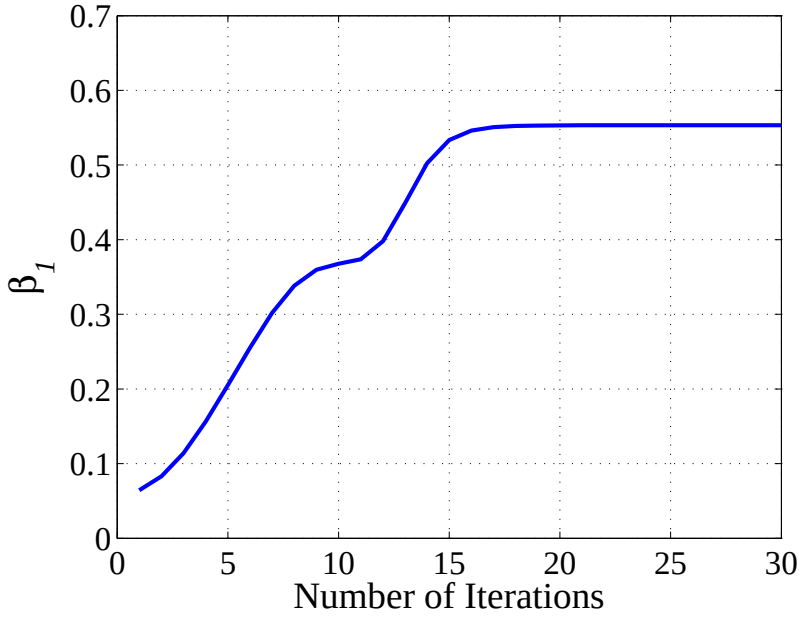

(b)

Figure 3.14. Convergence of the estimated parameters of the first viscoelastic term (b_1 and β_1) during internal loop for a typical data set.

where n is the length of the measured response signal S. Then the sum of squares of residues is computed as,

$$S_{RES} = \sum_i (S_i - \bar{S}_i). \tag{3.27}$$

Here, $\bar{S}$ is the predicted response. The total sum of squares is then computed as

$$S_{TOT} = \sum_i (S_i - \mu_S). \tag{3.28}$$

Finally, the coefficient of determination R^2 is,

$$R^2 = 1 - \frac{S_{RES}}{S_{TOT}}. \tag{3.29}$$

3.5.1 Higher-Order Models

For tests with longer durations, T_5 and T_6, it is observed that a model with two viscoelastic terms ($N = 10$, $M_1 = 1$, and $M_2 = 1$) is not sufficient to capture the foam behavior and the estimated responses deviate from the experimental data at the beginning and in the middle region where there is reversal in loading, as shown in Figs. 3.15(a) and 3.15(b). In this case, the estimated time constant for the second viscoelastic term ($\frac{1}{\beta_1}$) is 5.47 s which is very small compared to the T_6 test duration of 2470 s. Therefore, the second viscoelastic term vanishes very fast. This problem can be solved by including more viscoelastic terms in the second viscoelastic component σ_{v2}. Figure 3.16 shows how the beginning and the middle of the predicted response improves as more terms are included in the second viscoelastic term. Here, M_2 was varied between 1 to 9. It is observed that by including more terms, $M_2 > 5$, the response predictions reach a limit and beyond it all results are almost similar.

The response prediction resulting from a fit of Model 4 with $N = 10$, $M_1 = 1$ and $M_2 = 5$ to T_6 test data is shown in Fig. 3.17. It is clear that the error in the response prediction is much smaller with this higher order second viscoelastic component. Increasing the number of terms in this component beyond 5 did not lead to better response predictions. The results for T_5 test data (not shown) are similar

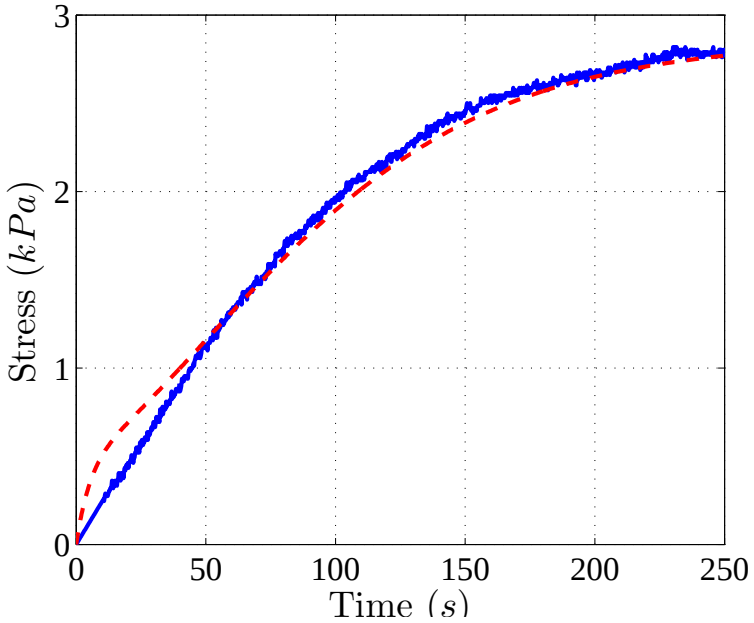

(a)

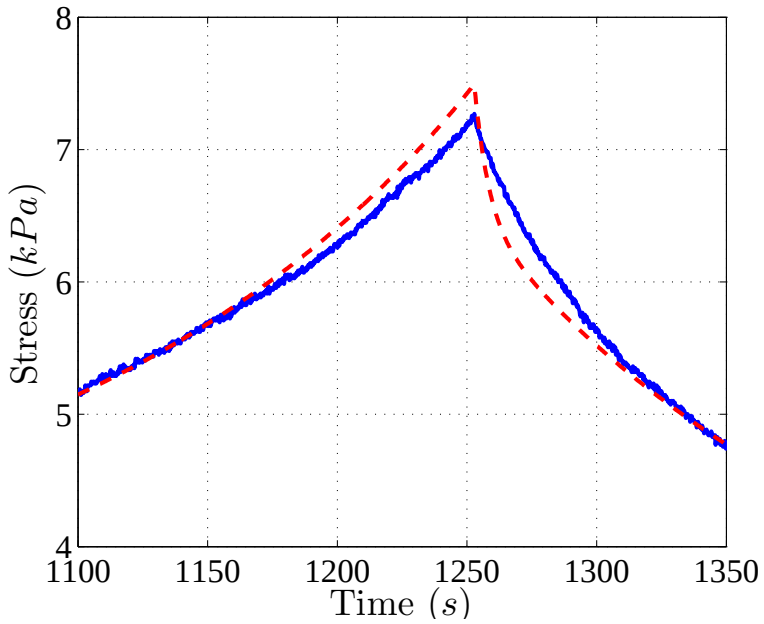

(b)

Figure 3.15. Stress versus time results for (a) Low strain region, and (b) the high stress region. Solid blue: T_6 test (slowest test), and dashed red: predicted response for Model 4 with $M_1 = M_2 = 1$ and $N = 10$.

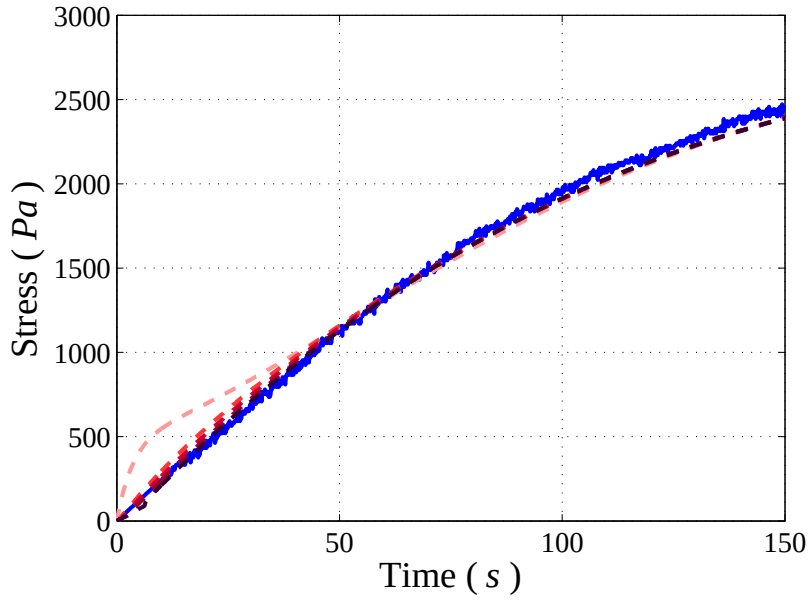

(a)

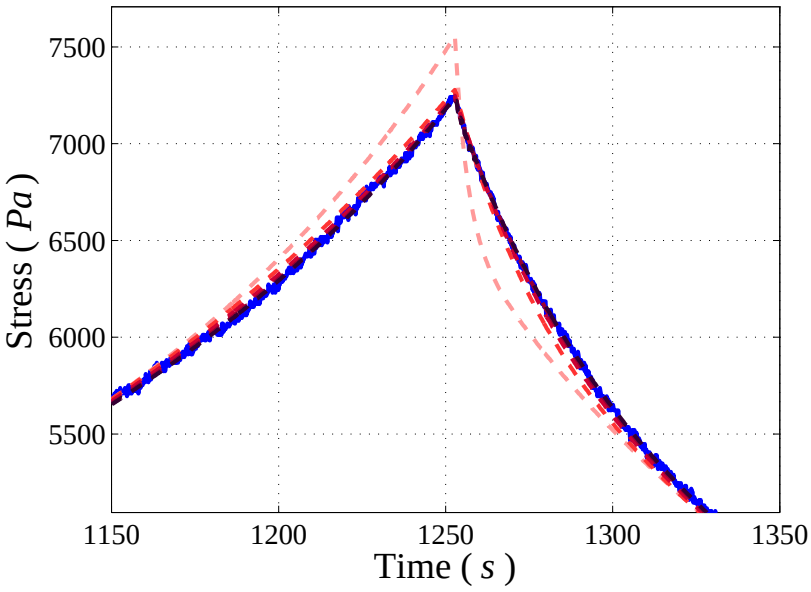

(b)

Figure 3.16. Predicted responses for T_6 test when more terms are included in the second viscoelastic term. Light to dark red indicates increasing M_2 from 1 to 9. (a) the beginning of the response, and (b) the middle of the response.

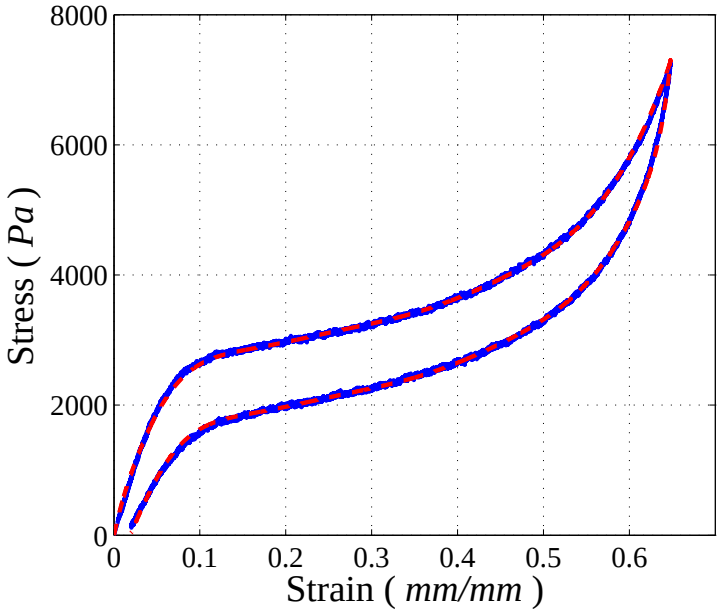

Figure 3.17. Response predictions resulting from Model 4 to data captured in T_6 with $N = 10$, $M_1 = 1$ and $M_2 = 5$. Solid blue: T_6 test (slowest test), dashed red: predicted response.

with the higher order model. The estimated parameters for the model fits to T_5 and T_6 test data are given in Tab. 3.5. Note that the estimated $\beta_2, \cdots, \beta_5$ are complex conjugates. Here the real part of β represents the inverse of the relaxation time. Also in general, the real and the imaginary parts can be related to the damping coefficient as well as the frequency of response. For more details see [31].

Model 4 structure produced the best fits to the data in all tests. The response predictions from all models estimated using T_1 test data are shown in Figs. 3.19 and 3.20. Model 1 and Model 4 give the best fit quality with R^2 values of 0.998 and 0.999, respectively. Model 2 and Model 3 also predict the foam response with R^2 value of 0.989 and 0.991, respectively. Similar results were obtained when all four models were fitted to other test data, from which it is concluded that Model 4 gives the best fit quality among all models considered.

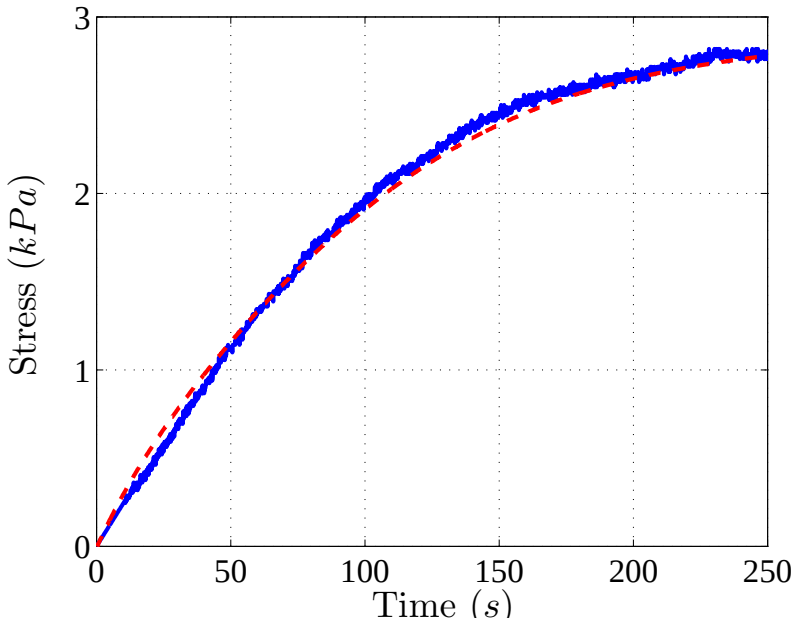

(a)

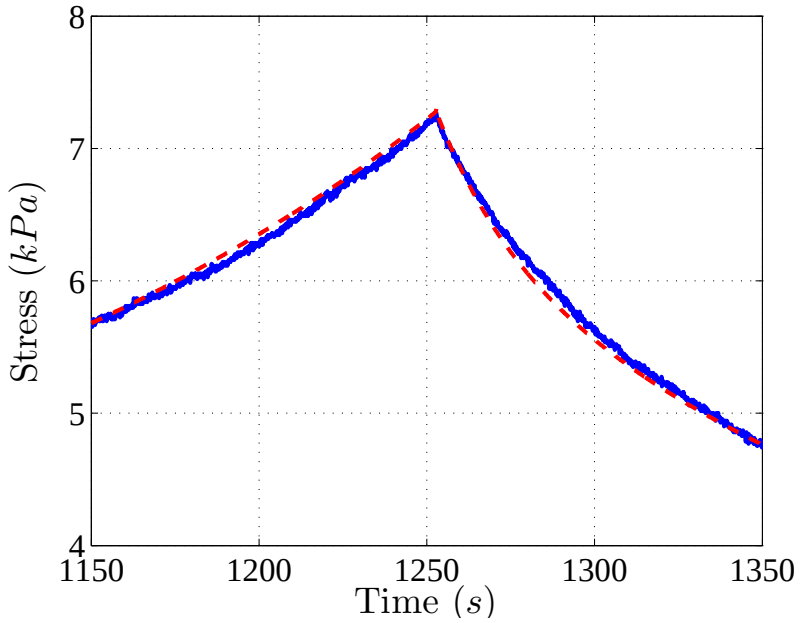

(b)

Figure 3.18. Response predictions resulting from Model 4 to data captured in T_6 with $N = 10$, $M_1 = 1$ and $M_2 = 5$. (a) low strain region (start of test), and (b) high stress region. Solid blue: T_6 test (slowest test), dashed red: predicted response.

Table 3.5. Estimated viscoelastic parameters for Model 4 for tests T_5 and T_6 where $N = 10$, $M_1 = 1$, and $M_2 = 5$. $\pm$ represents the standard deviation of the estimates given in Figs. 3.8 and 3.9.

	α_1	$\beta_1,\cdots,\beta_5$	a_1	$b_1,\cdots,b_5$
T_5	1.40	0.051 2.20±6.96i 2.48±13.00i	-0.152	3.34 -3.25±1.53 2.53±6.52
T_6	1.07	0.041 1.89±5.76i 2.27±10.91i	-0.123	38720 -98550±16410 130750±105620

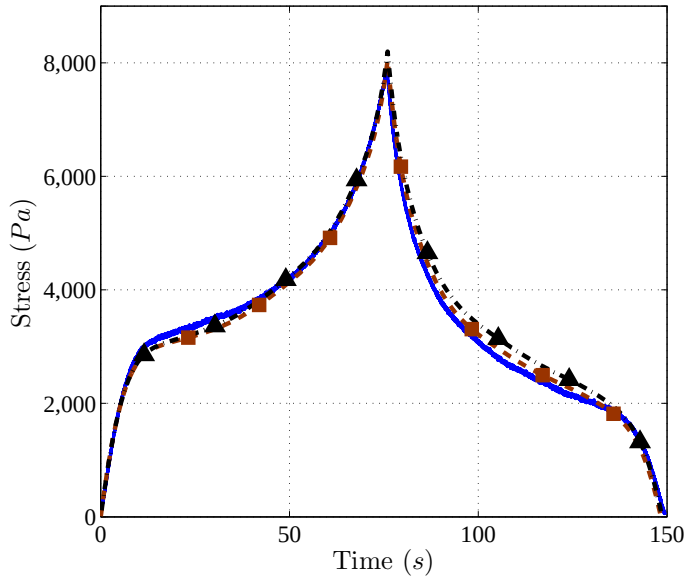

(a)

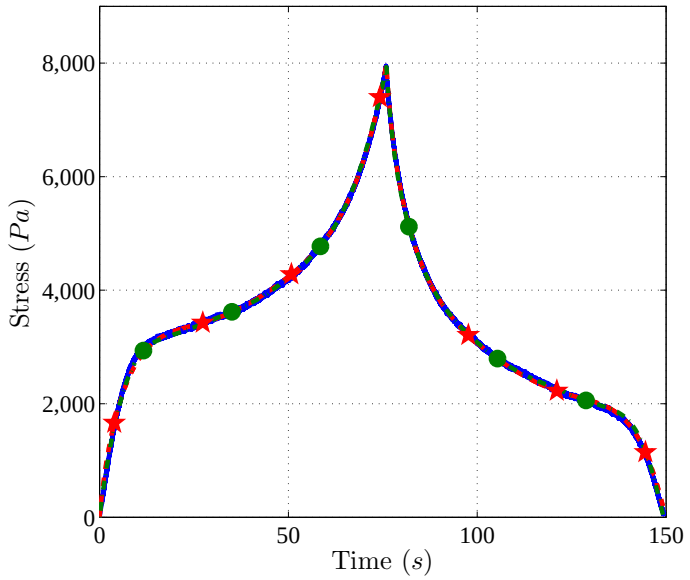

(b)

Figure 3.19. Predictions of the response resulting from fitting all four models to T_1 test data. Experimental data (blue) and Model 1 (red/star), Model 2 (black/triangle), Model 3 (brown/square) and Model 4 (green/circle) fits. Complete response and (a) Models 2 and 3 estimations and (b) Models 1 and 4 estimations.

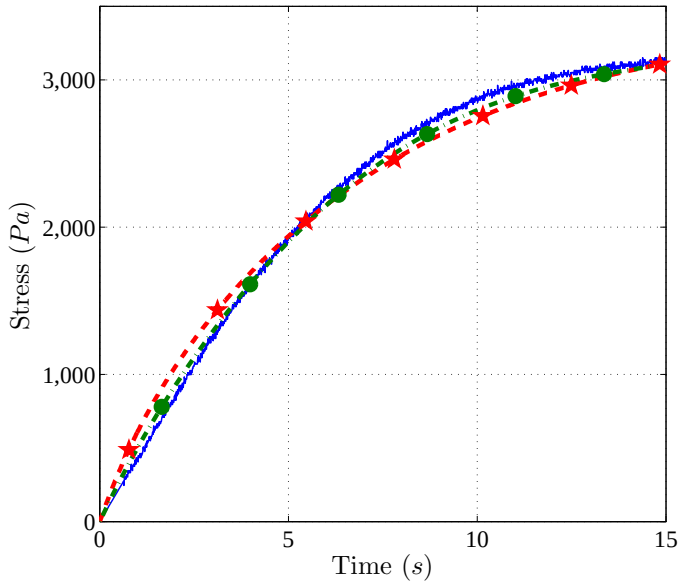

(a)

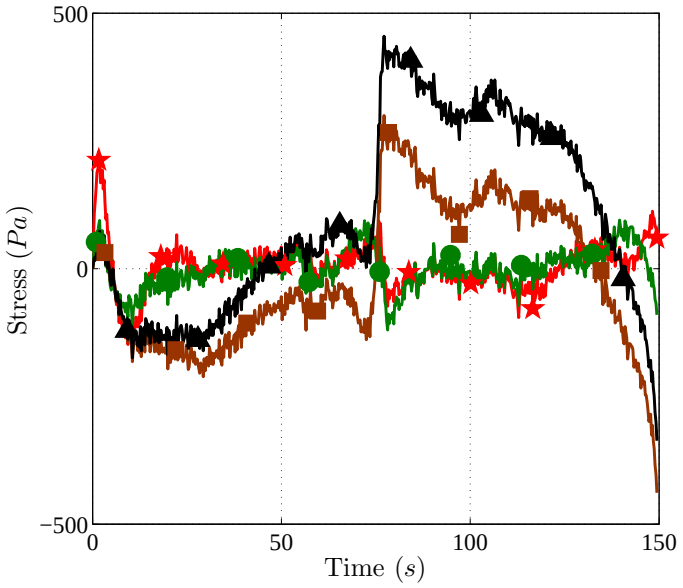

(b)

Figure 3.20. Predictions of the response resulting from fitting all four models to T_1 test data. Experimental data (blue) and Model 1 (red/star), Model 2 (black/triangle), Model 3 (brown/square) and Model 4 (green/circle) fits. (a) the response at the start of the test and (b) estimation errors with different models.

3.5.2 Models with Strain-Rate Dependant Parameters

As is observed in Tables 3.3 and 3.5, the estimated system parameters depend on the strain rate and so can be expressed as a function of strain rates. Simple linear functions can be developed to express the relationship between the estimated parameters and the input strain rates for the first four tests, T_1,$\cdots$,T_4. Examples of such functions are presented in Figs. 3.21 and 3.23 where dots represent the estimated parameters reported before in Table 3.3 and dashed lines are the fitted functions. These four functions are expressed as:

$$a = -9.2\dot{\epsilon} - 0.027, \tag{3.30}$$

$$\alpha = 147.1\dot{\epsilon} + 0.21, \tag{3.31}$$

$$\frac{1}{b} = 1.6 \times 10^{-3}\dot{\epsilon} + 1.16 \times 10^{-5}, \tag{3.32}$$

$$\beta = 47.2\dot{\epsilon} + 0.14. \tag{3.33}$$

The predicted elastic stress from each of the four estimated models are shown in Fig. 3.23. These change very little with strain rate. Note that because the model order was different for tests T_5 and T_6, the parameters for those tests are not included in the development of strain-rate dependent models of the viscoelastic parameters.

In the next section, parameter estimation method is modified to estimate a model with the same set of system parameters utilizing all six data sets simultaneously. This is accomplished by assuming a more complicated model, i.e. a model with many more viscoelastic terms.

3.5.3 Estimation of Parameters for a Global Model

In the previous section, it was shown that estimated models with the structure of Model 4 produced the best predictions of the measured responses. It was also shown that the estimated viscoelastic model parameters could be expressed as linear functions of strain rate. Strain-rate dependency of estimated parameters can be

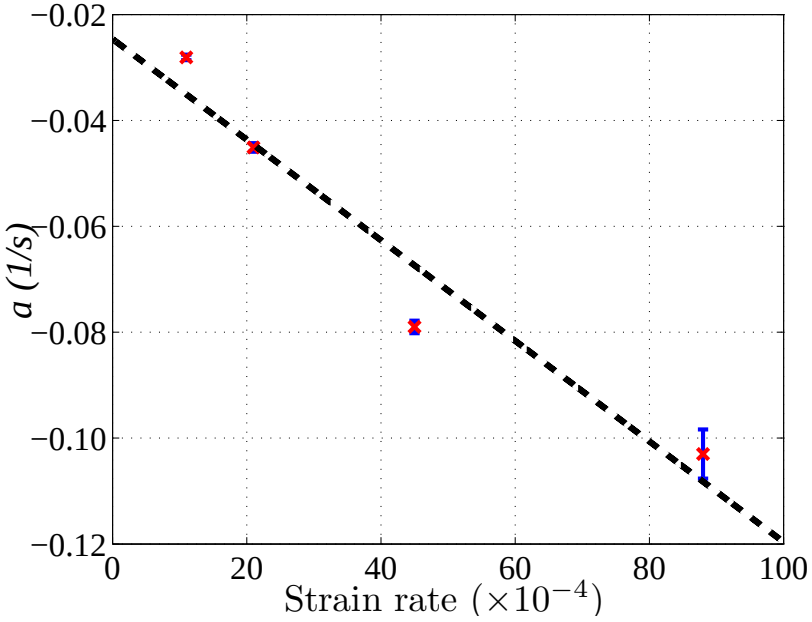

(a)

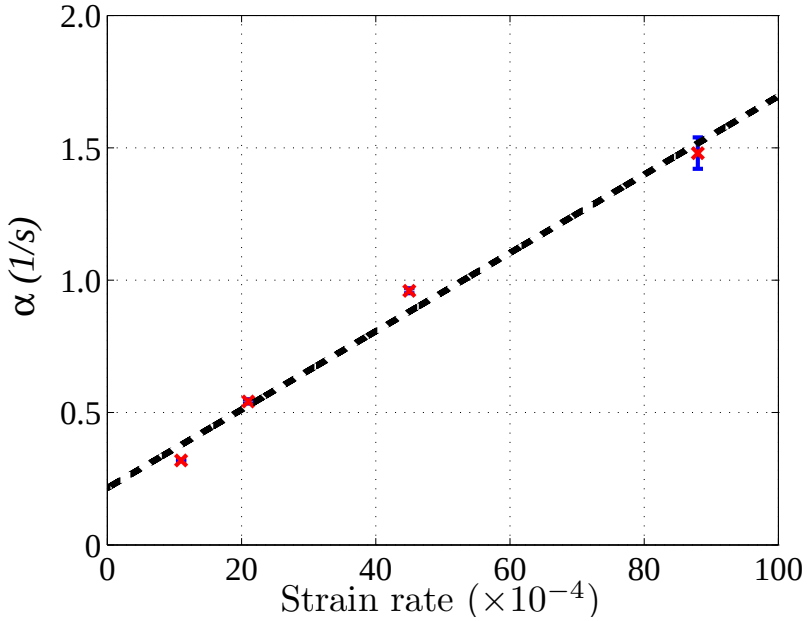

(b)

Figure 3.21. Fitting simple functions to the estimated parameters of the first viscoelastic component as functions of input strain rates: (a) $a(\dot{\epsilon})$, and (b) $\alpha(\dot{\epsilon})$. Red crosses represent the estimated parameters. Black line is the fitted functions.

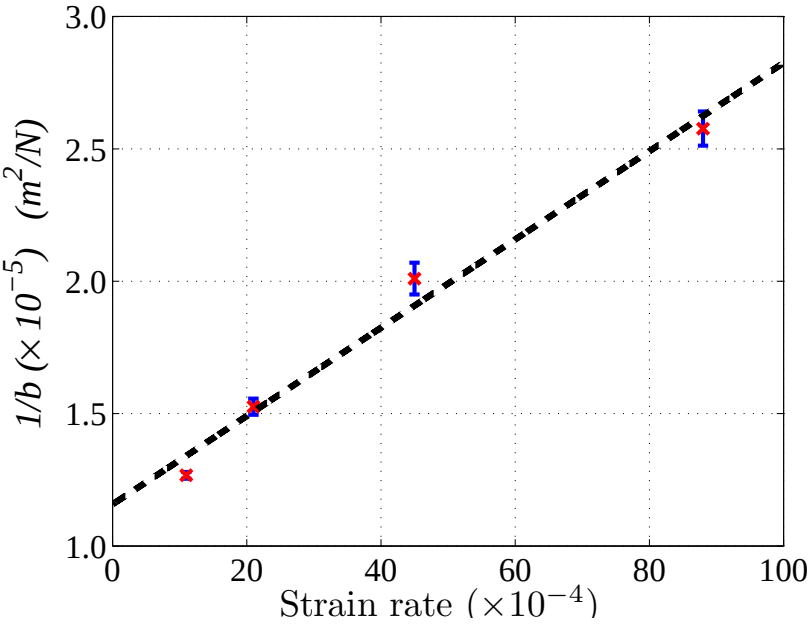

(a)

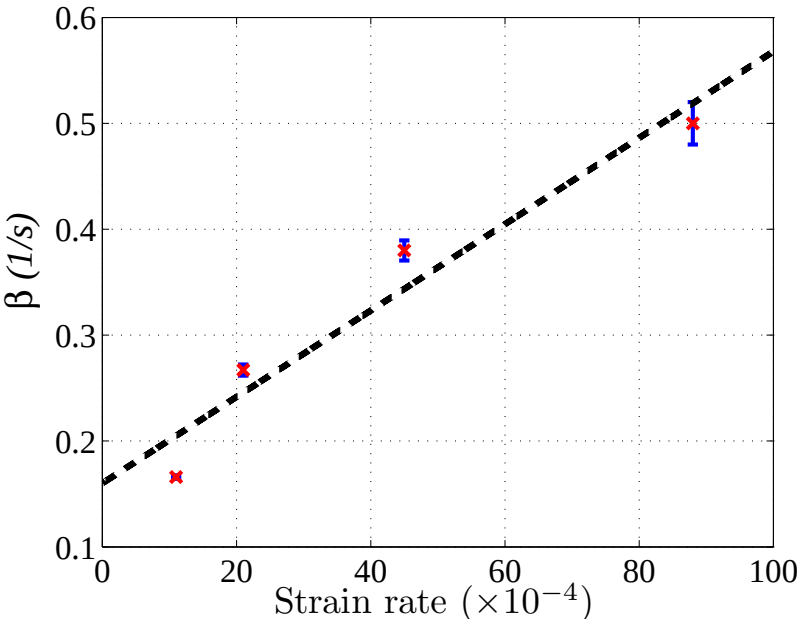

(b)

Figure 3.22. Fitting simple functions to the estimated parameters of the second viscoelastic component as functions of input strain rates: (a) $b(\dot{\epsilon})^{-1}$, and (b) $\beta(\dot{\epsilon})$. Red crosses represent the estimated parameters. Black line is the fitted functions.

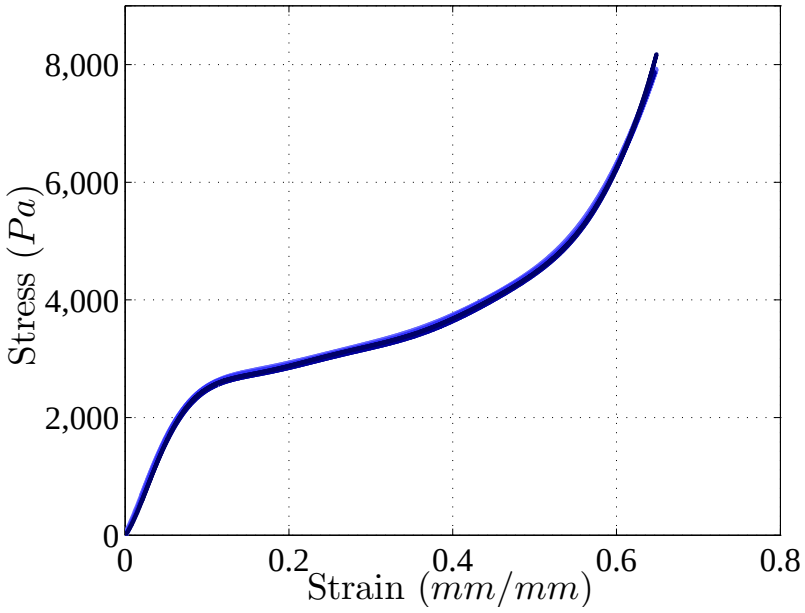

Figure 3.23. Estimated elastic stress σ_e for $T_1,\cdots,T_4$ ($N = 10,\ M_1 = 1$, and $M_2 = 1$). Light to dark blue curves indicate increasing strain rate from 0.0011 s^{-1} to 0.0088 s^{-1}.

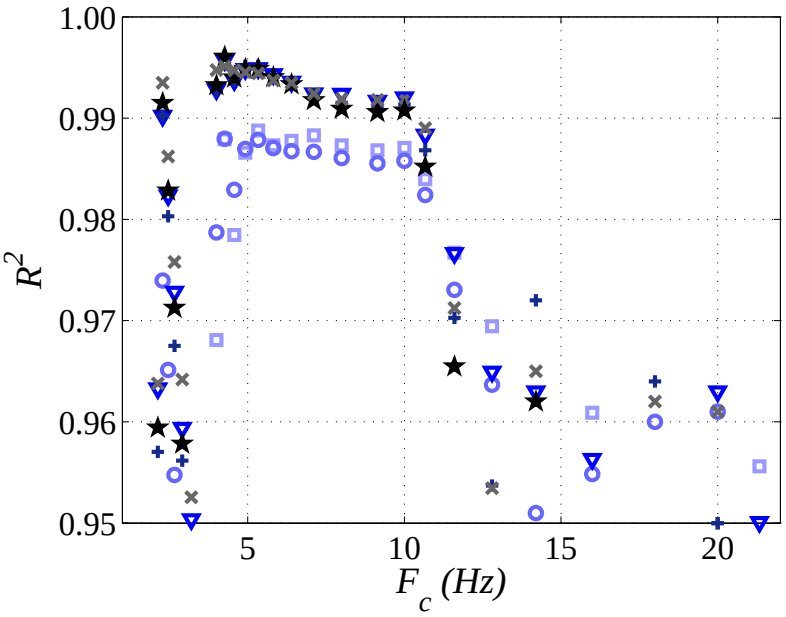

Figure 3.24. Effect of variations of low-pass filter cut-off frequency on the predicted responses. Low-pass filter cut-off frequency varies between 2 Hz and 20 Hz while $N = 10$, $M_1 = 11$, and $M_2 = 9$. Square, circle, triangle, plus, cross and star signs correspond to T_1 to T_6 tests, respectively. Light to dark blue also indicates decreasing strain rate from $0.0088/s$ to $0.00053/s$ (T_1 to T_6, respectively).

removed by using a single, much higher order model, with the structure of Model 4, that is fit to all data sets simultaneously.

The parameter estimation method introduced earlier is now modified by introducing new variables S_{m3}, S_{v2}, S_e, E and $\dot{E}$ as,

$$S_{m3} = [\sigma_{m3(T_1)}, \sigma_{m3(T_2)}, \cdots, \sigma_{m3(T_6)}]^T, \tag{3.34}$$

$$S_{v2} = [\sigma_{v2(T_1)}, \sigma_{v2(T_2)}, \cdots, \sigma_{v2(T_6)}]^T, \tag{3.35}$$

$$S_e = [\sigma_{e(T_1)}, \sigma_{e(T_2)}, \cdots, \sigma_{e(T_6)}]^T, \tag{3.36}$$

$$E = [\epsilon_{T_1}, \epsilon_{T_2}, \cdots, \epsilon_{T_6}]^T, \tag{3.37}$$

$$\dot{E} = [\dot{\epsilon}_{T_1}, \dot{\epsilon}_{T_2}, \cdots, \dot{\epsilon}_{T_6}]^T, \tag{3.38}$$

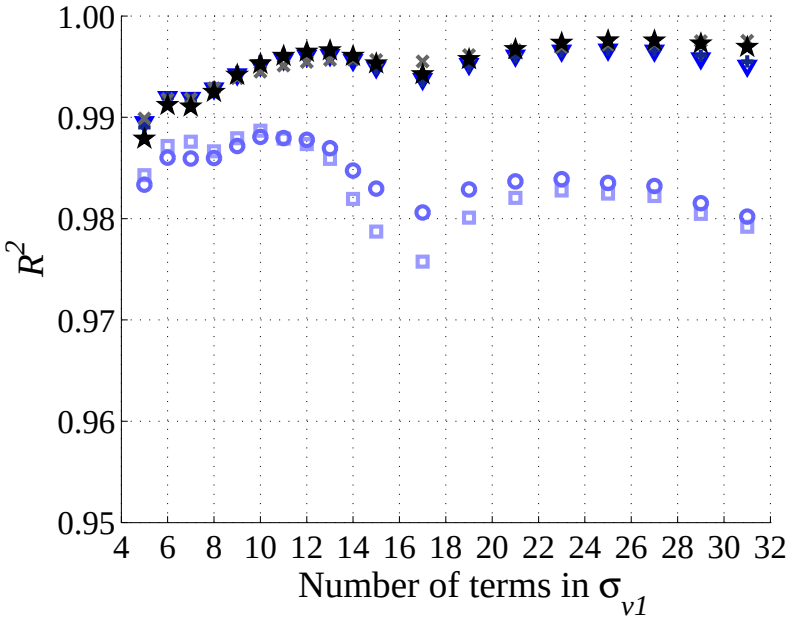

Figure 3.25. Effect of variations of viscoelastic model orders M_1 on the predicted responses when M_1 varies between 5 and 31 while $M_2 = 9$, $N = 10$ and $F_c = 5\ Hz$. Square, circle, triangle, plus, cross and star signs correspond to T_1 to T_6 tests, respectively. Light to dark blue also indicates decreasing strain rate from $0.0088/s$ to $0.00053/s$ (T_1 to T_6, respectively).

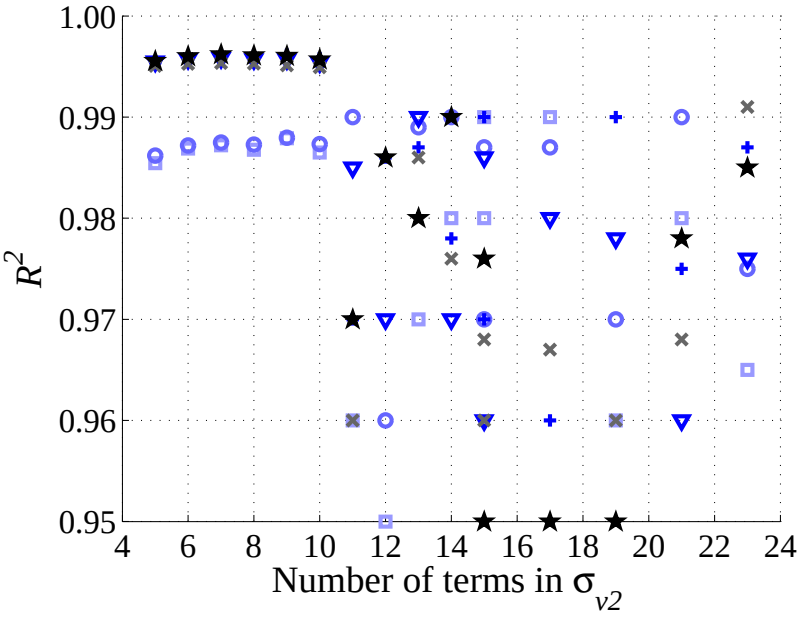

Figure 3.26. Effect of variations of viscoelastic model orders M_2 on the predicted responses when M_2 varies between 5 and 23 while $M_1 = 11$, $N = 10$ and $F_c = 5\ Hz$. Square, circle, triangle, plus, cross and star signs correspond to T_1 to T_6 tests, respectively. Light to dark blue also indicates decreasing strain rate from $0.0088/s$ to $0.00053/s$ (T_1 to T_6, respectively).

where $\sigma_{m3(T_i)}$, $\sigma_{v2(T_i)}$, $\sigma_{e(T_i)}$, ϵ_{T_i} and $\dot{\epsilon}_{T_i}$ correspond to $(\sigma - \sigma_{v2})$, $(\sigma - \sigma_{v2} - \sigma_e)$, elastic stress σ_e, strain ϵ and strain rate $\dot{\epsilon}$ for T_i data set, respectively. For this, step 5 of outer loop, and steps 3c and 3e of inner loop need to be modified by replacing σ, ϵ and $\dot{\epsilon}$ with S, E and $\dot{E}$.

Determining an appropriate system order (N, M_1 and M_2) is important to obtain the best possible model. As already noted in the previous section, it was observed that simple models with 2 viscoelastic terms, or 6 viscoelastic terms for slower tests, were sufficient to produce accurate predictions of the measured responses in each of the 6 tests. A systematic investigation to identify the optimum orders of the viscoelastic components (M_1, and M_2) and elastic component (N) of a single, comprehensive, constant-coefficient model that could be used to predict responses in all 6 tests was conducted. It was observed that high frequency components of the recorded compression test response do not affect the global response of foam and removing them helps to identify a better model. This is clearly shown in Fig. 3.24 where R^2 values of the predicted responses are shown for different low-pass filter cut-off frequencies ($F_c\ Hz$). It is observed that the best fits are achieved when the low-pass filter cut-off frequency is close to 5 Hz. There is a small deterioration in the R^2 values as the cut-off frequency is increased to 10 Hz , and then there is a significant drop in the R^2 values when the cut-off frequency is above 10 Hz.

From previous studies [84], it was observed that the order of the polynomial describing elastic stress will not affect the fit quality as much as the order of viscoelastic parameters. Therefore, the number of terms in the elastic component is kept fixed at 10 and the effects of varying the number of terms in the viscoelastic components on fit quality are examined by evaluating the error between the response predicted using the estimated Model 4 and the experimental response data for each test, and then calculating the corresponding R^2 values. Results of varying number of viscoelastic terms in σ_{v1} and σ_{v2} are shown in Figs. 3.5.3 and 3.5.3, respectively. In Fig. 3.5.3, M_1 is varied between 5 to 31 while M_2 is held constant and set equal to 9. It is observed that $M_1 = 11$ gives the highest overall R^2 values. In Fig. 3.5.3, M_2 is varied

between 5 to 23 while M_1 is held constant equal to 11. It is observed that $M_2 = 9$ gives the best overall fit. Increasing the number of terms in σ_{v2} beyond 10 terms significantly deteriorates the fit. Therefore, a model with 11 viscoelastic terms in σ_{v1} and 9 viscoelastic terms in σ_{v2} is considered in further study. Note that identifying the best possible fit is an iterative process and the best possible combination of M_1 and M_2 is found usually after a few iterations. The results of fitting Model 4 with $N = 10$, $M_1 = 11$ and $M_2 = 9$ are shown in Fig. 3.27. Note here that, the model with the same system parameters (k_i, a_j, b_l, α_j and β_l) reproduces the individual data sets reasonably well (respectively, 98.8, 98.8, 99.6, 99.6, 99.5, 99.6 for the T_1,$\cdots$,T_6 data).

To evaluate the robustness of the proposed model and parameter estimation technique, the same procedures are applied to similar data collected for another foam sample. This type of open cell foam is also used in car seats and the foam tested has a relative density= 0.05 (first foam has a relative density= 0.027). The new foam is also a seating foam but is stiffer compared to the previous foam (compare the peak stresses in Figs. 3.27 and 3.28). Following the same procedures explained above, it is observed that a model with $N = 10$, $M_1 = 12$, and $M_2 = 9$ gives the best fit, and then is able to reproduce the individual data sets, respectively, as 98.4, 99.1, 99.6, 98.8, 99.5, 99.3 for data of T_1,$\cdots$,T_6 tests.

In the next section of this chapter, to evaluate the robustness of the proposed model, the model performance for describing the mechanical behavior of high density CONFOR foams is studied.

3.6 CONFOR Foams

CONFOR foams are a family of urethane foams which have become popular especially for comfort management and protective padding applications. See [85–88] for some examples. These high density foams soften and conform when exposed to gentle load while acting as a high energy absorber when subjected to an impact. These contrasting behaviors, which are due to their strong nonlinear viscoelastic properties,

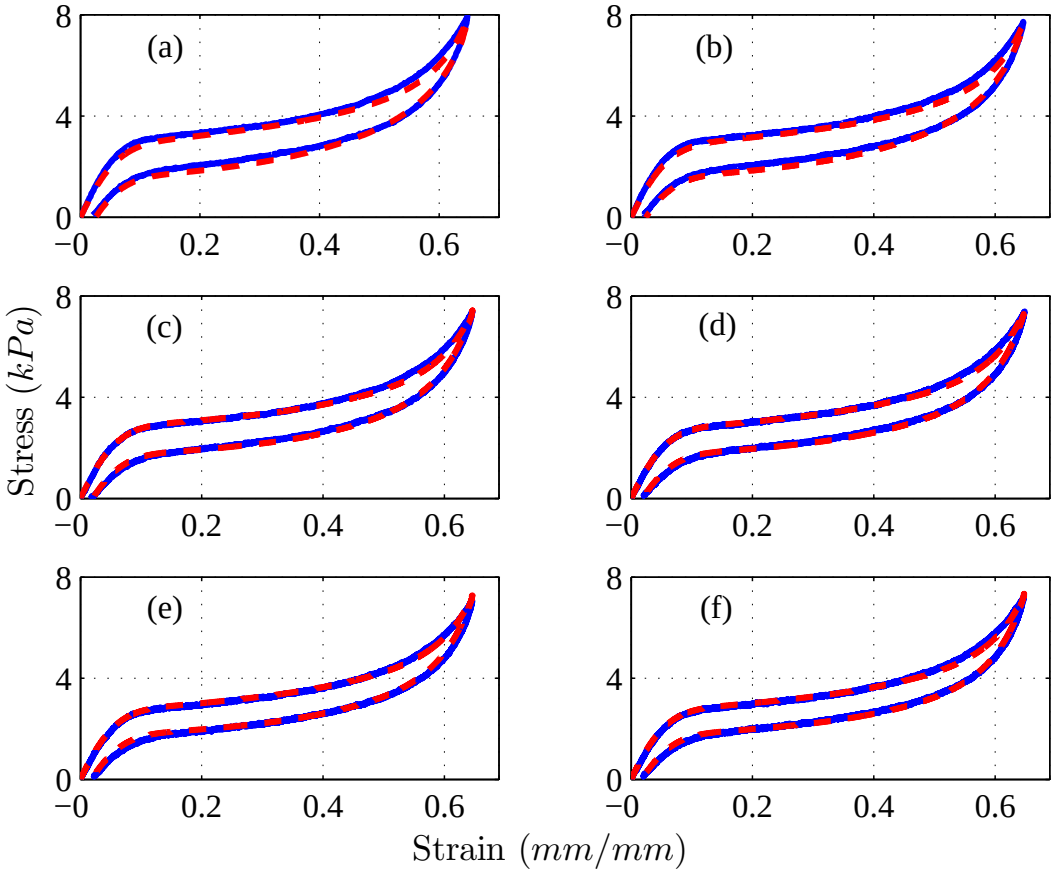

Figure 3.27. Results of simultaneously fitting Model 4 to all six data sets (foam A). R^2: 0.988, 0.988, 0.996, 0.996, 0.995 and 0.996, respectively. $N = 10$, $M_1 = 11$ and $M_2 = 9$. Solid blue and dashed red curves represent experimental data and estimated response, respectively. (a) T_1, (b) T_2, (c) T_3, (d) T_4, (e) T_5, and (f) T_6 data.

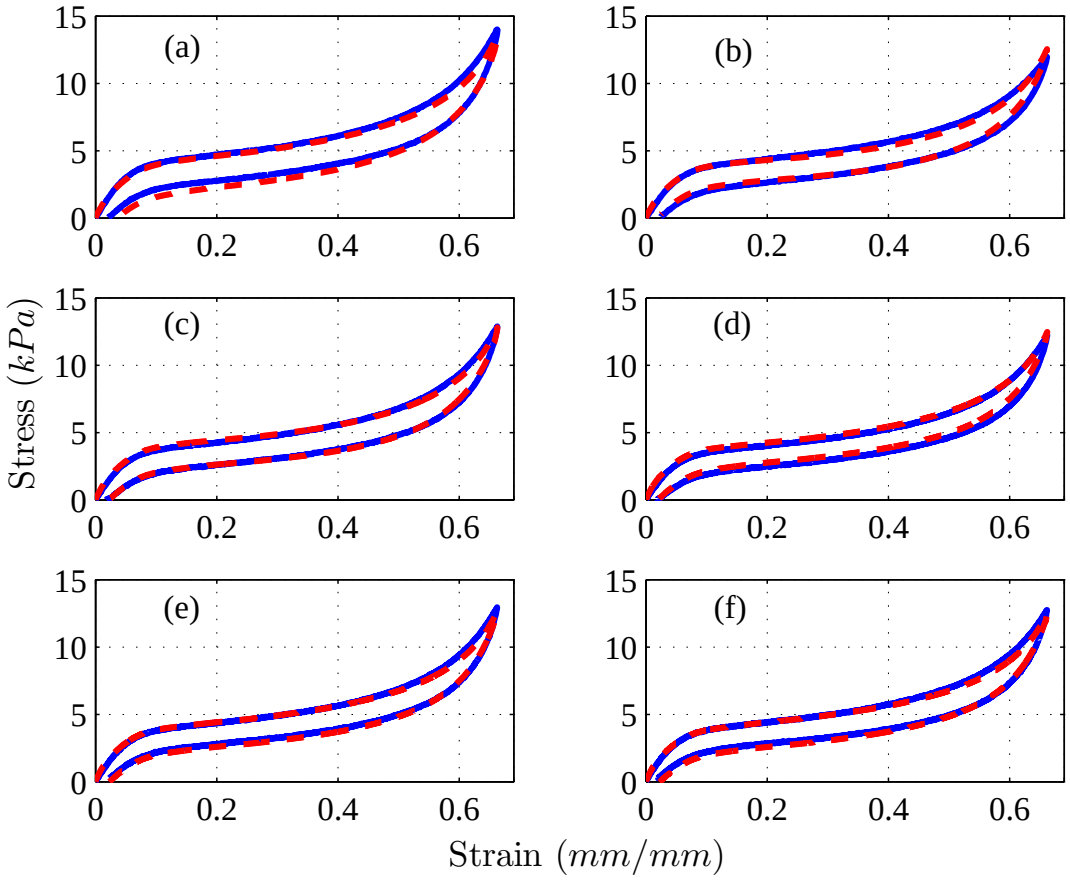

Figure 3.28. Results of simultaneously fitting Model 4 to all six data sets for another foam sample (foam D). R^2: 0.984, 0.991, 0.996, 0.988, 0.995 and 0.993, respectively. $N = 10$, $M_1 = 12$ and $M_2 = 9$. Solid blue and dashed red curves represent experimental data and estimated response, respectively. (a) T_1, (b) T_2, (c) T_3, (d) T_4, (e) T_5, and (f) T_6 data.

give them advantages over traditional polyurethane foams. In order to effectively utilize CONFOR foams in different engineering applications, it is required to develop mathematical models which characterize the mechanical behavior of CONFOR foams.

Although different models have been developed to describe the mechanical behavior of different types of polyurethane foams, very few of these models have been incorporated to characterize the mechanical behavior of high density CONFOR foams. One example of experimental studies includes the work by Davies and Mills [89] where they studied the rate dependency properties of CONFOR foams compressed at constant strain rate, impact and creep loadings. Their experimental studies show that the properties, such as compressive collapse stress, are strongly strain rate dependent. Matsui, Takagia, Takabayashib and Jimbob studied the behavior of CONFOR used in pedestrian legform impactor [90, 90]. They showed that the stress-strain responses of $CF45$ CONFOR foam is greatly affected by the level of humidity. Thorbole, Lankarani and Costello in [91] studied the dynamic characteristics of aircraft seat cushion made of CONFOR foam. They performed several quasi-static tests on cushions with different rate sensitivity and with different thickness, at extreme temperatures to determine the variations in their dynamic characteristics. Desbiens and Cutkosky studied the damping properties of a unmanned air vehicles suspension system made of CONFOR foam [92]. Their studies showed that the damping property of CONFOR foam is strongly affected by velocity, which is consistent with the previous study in [89]. Cappetti *et al*. studied the mechanical properties of CONFOR foam $CF45$, used in leg impactors, under impacts [93]. Also see [94] for a brief review of some other studies related to understanding the CONFOR foam mechanical behavior.

In the current chapter, the utility of the foam model introduced in the previous section in modeling the uniaxial behavior of CONFOR foam is studied. Following the same steps as explained before for the car seat foams, a series of large strain compression tests were conducted on three types of CONFOR foams at different rates. It was observed that the CONFOR foam behavior is strongly rate dependent. The model parameters are then estimated using the data from the uniaxial compression tests.

Similar to the studies in the previous section, first, simple models with strain rate dependent parameters are identified, which describe each foam behavior compressed at different rates. Then, comprehensive models, with many viscoelastic terms, are identified. The system parameters in the second models are strain rate independent.

3.6.1 CONFOR Foam Uniaxial Behavior

In this study, mechanical behavior of three types of CONFOR foams, specified as Foam 1, Foam 2 and Foam 3, were investigated. The properties of foams are given in Table 3.6. The microstructure of these foam samples are shown in Figure 3.29. These photos were taken from the cross sections of the foam blocks after cutting them into thin (2 mm) films. Then a high definition camera, with ($\times$15) optical magnification, was used to take the photos. The photos were then digitally magnified.

Table 3.6. CONFOR foams used in the experiments.

Foam	Foam name	Relative density
Foam 1	CF 40100 A	0.08019
Foam 2	CF 42075 A	0.08096
Foam 3	CF 40100 B	0.07858

In order to study the mechanical behavior of the three foam samples, quasi-static compression tests were performed on them using a MTS 858 Mini Bionix materials testing machine described in the previous section and shown in Figure 3.1(a). Similar to the experimental procedures explained in the previous section, the foam sample was placed on the lower plate of the MTS machine while the actuator followed the path shown in Figure 3.1(b) and compressed the foam until the maximum stress reaches 16500 Pa. To ensure that the tests are repeatable, each test was repeated

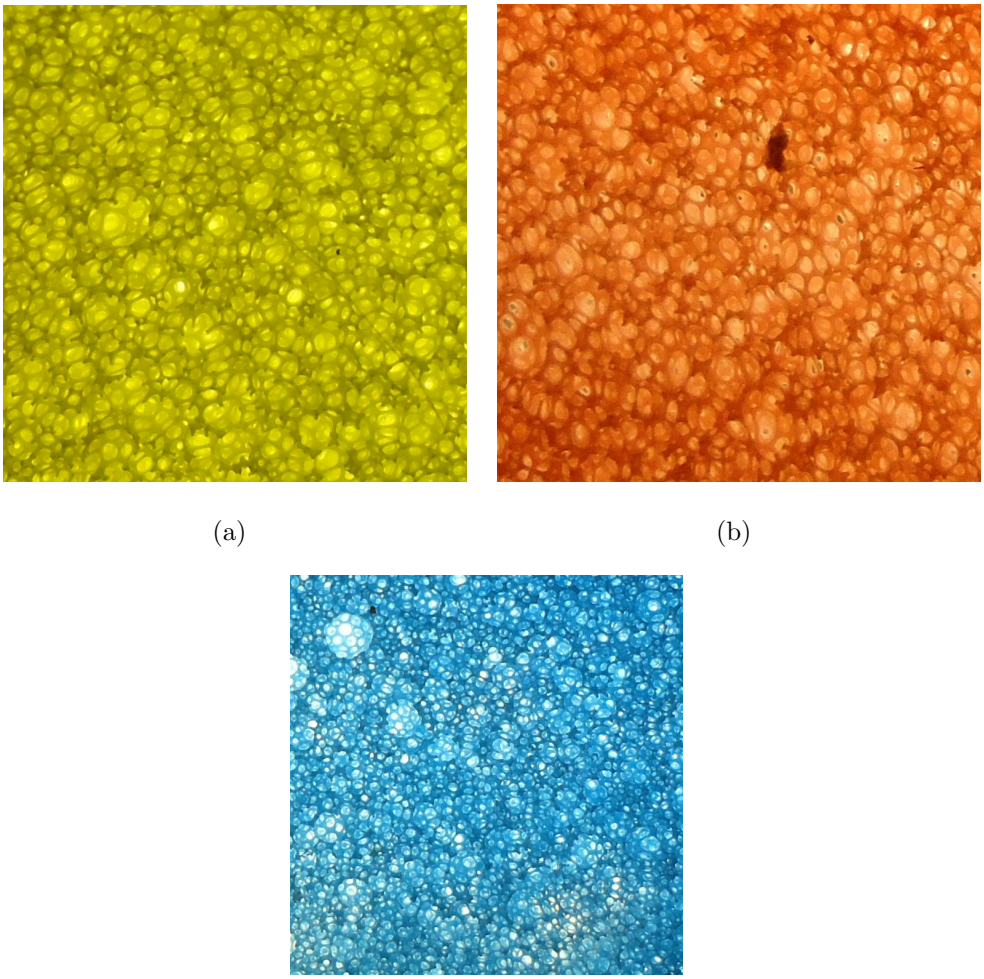

(a) (b)

(c)

Figure 3.29. Photographs of foam samples. Pictures are of 10 $mm \times$ 10 mm cross sections of the foam blocks. (a) Foam 1, (b) Foam 2, and (c) Foam 3.

several times under a same condition such as temperature and humidity. Detailed experimental procedures and protocol can be found in [3].

It is well known that CONFOR foam behavior is greatly strain rate dependent [89,93]. To study this property of foam, 4 tests were performed at different rates equal to $0.00438/s$, $0.00109/s$, $0.00052/s$, and $0.00026/s$ on each foam type. Throughout the work, these tests are referred to as TC_1, TC_2, TC_3, and TC_4 tests, respectively. Table 3.7 shows the different rates used in each case.

Table 3.7. Compression tests conducted at various rates.

Test	TC_1	TC_2	TC_3	TC_4
Compression Rate ($seconds^{-1}$)	43×10^{-4}	10×10^{-4}	5×10^{-4}	2×10^{-4}

Samples of measured stress-strain and stress-time responses for Foam 1 are shown in Figures 3.30. Although strain rate variations in the experiments are small, only differing by one decade, there is obvious strain-rate dependency as shown in Figures 3.30. The stress-strain responses of Foam 1, Foam 2 and Foam 3 compressed at the same rate of $0.00438/s$ (TC_1 test) are shown in Figure 3.31. It is observed that Foam 1 is the softest foam and Foam 2 is the stiffest foam among the three foam samples.

Also, it is well known that foams exhibit time dependent viscoelastic behavior. Figures 3.32 and 3.33 shows the time-dependency of the responses of the high density foams as well as the low density polyurethane foam studied before [95].

In all four cases, cubic $76.2\ mm \times 76.2\ mm \times 76.2\ mm$ foam samples were first compressed by 66% (or to 33% of foam's initial length). Then the load (applied by a steel plate) was removed almost instantaneously and the transient responses of the foam samples were recorded using a digital camera. Each experiment was repeated several time to ensure the repeatability of the tests. It is shown in Figures 3.32 and 3.33 the transient responses of the foams during the first few seconds after the load is removed and as the foam samples (initial compressed height shown by dashed-dotted line) gradually return to the uncompressed height (shown by dashed line). It

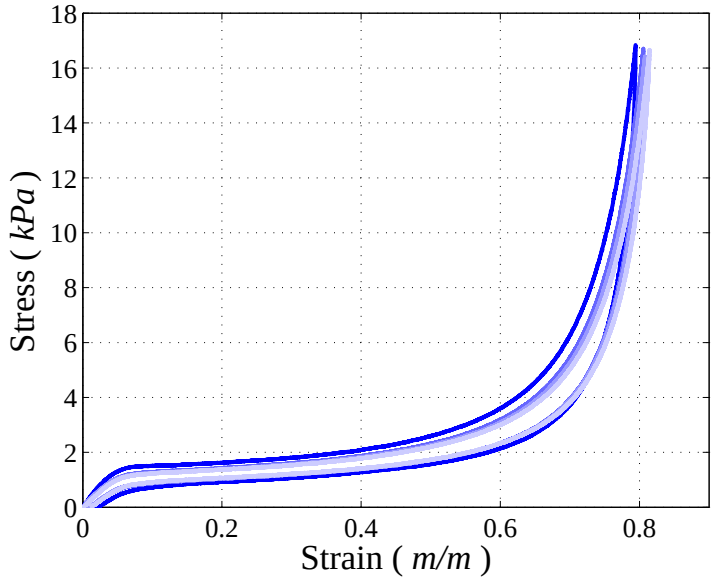

(a)

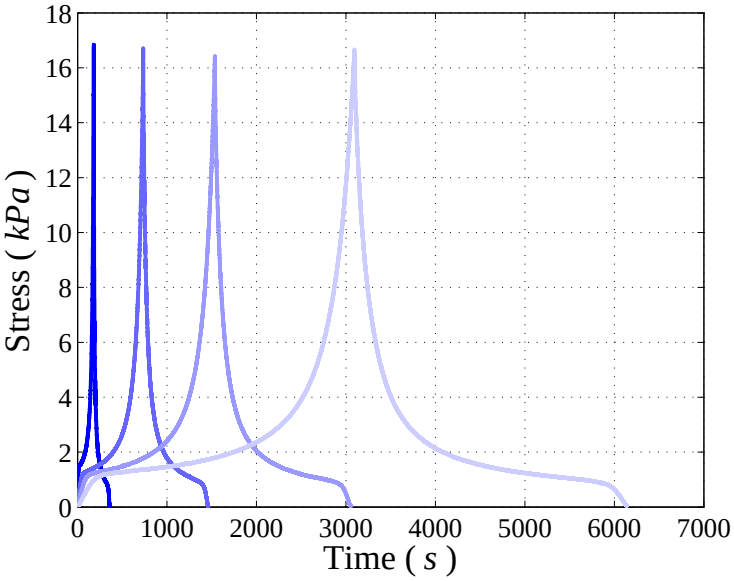

(b)

Figure 3.30. Results of four compression tests on Foam 1 at different rates. (a) Stress versus strain and, (b) the same data plotted against time. Dark to light blue indicates decreasing strain rate from $0.00438/s$ (TC_1), $0.00109/s$ (TC_2), $0.00052/s$ (TC_3), and $0.00026/s$ (TC_4).

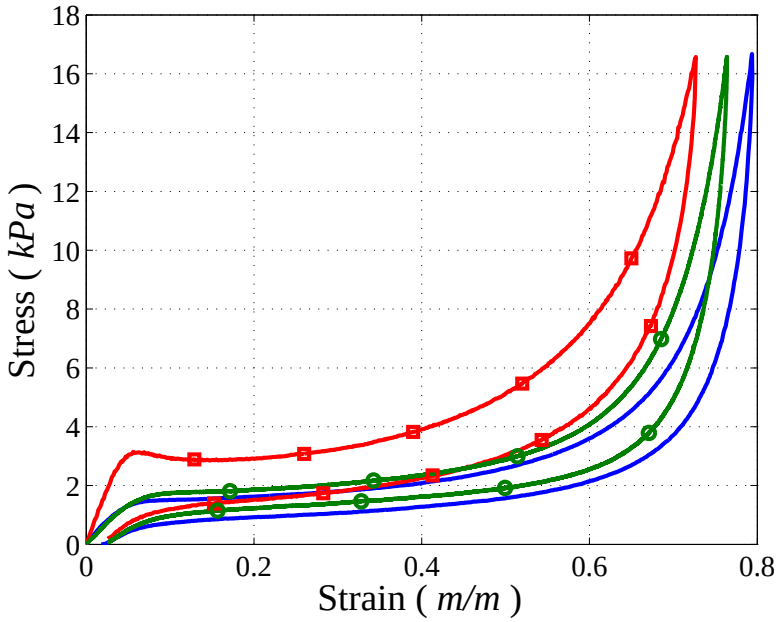

Figure 3.31. Results of TC_1 compression tests for three foams. Blue: Foam 1; red (square): Foam 2; green (circle): Foam 3. Strain rate is $0.00438/s$.

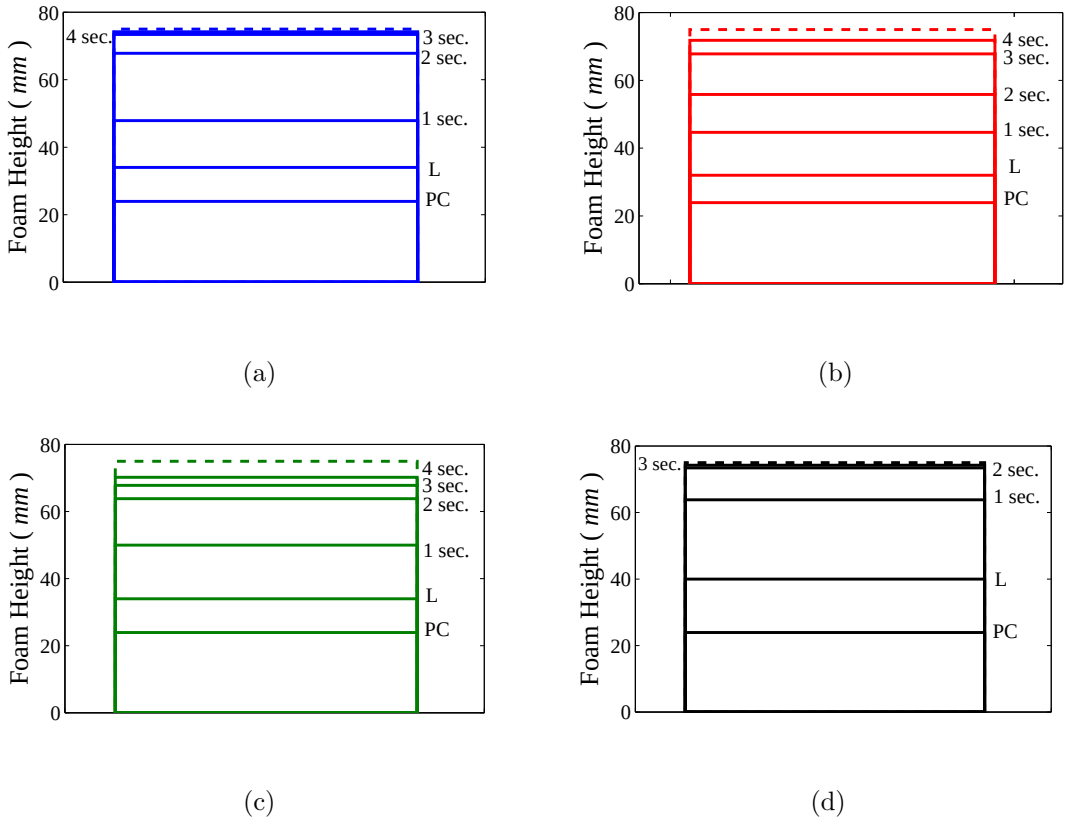

Figure 3.32. Time dependent responses of various foams. (a) Foam 1, (b) Foam 2, (c) Foam 3, and (d) car seat foam (relative density=0.027). Dashed line: uncompressed foam top surface, PC: full compression level, L: position where top plate loses contact with top surface of foam.

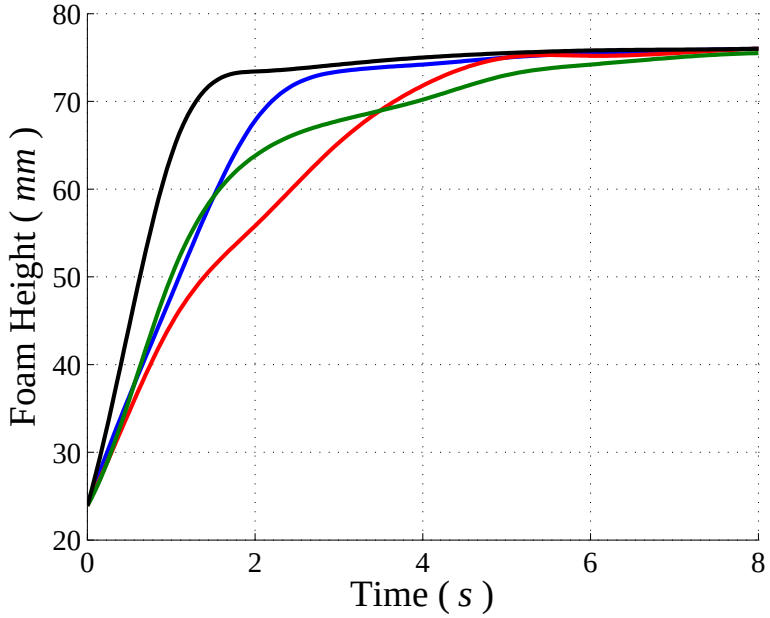

Figure 3.33. Time dependent responses of CONFOR foam samples. Blue: CONFOR Foam 1; red: Foam 2; green: Foam 3; black: low density foam considered in the previous section.

is clear that different foams exhibit different time-dependent behavior. For example, as shown in Figure 3.32(d) the low-density foam returns almost to its uncompressed state within 3 *seconds*. It takes much longer for the foam to fully recover. The relaxation time is longer for Foam 1 and Foam 3 as shown in Figures 3.32(a) and 3.32(c).

3.6.2 Strain-Rate Dependant Models

In this section the foam model introduced before and given by Equation (3.5) is fitted to the experimental data and the foam model parameters are estimated using the process introduced in the previous section. The foam model is first fitted to individual responses from tests TC_1, TC_2, TC_3 and TC_4 as described above. The model orders are gradually increased and the accuracy of the prediction is monitored in order to determine approximate values of N, M_1, and M_2. It is seen that the parameters estimated and the model orders required change from test to test. The development of a simple model that can be used to predict responses in all of tests is then described. It is also shown that if the foam model is complex enough, a unique model can describe the foam behavior at all compression rates.

3.6.3 Foam Model Estimation from Individual Compression Tests

One approach to determining the orders of the different terms in the model (N, M_1, and M_2) is to systematically vary the orders of terms and monitor the model predictions as was done earlier. Here, similar to the previous section, it is observed that simple models with $N = 15,\ M_1 = M_2 = 1$ characterize the foam responses compressed at a constant rate reasonably well. For example in Figure 3.34 the experimental data obtained from performing $TC_1, \cdots, TC_4$ tests on Foam 1 are shown along with the predicted responses. Note that the predicted responses shown were obtained using four distinct models with the same structure but different parameters. The estimated parameters for these models are given in Table 4.2. In order to quantify

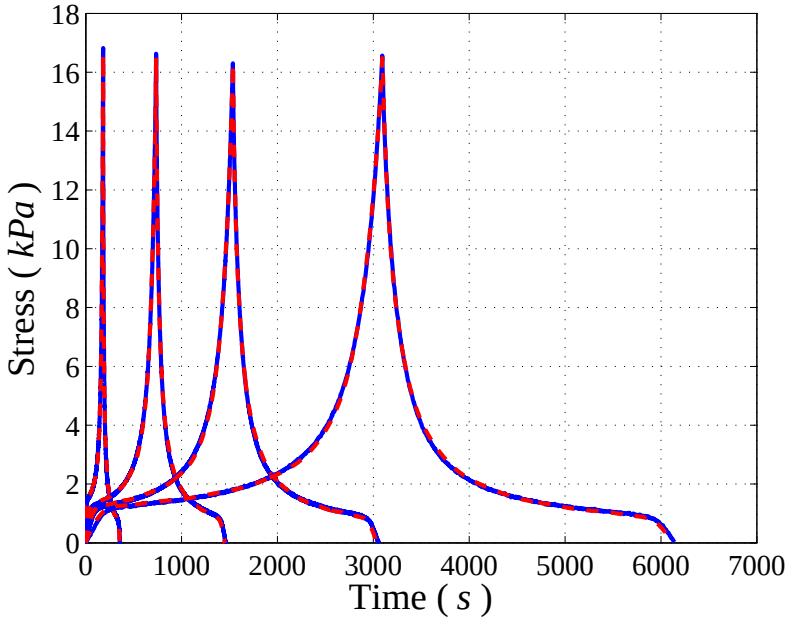

Figure 3.34. Blue line: measured response, and, red line: predicted responses of Foam 1 (two lines are very close). $N = 15$, $M_1 = M_2 = 1$. $TC_1, \cdots, TC_4$ tests with strain rates: $0.00438/s$, $0.00109/s$, $0.00052/s$, and $0.00026/s$. R^2: 0.9991, 0.9990, 0.9985, 0.9980, respectively.

the quality of predictions, the coefficient of calculated (R^2) has also been determined for each prediction. The corresponding R^2 values are 0.9991, 0.9990, 0.9985, 0.9980 for $TC_1, \cdots, TC_4$ tests, respectively.

Comparing the predicted responses and the experimental data shown in Figure 3.34, it can be seen that the predictions deteriorate as the model with the structure $N = 15,\ M_1 = M_2 = 1$ is fitted to slower tests. A similar behavior was also observed in the previous section, see Figure 3.18. The predicted response for the slowest test can be improved by increasing the number of viscoelastic terms in the first viscoelastic component. The response prediction resulting from a model with $N = 15,\ M_1 = 5$, and $M_2 = 1$ fitted to TC_4 test data is shown in Figure 3.35. The improvement is especially obvious comparing the predicted responses around $t = 200\ s$ and $t = 3500\ s$.

Table 3.8. Estimates of the viscoelastic parameters of Foam 1. ± represents the standard deviation of the estimates.

input strain rate	α_1	β_1
$0.00438/s$	0.431±0.001	0.442±0.007
$0.00109/s$	0.1541±0.0008	0.2069±0.002
$0.00052/s$	0.0943±0.0003	0.145±0.001
$0.00026/s$	0.0603±0.0002	0.0945±0.0004
input strain rate	a_1	b_1
$0.00438/s$	-0.2680±0.0008	37941±639
$0.00109/s$	-0.0830±0.0004	51216±486
$0.00052/s$	-0.0507±0.0001	61782±335
$0.00026/s$	-0.0319±0.0001	78941.06±334

Table 3.9. Estimates of the viscoelastic parameters of Foam 2. ± represents the standard deviation of the estimates.

input strain rate	α_1	β_1	a_1	b_1
$0.00438/s$	0.3539±0.002	0.301±0.006	-0.1988±0.0008	2237±101
$0.00109/s$	0.08±0.01	0.085±0.002	-0.0355±0.0005	2919±84
$0.00052/s$	0.0366±0.0003	0.066±0.001	-0.0154±0.0003	4348±102
$0.00026/s$	0.0167±0.0003	0.0200±0.0005	-0.0063±0.0003	6042±55

R^2 values go from 0.9980 to 0.9993 by increasing the order of the first viscoelastic term σ_{v1}.

Results of fitting foam models with $N = 15,\ M_1 = M_2 = 1$ to the data from compression tests conducted on Foam 2 and Foam 3 are shown in Figures 3.36. The elastic and viscoelastic components of the predicted responses are shown in Figure 3.37 for all three foams. The predicted elastic stress is shown in Figure 3.37(a) and the negative of the predicted viscoelastic stress ($-\sigma_v = -\sigma_{v1} - \sigma_{v2}$) is shown in Figure

Table 3.10. Estimates of the viscoelastic parameters of Foam 3. ± represents the standard deviation of the estimates.

input strain rate	α_1	β_1	a_1	b_1
$0.00438/s$	0.280±0.003	0.224±0.009	-0.152±0.001	6303±59
$0.00109/s$	0.0657±0.0005	0.061±0.001	-0.0300±0.0004	9460±408
$0.00052/s$	0.0342±0.0004	0.0309±0.0009	-0.0142±0.0003	11062±236
$0.00026/s$	0.0135±0.0003	0.0136±0.0006	-0.0048±0.0005	16418±334

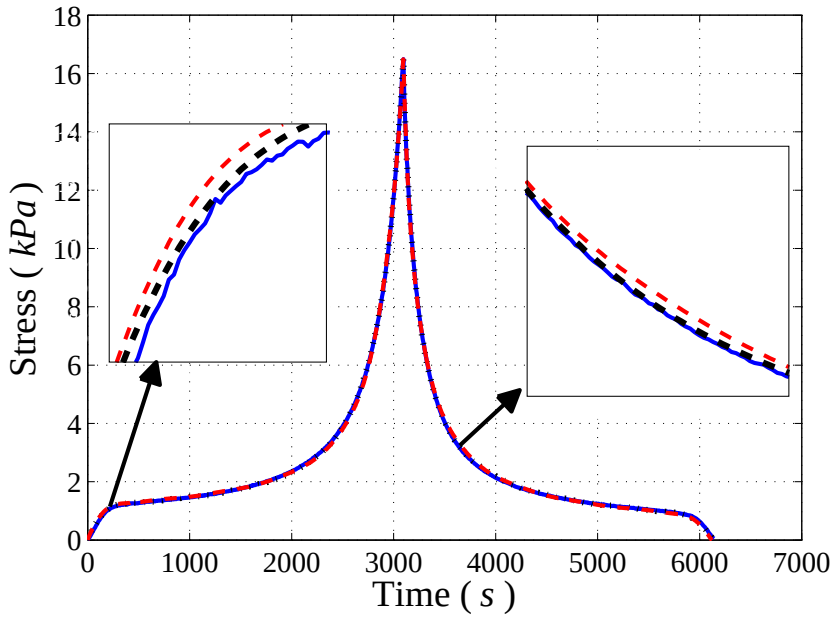

Figure 3.35. Measured and predicted responses resulting from fitting two foam models to the data from TC_4 test on Foam 1. Blue solid line: measured response, red dashed line: prediction using a model with $N = 15,\ M_1 = M_2 = 1$ and black dashed line: prediction using a model with $N = 15,\ M_1 = 5,\ M_2 = 1$.

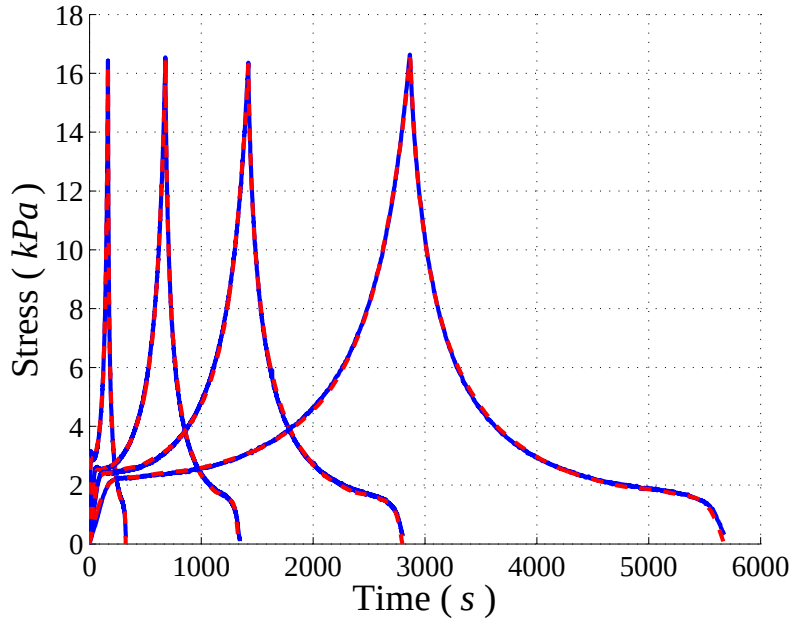

(a)

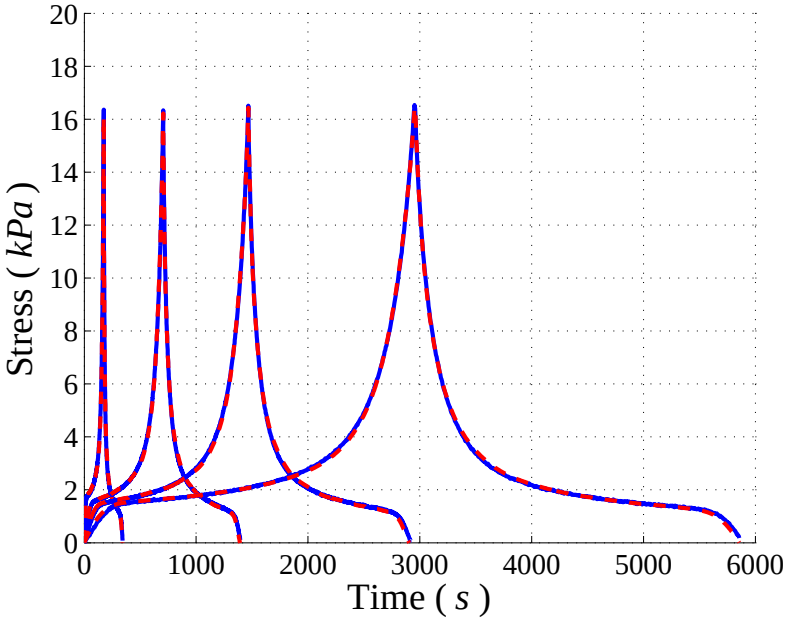

(b)

Figure 3.36. Results of fitting models with $N = 15$, $M_1 = M_2 = 1$ to $TC_1, \cdots, TC_4$ test data with strain rates: $0.00438/s$, $0.00109/s$, $0.00052/s$, and $0.00026/s$, respectively. (a) Foam 2, and (b) Foam 3. Blue solid line: measured; red dashed line: predicted (two lines are very close).

3.37(a). Overall, for a given compression level ϵ, Foam 2 and Foam 1 have the largest and the smallest elastic and viscoelastic stress components, respectively.

3.6.4 Strain-Rate Dependency of the Foam Model Parameters

The foam model parameters estimated from data from different tests are different, see Table 3.8, Tables 3.9 and 3.10. In Figures 3.38 and 3.39, the estimated parameters for models of Foam 1, Foam 2 and Foam 3 are plotted against the strain rates used in TC_1 through TC_4 tests. It is observed that in general, the viscoelastic parameters a, β, and α appear to be linear functions of the input strain rates. For the viscoelastic parameter β for Foam 1 and the parameter b for all three foams, the relationship does not appear to be linear. Therefore, in general, more complex functions need to be fitted to accurately capture the relationship between these parameters and the input strain rate. In the previous section, the inverse of the estimated b's were fitted to linear functions of the input strain rate, see Figure 3.22(a). Here also a logarithmic function was fitted to the inverse of the estimated b and the viscoelastic parameter β for Foam 1. The estimated functions for Foam 1 parameters are given by:

$$\begin{aligned} a &= -56.79|\dot{\epsilon}| - 0.019, \\ \alpha &= 88.33|\dot{\epsilon}| + 0.047, \\ b &= \frac{10^6}{4.857log(|\dot{\epsilon}|) + 52.718}, \\ \beta &= 0.126log(|\dot{\epsilon}|) + 1.116, \end{aligned} \tag{3.39}$$

where $|\dot{\epsilon}|$ is the absolute of the input strain rate. Also, similar to the observations before, the estimated elastic parameters from all four tests, $TC_1, \cdots, TC_4$, are close and just vary within a range of 10%, see Figure 3.40. Therefore, a single model, Equation (3.5), with strain rate dependent viscoelastic parameters, i.e. see Equation (3.39), can describe the foam behavior at different strain rates.

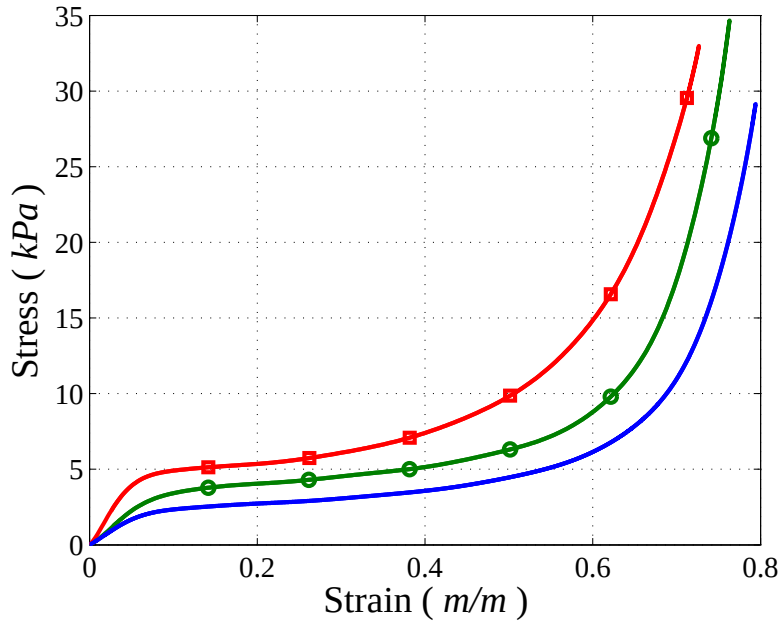

(a)

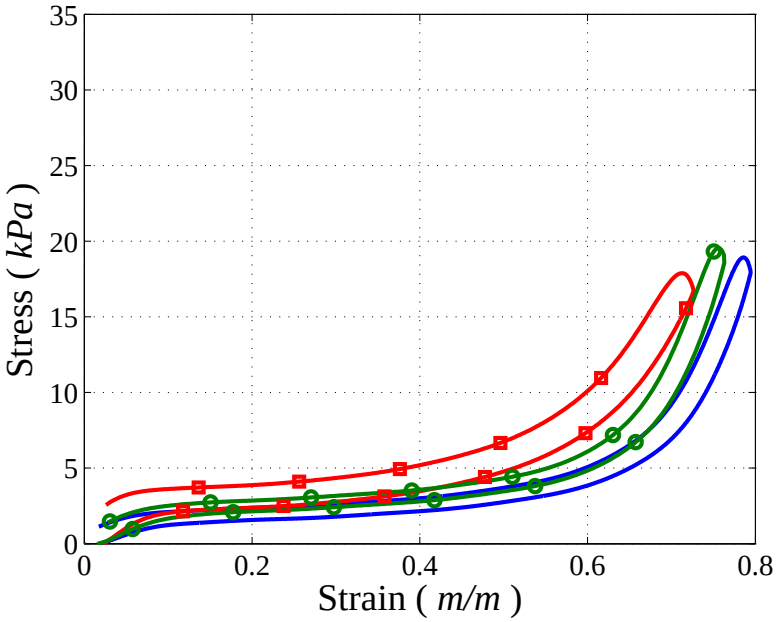

(b)

Figure 3.37. Predicted stress components. Blue: Foam 1; red (square): Foam 2; green (circle): Foam 3. (a) elastic stress σ_e, and (b) negative of viscoelastic stress $-\sigma_{v1} - \sigma_{v2}$. Results for TC_1 test (strain rate is $0.00438/s$).

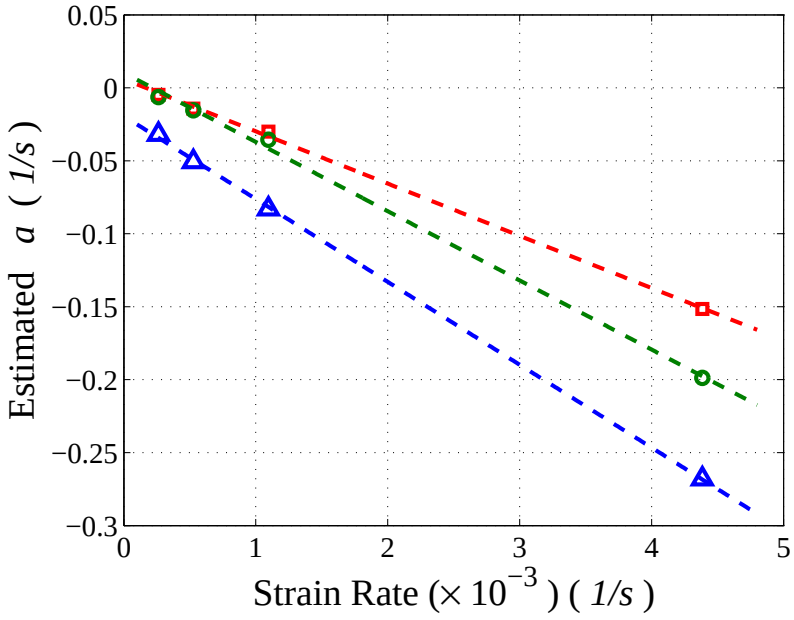

(a)

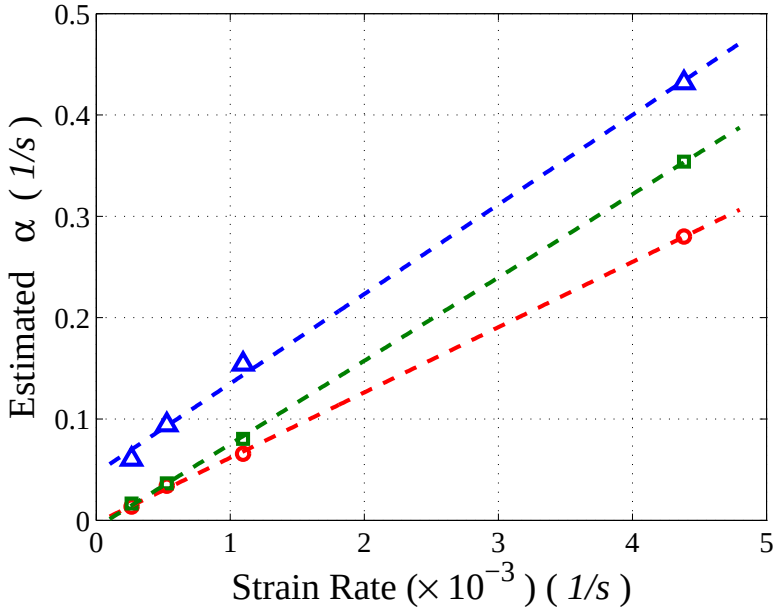

(b)

Figure 3.38. Fitting simple functions to the estimated parameters of the first viscoelastic term as functions of input strain rates: (a) $a(\dot{\epsilon})$, and (b) $\alpha(\dot{\epsilon})$. Blue (triangle): Foam 1; red (square): Foam 2; green (circle): Foam 3. Dashed lines represent the fitted linear functions described by Equation (3.39).

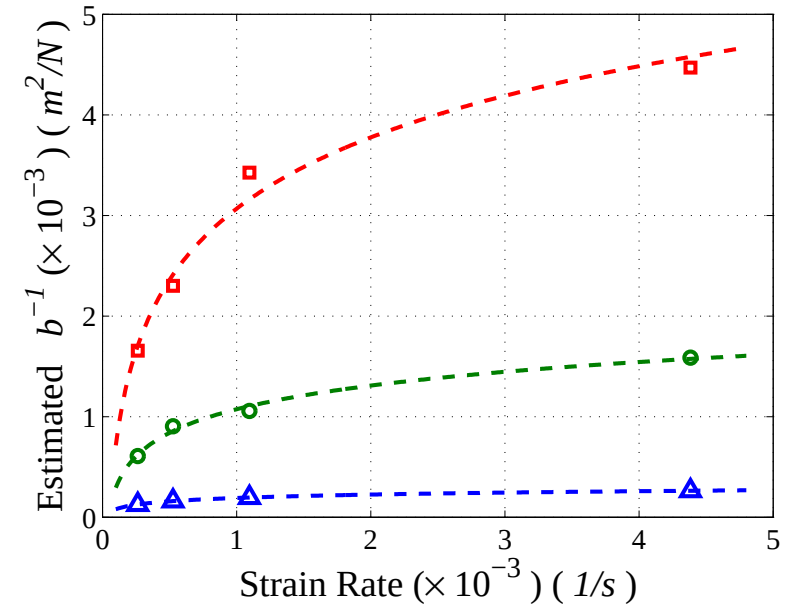

(a)

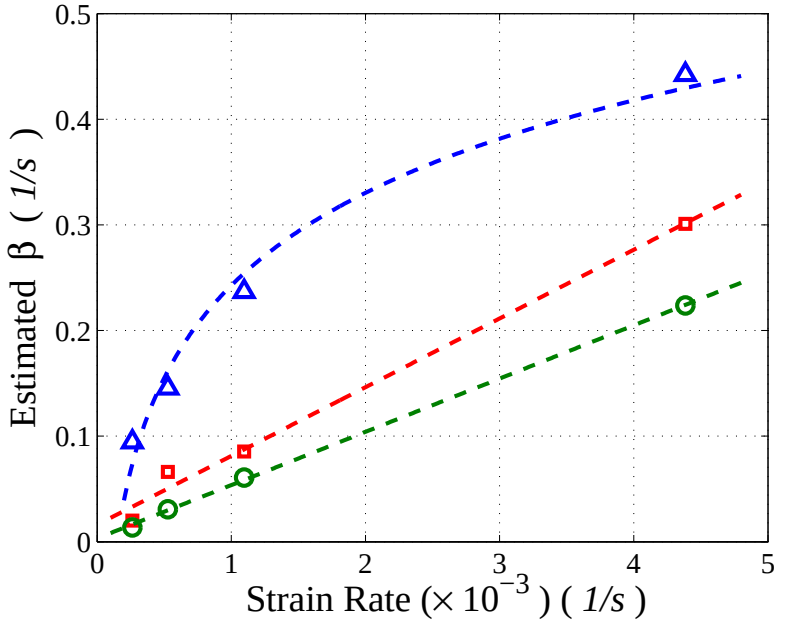

(b)

Figure 3.39. Fitting simple functions to the estimated parameters of the second viscoelastic term as functions of input strain rates: (a) $b(\dot{\epsilon})$, and (d) $\beta(\dot{\epsilon})$. Blue (triangle): Foam 1; red (square): Foam 2; green (circle): Foam 3. Dashed lines represent the fitted linear functions described by Equation (3.39).

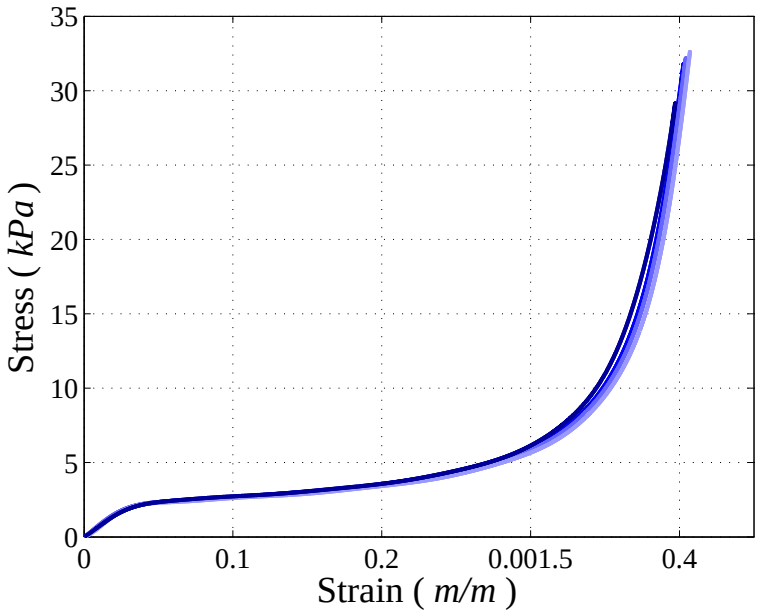

Figure 3.40. Predicted elastic stress σ_e for TC_1,$\cdots$,TC_4 tests ($N = 10$, $M_1 = 1$, and $M_2 = 1$). Light to dark blue curves indicate increasing strain rate from 0.00026 $1/s$ to 0.00438 $1/s$.

The predicted responses using the model with strain rate dependent parameters are shown in Figure 3.42. This model can reproduce the individual TC_1 to TC_4 compression tests well, with R^2 values 0.991, 0.997, 0.997, and 0.992, respectively.

3.6.5 Estimating a Comprehensive Foam Model

For each foam type, a higher order comprehensive model can be estimated by simultaneously fitting the foam model to all foam responses, from TC_1 test to TC_4 test. Following the procedure explained before for low density foams, the model orders are identified by varying N, M_1, and M_2 independently and systematically. Then the resultant model predictions are studied by comparing R^2 values of the predicted responses. It is observed that estimated responses are not very sensitive to the order of the elastic component, N, as long as its value is greater than a certain value, i.e. here $N = 15$. In order to determine orders of the viscoelastic components, the orders of the viscoelastic components, M_1 and M_2, are systematically varied and their effects on the R^2 values of the estimated responses are studied. It is observed that unlike the results shown in Figure 3.24, the estimated responses are not sensitive to the cut of frequency of the low-pass filter used to filter the experimental data. Determining the best orders of the viscoelastic component is usually an iterative process. To illustrate determination of orders of the viscoelastic components, one example of how varying the order of the viscoelastic components, M_1 and M_2, affects the estimated responses are shown for Foam 1 in Figures 3.43 and 3.44. In Figure 3.43, the R^2 values as M_1 is varied between 5 to 20 are given while $M_2 = 3$ and $N = 15$. It is observed that the R^2 value increases with increasing M_1 until it reaches its maximum value when $M_1 = 11$. Similarly, in Figure 3.44, M_2 is varied between 1 to 10 while $M_1 = 11$ and $N = 15$. It is observed that when $M_2 = 3$ the overall R^2 is maximum. In order to achieve the best prediction, several studies similar to the one shown in Figure 3.44 are needed. Here, a model with $N = 15$, $M_1 = 11$ and $M_2 = 3$ is chosen. The predicts for this model are shown in Figure 3.45. Note that by further increasing M_2, R^2 decreases

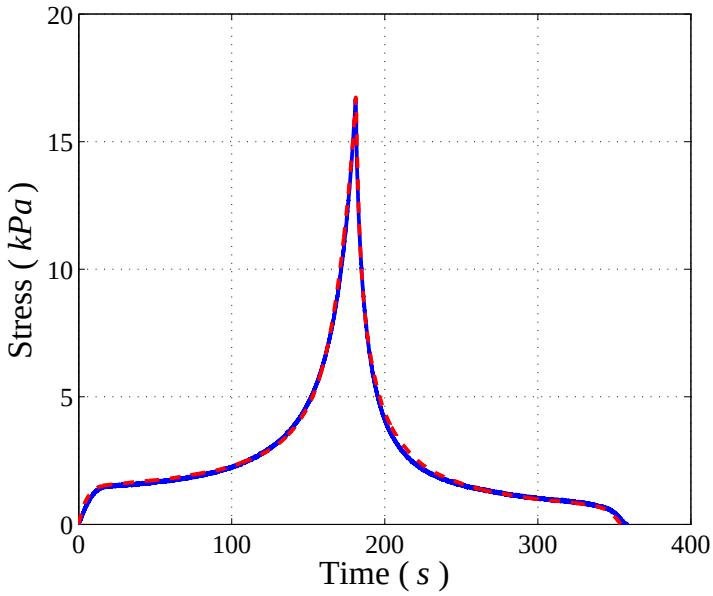

(a)

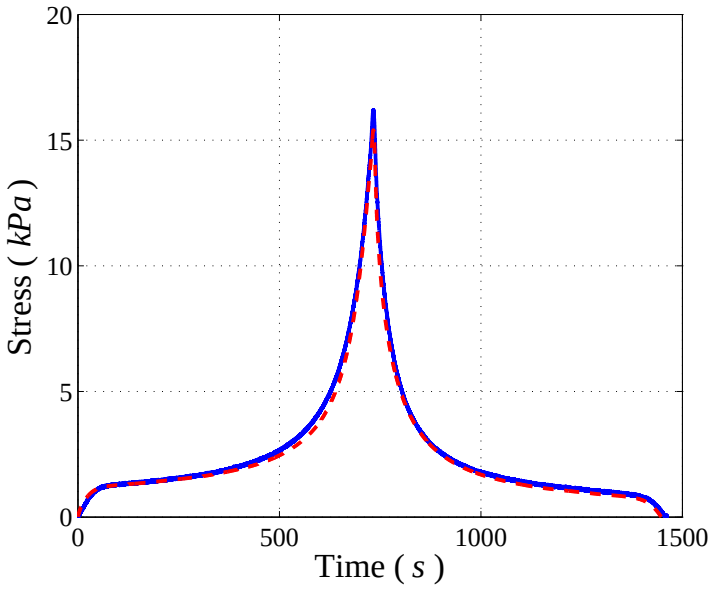

(b)

Figure 3.41. Predicting the responses of TC_1 and TC_2 tests from the model with strain rate dependent parameters for Foam 1. Blue: experimental measurement (solid); red: estimated response (dashed). (a) TC_1 test, and (b) TC_2 test.

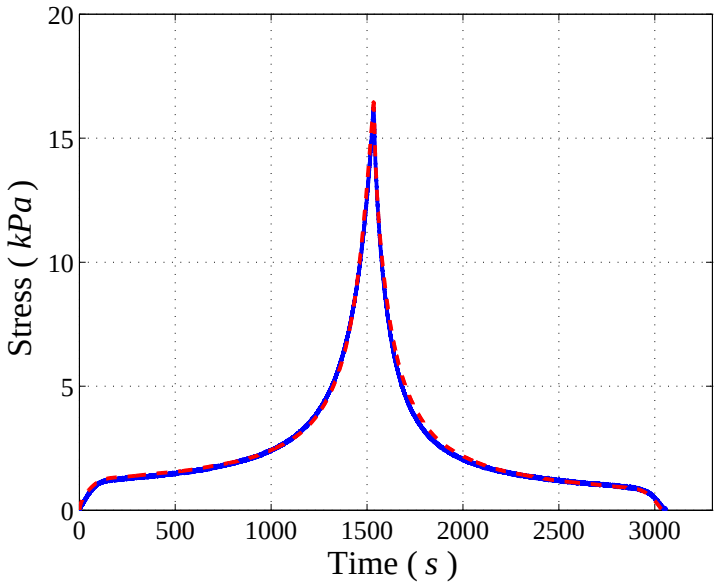

(a)

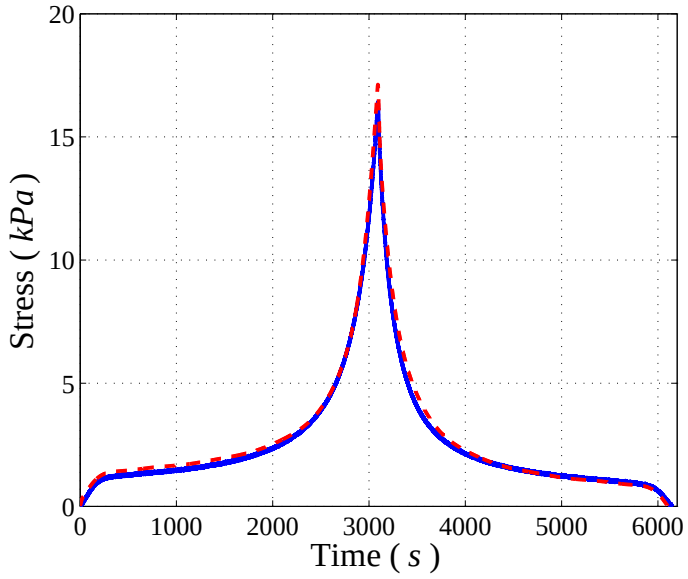

(b)

Figure 3.42. Predicting the responses of TC_1 and TC_2 tests from the model with strain rate dependent parameters for Foam 1. Blue: experimental measurement (solid); red: estimated response (dashed). (a) TC_3 test, and (b) TC_4 test.

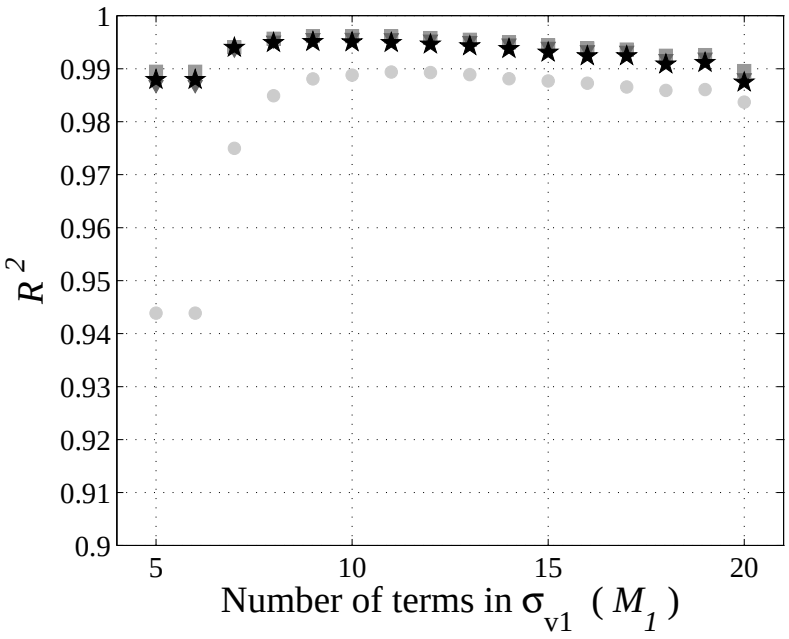

Figure 3.43. Effect of variations of the number of terms in the first viscoelastic component on the predicted responses for Foam 1 when M_1 varies between 5 and 20 while $M_2 = 3$ and $N = 15$. Circle, square, triangle, and star (light to dark) correspond to tests with the input strain rates of $0.00438/s$, $0.00109/s$, $0.00052/s$, and $0.00026/s$, respectively.

significantly as shown in Figures 3.43 and 3.44. Also, note that results for the fastest test are the worst.

A similar procedure is used to estimate the global models for Foam 2 and Foam 3. Following the same steps, it is found that a foam model with $N = 15,\ M_1 = 8$ and $M_2 = 8$ gives the best fit to Foam 2 compression test results as shown in Figure 3.46. This model can reproduce the individual TC_1 to TC_4 compression tests well, with R^2 values 0.991, 0.997, 0.996, and 0.997, respectively. Also a model with $N = 15,\ M_1 = 8$ and $M_2 = 12$ gives the best fit for Foam 3 compression test results. This model is then used to predict the compression test responses as shown in Figure 3.47. The R^2 values for tests TC_1 to TC_4 are 0.991, 0.997, 0.996 and 0.997, respectively.

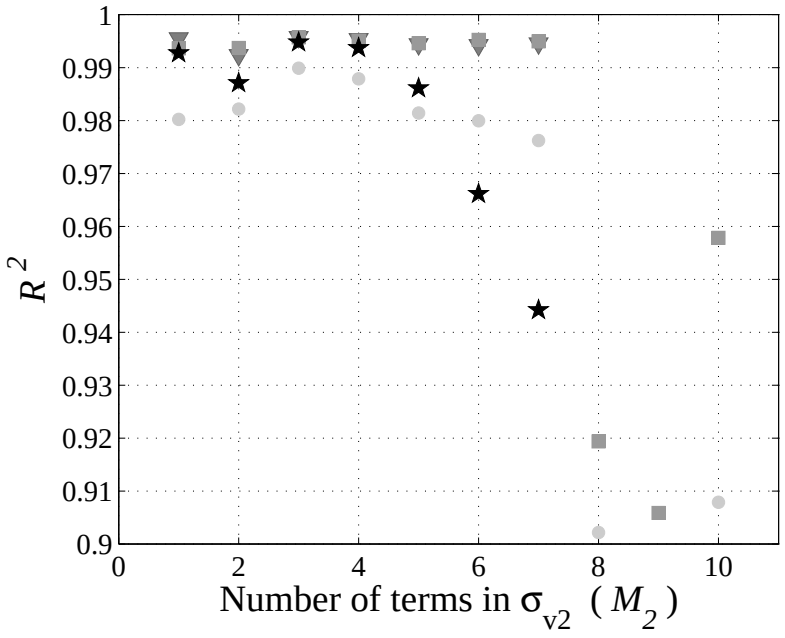

Figure 3.44. Effect of variations of the number of terms in the second viscoelastic component on the predicted responses for Foam 1 when M_2 varies between 1 and 10 while $M_1 = 11$ and $N = 15$. Circle, square, triangle, and star (light to dark) correspond to tests with the input strain rates of $0.00438/s$, $0.00109/s$, $0.00052/s$, and $0.00026/s$, respectively.

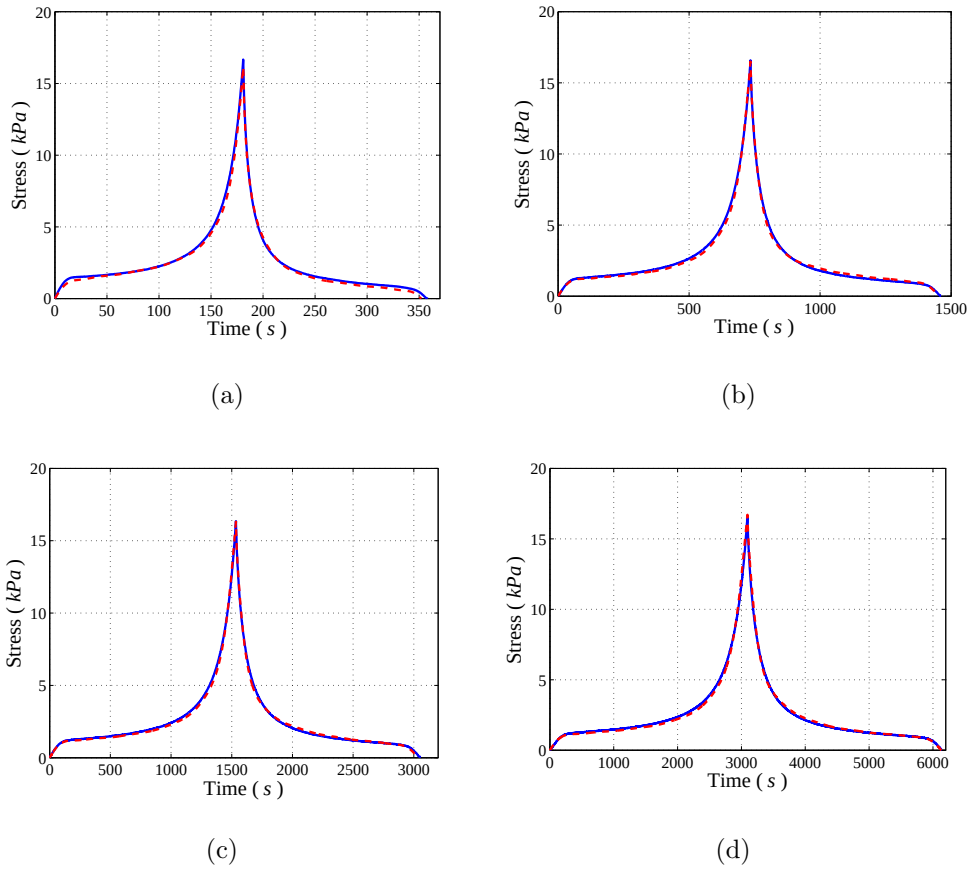

Figure 3.45. Results of simultaneously fitting the foam model to all compression test data for Foam 1. $M_1 = 11$, $M_2 = 3$, and $N = 15$. Blue: experiment (solid); red: estimated response (dashed). Input strain rate: (a) $0.00438/s$, (b) $0.00109/s$, (c) $0.00052/s$, (d) $0.00026/s$. R^2: 0.990, 0.996, 0.996 and 0.995, respectively.

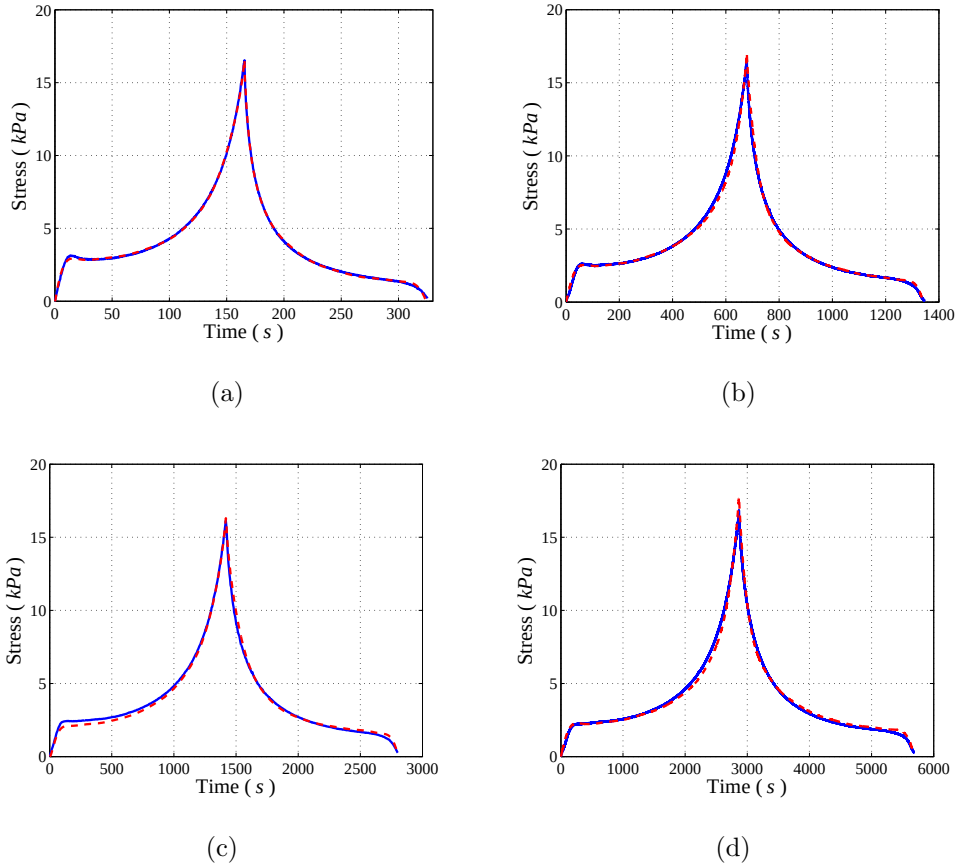

Figure 3.46. Results of simultaneously fitting the foam model to all compression test data for Foam 2. $M_1 = 8$, $M_2 = 8$, and $N = 15$. Blue: experiment (solid); red: estimated response (dashed). Input strain rate: (a) $0.00438/s$, (b) $0.00109/s$, (c) $0.00052/s$, (d) $0.00026/s$. R^2: 0.990, 0.996, 0.996 and 0.995, respectively.

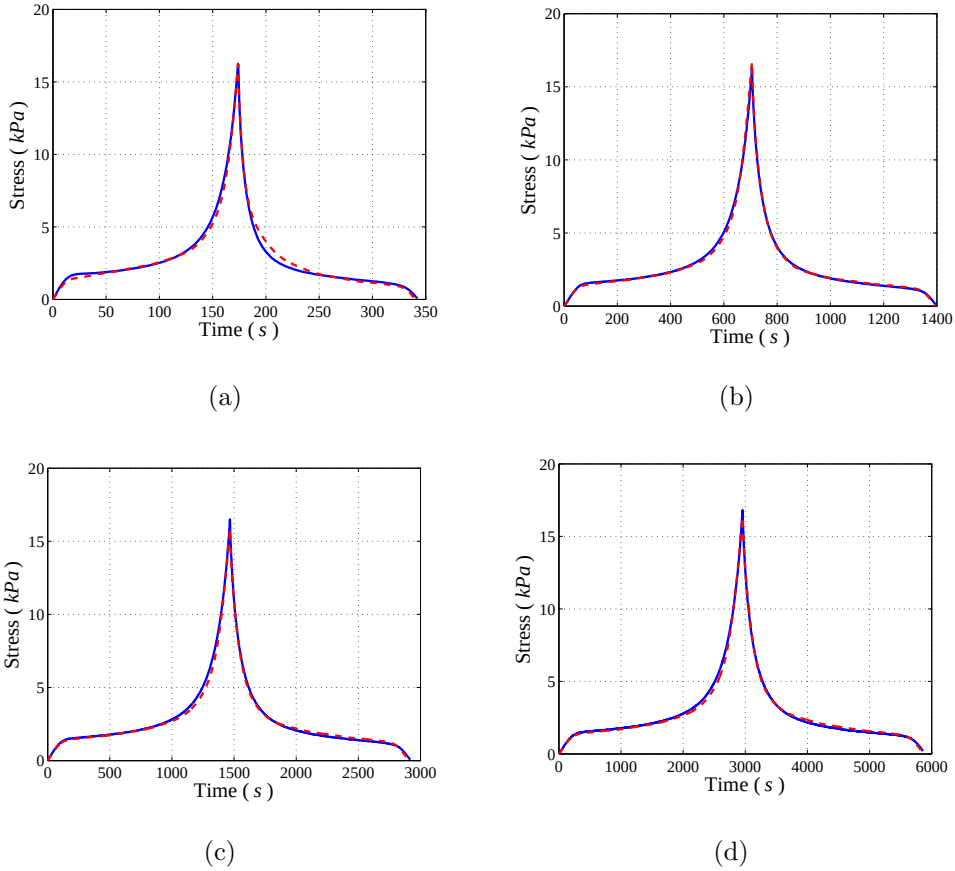

Figure 3.47. Results of simultaneously fitting the foam model to all compression test data for Foam 3. $M_1 = 8$, $M_2 = 12$, and $N = 15$. Blue: experiment (solid); red: estimated response (dashed). Input strain rate:(a) $0.00438/s$, (b) $0.00109/s$, (c) $0.00052/s$, (d) $0.00026/s$. R^2: 0.990, 0.996, 0.996 and 0.995, respectively.

3.7 Layered Foam System

In the first part of this chapter, a foam model was proposed. Then, the foam model was fitted to the measured responses from experiments conducted on 5 different foam types, i.e. 2 low density foams and 3 CONFOR foams, at different strain rates. In this section, mechanics of layered foam systems which is composed of two layers of CONFOR foams is studied. Such systems of layered viscoelastic materials have different applications in engineering, e.g. human flesh, seat cushions and even human soft tissues in the seat-occupant system. Here, the behavior of layered foam systems is predicted using the estimated foam models with strain rate dependent viscoelastic parameters. The models describe the mechanical behavior of viscoelastic materials in layers when the materials are subjected to inputs at different strain rates. In order to validate the predictions, experiments were conducted on layered foam systems when the systems are subjected to large strain compression at constant rates, see Figure 3.1(b). Although the layered foam system is compressed at a constant global rate, individual foam components are compressed at different rates. Therefore, a methods is also proposed which can be used to predict compression rates in each foam given the input constant strain rate.

3.7.1 Experiments

Deshmukh [3] performed uniaxial compression tests on a 2-layer CONFOR foam system. The experimental setup and procedures are similar to the ones described earlier for single-layer foams. The layered foam, composed of CONFOR Foam 1 and Foam 2, were compressed at different strain rates by applying a ramp input displacement to the top surface of the layered foams. The composite foam is compressed by 80% at two different rates equal to $4.6 \times 10^{-3}\ s^{-1}$ and $5.2632 \times 10^{-4}\ s^{-1}$. The measured stress-time and stress-strain responses are shown in Figures 3.48 and 3.49. The measured stress-time and stress-strain responses of single-layer foam blocks were shown in Figures 3.30 and 3.31. Since two foams in the system have different elastic

and viscoelastic properties, the stress-strain (or stress-time) response of the system is different from the stress-strain (or stress-time) responses of the foams in the layers. One obvious difference is a bump, e.g. non-monotonic stress response, which appears in the system response around 80 s in the fastest experiment, as shown in Figure 3.48(a).

3.7.2 Methodology for Estimating the Mechanical Behavior of Layered Foam

Deshmukh [3] developed and tested a method for estimating the response of layered foam systems. This method is based on the concept of springs in series which represent the layered system. A 2-layer composite foam with its equivalent springs in series is shown in Figure 3.50. For springs in series, the force through the layered foam system is

$$\sigma = \sigma_1 = \sigma_2, \tag{3.40}$$

where σ, σ_1 and σ_2 represent total stress, stress in Foam 1 and stress in Foam 2, respectively. Also, the deformation in the system is given by

$$x = x_1 + x_2, \tag{3.41}$$

where, x_1 and x_2 are deformations in Foam 1 and Foam 2, respectively. The deformation x is the externally applied compression to the layered foam system. This expression can be written in terms of strains as

$$\varepsilon = \varepsilon_1 \frac{L_1}{L} + \varepsilon_2 \frac{L_2}{L}, \tag{3.42}$$

where, ε is the global strain in the layered system, ε_1 and ε_2 are the strains in Foam 1 and Foam 2 respectively, L_1 and L_2 are the undeformed thicknesses of Foam 1 and Foam 2, respectively and $L = L_1 + L_2$. In order to predict the layered foam stress responses, Deshmukh [3] used the stress-strain-curves for individual layers and combine them using the concept of equivalent spring for springs in series to obtain a prediction for stress-strain curve for the layered system. For complete procedures refer to [3].

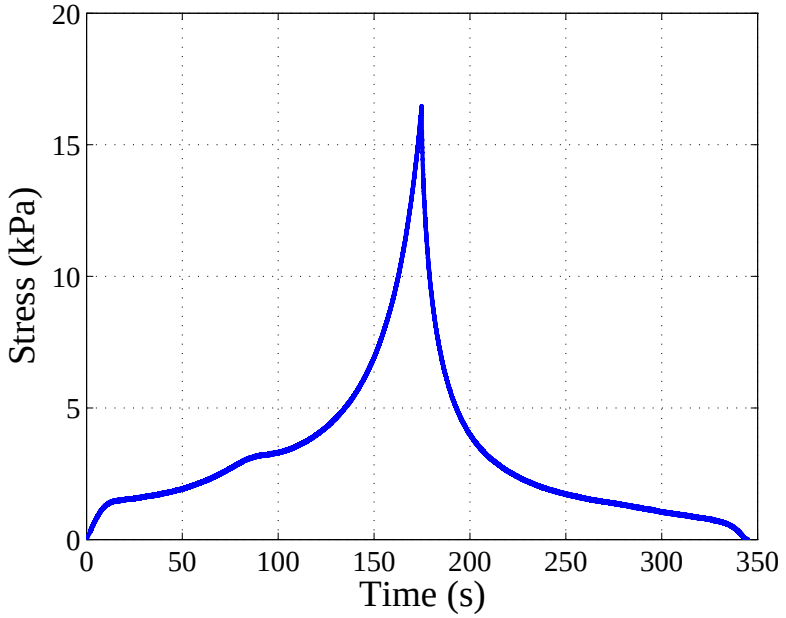

(a)

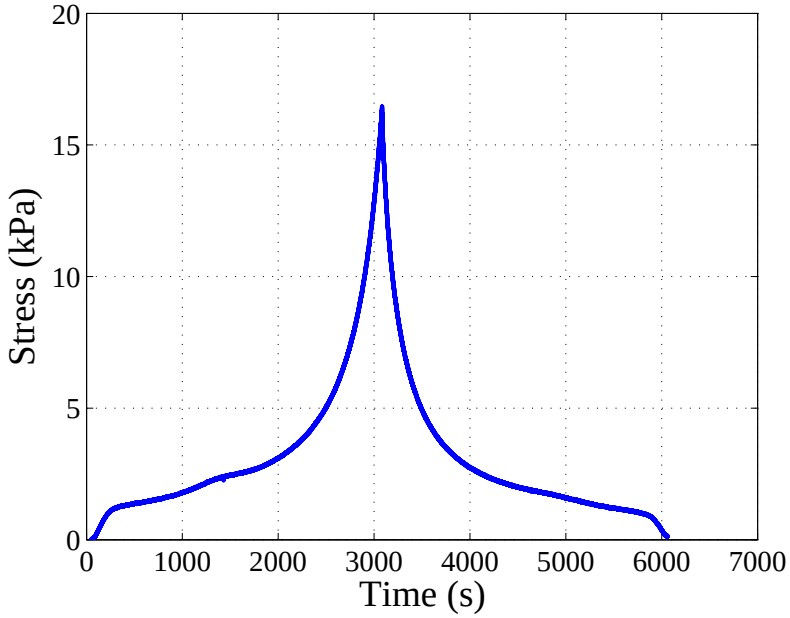

(b)

Figure 3.48. Results of compression tests on layered or composite foam composed of CONFOR Foam 1 and Foam 2. Stress versus time and the input strain rate (a) $4.6 \times 10^{-3}\ s^{-1}$, and (b) $5.2632 \times 10^{-4}\ s^{-1}$.

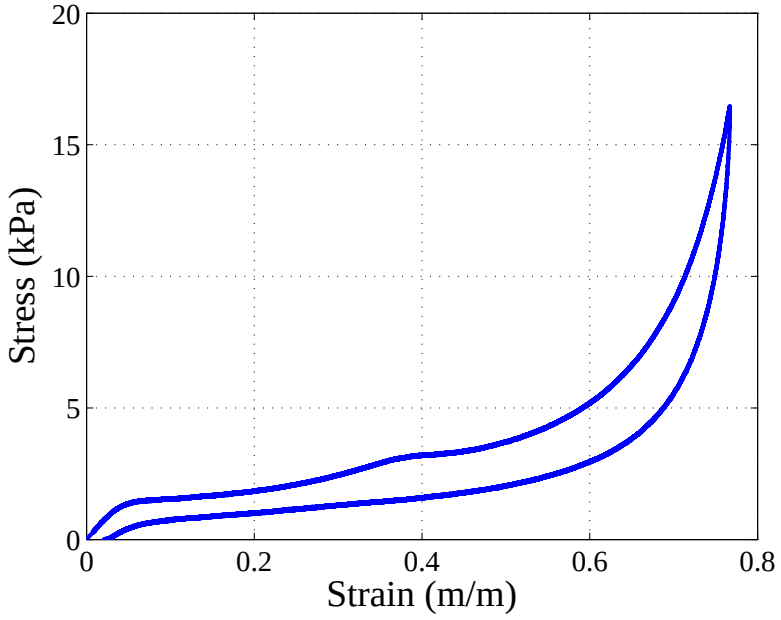

(a)

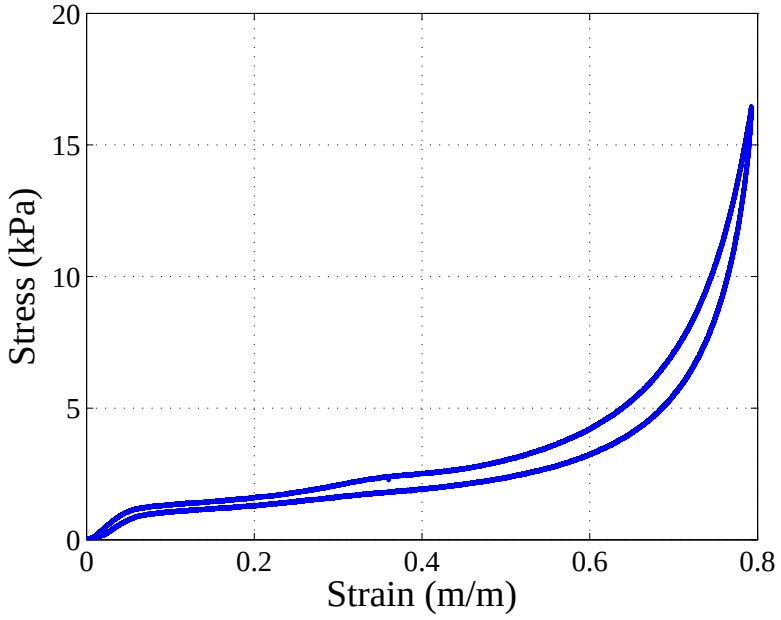

(b)

Figure 3.49. Results of compression tests on layered foam composed of CONFOR Foam 1 and Foam 2. Stress versus strain and the input strain rate (a) $4.6 \times 10^{-3}\ s^{-1}$, and (b) $5.2632 \times 10^{-4}\ s^{-1}$.

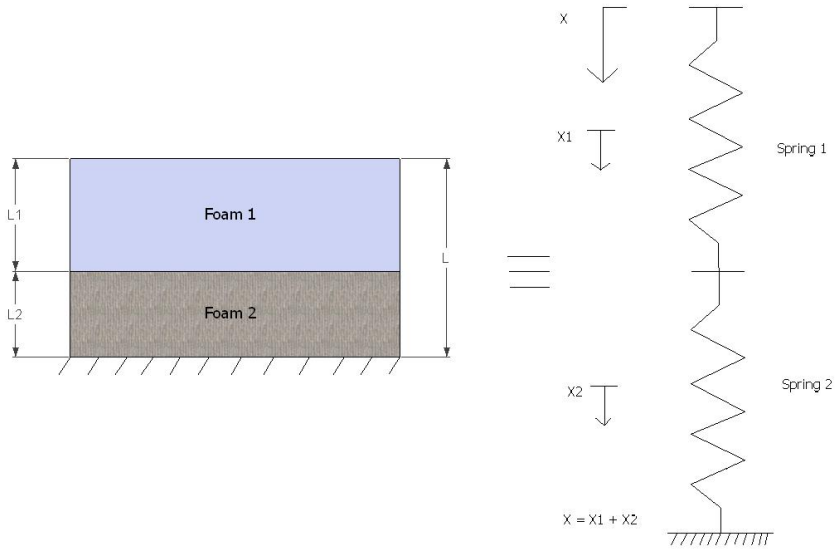

Figure 3.50. Schematic view of the geometry of a 2-layer foam system with its equivalent springs-in-series representation [3].

The method described above is based on the assumption that as the layered foam system is compressed at a single strain rate, each foam in the layers is also compressed at the same rate. However, it is well known that as the layered-foam is compressed, different foams in the layers are compressed at different rates due to their different elastic and viscoelastic properties. Here, a new estimation technique is developed, which considers the strain rate dependency of different materials in the layers, e.g. different layers compressed at different rates. First it is assumed that the force, or stress, through the layered foam system as well as the individual layers is the same. Assuming the external compression, i.e. input displacement applied on the top surface of the system, is x, see Figure 3.48, the total strain in the layered foam is,

$$\epsilon = \frac{x}{L_1 + L_2}, \tag{3.43}$$

where L_1 and L_2 are the undeformed thicknesses of the top foam and the bottom foam, respectively. The absolute deformations of the top foam and the bottom foam are denoted by x_1 and x_2. Therefore, the strain in each layer is,

$$\epsilon_1 = \frac{x - x_1}{L_1}, \tag{3.44}$$

$$\epsilon_2 = \frac{x_2}{L_2}. \tag{3.45}$$

Combining Equations (3.43) and (3.45), the strain in the top layer can be expressed as a function of the input strain ϵ and the strain in the second layer ϵ_2 as,

$$\epsilon_1 = \frac{(L_1 + L_2)\epsilon - \epsilon_2 L_2}{L_1}. \tag{3.46}$$

Note that the stress in the individual layers is expressed by Equation (3.5). Substituting Equation (3.46) into Equation (3.5), the stress in each layer is given by

$$\sigma_1 = \sum_{i=1}^{N} k_i \epsilon_1^i + \int_0^t a_1 e^{-\alpha_1(t-\tau)} \sum_{i=1}^{N} k_i \epsilon_1^i(\tau) d\tau + \int_0^t b_1 e^{-\beta_1(t-\tau)} \dot{\epsilon}_1(\tau) d\tau, \tag{3.47}$$

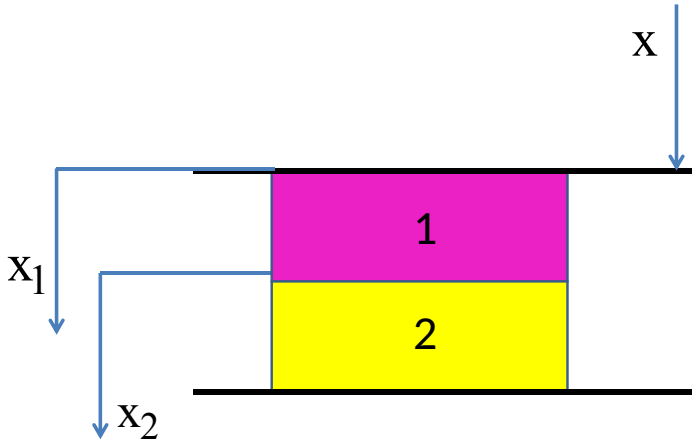

Figure 3.51. Schematic view of the geometry of a 2-layer foam system.

or,

$$\begin{aligned}\sigma_1 &= \sum_{i=1}^{N} k_i(\frac{(L_1+L_2)\epsilon-\epsilon_2 L_2}{L_1})^i \\ &+ \int_0^t a_1 e^{-\alpha_1(t-\tau)} \sum_{i=1}^{N} k_i(\frac{(L_1+L_2)\epsilon-\epsilon_2 L_2}{L_1})^i d\tau \\ &+ \int_0^t b_1 e^{-\beta_1(t-\tau)}(\frac{(L_1+L_2)\dot{\epsilon}-\dot{\epsilon}_2 L_2}{L_1})d\tau,\end{aligned} \tag{3.48}$$

and

$$\sigma_2 = \sum_{i=1}^{N} h_i \epsilon_2^i(t) + \int_0^t a_2 e^{-\alpha_2(t-\tau)} \sum_{i=1}^{N} k_i \epsilon_2^i(\tau) d\tau + \int_0^t b_2 e^{-\beta_2(t-\tau)} \dot{\epsilon}_2(\tau) d\tau. \tag{3.49}$$

Here, k_i, h_i, a_1, b_1, α_1, β_1, a_2, b_2, α_2, β_2 are the elastic and viscoelastic parameters and are functions of the strain rate. Recall that the stresses in the two layers are the same ($\sigma_1 = \sigma_2$), Equations (3.49) and (3.49) give,

$$\begin{aligned}\sum_{i=1}^{N} k_i(\frac{(L_1+L_2)\epsilon-\epsilon_2 L_2}{L_1})^i &+ \int_0^t a_1 e^{-\alpha_1(t-\tau)} \sum_{i=1}^{N} k_i(\frac{(L_1+L_2)\epsilon-\epsilon_2 L_2}{L_1})^i d\tau \\ &+ \int_0^t b_1 e^{-\beta_1(t-\tau)}(\frac{(L_1+L_2)\dot{\epsilon}-\dot{\epsilon}_2 L_2}{L_1})d\tau \\ &= \sum_{i=1}^{N} h_i \epsilon_2(t)^i + \int_0^t a_2 e^{-\alpha_2(t-\tau)} \sum_{i=1}^{N} k_i \epsilon_2^i d\tau \\ &+ \int_0^t b_2 e^{-\beta_2(t-\tau)} \dot{\epsilon}_2 d\tau.\end{aligned} \tag{3.50}$$

Note that Equation (3.51) is an integro-algebraic equation. Following the steps described in [95], the integrals in Equation (3.51) can be converted to first order differential equations. Therefore, Equation (3.51) can be replaced by 5 equations as,

$$\begin{aligned}\sum_{i=1}^{N} k_i(\frac{(L_1+L_2)\epsilon-\epsilon_2 L_2}{L_1})^i + \sigma_{v1} + \sigma_{v2} &= \sum_{i=1}^{N} h_i \epsilon_2^i + \sigma_{v3} + \sigma_{v4}, \\ \dot{\sigma}_{v1} + \alpha_1 \sigma_{v1} &= a_1 \sum_{i=1}^{N} k_i(\frac{(L_1+L_2)\epsilon-\epsilon_2 L_2}{L_1})^i, \\ \dot{\sigma}_{v2} + \beta_1 \sigma_{v2} &= b_1(\frac{(L_1+L_2)\dot{\epsilon}-\dot{\epsilon}_2 L_2}{L_1}), \\ \dot{\sigma}_{v3} + \alpha_2 \sigma_{v3} &= a_2 \sum_{i=1}^{N} h_i \epsilon_2^i, \\ \dot{\sigma}_{v4} + \beta_2 \sigma_{v4} &= b_2 \dot{\epsilon}_2.\end{aligned} \tag{3.51}$$

The resulting Equation (3.52) are algebraic-differential equations. These five equations can solved simultaneously to find the five unknowns ϵ_2, σ_{v1}, σ_{v2}, σ_{v3} and σ_{v4}. Knowing ϵ_2, ϵ_1 can be computed using Equation (3.46). Then, using the estimated ϵ_1, σ_{v1} and σ_{v2} (or ϵ_2, σ_{v3} and σ_{v4}), the total stress in the layered foam system σ can be computed as,

$$\sigma = \sigma_1 = \sum_{i=1}^{N} k_i \epsilon_1^i + \sigma_{v1} + \sigma_{v2}, \tag{3.52}$$

or,

$$\sigma = \sigma_2 = \sum_{i=1}^{N} h_i \epsilon_2^i + \sigma_{v3} + \sigma_{v4}. \tag{3.53}$$

In the next section, the process explained in this section is used to estimate the responses of the layered foam system and the estimations will be compared to the experimental data.

3.7.3 Results

As the layered foam system is subjected to inputs with constant strain rates, two foams in the layers are compressed at different compression rates. Since the compression rates in two foams are not constant, simpler foam models such as models 1, 2 and 3 with constant, i.e. strain rate independent viscoelastic parameters are not expected to be effective.

In the second part of this chapter, foam models were estimated, which describe the uniaxial behavior of CONFOR Foam 1 and CONFOR Foam 2. The viscoelastic parameters of the estimated models are strain rate dependent, as shown in Figures 3.38 and 3.39. Here, the strain rate dependent foam models are used to predict the responses of layered foam composed of Foam 1 and Foam 2.

With the input strain shown in Figure 3.52, the estimated strains in the top foam and the bottom foam in the layered system are shown in Figure 3.53. The results are obtained by solving the algebraic-differential equations given in Equation (3.52). As is seen in Figure 3.53, the estimated strains are different in each layer. Interestingly, it is seen that the maximum strain in the bottom layer is larger than the maximum

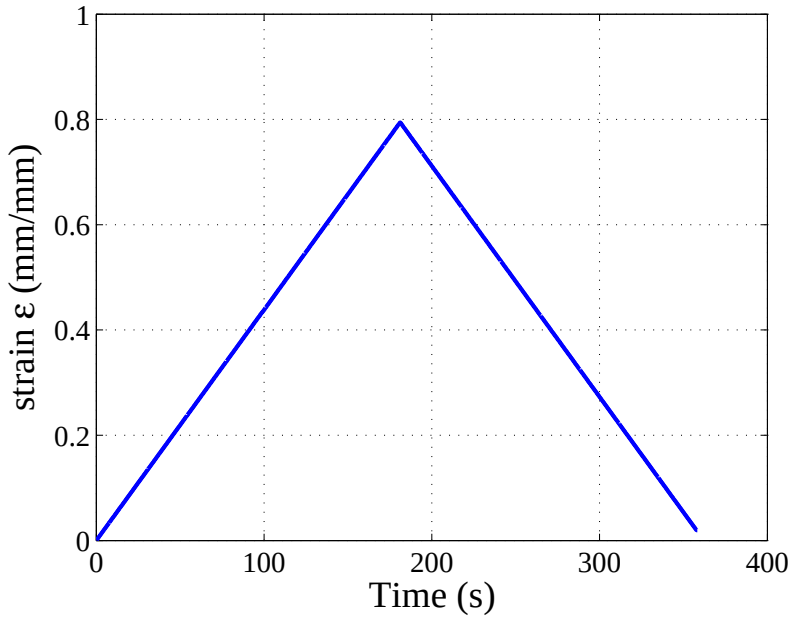

Figure 3.52. Input strain.

strain in the top layer. Also, the strain rate in both layers are functions of time although the input strain rate is constant during loading and in unloading cycles, see Figure 3.52. Also, Figure 3.54 shows the layered foam system at different time instances as the system undergoes a loading and unloading cycle.

The estimated stress response of the layered system for the fastest test (strain rate=$4.6 \times 10^{-3}\ s^{-1}$) is shown in Figure 3.55. Solving the algebraic-differential Equation (3.52) leads to the estimation of the strain in the top layer ϵ_1, or lower layer ϵ_2, as well as the viscoelastic stresses σ_{v1} and σ_{v2}, or σ_{v3} and σ_{v4}. Using the estimated strains, the elastic stress in each layer can be estimated. Finally, using estimated elastic stress and viscoelastic stress, the total stress can be computed as shown in Figure 3.55. This figure also shows the measured experimental stress response of the layered system. It is observed that the predicted response is in reasonable agreement with measured response, though, there are some differences with the predicted stress being higher than the measured response in the beginning of the loading cycle (0 *sec* to 50 *s*) and lower than the measured response at the end of the unloading cycle (300 *sec* to 350 *s*).

The estimated stress response of the layered system for the slower test (strain rate=$5.2632 \times 10^{-4}\ s^{-1}$) is shown in Figure 3.54. Also shown in the figure is the measured experimental response. As before, the predicted response is in good agreement with measured response. In the present case, interestingly, the predicted stress using the model is lower than the measured response at the end of the unloading cycle (5500 *s* to 6000 *s*).

3.8 Chapter Summary

In this chapter, a nonlinear viscoelastic model for predicting the uniaxial response of flexible polyurethane foam under large strain compression was introduced. The model structure combines features of many previously developed models. It differs from those models in that it can be used to make accurate predictions of responses

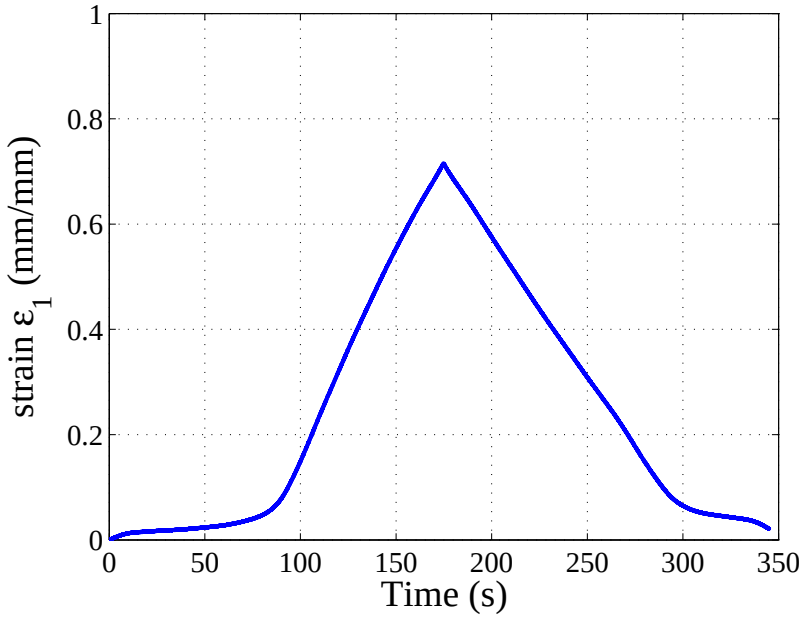

(a)

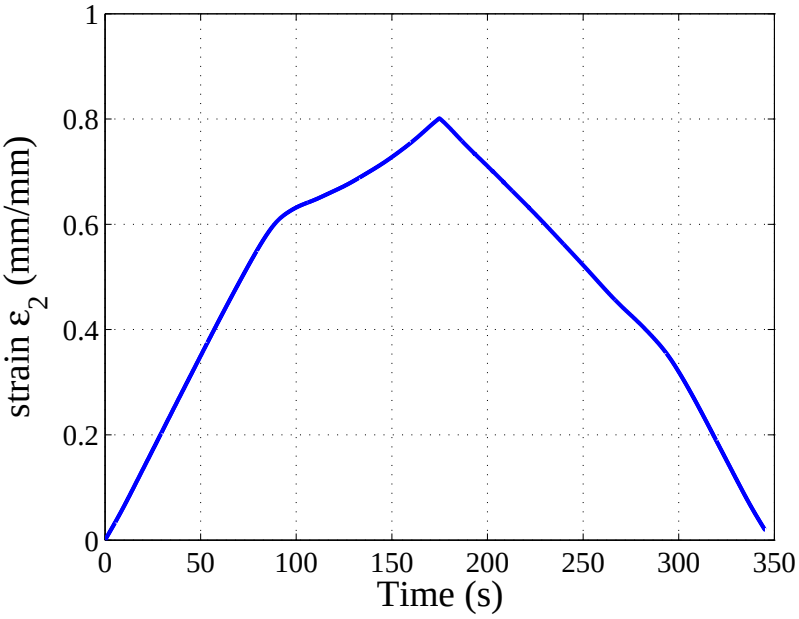

(b)

Figure 3.53. Predicted strains in (a) the top foam (Foam 1), (b) the bottom foam (Foam 2).

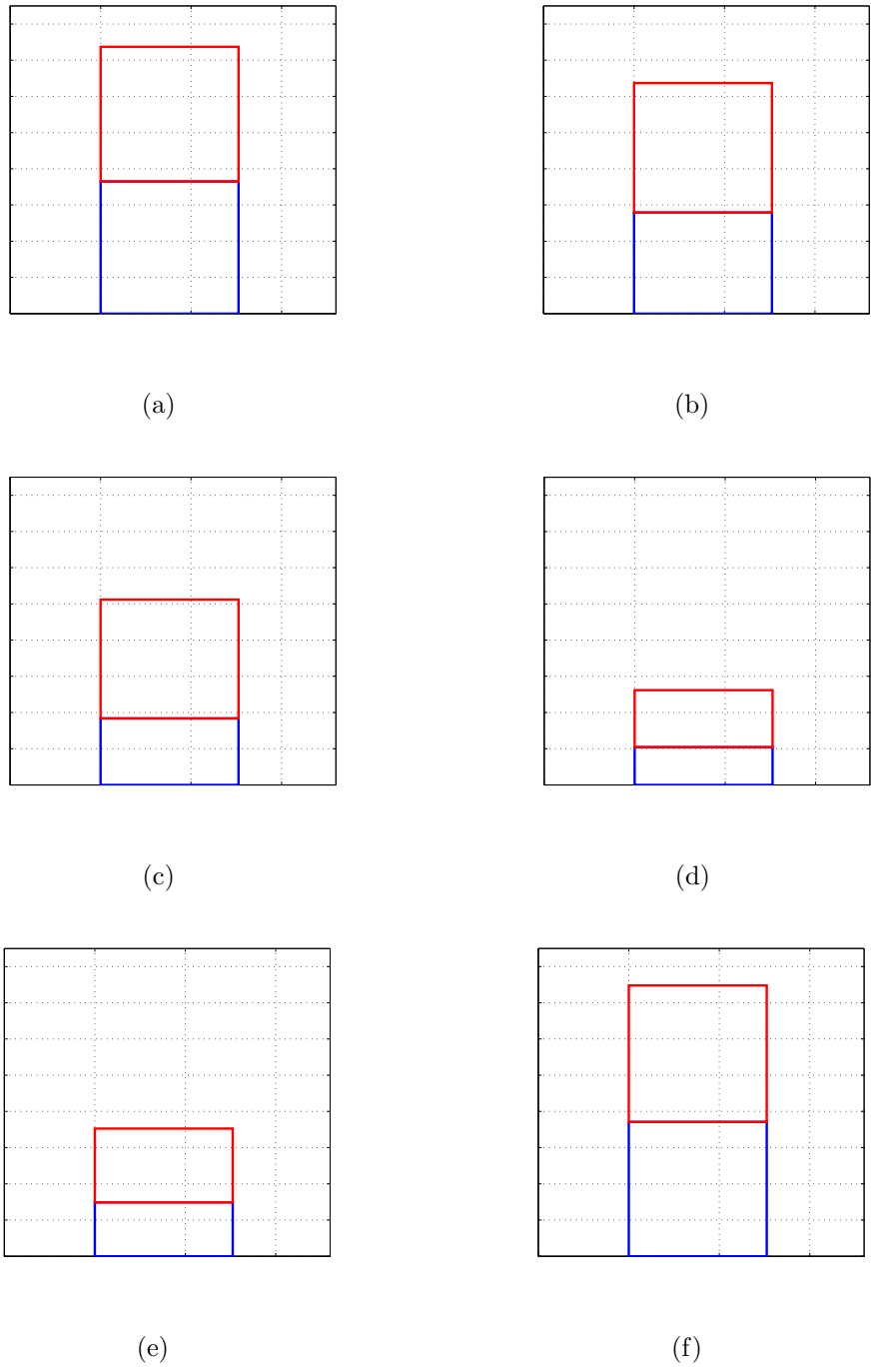

Figure 3.54. Predicted responses in the layer foam system after (a) $t = 10\ s$, (b) $t = 40\ s$, (c) $t = 80\ s$, (d) $t = 160\ s$, (e) $t = 230\ s$ and (f) $t = 355\ s$. Top: Foam 1, and Bottom: Foam 2.

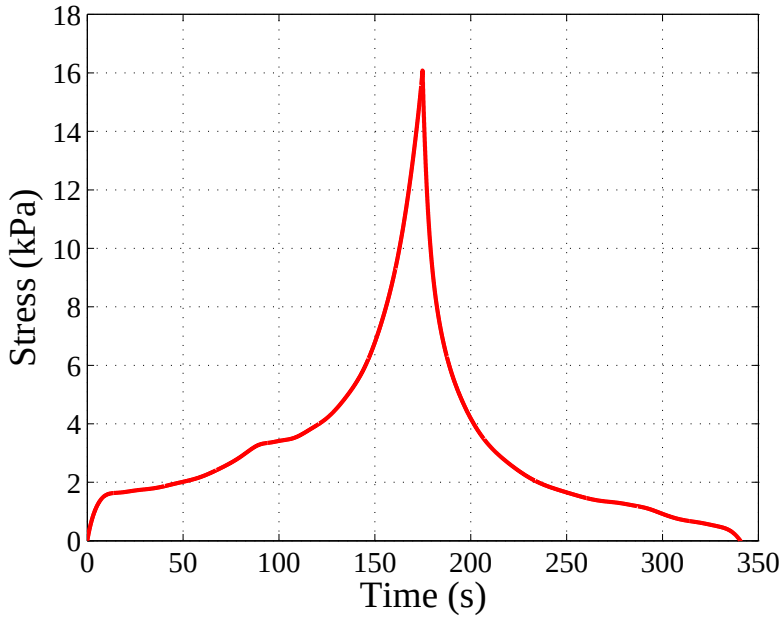

Figure 3.55. Predicted response of the layered foam system. Input strain rate=$4.6 \times 10^{-3}\ s^{-1}$.

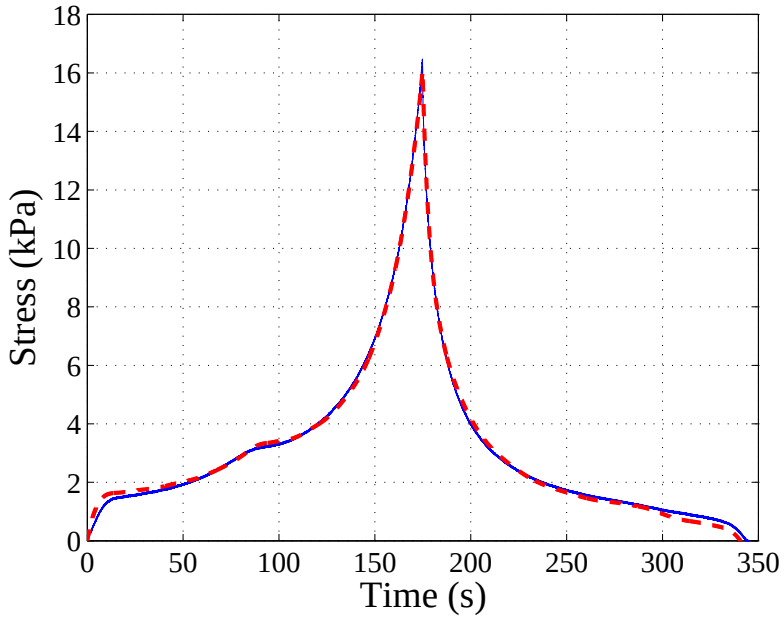

Figure 3.56. Response of the layered foam system. Blue: predicted response and red: experimental measurements. Input strain rate=$4.6 \times 10^{-3}\ s^{-1}$.

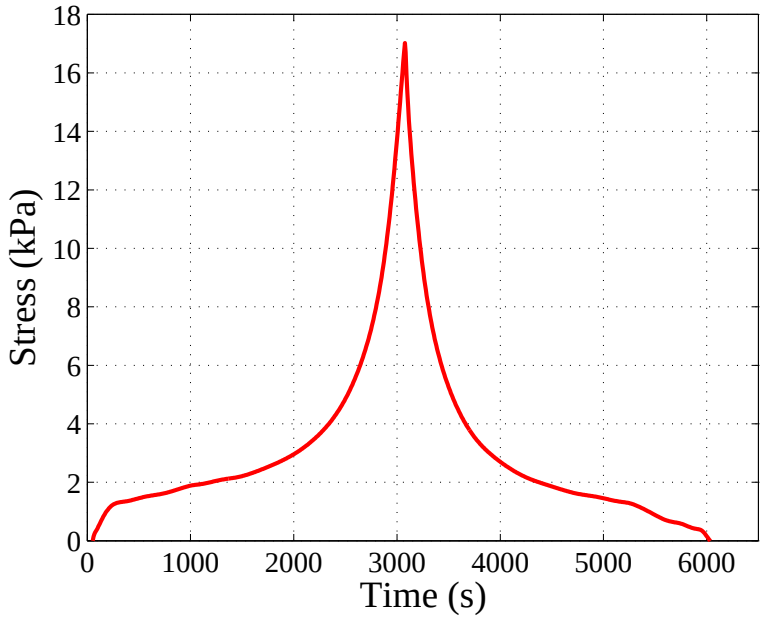

Figure 3.57. Predicted response of the layered foam system. Input strain rate=$5.2632 \times 10^{-4}\ s^{-1}$.

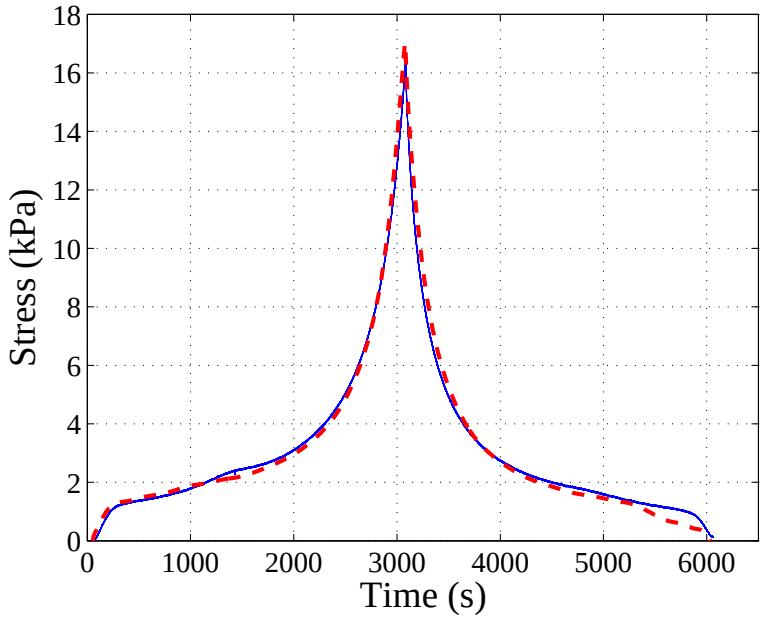

Figure 3.58. Response of the layered foam system. Blue: predicted response and red: experiment measurements. Input strain rate=$5.2632 \times 10^{-4}\ s^{-1}$.

measured in a series of cyclic experiments where strain rates were varied. It was shown that the estimated parameters of the viscoelastic components of the model were functions of the input strain rates and vary for different tests. This was addressed by:

- introducing a general model whose viscoelastic parameters were simple functions of the input strain rate,
- increasing the orders of the viscoelastic hereditary kernels and constructing a comprehensive model where estimated parameters could be treated as constants, and are not functions of the strain rates.

In the first case, the model is very simple, i.e. a total of four viscoelastic parameters are required, which makes it ideal for the seat-occupant modeling. Unlike the first approach, the second method is complex and the viscoelastic kernels have many terms. The technique was verified using results obtained from experiments on five different foam samples including two low density foams used in a car seat as well as on three types of high density CONFOR foams. Also, a methodology was developed to predict the mechanical behavior of a 2-layered foam system using the strain rate dependent model estimated for individual foams in the layers. It was observed that although the system was compressed at a constant strain rate, foams in different layers underwent compression at different rates. Also it was observed the compression rates in foams were functions of time. The predicted stress responses of the layer system is in general agreement with the measured responses in a layered foam system.

4. ANALYSIS OF THE STEADY-STATE RESPONSES OF A SINGLE DEGREE OF FREEDOM FOAM-MASS SYSTEM SUBJECTED TO HARMONIC BASE EXCITATION

In the previous chapter, a nonlinear viscoelastic foam model was introduced. This model can be used to model the mechanical behavior of car seat in a seat-occupant model. It is well known that the behavior of a seat-occupant system is strongly affected by the properties of seating foam. Therefore understanding the seat, or cushion, and the occupant interaction is of great interests and needs to be studied in details. The simplest model representing a seat-occupant system is a single-degree-of-freedom foam-mass system. In this simplified seat-occupant model, the seat is represented by a foam block, and the occupant is represented by a mass. In this chapter, first, the governing equations of the single-degree-of-freedom foam-mass system are derived for three different nonlinear viscoelastic foam models, i.e. foam Models 1, 3 and 4. Foam Model 2 is not considered here as this foam model is a especial case of Model 3. The governing equations are traditionally solved using numerical techniques such as direct-time integration of the governing equations. However, being highly nonlinear, such numerical methods are inefficient and very limited, e.g. when the system takes a long time to reach a steady state. Deng [96] and Singh [97] both used the harmonic balance method to study a similar single degree-of-freedom foam-mass system. However, their solutions were limited to two harmonic components due to the difficulty of including more harmonics in their solution using the standard harmonic balance solution approach. In this chapter, the incremental harmonic balance method is used to determine the steady-state behavior of the system subjected to a harmonic base excitation at different excitation levels and frequencies. The effects of riding mass, base excitation levels, system parameters and damping coefficients on the predicted responses are investigated. Also, the computation times needed by the incremental

harmonic balance and direct-time integration are compared. To verify the response predictions of the three developed foam-mass models, a set of tests were conducted on an experimental foam-mass system. The experimental set-up consists of a single-degree-of-freedom foam-mass system where the foam sample is similar to the one used in compression tests. It was observed that the simulated responses from each of the three models deviated significantly from the results from experiments. It was hypothesized that this was likely due to the strain rate dependence of foam parameters and the frequencies observed in resonant response of the experimental system were much higher compared to the strain rates in test data used for estimating the foam model parameters. Thus, foam Model 4 was modified to include the rate dependence of foam parameters [98, 99] and the results were evaluated.

This chapter is organized as follows: In the next section, the single-degree-of-freedom foam-mass system is introduced and the governing equations are derived. Next, the incremental harmonic balance approach is applied to construct the periodic solutions. The set of equations needed to determine the increments for updating the harmonic amplitudes are described. Computational issues are also discussed. The method is then used to examine the harmonic response behavior of the foam-mass system for three different foam models, three levels of base excitations, and two riding masses. Next, the experimental set-up and test procedures are introduced and experimental results are compared to the results from simulations. Deficiencies in the foam models are then discussed and one of the foam models is modified to address these issues. Finally, some concluding comments are given.

4.1 The Single-Degree-of-Freedom Model of a Foam-Mass System

A single-degree-of-freedom foam-mass model, which can be thought of as a very simple model of a seat-occupant system, is used to gain a better understanding of how the foam and the mass interact and how different foam models developed earlier predict the dynamic response of this system.

(a)

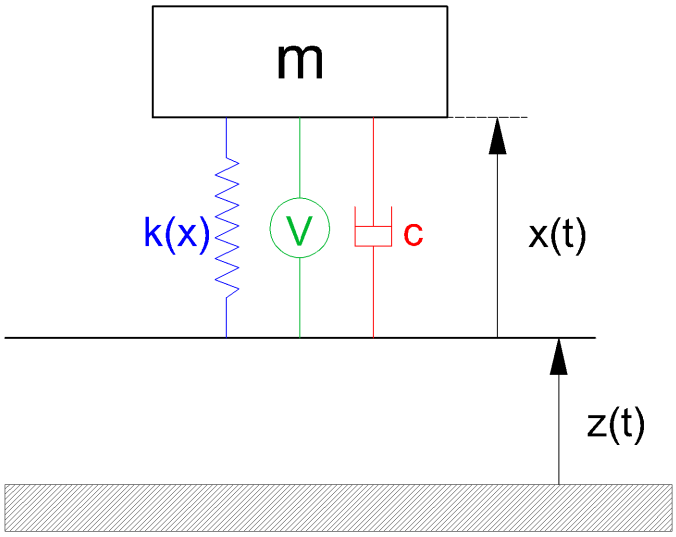

(b)

Figure 4.1. (a) The single-degree-of-freedom foam-mass system. (b) A schematic of the corresponding mass-viscoelastic-spring-damper model. Blue: nonlinear spring, green: viscoelastic element, and red: viscous damper. $x(t)$ is the displacement of the mass relative to the base, and $z(t)$ is the base displacement.

The physical foam-mass system, shown in Figure 4.1(a), consists of a foam cube with a mass on top. In order to ensure that the mass motion is uniaxial, the riding mass (top plate with mass attached) is guided by four vertical guide posts that constrain the motion of the mass in the vertical direction. This set-up can be represented by the model shown in schematic form in Figure 4.1(b), where the foam is replaced by a nonlinear spring element, a viscoelastic element, and a viscous damper. The viscous damper is added to account for additional damping in the foam not modeled by the viscoelastic component.

The equation of motion for this system, when undergoing base excitation is given by:

$$m\ddot{x} + c\dot{x} + \sum_{i=1}^{N} k_i x^i + V = -mg - m\ddot{z}, \tag{4.1}$$

where, m is the mass, c is the viscous damping coefficient, k_i are the nonlinear spring coefficients, V represents the viscoelastic contribution, $z(t)$ is the base motion, and $x(t)$ is the displacement of the mass relative to the base.

In the previous chapter, different viscoelastic models were reviewed. The viscoelastic foam models are hereditary type models in which the viscoelastic component is described as a convolution of relaxation kernels (sum of exponential terms) and functions of displacement and velocity. It was assumed that this function is separated into a nonlinear function of displacement and a linear function of velocity. In one form of the model, the nonlinear function of displacement is considered to be equal to the nonlinear spring force term in Equation (4.1) ($\sum_{i=1}^{N} k_i x^i$). The viscoelastic term in Equation (4.1) can be decomposed into two viscoelastic terms, $V = V_1 + V_2$. As discussed in the previous chapter, these two viscoelastic components can be written as,

$$V_1 = \int_0^t \sum_{j=1}^{M_1} a_j e^{-\alpha_j (t-\tau)} \sum_{i=1}^{N} k_i x^i(\tau) d\tau, \tag{4.2}$$

and

$$V_2 = \int_0^t \sum_{l=1}^{M_2} b_l e^{-\beta_l (t-\tau)} \dot{x}(\tau) d\tau. \tag{4.3}$$

Note that V_1 and V_2 can also be represented by M_1^{th} and M_2^{th} order differential equations, respectively. These equations can be derived by taking the Laplace transform of the convolution and recognizing s as a differential operator. For example, for the simplest case, when there is only one exponential term in the kernel ($M_1 = M_2 = 1$), $L\{V_1\} = \frac{a_1}{s+\alpha_1} L\{\sum_{i=1}^{N} k_i x^i\}$ and $L\{V_2\} = \frac{b_1 s}{s+\beta_1} L\{x\}$. Then, V_1 can be identified as a solution of the differential equation

$$\dot{V}_1 + \alpha_1 V_1 = a_1 \sum_{i=1}^{N} k_i x^i, \tag{4.4}$$

and V_2 as a solution of

$$\dot{V}_2 + \beta_1 V_2 = b_1 \dot{x}. \tag{4.5}$$

Thus, V_1 is a low-pass filtered elastic force and V_2 is a low-pass filtered response velocity. For higher-order hereditary kernels, these equations just become higher-order differential equations. Different combinations of these two viscoelastic terms (V_1 and V_2) lead to three different viscoelastic models, see Table 3.2, referred to as Model 1, Model 3 and Model 4 in this paper and summarized in Table 7.1. Note that foam Model 2 which was reviewed in Chapter 3 is not considered here as this model is an especial case of Model 3. Viscoelastic parameters, a_j, b_l, α_j and β_l ($j = 1, \cdots, M_1$ and $l = 1, \cdots, M_2$), along with the nonlinear spring coefficients, k_i ($i = 1, \cdots, N$), were estimated by fitting the model (neglecting the effect of inertia and without the viscous damping term, $c\dot{x}$ in Equation (4.1)) to quasi-static compression test data, which were given in Chapter 3, see Tables 3.3 and 3.4. Also, note that the viscous damping term $c\dot{x}$ is included in the dynamic model to account for other damping factors which are not modeled by viscoelastic damping mechanisms in the foam and thus may not be contributing in very slow or quasi-static tests. One example of such factors is the damping effect caused by air passing through foam at higher frequencies. In this research, initially, the viscous damping coefficient c is chosen based on previous experimental investigations on the base excited foam-mass system. But this value is later modified based on experimental data given later in this chapter.

Table 4.1. The three viscoelastic models for foam.

Model #	Viscoelastic Terms
1	$V = V_2 = \int_0^t \sum_{l=1}^{M_2} b_l e^{-\beta_l (t-\tau)} \dot{x}(\tau) d\tau$
3	$V = V_1 = \int_0^t \sum_{j=1}^{M_1} a_j e^{-\alpha_j (t-\tau)} \sum_{i=1}^{N} k_i x^i(\tau) d\tau$
4	$V = V_1 + V_2 = \int_0^t \sum_{j=1}^{M_1} a_j e^{-\alpha_j (t-\tau)} \sum_{i=1}^{N} k_i x^i(\tau) d\tau$ $+ \int_0^t \sum_{l=1}^{M_2} b_l e^{-\beta_l (t-\tau)} \dot{x}(\tau) d\tau$

4.2 The Incremental Harmonic Balance Method

Joshi [100] examined solutions of the foam-mass system in Equation (4.1) by direct-time integration for Model 1. Here, the incremental harmonic balance method is used to determine a sum of harmonics approximation to the steady-state solution of Equation (4.1). The method was adopted to address problems inherent in time integration including the time taken to reach steady states, the computational power required, and the inability to track unstable solutions possible in nonlinear systems.

First, Equation (4.1) is transformed into a set of incremental equations assuming that an estimate of a periodic solution is known. The time variable is rescaled based on the frequency of harmonic base excitation. Setting $\tau = \omega t$ gives $\frac{d}{dt} = \frac{d}{d\tau}\frac{d\tau}{dt} = \omega \frac{d}{d\tau}$. Therefore, for the case when $M_1 = M_2 = 1$, combining Equations (4.1), (4.4) and

(4.5) with this time transformation and replacing x by $x + \Delta x$, V_1 by $V_1 + \Delta V_1$, V_2 by $V_2 + \Delta V_2$ and ω by $\omega + \Delta\omega$, we obtain the following incremental equations:

$$\begin{aligned} &m\omega^2\Delta\ddot{x} + c\omega\Delta\dot{x} + \sum_{i=1}^{N} ik_i x^{i-1}\Delta x + \Delta V_1 + \Delta V_2 + (2m\omega\ddot{x} + c\dot{x})\Delta\omega + R_1 = 0, \\ &\omega\Delta\dot{V}_1 + \alpha_1\Delta V_1 - a_1\sum_{i=1}^{N} ik_i x^{i-1}\Delta x + \dot{V}_1\Delta\omega + R_2 = 0, \\ &\omega\Delta\dot{V}_2 + \beta_1\Delta V_2 - b_1\omega\Delta\dot{x} + (\dot{V}_2 - b_1\dot{x})\Delta\omega + R_3 = 0. \end{aligned} \tag{4.6}$$

Here x, V_1 and V_2 are the approximations of a periodic solution at frequency ω, Δx, ΔV_1 and ΔV_2 are the incremental improvements, and R_1, R_2 and R_3 are the residues given by:

$$\begin{aligned} R_1 &= m\omega^2\ddot{x} + c\omega\dot{x} + \sum_{i=1}^{N} k_i x^i + V_1 + V_2 + mg + m\omega^2\ddot{z}, \\ R_2 &= \omega\dot{V}_1 + \alpha V_1 - a\sum_{i=1}^{N} k_i x^i, \\ R_3 &= \omega\dot{V}_2 + \beta V_2 - b\omega\dot{x}. \end{aligned} \tag{4.7}$$

Note that the residues R_1, R_2 and R_3 will be zero if $x(t)$ is an exact solution for input $z(t)$ at a given frequency ω. With the time normalization ($\tau = \omega t$), the steady-state

responses are periodic with period 2π. Therefore, the responses and their increments are expressed as the following NT-term harmonic series approximations:

$$\begin{aligned}
x(\tau) &= A_{1,0} + \sum_{n=1}^{NT}[A_{1,n}\cos(n\tau) + B_{1,n}\sin n\tau], \\
\Delta x(\tau) &= \Delta A_{1,0} + \sum_{n=1}^{NT}[\Delta A_{1,n}\cos(n\tau) + \Delta B_{1,n}\sin n\tau], \\
V_1(\tau) &= A_{2,0} + \sum_{n=1}^{NT}[A_{2,n}\cos(n\tau) + B_{2,n}\sin n\tau], \\
\Delta V_1(\tau) &= \Delta A_{2,0} + \sum_{n=1}^{NT}[\Delta A_{2,n}\cos(n\tau) + \Delta B_{2,n}\sin n\tau], \\
V_2(\tau) &= A_{3,0} + \sum_{n=1}^{NT}[A_{3,n}\cos(n\tau) + B_{3,n}\sin n\tau], \\
\Delta V_2(\tau) &= \Delta A_{3,0} + \sum_{n=1}^{NT}[\Delta A_{3,n}\cos(n\tau) + \Delta B_{3,n}\sin n\tau].
\end{aligned} \tag{4.8}$$

The coefficients $\Delta A_{i,j}$ and $\Delta B_{i,j}$ are unknown and need to be calculated in order to update the current estimate of the NT-harmonic solution to Equation (4.1), i.e. the current estimates of $A_{m,n}$ and $B_{m,n}$ $m = 1, 2, 3$ and $n = 0, 1, \cdots, NT$. Substituting Equation (4.8) into Equation (4.6) and applying Galerkin's method to identify the unknown coefficients $\Delta A_{i,j}$ and $\Delta B_{i,j}$ yields,

$$\begin{aligned}
&\int_0^{2\pi}[m\omega^2\Delta\ddot{x} + c\omega\dot{x} + \sum_{i=1}^{N} ik_i x^{i-1}\Delta x + \Delta V_1 + \Delta V_2 + (2m\omega\ddot{x} + c\dot{x})\Delta\omega + R_1]\chi(\tau)d\tau = 0, \\
&\int_0^{2\pi}[\omega\Delta\dot{V}_1 + \alpha_1\Delta V_1 - a_1\sum_{i=1}^{N} ik_i x^{i-1}\Delta x + \dot{V}_1\Delta\omega + R_2]\chi(\tau)d\tau = 0, \\
&\int_0^{2\pi}[\omega\Delta\dot{V}_2 + \beta_1\Delta V_2 - b_1\omega\Delta\dot{x} + (\dot{V}_2 - b_1\dot{x})\Delta\omega + R_3]\chi(\tau)d\tau = 0,
\end{aligned} \tag{4.9}$$

where, x, Δx, V_1, ΔV_1, V_2 and ΔV_2 are given in Equation (4.8). The vector $\chi(\tau)$ is defined as

$$\chi(\tau) = [1, \cos(\tau), \cos(2\tau), \cdots, \cos(NT\tau), \sin(\tau), \sin(2\tau), \cdots, \sin(NT\tau)]^T. \tag{4.10}$$

The integrations in Equation (4.9) can be solved analytically and computed using current estimates of the harmonic amplitudes of x, V_1 and V_2 to produce equations that

are linear functions of the coefficients of $\Delta x(t)$, $\Delta V_1(t)$ and $\Delta V_2(t)$. The equations can be expressed in the following form:

$$[\Pi(B_{0,0}, B_{0,1}, \cdots, A_{1,1}, \cdots, \omega)]\Delta X + \Theta(B_{0,0}, B_{0,1}, \cdots, A_{1,1}, \cdots, \omega)\Delta\omega + [R] = 0, \tag{4.11}$$

where, $\Delta X = [\Delta A_{0,0}, \Delta A_{0,1}, \cdots, \Delta B_{0,1}, \cdots]^T$. The vector Θ contains the $3(2NT+1)$ terms resulting from the $\Delta\omega$ terms in Equation (4.9) and the R vector contains the $3(2NT+1)$ terms resulting from the R_1, R_2 and R_3 terms in Equation (4.9). This set of $3(2NT+1)$ equations are used to determine ΔX. If Equation (4.1) is excited at a single frequency (i.e. $\Delta\omega = 0$), the steady-state solution is found as follows. Estimates of the $3(2NT+1)$ harmonic coefficients for each of x, V_1 and V_2, e.g. obtained from linearized system, are used to calculate the terms in the matrix Π and vector R. The set of linear equations are solved to determine the incremental harmonic amplitudes (Δx, ΔV_1 and ΔV_2) and the estimates for x, V_1 and V_2 are updated. This process is repeated until convergence (as defined by preset tolerances for the differences between successive approximations) is obtained, i.e. here less than 0.01%. As the estimates of the coefficients in the harmonic approximations of x, V_1 and V_2 converge, the terms in R get smaller tending to zero if NT is sufficiently large. The first estimate of the harmonic amplitudes could be the solution to the linearized equations or a solution when the system was excited at nearby frequency.

If a solution path is of interest, Equation (7.2) can be augmented by coupling the solution with an arc-length continuation method [101–104] to track the solution path. This is done by introducing a path parameter η, and adding an equation:

$$g(v) - \eta = 0, \tag{4.12}$$

where, $v = [X, \omega]$. $g = v^T v$ is often used and it can be related arc length of the solution path [101]. Expressing η as $\eta + \Delta\eta$, an additional incremental equation can be constructed:

$$\frac{\partial g}{\partial X}\Delta X + \frac{\partial g}{\partial \omega}\Delta\omega - \Delta\eta + g - \eta = \frac{\partial g}{\partial X}\Delta X + \frac{\partial g}{\partial \omega}\Delta\omega - \Delta\eta + R_4 = 0, \tag{4.13}$$

where R_4 is the residue of the path equation. This equation is combined with those in Equation (7.2), $\Delta\eta$ is specified and $\Delta\omega$ and ΔX are solved for simultaneously. When solutions for a range of frequencies are required, the solution at the first frequency is used as an initial guess for the solution at the next point which should be close to the previous point. This process is repeated until the full solution path is obtained. Note that η is the distance along the solution path and $\Delta\eta$ determines the position of the next point on the solution path. Thus, with smaller $\Delta\eta$, a more finely resolved path is obtained. Also, smaller $\Delta\eta$ helps reduce the convergence time at each step. In this work, $\Delta\eta$ is chosen adaptively based on the number of iterations required for the previous two points [102]. $\Delta\eta$ is adjusted as:

$$\Delta\eta_n = \Delta\eta_{n-1}\frac{i_{n-2}}{i_{n-1}}, \tag{4.14}$$

where $\Delta\eta_n$ and $\Delta\eta_{n-1}$ are $\Delta\eta$ for the current and the previous point, respectively. i_{n-1} and i_{n-2} are the number of iterations needed for the program to converge to the solutions of the last two parameter points, i.e. frequencies. Therefore, if the incremental harmonic balance method needs more iterations to converge as it moves forward on the path, $\Delta\eta$ becomes smaller and vice versa. Additional solution paths can also be identified with this method which is described in detail in [101, 105].

4.3 Issues in Computation

Methods to speed up the computation of the terms in the matrix Π and vectors Θ and R in Equation (7.2) have been examined. These terms involve functions of the current harmonic series amplitudes and more the Fourier terms (higher NT) desired for a solution, more is the time used in the computations.

When the functions in these matrices involve products of harmonic series (as they do with the models considered here), the harmonic series can be expressed in their complex form and the coefficients of the harmonic series of the result of the product can be determined by convolving the coefficients of the two complex harmonic series being multiplied together. For example $2N_1 + 1$ terms in the first

series and $2N_2+1$ terms in the second series results in a $2(N_1+N_2)+1$ series after the convolution. For powers of harmonic series, or multiple products of different harmonic functions, the result can be determined by multiple successive convolutions. For example, applying this approach to the $k(x)$ term in R_1 and adding up contributions for each term in the polynomial would result in the complex harmonic series $k(x) = \sum_{n=-N.NT}^{N.NT} R_n e^{jn\tau} = P_0 + \sum_{n=1}^{N.NT}[P_n \cos(n\tau) + Q_n \sin(n\tau)]$. The relationship between the complex coefficients and the sines and cosines form of the Fourier series is: $R_0 = P_0$, $P_n = 2Real(R_n)$ and $Q_n = -2Imaginary(R_n)$. Thus P_0, P_1 to P_{NT} and Q_1 to Q_{NT} are easily derived. Also, once the complex harmonic series has been determined the results of Galerkin method are also known.

An alternative approach to doing these computations is as follows. At each stage in the iterative solution procedure, the current estimates of x, V_1 and V_2 can be discretized ($\tau = p\Delta$ and $p = 0, 1, \cdots, NP-1$ where $NP.\Delta = 2\pi$), choosing a sample rate $f_s = \frac{1}{\Delta}$ taking into account the highest frequency that will result after nonlinear operations on x have taken place (f_s chosen to be $> 2f_{max}$). The harmonic series coefficients of the harmonic nonlinear function of x, V_1, and/or V_2 can be determined by taking the NP-point discrete Fourier transform of the result after performing the nonlinear operations on the sampled versions of the signals and dividing by NP. This approach has the advantage that it should work with more complicated nonlinear functions of the variables, so long as the sample rate is chosen so that any effects of aliasing due to sampling of the harmonic functions over one period are very small. Note that NP is typically chosen to be a power of 2 to make this more efficient.

4.4 Results for Different Viscoelastic Models

The incremental harmonic balance method was applied to examine the steady-state harmonic response of the foam-mass system whose parameters are given in Ap-

pendix C and the parameters are the same as the viscoelastic and elastic parameters which were given in Tables 3.3 and 3.4 after rescaling them.

Also, to each of the models a linear viscous damping $c\dot{x}$ term was added with $c = 10\ Ns/m$. The viscous damping was initially introduced to decrease the transient response duration in the beginning of the response [100]. Previous experimental studies have also shown that the existence of this term is necessary in the model [96].

While all three foam models produced, as shown in Chapter 3, a reasonably good fit to the quasi-static compression data, interest here is in how these models perform under harmonic excitation and how the viscoelastic terms identified affect the frequency responses. Here, in the solution procedure, 10 harmonics were included and inclusion of a higher number of harmonics did not increase the accuracy significantly. Given Equation (4.8), the harmonic amplitudes are calculated by using:

$$H_n = \sqrt{A_{1,n}^2 + B_{1,n}^2}, \qquad n = 1, 2, ..., NT, \tag{4.15}$$

where H_n denotes the amplitude of the n^{th} harmonic in the solution of Equation (4.1).

Similarly, the response acceleration can be calculated noting that $z(\tau) = \frac{Z}{\omega^2}\sin(\tau)$ and thus $\ddot{z}(\tau) = -Z\sin(\tau)$. The absolute acceleration of the mass is expressed as,

$$\begin{aligned} \ddot{r}(\tau) &= \ddot{x}(\tau) + \ddot{z}(\tau) = \\ &= -\omega^2 A_{1,1} cos(\tau) - [\omega^2 B_{1,1} + Z] sin(\tau) - \omega^2 \sum_{n=2}^{NT} [n^2 A_{1,n} \cos(n\tau) + n^2 B_{1,n} \sin n\tau], \end{aligned} \tag{4.16}$$

where $\ddot{r}$ is the absolute acceleration of the mass. Using Equation (4.16), the acceleration associated with first harmonic is:

$$G_1 = \sqrt{(\omega^2 A_{1,1})^2 + (\omega^2 B_{1,1} + Z)^2}. \tag{4.17}$$

Finally, G_1 can be normalized by the input acceleration at the driving frequency ω as,

$$GN_1 = \frac{\sqrt{(\omega^2 A_{1,1})^2 + (\omega^2 B_{1,1} + Z)^2}}{Z}. \tag{4.18}$$

For higher harmonics, an equation similar to Equation (4.18) can also be modified as,

$$GN_n = \frac{\sqrt{(\omega^2 n^2 A_{1,n})^2 + (\omega^2 n^2 B_{1,n})^2}}{Z}. \tag{4.19}$$

In rest of this section, results of solving Equation (4.1) for three different viscoelastic models (Model 1, Model 3 and Model 4), two riding masses (1.3 kg and 2 kg), and three levels of base excitation (0.1 g, 0.2 g and 0.25g m/s^2) are presented. In each case, GN_1, see Equation (4.18), is plotted over a range of frequencies as shown in Figures 4.2, 6.12 and 6.13. Also shown in Figure 4.2 are the results when the viscoelastic terms are removed from Equation (4.1) (light dashed lines). It is observed that removing the viscoelastic terms from the governing equations affect the first harmonic frequency response by as much as 50% which emphasizes the importance of including the viscoelastic terms in the model. It also worth noting that removing the viscoelastic term described by Model 3 shifts the frequency response to the right (red curves in Figure 4.2) while removing the viscoelastic terms described by Model 1, or Model 4, shifts the frequency response to the left (blue and green curves in Figure 4.2). This can be explained by noting the negative sign of Model 3, a_1, given in Appendix H.

On examining Figures 4.2 to 6.13 it can be seen that as the base acceleration is increased from 0.1 g to 0.25 g m/s^2, nonlinearity starts influencing the response with the presence of a superharmonic in the response of Model 3 (red curve) near 2 Hz in Figure 6.13. The nonlinear behavior is more clearly evident for Model 3 (see Figure 6.12(b) and in Figure 6.13(b)) where the resonance peak shifts slightly to the right with increase in the base acceleration to 0.25 g m/s^2 indicating hardening behavior of the foam.

4.4.1 Higher Harmonics

As mentioned earlier, 10 harmonics were used for approximating the periodic solutions. For the strongest excitation level considered here, 0.25 g, the second, third and fourth harmonic components of the response for Model 4 are shown in Figure 6.14. It is seen that the strongest component is that of the second harmonic. However, even the second harmonic amplitude is small compared to the amplitude of

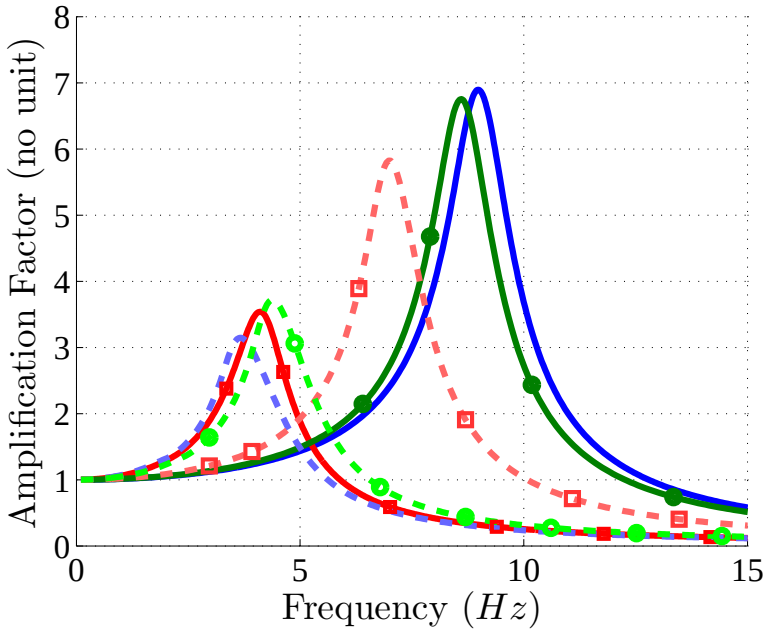

(a)

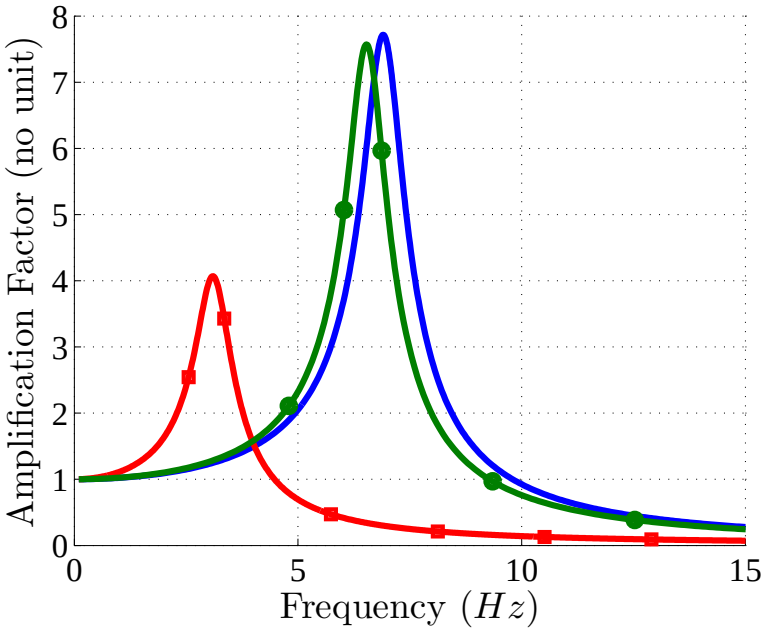

(b)

Figure 4.2. Frequency responses of the foam-mass system for different foam models for 0.1 g m/s^2 base excitation. blue - Model 1, red (square) - Model 3, green (circle) - Model 4. The light dashed lines are solutions with the viscoelastic terms removed from the models. (a) $m = 1.3$ kg, (b) $m = 2$ kg.

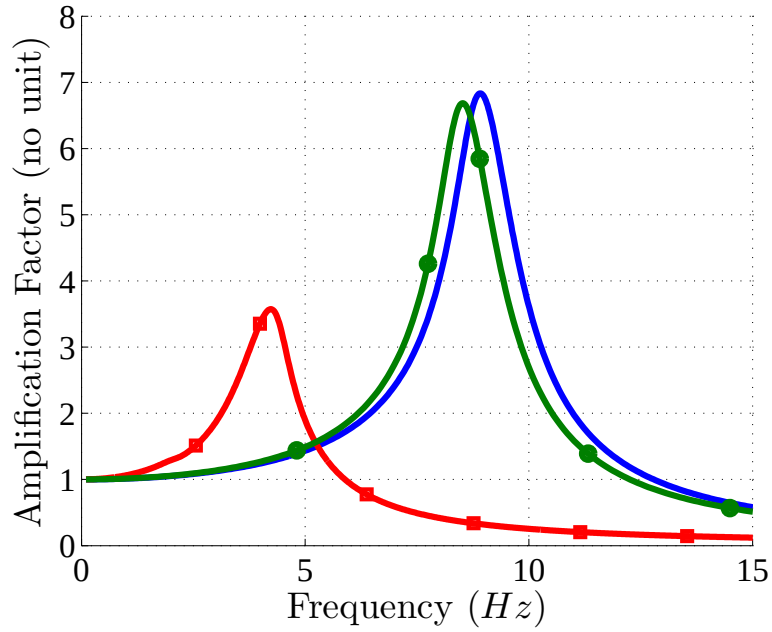

(a)

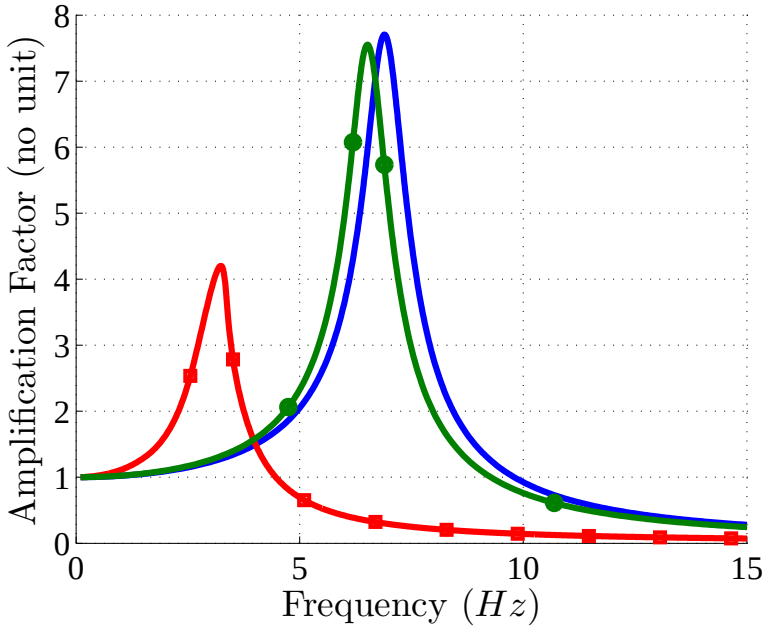

(b)

Figure 4.3. Frequency responses of the foam-mass system for different foam models for 0.2 g m/s^2 base excitation. blue - Model 1, red (square) - Model 3, and green (circle) - Model 4. (a) $m = 1.3$ kg, (b) $m = 2$ kg.

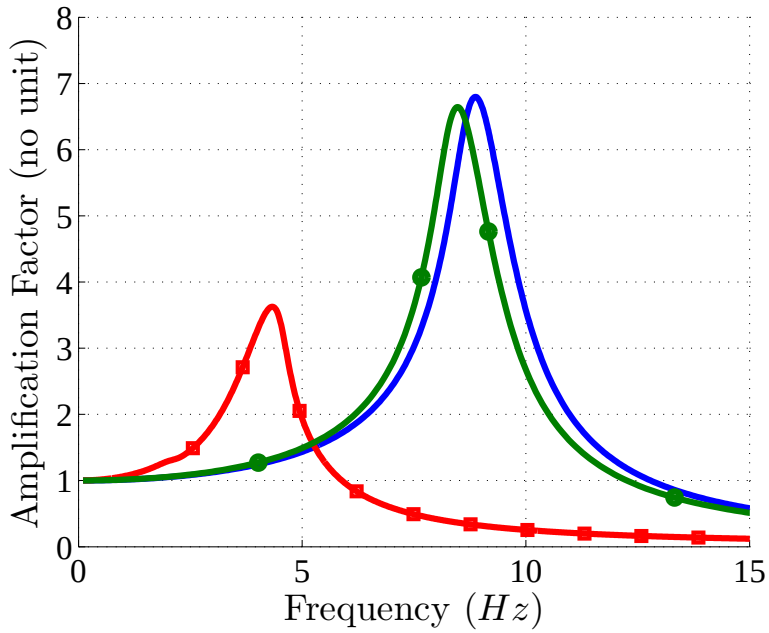

(a)

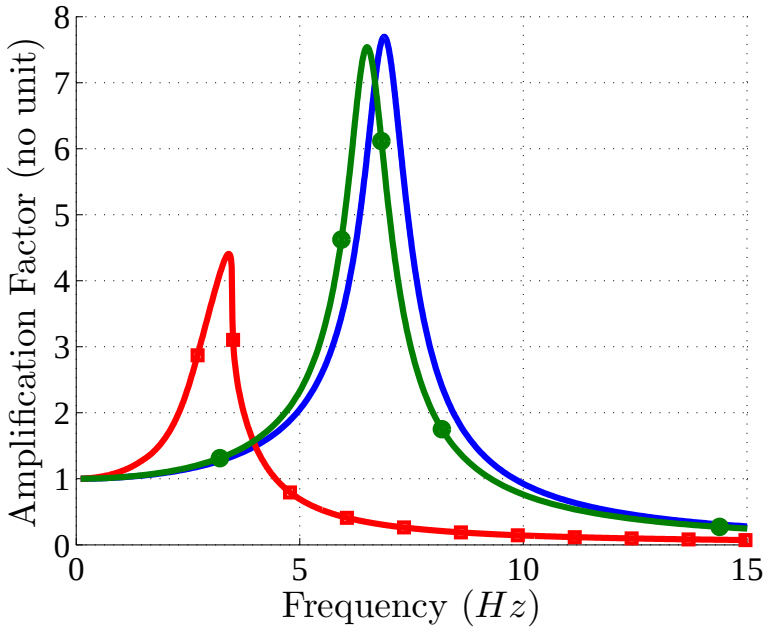

(b)

Figure 4.4. Frequency responses of the foam-mass system for different foam model for 0.25 g m/s^2 base excitation. blue - Model 1, red (square) - Model 3, and green (circle) - Model 4. (a) $m = 1.3$ kg, (b) $m = 2$ kg.

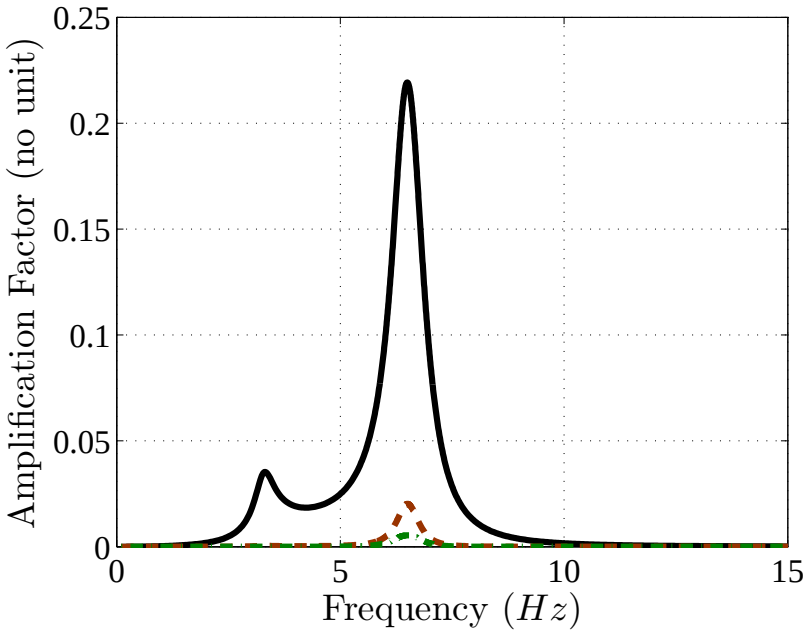

Figure 4.5. Higher harmonics in the system response for $m = 2\ kg$ and $0.25\ g\ m/s^2$ for foam Model 4. Black - second harmonic, dashed brown - third harmonic and dashed-dotted green - fourth harmonic.

the first harmonic (at most 3%). This confirms that higher harmonics beyond three don't play much role in the solution.

4.4.2 Predicting Settling Point and Natural Frequencies of the Linearized System

Given the nonlinear nature of foam, different riding masses produce different compression in the foam, also known as different "settling points". The settling point can be estimated by setting $\ddot{x} = \dot{x} = 0$ in Equation (4.1) and letting t to infinity in the viscoelastic terms. Using Model 4 with $M_1 = M_2 = 1$, Equation (4.1) reduces to:

$$\sum_{i=1}^{N} k_i x_{set}^i [1 + \sum_{j=1}^{M_1} \frac{a_j}{\alpha_j}] = mg. \tag{4.20}$$

This is a N^{th} order polynomial whose real root corresponds to the settling point x_{set} for a riding mass m. Figure 4.6(a) shows the compression produced in the foam for a range of riding masses.

Equation (4.1) can be linearized about the settling point x_{set} to analytically determine natural frequency of the system for small amplitude oscillations around the settling or equilibrium point. The damped natural frequencies of the linearized system are the imaginary part of the roots of the system characteristic equation. It is straight forward to show that the characteristic equation is:

$$ms^4 + (c + \alpha_1 m + \beta_1 m)s^3 + (b_1 + k_L + \alpha_1 c + \beta_1 c + \alpha_1\beta_1 m)s^2 + \\ (\alpha_1 b_1 + a_1 k_L + \alpha_1 k_L + \beta_1 k_L + \alpha_1\beta_1 c)s + a_1\beta_1 k_L + \alpha_1\beta_1 k_L = 0, \tag{4.21}$$

where k_L is the linearized stiffness $k_L = \sum_{i=1}^{N} i k_i x_{set}^{i-1}$. Estimated damped natural frequencies are plotted for a range of riding masses in Figure 6.1. The estimated natural frequencies for $m = 1.3\ kg$ and $m = 2\ kg$ are approximately 8.6 Hz, and 6.44 Hz, respectively, which agree with the peak locations in Figure 4.4. This is especially true given that in this case the base excitation is small and the system behavior is close to the linear one.

4.4.3 Incremental Harmonic Balance Method Efficiency

Incremental harmonic balance method, as expected, significantly improved the time needed to construct frequency responses of the foam-mass system. In Table 4.2 the CPU times needed to solve Equation (4.1) by incremental harmonic balance and by direct-time integration are compared. Results are reported for the highest level of base excitation (0.25 $g\ m/s^2$) with Model 4 describing the viscoelastic contribution and for two base excitation frequencies, 0.5 Hz and 6.4 Hz (peak resonance location). CPU time for a complete response curve consisting of 700 points are also reported.

The solution at 0.5 Hz is close to the linear response and the incremental harmonic balance converges to the true response in 11 iterations. However, when the system was subjected to base excitation at 6.4 Hz, 14 iterations were required for convergence.

To summarize, the incremental harmonic balance method was used to generate frequency responses for the foam-mass system for three different foam models. It was especially observed that the system responses predicted by these three models are

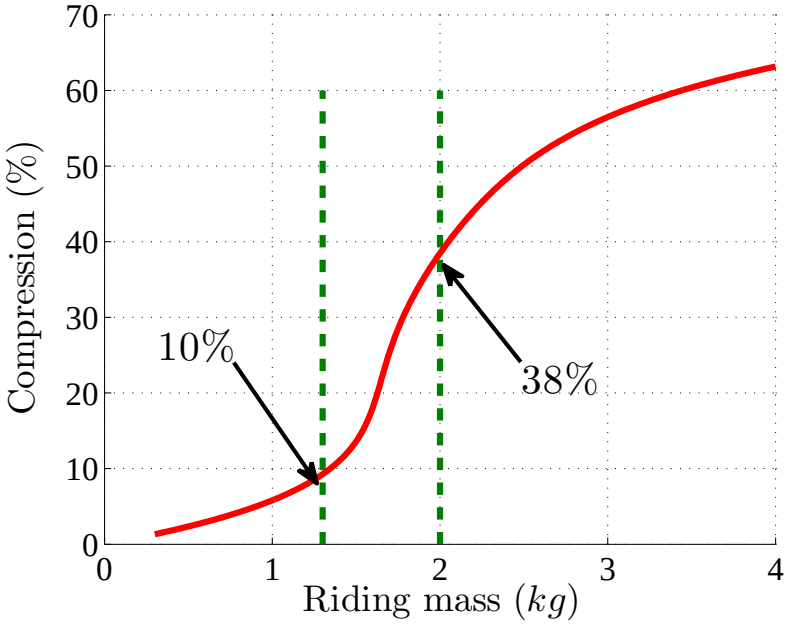

(a)

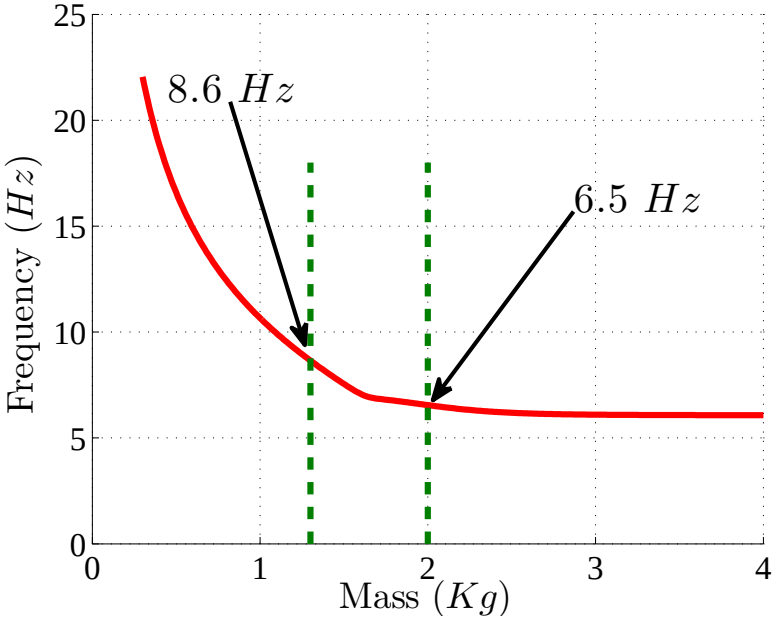

(b)

Figure 4.6. Effect of different riding masses on (a) Percentage compression in the foam, and (b) the natural frequency of the linearized system. Green lines show $m = 1.3\ kg$ and $m = 2\ kg$.

Table 4.2. CPU time used by incremental harmonic balance method and by direct-time integration for $0.25g\ m/s^2$ base excitation and foam Model 4.

Frequency of Base Excitation (Hz)	Incremental Harmonic Balance (s)	Time Integration (s)
0.5	1	1000
6.4	1	1460
Complete Frequency Response Response Curve (700 points)	765	$700\times\ 1000 < Time < 700 \times 1460$

different, although these models were estimated using an identical quasi-static compression test data. In the next section, detailed experiments with a foam-mass system set-up are reported and then the simulation results are compared to the experimental results. This will help shed light on the approximate foam model that should be used in modeling the seat-occupant system.

4.5 Experimental Verification and Model Improvements

The experimental setup and instrumentation are first described here. Results of experiments at different excitation levels are then presented and are compared to the model predictions shown earlier. Model adjustments are then considered to help improving the predictions.

4.5.1 Experiments

To study the dynamic response of the single-degree-of-freedom foam-mass system introduced in this chapter, a series of experiments were performed. The foam used in the systems was a 3 *inch* cube open cell polyurethane foam sample (a relative density = 0.027) cut from a car seat cushion which was identical to the one used in Chapter 3

in the quasi-static compression tests. Additional mass blocks can also be added to the upper plate in the foam-mass set-up to study systems with different riding masses. In the rest of this section, the experimental setup and procedures are explained.

4.5.1.1 Experimental Setup

To study the case of harmonic base excitation, the fixture in Figure 6.15(a) was bolted on to a hydraulic shaker table, see Figure 6.15(b). The fixture of the foam-mass system was mounted on the shaker table, as shown in Figure 6.15(b). The fixture was designed to constrain the motion of the mass riding on foam block to a single axis using four vertical posts. Additional mass blocks can also be added to the upper plate in the foam-mass set-up to study systems with different riding masses. The upper plate slides along the four vertical posts using low-friction bearings which help to reduce friction in the system significantly. The hydraulic shaker which was used to provide the base excitation to the foam-mass system had a displacement span of ± 2 *inches* and also an inbuilt MTS 458.90 type function generator that was capable of generating various input wave forms. Five PCB 3741B1210G type accelerometers conditioned by the PCB signal conditioner model 482C27 were used to acquire the input and response accelerations. One accelerometer was placed on the shaker table and the other four were placed on top plate of the foam-mass system, as shown in Figure 4.7. All the five acquisitions were passed through anti-aliasing filter Wavetek Model 852 with a cutoff frequency of 128 Hz. The signals were then sampled using a National Instruments Data Acquisition Card at a rate of 4096 $samples/second$. For full description of the setup, refer to [80].

4.5.1.2 Experiment Procedures

In this work, the amplitude and the phase of motion of the foam-mass system was recorded by varying the base excitation frequency maintaining a constant input acceleration. For each excitation frequency, the input acceleration was kept constant by finely adjusting the span of the hydraulic shaker at each frequency. The foam-mass system was subjected to different base excitations where the input signal to the system was stepped through a set of discrete frequencies and the responses of the system were recorded. The measurements were done by increasing the frequency from 2 Hz to 10 Hz in steps of 0.5 Hz in region away from resonance and in steps of 0.25 Hz near resonance. The same procedure was repeated and measurements were taken by also reducing the frequency from 10 Hz to 2 Hz following the same protocol. At each frequency, the system was excited till it reaches a steady state after changing the frequency from the previous setting. The steady state condition was ensured by comparing the response amplitudes of three consecutive 5 *second* measurements. If the amplitude change was less than 5% between the three consecutive measurements, it was assumed that the responses have reached steady state and final response was measured in that setting. In each experiment, the repeatability of response measurements was ensured by conducting several tests, under similar conditions, and comparing the measurements. It was observed that the variation between repeated measurements is small. The complete experiment protocol and procedures can be found in [106].

4.5.2 Comparison Between Simulation and Experimental Results

The set-up shown in Figure 4.7 was used to conduct a set of experiments on the foam-mass system with $m = 1.3\ kg$. Harmonic displacement was applied to the base plate at three different acceleration levels (peak acceleration equals to $0.1g$, $0.2g$, and $0.25g\ m/s^2$) while the excitation frequency was varied between 2 Hz and 10 Hz.

(a)

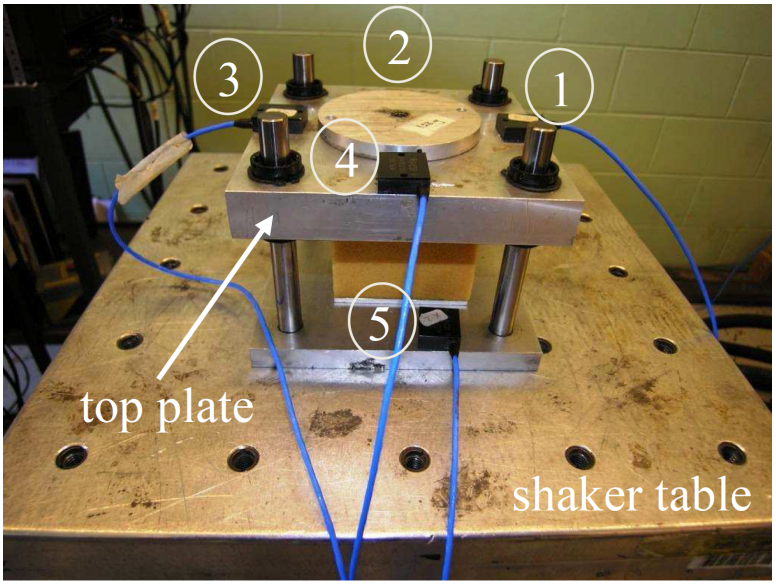

(b)

Figure 4.7. Experimental foam-mass system. (a) Different components of the experimental set-up: moving plate, fixed plate and four posts, and the foam sample; (b) assembled foam-mass system on the hydraulic shaker. (1)-(5) accelerometers measuring the top plate responses and base acceleration.

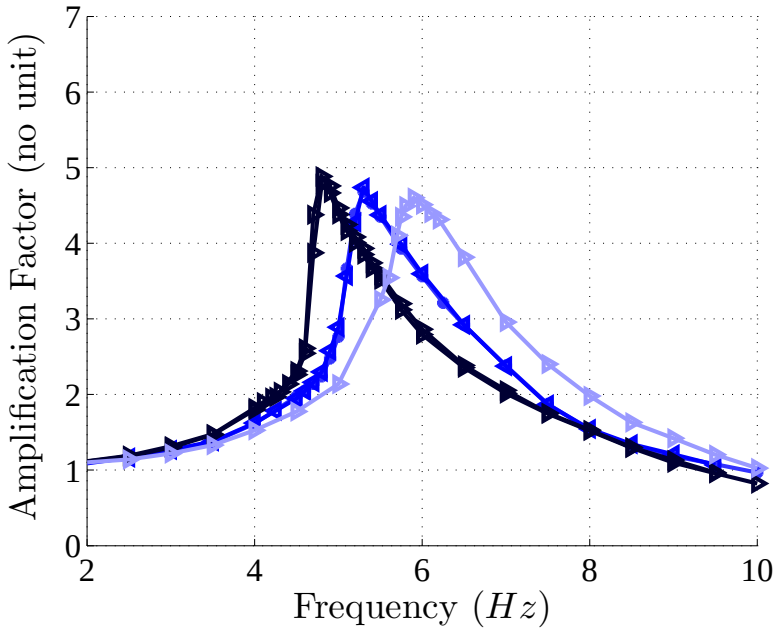

Figure 4.8. Experimental frequency response curves for the foam-mass system with $m = 1.3\ kg$ in Figure 4.7. Light blue: $0.15g\ m/s^2$ base acceleration; blue: $0.2g\ m/s^2$ base acceleration; black: $0.25g\ m/s^2$ base acceleration.

At each input frequency, the system was excited long enough to make sure that the response reached its steady-state. Then, the steady-state acceleration was recorded, its amplitude was normalized by the input acceleration (see Equation (4.18)) and plotted versus the input frequency. These plots are shown in Figure 4.8 for the three levels of base excitation.

The frequency response curves obtained from experiments and simulating Equation (4.1) with different foam models for $m = 1.3\ kg$ and $0.2g$ base acceleration are plotted in Figure 4.9. Similar to our previous observations, the simulated system responses are functions of the viscoelastic model used to generate the response curves and particularly none of the models are successful in predicting a response curve close to the one obtained from experiments. One possible explanation for this big difference can be that the three foam models were identified using a quasi-static compression test data with a time period of 5 *minutes* ($f = 0.0033\ Hz$). However, as observed

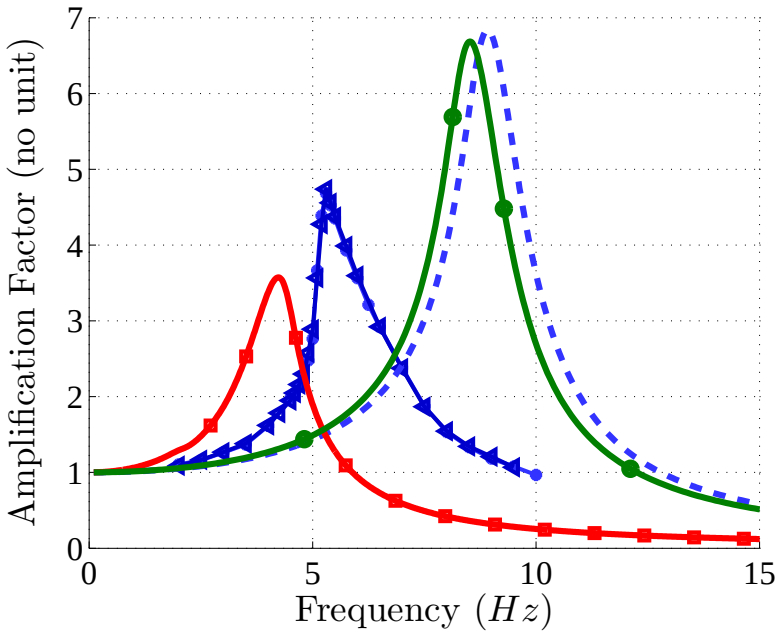

Figure 4.9. Experimental and simulated frequency responses for the foam-mass system for $m = 1.3\ kg$ and $0.2g\ m/s^2$ base acceleration. Dark blue: experiment, dashed blue: Model 1, red (square): Model 3, green (circle): Model 4.

in Chapter 3, for the foam models used in this research, the model parameters are functions of the input compression rate. For example, if another data set with different compression rate was used to estimate the foam parameters, the estimated parameters would be different.

Recall that in Chapter 3, simple functions were identified which govern the relationships between estimated viscoelastic parameters of foam Model 4 and the input strain rate, see Figures 3.21 and 3.22. The estimated parameters are given as:

$$\begin{aligned} a_1(|\dot{\epsilon}|) &= -9.2|\dot{\epsilon}| - 0.027, \\ \alpha_1(|\dot{\epsilon}|) &= 147.1|\dot{\epsilon}| + 0.21, \\ b_1(|\dot{\epsilon}|) &= \frac{1}{1.6 \times 10^{-3}|\dot{\epsilon}| + 1.16 \times 10^{-5}}, \\ \beta_1(|\dot{\epsilon}|) &= 47.2|\dot{\epsilon}| + 0.14, \end{aligned} \tag{4.22}$$

where $\dot{\epsilon}$ is the input strain rate. It was also shown that the estimated elastic parameters k_i for the six tests showed significantly less variation (by $< 5\%$). The resulting estimated elastic forces are shown in Figure 3.23. In the rest of this study, the foam Model 4 that also incorporates this dependence of viscoelastic model parameters on the strain rate is used. Thus the updated model of the single-degree-of-freedom foam-mass system is:

$$\begin{aligned} m\ddot{x} + c\dot{x} + \sum_{i=1}^{N} k_i x^i + V &= -mg - m\ddot{z}, \\ \dot{V}_1 + \alpha_1(|\dot{\epsilon}|)V_1 &= a_1(|\dot{\epsilon}|)\sum_{i=1}^{N} k_i x^i, \\ \dot{V}_2 + \beta_1(|\dot{\epsilon}|)V_2 &= b_1(|\dot{\epsilon}|)\dot{x}, \end{aligned} \tag{4.23}$$

where the elastic parameters are taken to be average over the six strain rates (see Figure 3.23). The incremental harmonic balance method is now applied to the foam-mass model represented by Equation (4.23). At each excitation frequency, Equations (4.6)-(7.2) are modified by replacing the viscoelastic parameters, a_1, α_1, b_1, and β_1, by functions, $a_1(\dot{\epsilon})$, $\alpha_1(\dot{\epsilon})$, $b_1(\dot{\epsilon})$, and $\beta_1(\dot{\epsilon})$.

The system frequency response curve obtained by solving Equation (4.23) for $m = 1.3\ kg$ and $0.2g\ m/s^2$ base acceleration is presented in Figure 4.10. In these results, the value of the viscous damper was adjusted to $c = 8.6\ Ns/m$ in order to match the peak amplitudes in the experimental results and simulations. Clearly, agreement between the simulated response curve and the experimental curves has significantly improved, although, the peak frequencies in experiment and simulations differ slightly by 2%. In the previous section, it was shown that there are some uncertainties in estimating the strain rate dependence given in Equation (4.22). Also, averages of the estimated elastic parameters k_i were used to generate the frequency response curve in Figure 4.10 which also adds additional uncertainty. In the next section, the effect of each of the system parameters on the response is investigated.

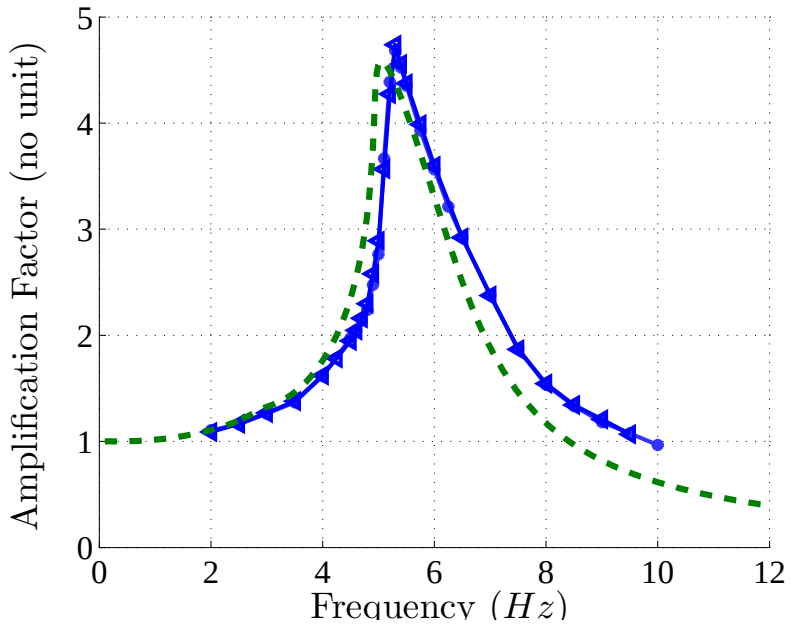

Figure 4.10. Comparison of experimental and simulation results for the foam-mass system for $m = 1.3\,kg$ and $0.2g\,m/s^2$ base acceleration. Solid blue (triangle): experiment and dashed green: simulation. The strain rate dependence of foam model parameters are described in Eqs. (4.22).

These observations will be used to then further modify the proposed model to further improve the correlation between experimental and simulated results.

4.5.3 Parameter Variation

In the previous section, the foam model was modified by the incorporation of compression-rate dependent viscoelastic parameters. It was shown that the simulated response curve is in significant agreement with the experimental curve although some differences still exist. In Figures 3.21 and 3.22, showing the strain rate dependence of viscoelastic parameters in Model 4, the red cross and the blue bar, respectively, represent the mean value and the standard deviation at each strain rate. The effect of this uncertainty on system response can be examined by simulating the response by varying one of the system parameters while the other parameters are kept constant and results are compared to the experimental result. Sample results are shown in Figures 4.11 to 4.13.

Response curves in Figures 4.11(a)-4.12(b) illustrate how variations in $a(\dot{\epsilon})$, $b(\dot{\epsilon})$, $\alpha(\dot{\epsilon})$, and $\beta(\dot{\epsilon})$ affect the frequency response curves. In each figure, the parameter under study is varied between 50% to 150% of its actual value, given in Equation (4.22). Figure 4.11(a) shows that decreasing $a(\dot{\epsilon})$, increases the peak frequency by 22% and peak amplitude by 33%. Results in Figure 4.12(a) show that by increasing $\alpha(\dot{\epsilon})$, the peak frequency and amplitude increase by 21% and 30%, respectively. These two figures can lead us to conclude that decreasing $a(\dot{\epsilon})$ by 15%, or increasing $\alpha(\dot{\epsilon})$ by 16%, can reduce differences in experimental and predicted response shown in Figure 4.10. However, these values are greater than the permissible variations which are dictated by estimation standard deviations (see Tables 3.3-3.5) for $a(\dot{\epsilon})$, or $\alpha(\dot{\epsilon})$. Figures 4.11(b) and 4.12(b) show that varying $b(\dot{\epsilon})$ and $\beta(\dot{\epsilon})$ results in only small changes in response curves. Results of changing the viscous damper coefficient between 90% and 110% of its previous value, $c = 8\ Ns/m$, are shown in Figure 4.13(a). As is expected, decreasing the viscous damping coefficient increases the peak amplitude. Softening

behavior also becomes more prominent for smaller values of c. Figure 4.13(b) shows the effect of varying $K(x)$ between 98% to 120% of its original value (the average of curves shown in Figure 3.23). It is observed that increasing the elastic component $K(x)$ increases the peak frequency as well as the peak amplitude. For example, increasing $K(x)$ by 4% results in an amplitude curve which is very close to the experimental curve. Using this, a new elastic function is defined as $K^*(x) = 1.05 \times K(x)$, where $K(x)$ is the original elastic function used (the average of curves shown in Figure 3.23). Also, noting that the estimated elastic functions plotted in Figure 3.23 vary by 6%, the newly defined elastic function $K^*(x)$ is within the allowable variation.

The frequency response curve is now generated for 1.3 kg mass and $0.2g$ m/s^2 base acceleration by replacing $K(x)$ by $K^*(x)$ ($K^*(x) = 1.05 \times K(x)$) in Equation (4.23) and the result is shown in Figure 4.14. Clearly, the response curve obtained using the modified elastic function $K^*(x)$ is in good agreement with the experimental results. The modified elastic material model is used to also generate frequency response curves for $m = 1.3$ kg and two additional base excitation levels, $0.1g$ and $0.25g$, and the results are given in Figures 4.15. Both plots show good agreement between the simulation and the experimental results. Therefore, by incorporating the modified foam model, with compression-rate dependent parameters and the adjusted elastic function, all the predicted response curves agree with the corresponding experimental responses. Note that for all the results presented in Figures 4.14 and 4.15, the viscous damping parameter was set to $c = 15$ Ns/m.

4.5.4 Importance of Inclusion of V_2 in the Foam Model

It was seen in Figures 4.11 to 4.13 that $b(\dot{\epsilon})$ or $\beta(\dot{\epsilon})$ does not much affect the estimated frequency response curves. In this section, the importance of inclusion of the second viscoelastic component V_2 in the foam model is studied. Figure 4.16 shows the estimated frequency response curves for $m = 1.3$ kg and $0.2g$ m/s^2 base acceleration using the modified foam model developed before. The green curve represents the

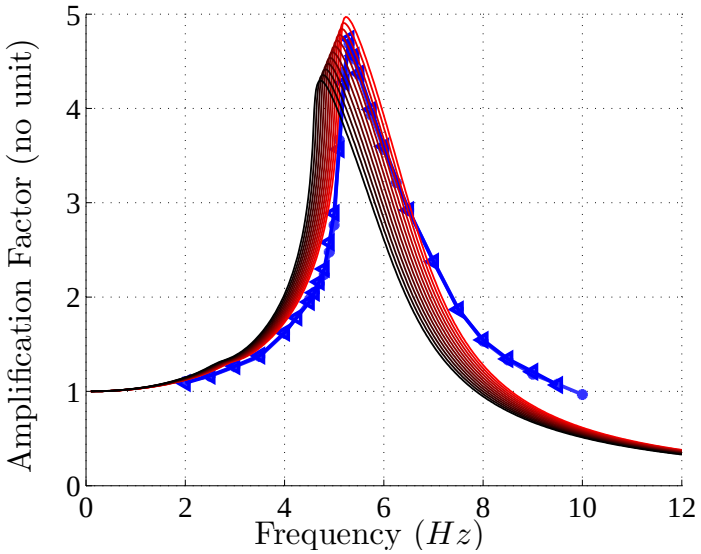

(a)

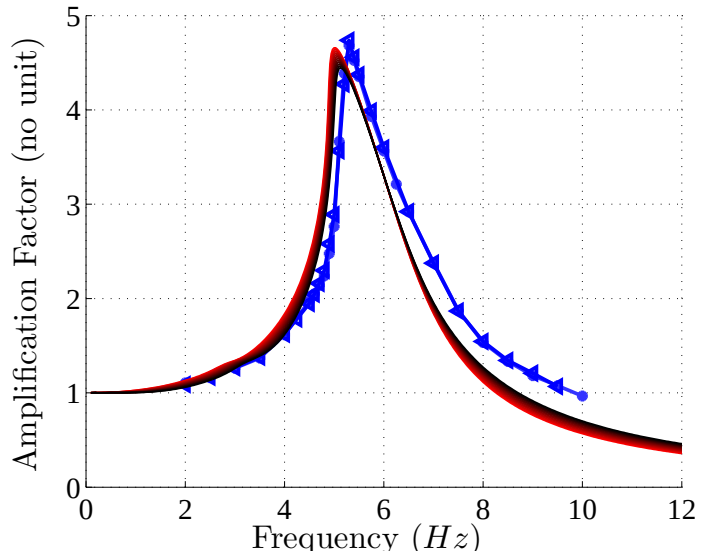

(b)

Figure 4.11. Effect of varying system parameters on the response. (a) varying $a(\dot{\epsilon})$, and (b) varying $b(\dot{\epsilon})$ between 50% and 150% (light red to dark black) of their actual values given in Equation (4.22).

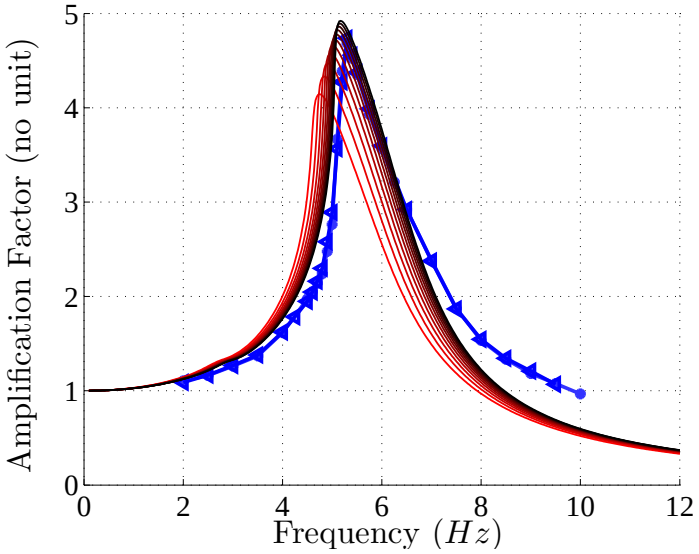

(a)

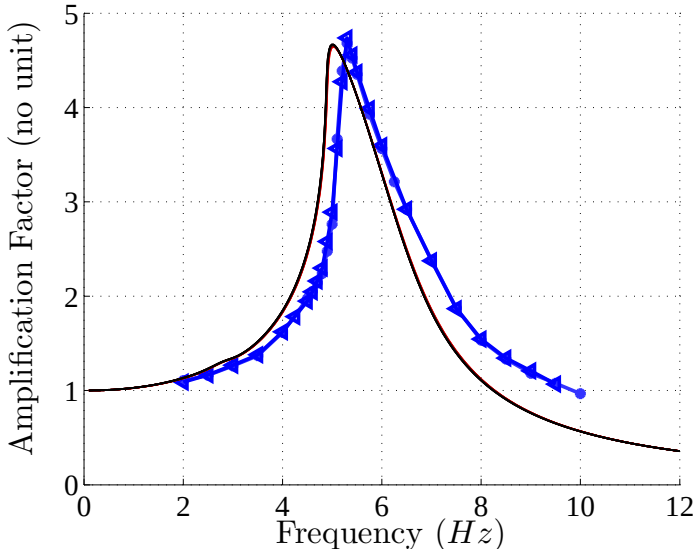

(b)

Figure 4.12. Effect of varying system parameters on the response. (a) varying $\alpha(\dot{\epsilon})$, and (b) varying $\beta(\dot{\epsilon})$ between 50% and 150% (light red to dark black) of their actual values given in Equation (4.22).

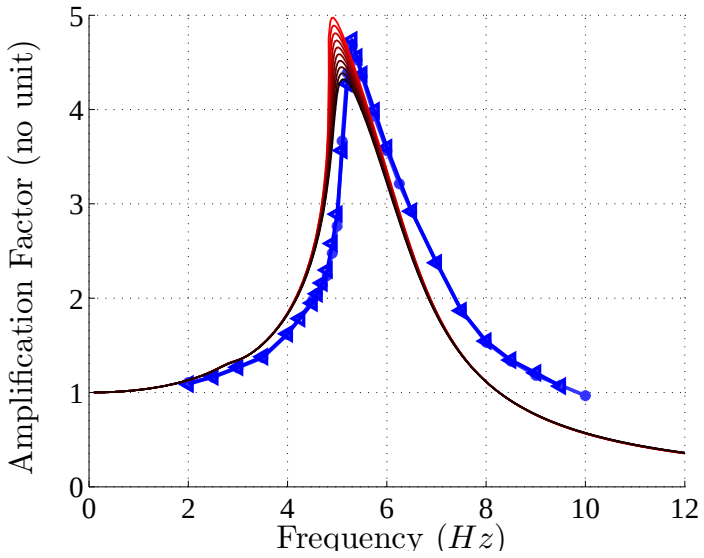

(a)

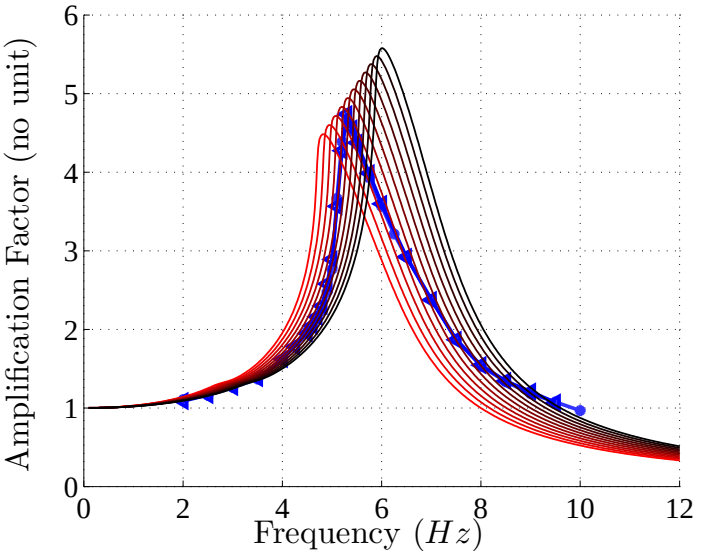

(b)

Figure 4.13. Effect of varying system parameters on the response. (a) varying c between 7 Ns/m and 9 Ns/m (light red to dark black), and (b) varying $K(x)$ between 98% to 120% (light red to dark black) of it's actual value (average of curves in Figure 3.23).

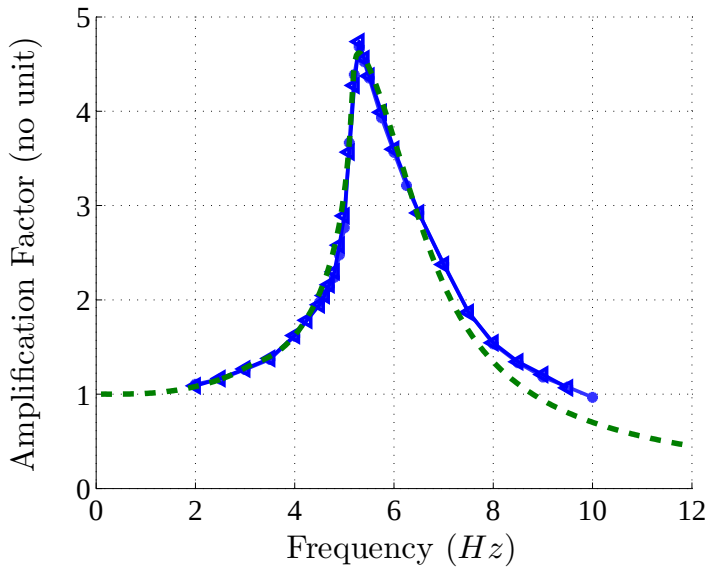

chch

Figure 4.14. Comparison of experimental and simulation results for the foam-mass system for $m = 1.3\ kg$ and $0.2g\ m/s^2$ base acceleration, and modified elastic system $K^*(\epsilon)$. Solid blue (triangle): experiment and dashed green: simulation.

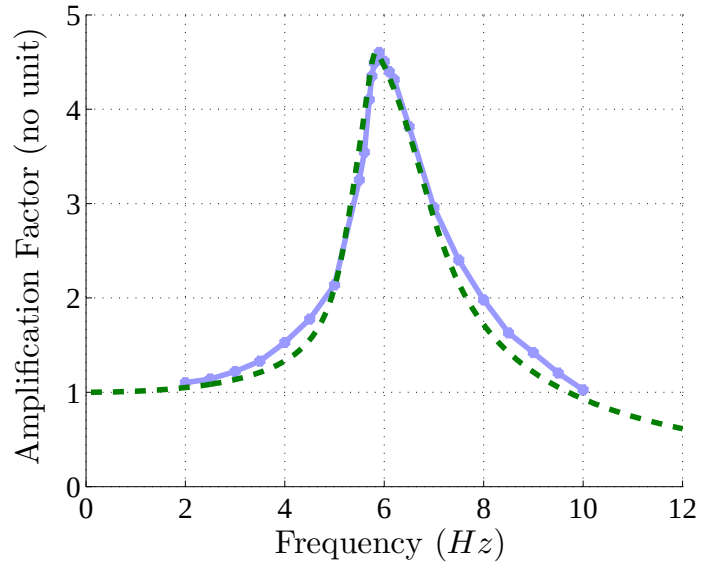

(a)

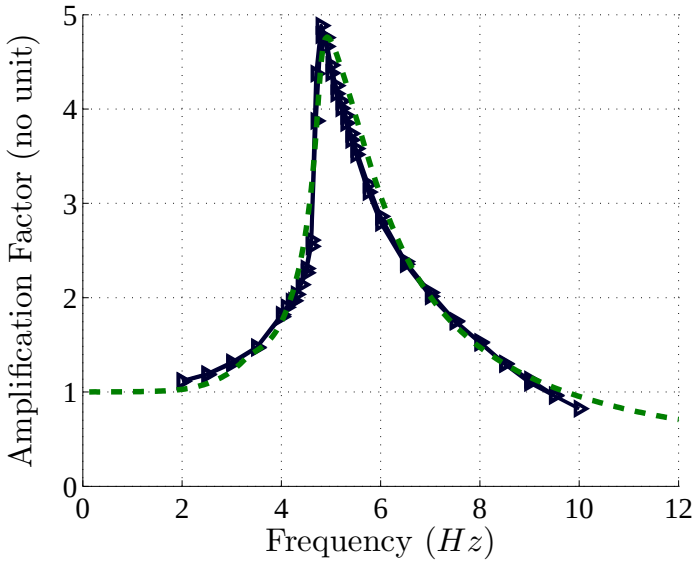

(b)

Figure 4.15. Response curves from experiments and simulations for 1.3 kg and modified system parameters $K^*(\epsilon)$. (a) $0.1g$ m/s^2 level of base excitation, (b) $0.25g$ m/s^2 level of base excitation. Solid curves: experiment, and dashed curves: simulation.

response curve generated using the model with both viscoelastic components (V_1 and V_2) while the black curve was generated using a model without the second viscoelastic curve (V_2). In the frequency range shown in this figure, the model without the second viscoelastic term is sufficient to produce a reasonable result. To understand this behavior $b(\dot{\epsilon})$ was plotted again for a wider range of input strain rates in Figure 4.17. This figure shows that for higher input strain rates, $b(\dot{\epsilon})$, i.e. V_2, is close to zero. For the frequency range used in the experiment, the average strain rate is greater than 1 and the second viscoelastic term becomes negligible. However, it is anticipated that for lower input frequencies, the second viscoelastic term will become important. To demonstrate this, the steady-state response of the foam-mass system was simulated for two input frequencies 0.001 Hz and 10 Hz with and without the second viscoelastic term V_2. Figure 4.18(a) shows the steady-state response of the system subjected to 10 Hz base excitation. The response obtained by including the complete foam model in Equation (4.23) is shown by green while the response obtained without the second viscoelastic term is shown by black. As we observed before, removing the second viscoelastic term does not affect the response. However, as the base excitation frequency is reduced to 0.001 Hz, see Figure 4.18(b), the system responses are different and the second viscoelastic component becomes prominent. This indicates that the second viscoelastic term is needed in the model and it becomes important when the compression rate, or input frequency, is small.

4.6 Chapter Summary

In this chapter, a single-degree-of-freedom foam-mass system is developed. The system model incorporates various nonlinear viscoelastic models of flexible polyurethane foam studied before. The foam models consisted of nonlinear elastic as well as nonlinear memory components. A viscous damping term was added to account for damping mechanisms not modeled by the viscoelastic models. The incremental harmonic balance method was used to find steady-state periodic responses when the foam-mass

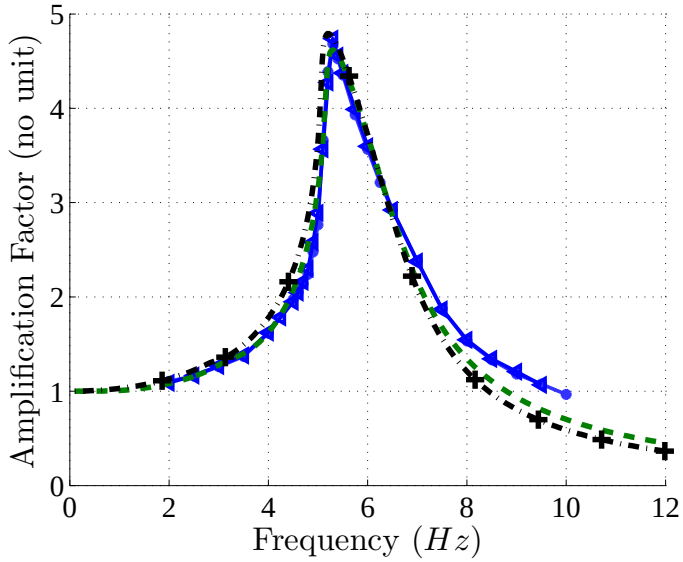

Figure 4.16. Comparison of simulated and experimental frequency response curves accounting for the viscoelastic term V_2 in the model for $m = 1.3\ kg$ ad $0.2g$ base acceleration. Blue: experimental curve, dashed green: model including V_2, black (cross): model without V_2.

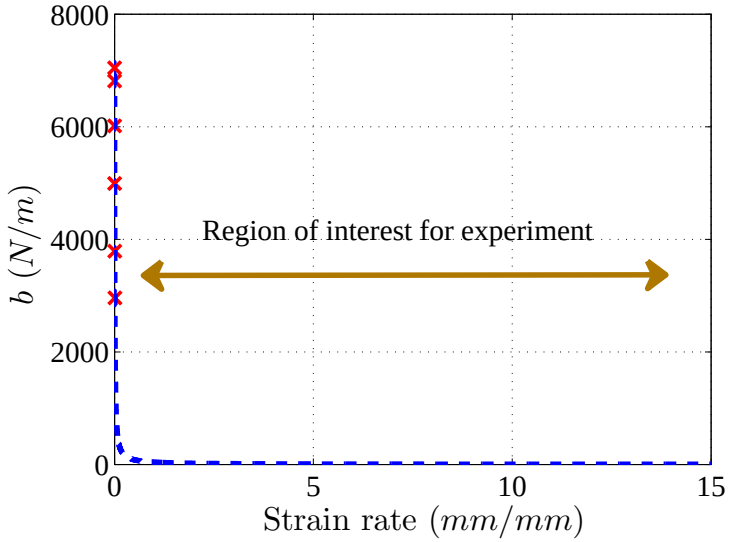

Figure 4.17. Function fitted to the estimated $b(\dot{\epsilon})$ at higher strain rates.

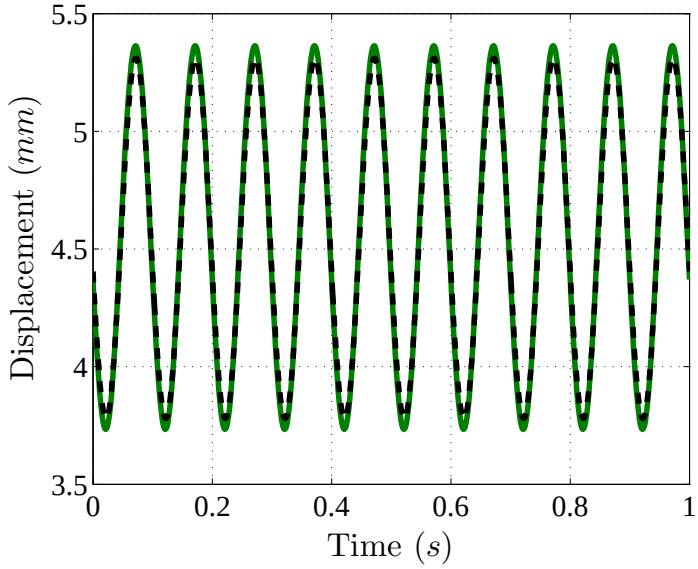

(a)

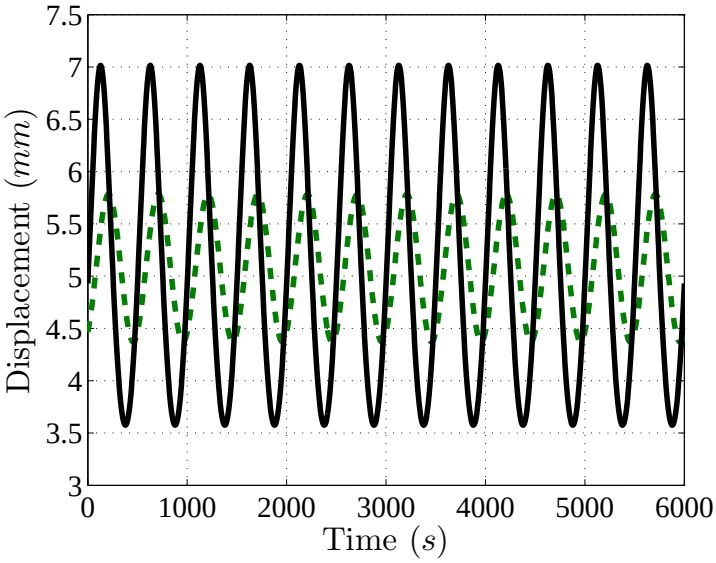

(b)

Figure 4.18. Effect of including and not including the second viscoelastic term on the response. Steady-state of the system subjected (a) 10 Hz base excitation, and (b) 0.001 Hz base excitation. Dashed green: model with V_2, black: model without V_2.

system is subjected to a sinusoidal base excitation. The system frequency response curves were simulated for 2 riding masses, 3 base excitation levels, and three different hereditary-type viscoelastic models. It was observed that system models with different viscoelastic model forms predict different response curves including different peak response frequencies although all three model system parameters were estimated from the same compression test data. It was also observed that there was significant difference in the first harmonic frequency response when only the nonlinear elastic component was used for modeling the foam. The natural frequency of the system, for the lowest base excitation level, could be predicted reasonably well by analyzing the linearized models. Finally, a set of experiments were conducted on the actual foam-mass system. The frequency response results for the developed models and experiments were not in agreement. The foam model was modified to include strain rate-dependence of the viscoelastic parameters. This modified model, after some further modifications, predicts responses which are found to be in good agreement with the experimental results. Finally, the importance of different viscoelastic components of the modified foam model was also discussed. It was shown that the linear hereditary term in the viscoelastic foam model is more significant for lower compression rates while it is not required in the model at high strain rates.

5. SEAT-OCCUPANT MODELING

Understanding the mechanical behavior of a seat-occupant system requires a realistic seat-occupant model. This model can also be used as a design tool to analyze the seat mechanical behavior and to optimize the seat design. Traditionally, there are three different techniques that can be used to models the seat-occupant system: lumped-parameter models, multibody models and finite element models. As discussed in the Chapter 2, among the three techniques, multibody models are usually more suitable for use in the car seat predesign cycle. Multibody models are more computationally efficient than finite element seat occupant models and are more realistic than lumped-parameter models, i.e. it is easy to relate the model components to components in an actual seat and occupant system. In this chapter a multibody seat occupant model is described. The model has been used to predict the transient response of the seated occupant system as well as the dynamic response of the system subjected harmonic excitation applied at the seat base. This multibody model is a refinement of a model developed by a series of researchers. The original form was based on the model of Nishiyama [107–109]. White and Kim [106], Hagermeyer and Ippilli [110], Puri [32] and Joshi [47] made further developments. The limitations of their models addressed in this research are as follows.

1. The occupants femur and torso, the springs that model the foam properties were attached at right angles to the center line of the femur and torso, and slid along the seat frame.

2. The interfacial behavior between the car seat and the occupant was modeled by a simple Coulomb friction model where the friction force direction isn't a function of the relative motion between the occupant and the seat,

3. The foam model was used estimated from a single quasi-static compression test with a low order viscoelastic model and did not take into account strain-rate dependencies

A description of the seat-occupant model and the improvements to address these problems are given in this chapter. This is followed by a description of the procedures used to model the car seat, the profile of the anthropometric dummy, the discrete viscoelastic elements or springs and the interfacial forces. There are two geometric constraints in the model related to the movement of the foot along the floor pan. The equations of motion describing the seat-occupant system dynamics are formulated by using a constraint Lagrangian approach.

5.1 Description of the Seat-Occupant Model

The multi-body seat-occupant model consists of two main elements: the car seat and the occupant. Most car seats are complex structure that include many components (up to 200). The main components of the seats and surrounding area of car seat are the seat suspension system, the seat rail, the foot rest (floor pan), the seat cover, the seat bottom and the seat back. In this study, for simplicity, the behavior of seat cover, though important, is mostly ignored (incorporated into the simple interfacial friction model) and the seat suspension system is not included in the model. For dynamic analysis, e.g. vibration transmissibility, it is assumed that the suspension system is below the seat rail and the rail to the occupant vibration transmissibility is of interest.

The occupant model consists of different elements of a human body. In this study, the occupant model consists of the torso, the femur and the shin. The head was removed in the model because the head of the mannequin was removed in experiments due to difficulties with the mannequin's neck joint. It would be straightforward to add the head (an additional mass) and neck joint (torsional spring and damper) to the model. The arms and hands are included by adjusting the torso mass to include

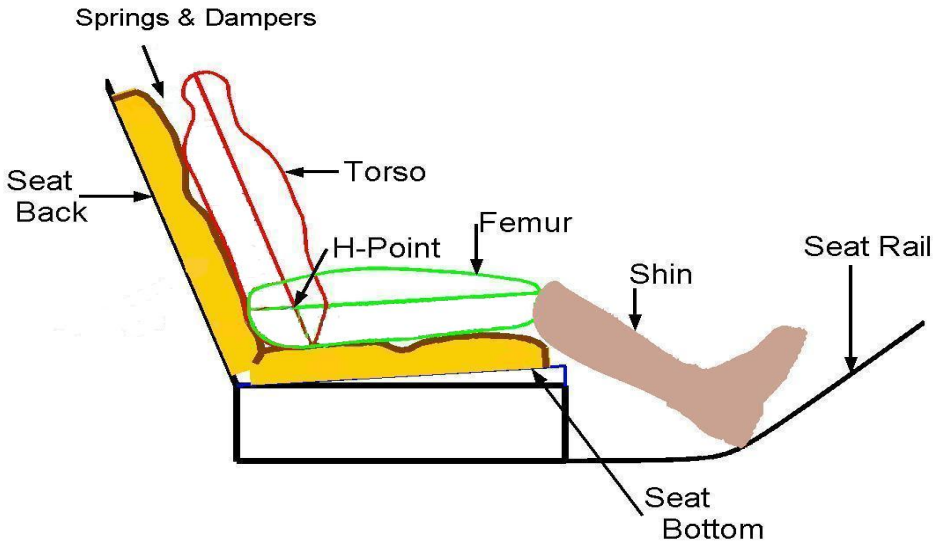

Figure 5.1. The multibody seat-occupant model.

the mass of the arms. The occupant model incorporates the profiles of the seated occupant. Various elements of the seat-occupant model that have been modeled are shown in Figure 5.1. Detailed descriptions of the techniques used for modeling the various components of the seat-occupant model are described in the following.

5.1.1 Modeling the Occupant

The occupant model consists of three main bodies: torso, femur and shim. The occupant's femur and torso can slid along, the seat back and the seat bottom. Also the occupant's shin is constrained to slid along the foot rest as shown in Figure 5.1. Also it is shown in Figure 6.1(a), geometric variables of the occupant in the seat-occupant model. In order to generate realistic models of the occupant, it is important to model the profiles of the torso, the femur and the shin. This affects the deformation pattern of the seat foam significantly, and thus the pressure distribution on the seat bottom and the seat back. Two dimensional actual profiles of a 50^{th} male crash test

dummy were previously derived and incorporated into the seat-occupant model [32]. For completeness, the process of deriving the occupant profile is described here. The complete procedure for modeling the profiles of the torso, the femur and the shin is given in [32]. The process consists of 5 steps:

1. The light colored object (mannequin in this case) is placed against and black background and a color digital photograph is taken.

2. The color photograph is converted into a black and white image by using any standard image processing software such as Photoshop or the Image Processing Toolbox in MATLAB.

3. Using an edge detection routine (e.g. the Edge_Break_Polyfit.m program in MATLAB) the edge of the object is extracted.

4. The extracted edge is scaled to reflect the actual dimensions of the object.

5. The extracted edge is partitioned into different regions so that the edge in each partition can be represented mathematically by a polynomial. The equations of the polynomials representing the two edges are derived by considering the H-point as the origin.

5.1.2 Modeling the Car Seat

The car seat model consist of the seat back, the seat bottom and the floor pan. Various geometric variables characterizing the basic car seat are shown in Figure 6.1(b). The inclination of the seat back, θ_s, is given by the angle between the seat back and the seat base. The inclination of the seat bottom, α, is given by the angle between the seat bottom and the seat base, see Figure 6.1(b). The seat back is allowed to have angular motion about its joint with the seat base. M_s, I_s denote the inertial properties (mass and moment of inertia) of the car seat back and the joint between

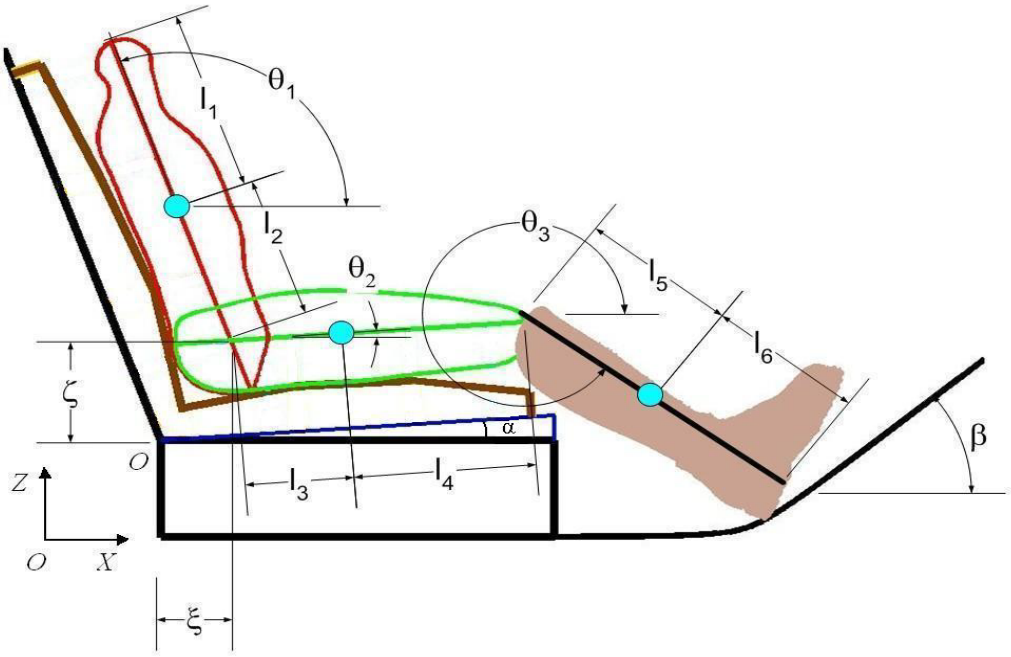

(a)

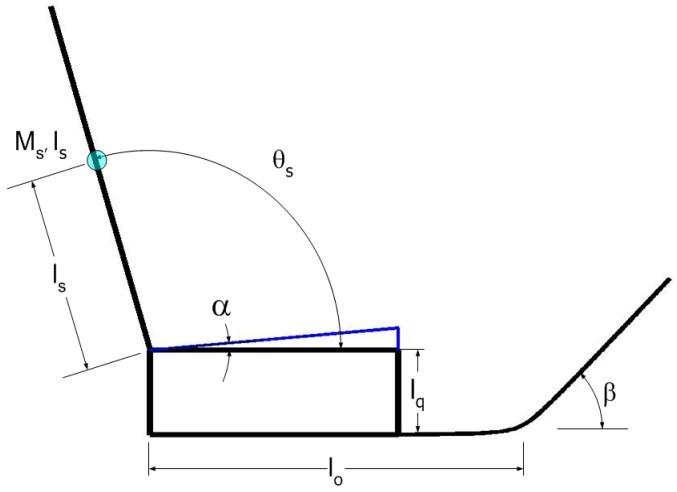

(b)

Figure 5.2. Geometric parameters and variables of the seat-occupant model. (a) geometric parameters of the occupant and (b) geometric variables of the car seat.

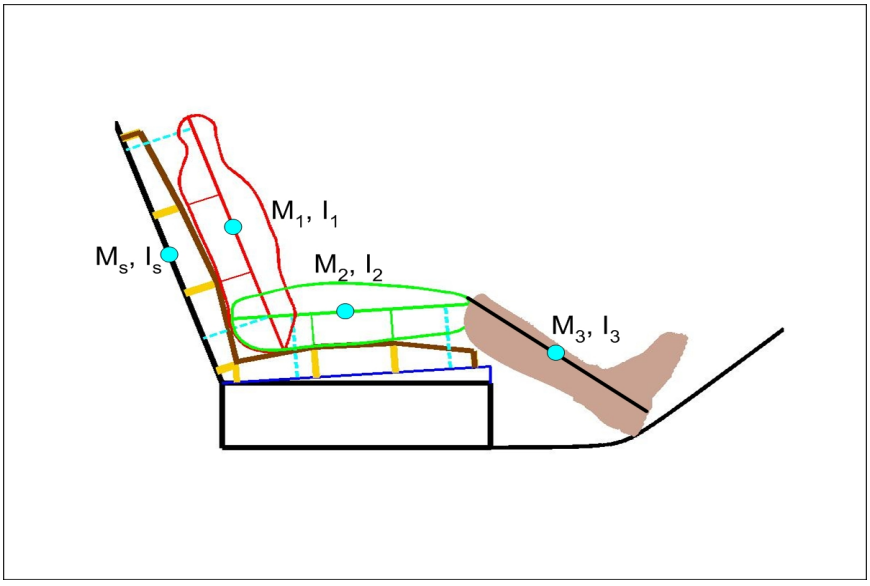

Figure 5.3. Schematic of seat-occupant system to show the nomenclature used to describe the inertial properties of the car seat and the occupant.

the seat back and the seat bottom can be modeled with a very stiff torsional spring, see Figure 5.3.

Traditionally, in multibody seat-occupant models, the seat cushion is modeled by springs and dampers. For example, Ippili [68] replaced the seat back and the seat bottom by four springs and dampers. In this study, following an approach developed by Puri [32], the seat is represented by a series of nonlinear viscoelastic elements and linear viscous dampers. As discussed in Chapter 4, the viscous dampers are included to model the damping mechanisms which are not modeled by the viscoelastic elements for foam. In the present model the seat can be replaced by an arbitrary number of nonlinear viscoelastic elements and dampers. Including large number of elements in the seat back and the seat bottom, help in modeling cushion behavior more realistically and allowing the model to predict the seat-occupant interface force more accurately.

For replicating actual foam behavior it is assumed that the mechanical behavior of the nonlinear viscoelastic elements is described by foam Model 4 as discussed in Chapter 3. Therefore, the force exerted by any of the elements is given by:

$$F_{element} = \chi\left(\sigma_e + \sigma_{v1} + \sigma_{v2}\right), \tag{5.1}$$

$$\begin{aligned} F_{element} &= \chi\left(\sum_{i=1}^{N} k_i\epsilon^i + \int_0^t \sum_{j=1}^{M_1} a_j e^{-\alpha_j(t-\tau)} \sum_{i=1}^{N} k_i\epsilon^i(\tau)d\tau\right. \\ &+ \left.\int_0^t \sum_{l=1}^{M_2} b_l e^{-\beta_l(t-\tau)}\dot{\epsilon}(\tau)d\tau\right), \end{aligned} \tag{5.2}$$

where σ_e, σ_{v1} and σ_{v2} are the elastic and two viscoelastic components, respectively. Also k_i, a_j, α_j, b_j and β_j are elastic and viscoelastic model parameters as described in detail in Chapter 3. χ is the area of the foam represented by the nonlinear spring-viscoelastic-viscous element and can be obtained for the seat bottom by dividing the total contact area of the seat bottom by the number of elements representing the seat bottom. Similarly, the value of χ for the seat back can be obtained by dividing the total contact area of the seat back by the number of elements representing the seat

back behavior. The strain ϵ is computed by dividing the compression in the elements by the initial length of the uncompressed element.

It is assumed that one end of each elements are attached to the seated occupant at the center line that passes through the H-Point and the center of gravity of the corresponding body element (torso or femur) and each element is at 90 degrees to the center line. The other end of the elements are in contact with the seat frame and are free to slid over the seat frame. In order to compute the force exerted by the elements, as defined by Equation (5.2), at each instance the location of the elements as well as the strain $\epsilon(t)$ for each element need to be computed. Using the distances defined in Figure 5.4 and angles defined in Figure 5.2, it is can be shown that at each instance the location of the end of each element on the fixed rail is given by:

$$l = \frac{\xi \cos(\theta_2) + \zeta \sin(\theta_2) + f}{cos(\alpha - \theta_2)}, \tag{5.3}$$

where ξ and ζ are the horizontal and vertical position of the H-Point, f is the element location measured with respect to the relative coordinate located at the H-Point, α is the angle between the seat frame and the horizontal axis, and θ_2 is the angle between the femur and the horizontal axis (see Figure 6.1(a)). The strain in elements can also be calculated by dividing the compression in each spring by its uncompressed length. This uncompressed length is defined as the initial height of the seat foam below the point where the spring is attached (denoted as q in Figure 5.4). It is straightforward to show that the length of each spring h attached to femur is:

$$h = f \tan(\theta_2 - \alpha) + \frac{(\zeta - \xi \tan(\alpha)) \cos(\alpha)}{\cos(\theta_2 - \alpha)}, \tag{5.4}$$

where the parameters are shown in Figures 4.6 and 5.4. The compression, or tension, in each spring can be calculated by subtracting h from its initial length. This length consists of the thickness of the occupant body, i.e. femur, below the center line connecting the H-Point to the center of gravity of that body (denoted by p in Figure 5.4) and the uncompressed height of the foam q below the point where the spring is attached. The initial length for all the spring locations can be computed using the

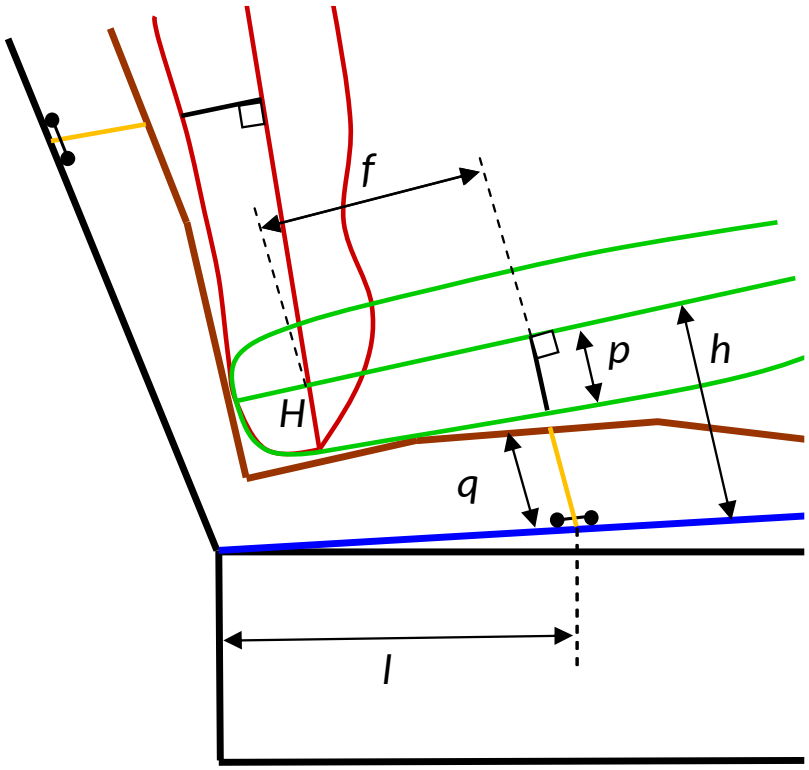

Figure 5.4. A section of the seat-occupant model showing the arrangement of springs at the seat back and the seat bottom. p is fixed and q is the depth of the foam.

measured seat and occupant profiles. Finally, if the foam is compressed, the strain is calculated as:

$$\epsilon_{bottom} = -\frac{h-p-q}{q}. \tag{5.5}$$

When $(h-p)$ is greater than the uncompressed length of the foam at that point, $\epsilon = 0$ (femur has lost contact with the foam at that location). Note that this loss of contact with the foam is modeled by using sigmoidal functions described later in this chapter.

A similar expression can also be computed for the seat back. It is easy to show that at each instance for a stiff seat back the location of each seat back element along the seat back frame (see Figure 5.5) is given by:

$$b = \frac{\xi \cos(\theta_1) + \zeta \sin(\theta_1) + t}{cos(\theta_s - \theta_1)}, \tag{5.6}$$

where ξ and ζ are the horizontal and vertical position of the H-Point, t is the element location measured with respect to the relative coordinate located at the H-Point, θ_s is the angle between the seat back frame and the horizontal axis, and θ_1 is the angle between the torso and the horizontal axis. The strain in elements can also be calcu-

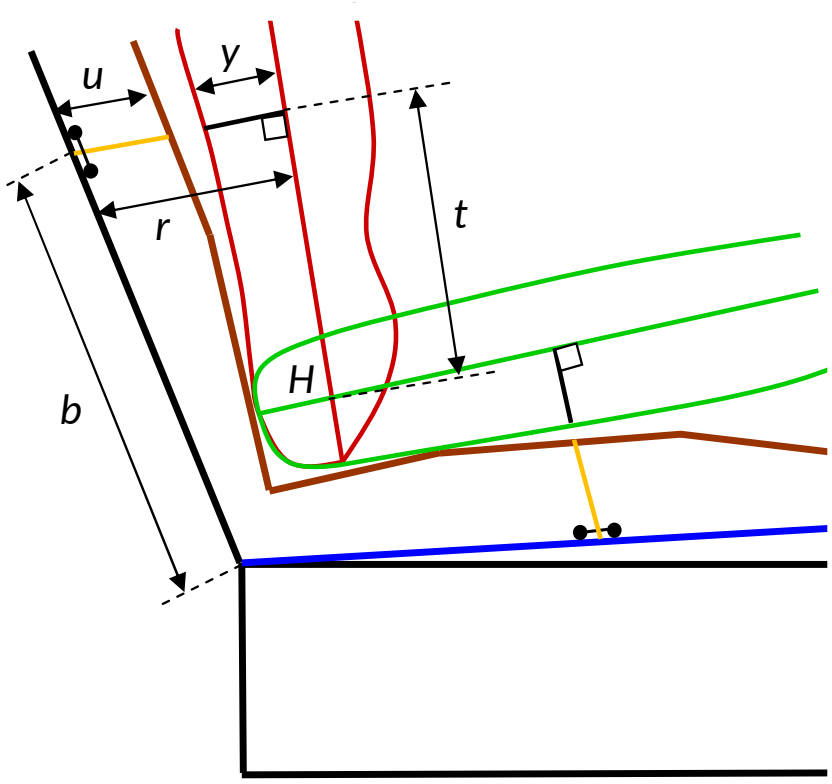

Figure 5.5. A section of the seat-occupant model showing the arrangement of springs at the seat back and the seat bottom. y is fixed and u is the depth of the foam.

lated by dividing the compression in each spring by its uncompressed length. This uncompressed length is defined as the initial height of the seat back foam (denoted

as u in Figure 5.5). It is straightforward to show that the length of each elements r attached to femur is:

$$r = t\tan(\theta_s - \theta_1) + \frac{(\xi - \zeta\cot(\theta_s))\sin(\theta_s)}{\cos(\theta_1 - \theta_s)}, \tag{5.7}$$

where the parameters are shown in Figures 4.6 and 5.5. The compression, or tension, in each spring can be calculated by subtracting r from its initial length. This length consists of the thickness of the occupant body, i.e. torso, below the center line connecting the H-Point to the center of gravity of that body (denoted by y in Figure 5.5) and the uncompressed height of the foam u below the point where the spring is attached. The initial length for all the spring locations can be computed using the measured seat and occupant profiles. Finally, if the foam is compressed, the strain is calculated as:

$$\epsilon_{back} = -\frac{r - u - y}{u}. \tag{5.8}$$

When $(r-y)$ is greater than the uncompressed length of the foam at that point, $\epsilon = 0$ (torso has lost contact with the foam at that location). Note that this loss of contact with the foam is modeled by using sigmoidal functions.

The foam force computed from Equation (5.2) predicts the foam force accurately for compression levels between 0% and 66%. This foam force needs be modified so that the force exerted by foam increases significantly as foam compression approaches 100%. At very high compression levels the polyurethane structure is flattened (air squeezed out of the foam) and the polyurethane elements contact each other. As compression increases the polyurethane material itself becomes compacted. Clearly, at very high compression levels the polyurethane of the foam material begins to deform due to contact in the compaction region of foam behavior resulting in a rapid increase in the foam force. Also, the foam force should be zero for all compression levels less than 0% because the seat occupant loses contact with the foam when compression becomes zero, and seat-occupant interaction does not support tension in foam. To model this behavior the approach adopted by Ippili [111] is used here

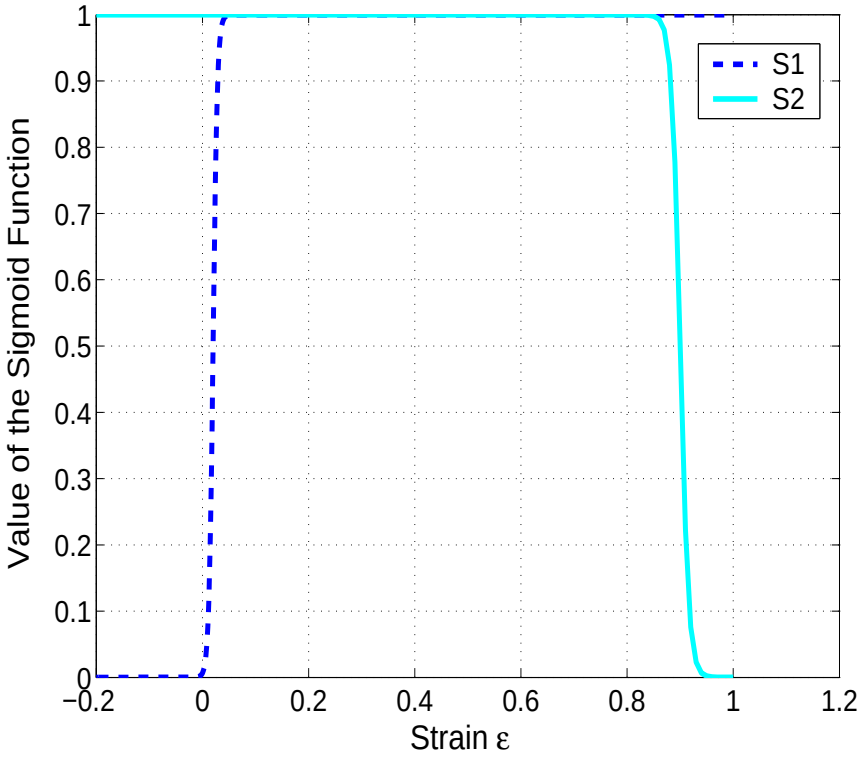

Figure 5.6. Sigmoid functions used to modify the foam force function. The dashed black line represents S_1 used to limit the force in foam only to compression and the solid gray line represents S_2 which is used to make the force very large as the foam thickness goes to zero.

as well. Ippili [111] modified the computed foam force with the help of two sigmoid functions.

$$S_1 = 1/(1 + e^{(250\times((1-\varepsilon)-0.98))}), \tag{5.9}$$

$$S_2 = 1/(1 + e^{(-125\times((1-\varepsilon)-0.10))}). \tag{5.10}$$

Multiplication with the first sigmoid function S_1 makes the force zero if the strain $\varepsilon < 0$. Dividing the force by the second sigmoid function S_2 makes the force becomes very large when $\varepsilon = 0.90$. The two sigmoid function are shown in Figure 5.6.

5.1.3 Modeling of the Interfacial Behavior

The forces at the seat-occupant interfaces affect the position of the H-Point. Modeling the interfacial forces is a difficult task due to the presence of shear effects in the foam, and also due to multiple layers of materials such as the foam, seat cover, clothing etc. In this study, this complex interfacial behavior is represented by a simple friction model. It is assumed that these forces act parallel to the center line passing through the center of mass of the body element (perpendicular to the element), and at the points where the elements connect to the body. This friction force is always in the direction opposite to the direction of relative motion between the occupant and the seat. This force at a given point on the interface is given as,

$$F_{int} = -\mu |F_{element}| sign(u_{relative}), \tag{5.11}$$

where $F_{element}$ is given in Equation (5.2), $u_{relative}$ is the relative velocity between the occupant and the seat, and $sign$ is the sign function:

$$sign(u_{relative}) = \begin{cases} 1 & \text{if } u_{relative} \geq 0 \\ -1 & \text{if } u_{relative} < 0. \end{cases} \tag{5.12}$$

At each instance, $u_{relative}$ can be calculated by computing the cross product of the absolute velocity of the occupant's body element and the seat frame unit vector. For bottom frame this vector is given by $(cos\alpha, sin\alpha)$ where α is the angle between the seat frame and the horizontal axis as shown in Figure 6.1. $u_{relative}$ for a point on the femur at a distance of f from the H-Point (see Figure 5.4) is given by,

$$u_{relative} = (\dot{\xi} - f \sin(\theta_2)\dot{\theta}_2) \cos\alpha + (\dot{\zeta} + f \cos(\theta_2)\dot{\theta}_2) \sin\alpha, \tag{5.13}$$

where $\dot{\xi}$ and $\dot{\zeta}$ are the horizontal and the vertical velocities of the H-Point and $\dot{\theta}_2$ is the angular velocity of the femur.

The heel of the foot is constrained to move along the floor pan. Therefore, another friction force is added to the model to oppose the free motion between the heel and the footrest. The friction force at the foot acts along the floor pan in a direction

tangential to the floor pan which is shaped like a hyperbola. This friction force is also modeled using Equation (5.11) with $u_{relative}$ referring to the relative velocity between the heel and the footrest. For more details refer to [32].

5.2 Governing Equations of the Seat-Occupant Model

The constrained Lagrangian formulation is used to derive the governing equations of the multibody seat-occupant system [32, 47, 111]. Also, a holonomic constraint is imposed on the motion as the occupant's foot is constrained to slide along the floor pan. In general the Lagrangian formulation consists of n second-order differential equations that define the motion of a system with n generalized coordinates. As mentioned earlier, the seat-occupant system has 5 degrees-of-freedom and 5 generalized coordinates, i.e. the horizontal and vertical position of the H-Point and three angles of torso, femur and shin, need to be defined. By solving the governing equation, the occupant's dynamic transient response can be computed. It is also of interest to study the dynamic response of the occupant when the seat-occupant system is subjected to harmonic base excitation. In that case, an additional generalized coordinate z is defined which represents the input base excitation. In this Chapter, all the equations are derived considering 6 generalized coordinates, i.e. the horizontal and vertical position of the H-Point, the three angles of the torso, femur, and shin rotation, and the base excitation. Later, if the transient response of the system is of interest, the last generalized coordinate is set to zero.

Lagranges equations of motion for the constrained seat-occupant system are given by:

$$\frac{d}{dt}\left(\frac{\partial T}{\partial \dot{q}_r}\right) - \frac{\partial T}{\partial q_r} + \frac{\partial U}{\partial q_r} + \frac{\partial D}{\partial \dot{q}_r} + f_r = Q_r \ , \qquad r = 1, 2, .., n, \tag{5.14}$$

where $q_r, r = 1, 2, ..., 6$ denote the generalized co-ordinates of the system. $T = T(q_r, \dot{q_r})$, $U = U(q_r)$, $D(\dot{q_r})$ and $Q_r(q_r, \dot{q_r}, t)$ are the kinetic energy of the system, the potential energy of the system, the dissipation function and the generalized forces,

respectively. f_r represents a constraint force due to a geometric (or holonomic) constraint which is imposed on the motion of the foot which always slides along the floor pan. This constraint can be written in the following form:

$$\phi(q_1, ..., q_5) = 0. \tag{5.15}$$

The above constraint is introduced into Lagrange's equations of motion by using the method of Lagrangian multipliers [112]. The constraint forces, expressed in terms of the Lagrange multiplier λ, are given by:

$$f_r = \lambda \frac{\partial \phi}{\partial q_r} = \lambda B_r^T, \tag{5.16}$$

where $[B]$ is the Jacobian matrix and its elements are given by:

$$B_r^T = \frac{\partial \phi}{\partial q_r}. \tag{5.17}$$

The kinetic energy, the potential energy, the generalized forces and the dissipation function for the seat-occupant system are given by:

$$T = \frac{1}{2}\sum_{i=1}^{3} m_i(\dot{x}_i^2 + \dot{y}_i^2) + \frac{1}{2}\sum_{i=1}^{3} I_i\dot{\theta}_i^2, \tag{5.18}$$

$$U = g\sum_{i=1}^{3} m_i y_i, \tag{5.19}$$

$$Q_i = \sum_{j=1}^{r} \mathbf{F}_j^{interface,torso} . \frac{\partial \mathbf{r}_j}{\partial q_i} + \sum_{j=1}^{w} \mathbf{F}_j^{interface,femur} . \frac{\partial \mathbf{r}_j}{\partial q_i}, \tag{5.20}$$

$$D = \frac{1}{2}\sum_{i=1}^{u} c_i\dot{\delta}_i^2, \tag{5.21}$$

where m_i is the mass of the i^{th} body element and I_i is the moment of inertia of the i^{th} body element about its center of mass (see Figure 5.3). w denotes the number of springs at the seat bottom, r denotes the number of springs at the seat back and u denotes the total number of dampers. $V_i(\delta_i)$ represents the potential energy of the i^{th} spring. $\delta_i = \epsilon_{bottom_i}$ for springs attached to the femur and $\delta_i == \epsilon_{back_i}$ for springs attached to the torso. $\mathbf{F}_j^{interface}$ denotes the interfacial force at the j^{th} spring due to elastic and viscoelastic effects. The coordinates (x_i, y_i) define the locations of the

center of mass of the torso, the femur and the shin. They can be defined in terms of the generalized coordinates as:

$$\begin{aligned} x_1 &= \xi + l_2\cos(\theta_1), & y_1 &= \zeta + z + l_2\sin(\theta_1), \\ x_2 &= \xi + l_3\cos(\theta_2), & y_2 &= \zeta + z + l_3\sin(\theta_2), \\ x_3 &= \xi + (l_3 + l_4)\cos(\theta_2) + l_5\cos(\theta_3), & & \\ y_3 &= \zeta + z + (l_3 + l_4)\sin(\theta_2) + l_5\sin(\theta_3), & & \end{aligned} \tag{5.22}$$

where z is the displacement of the seat base due to the external vertical excitation applied at the seat base.

The foot slides (see Figure 5.1) has been modeled as a hyperbola. The equation for imposing this constraint is given by:

$$\phi = -a\frac{sin(\beta)}{x_f} + z_f\cot(\beta) - x_f, \tag{5.23}$$

where $a = l_o/1285.57$, see [47]. x_f and z_f are given by:

$$x_f = -l_o + \xi(t) + (l_3 + l_4)\cos(\theta_2(t)) + (l_5 + l_6)\cos(\theta_3(t)), \tag{5.24}$$

$$z_f = l_q + \zeta(t) + (l_3 + l_4)\sin(\theta_2(t)) + (l_5 + l_6)\sin(\theta_3(t)). \tag{5.25}$$

The constraint forces f_r can now be calculated by substituting Equation (5.24) and Equation (5.25) into Equation (5.23) and then using Equation (5.16). f_r and Equations (5.18)-(5.21) can then be substituted into Equation (5.14) to obtain the set of differential equations that define the motion of the seat-occupant system. On simplification Equation (5.14) lead to the following system of differential equations:

$$\begin{bmatrix} M_1 & 0 & A_1 & A_2 & A_3 & 0 \\ 0 & M_1 & B_1 & B_2 & B_3 & M_1 \\ C_1 & C_2 & M_7 & 0 & 0 & M_2\cos(\theta_1) \\ D_1 & D_2 & 0 & M_8 & D_3 & (M_3 + M_4)\cos(\theta_2) \\ E_1 & E_2 & 0 & E_3 & M_9 & M_5\cos(\theta_3) \\ 0 & 0 & 0 & 0 & 0 & 1 \end{bmatrix} \begin{Bmatrix} \ddot{\xi} \\ \ddot{\zeta} \\ \ddot{\theta}_1 \\ \ddot{\theta}_2 \\ \ddot{\theta}_3 \\ \ddot{z} \end{Bmatrix} = \begin{Bmatrix} -A_4 \\ -B_4 \\ -C_3 \\ -D_4 \\ -E_4 \\ -\omega^2 z \end{Bmatrix} - \lambda \begin{Bmatrix} B_{11} \\ B_{21} \\ B_{31} \\ B_{41} \\ B_{51} \\ B_{61} \end{Bmatrix}, \tag{5.26}$$

where the matrix elements are defined by the following expressions:

$$\begin{aligned}
M_1 &= m_1 + m_2 + m_3, & M_2 &= m_1 l_2, \\
M_3 &= m_2 l_3, & M_4 &= m_3(l_3 + l_4), \\
M_5 &= m_3 l_5, & M_6 &= m_3 l_5 (l_3 + l_4), \\
M_7 &= I_1 + m_1 l_2^2, & M_8 &= m_3(l_3 + l_4)^2 + m_2 l_3^2 + I_2, \\
M_9 &= I_3 + m_3 l_5^2 & & \\
A_1 &= -M_2 \sin(\theta_1), & A_2 &= -\sin(\theta_2)(M_3 + M_4), \\
A_3 &= -M_5 \sin(\theta_3), & B_1 &= M_2 \cos(\theta_1), \\
B_2 &= \cos(\theta_2)(M_3 + M_4), & B_3 &= M_5 \cos(\theta_3), \\
C_1 &= -M_2 \sin(\theta_1), & C_2 &= M_2 \cos(\theta_1), \\
D_1 &= -\sin(\theta_2)(M_3 + M_4), & D_2 &= \cos(\theta_2)(M_3 + M_4), \\
D_3 &= M_6 \cos(\theta_2 - \theta_3), & E_1 &= -M_5 \sin(\theta_3), \\
E_2 &= M_5 \cos(\theta_3), & E_3 &= M_6 \cos(\theta_3 - \theta_2).
\end{aligned} \tag{5.27}$$

The variables on the right side of Equation (5.26) are given by:

$$\begin{aligned}
A_4 &= -M_2 \cos(\theta_1)\dot{\theta_1}(t)^2 - \cos(\theta_2)\dot{\theta_2}(t)^2(M_3 + M_4), \\
&\quad -M_5 \cos(\theta_3)\dot{\theta_3}(t)^2 - \cos(\theta_1)\textstyle\sum_{j=1}^{r} F_j^{interface,torso} \\
&\quad + \cos(\theta_2)\textstyle\sum_{j=1}^{w} F_j^{interface,femur} + \Delta_\xi, \\
B_4 &= -M_2 \sin(\theta_1)\dot{\theta_1}(t)^2 - \sin(\theta_2)\dot{\theta_2}(t)^2(M_3 + M_4), \\
&\quad -M_5 \sin(\theta_3)\dot{\theta_3}(t)^2 + M_1 g \\
&\quad - \sin(\theta_1)\textstyle\sum_{j=r}^{w} F_j^{interface,torso} + \sin(\theta_2)\sum_{j=1}^{w} F_j^{interface,femur} + \Delta_\zeta, \\
C_3 &= M_1 g \cos(\theta_1) + \Delta_{\theta_1}, \\
D_4 &= g\cos(\theta_2)(M_3 + M_4) + m_3(l_3 l_5 + l_5 l_4)\sin(\theta_2 - \theta_3)(\dot{\theta_3})(t)^2 + \Delta_{\theta_2}, \\
E_4 &= M_5 g \cos(\theta_3) + M_6 \sin(\theta_3 - \theta_2)(\dot{\theta_2})(t)^2.
\end{aligned} \tag{5.28}$$

The Δ terms in the above expressions are given by:

$$\begin{aligned}
\Delta_\xi &= \textstyle\sum_{i=1}^{w+r} F(\delta_i)\frac{\partial \delta_i}{\partial \xi} + \sum_{i=1}^{u} c_i \dot{\delta}_i \frac{\partial \dot{\delta}_i}{\partial \dot{\xi}}, & \Delta_\zeta &= \textstyle\sum_{i=1}^{w+r} F(\delta_i)\frac{\partial \delta_i}{\partial \zeta} + \sum_{i=1}^{u} c_i \dot{\delta}_i \frac{\partial \dot{\delta}_i}{\partial \dot{\zeta}}, \\
\Delta_{\theta_1} &= \textstyle\sum_{i=1}^{w+r} F(\delta_i)\frac{\partial \delta_i}{\partial \theta_1} + \sum_{i=1}^{u} c_i \dot{\delta}_i \frac{\partial \dot{\delta}_i}{\partial \dot{\theta}_1}, & \Delta_{\theta_2} &= \textstyle\sum_{i=1}^{w+r} F(\delta_i)\frac{\partial \delta_i}{\partial \theta_2} + \sum_{i=1}^{u} c_i \dot{\delta}_i \frac{\partial \dot{\delta}_i}{\partial \dot{\theta}_2}.
\end{aligned} \tag{5.29}$$

The force $F(\delta_i)$ was previously defined in Equation (5.2). Although it is possible to evaluate σ_{v1} and σ_{v2} by integrating the integrals in Equation (5.2) numerically, it

is more efficient to convert these components, σ_{v1} and σ_{v2}, into M_1^{th} and M_2^{th} order differential equations, respectively. These equations can be derived by taking the Laplace transform of the convolution and recognizing s as a differential operator. For example, for the simplest case, where the terms have only one exponential term in the kernel ($M_1 = M_2 = 1$), $L\{\sigma_{v1}\} = \frac{a_1}{s+\alpha_1} L\{\sum_{i=1}^{N} k_i \epsilon^i\}$ and $L\{\sigma_{v2}\} = \frac{b_1 s}{s+\beta_1} L\{\epsilon\}$. Then, σ_{v1} can be expressed as,

$$\dot{\sigma}_{v1} + \alpha_1 \sigma_{v1} = a_1 \sum_{i=1}^{N} k_i \epsilon^i, \tag{5.30}$$

and σ_{v2} as,

$$\dot{\sigma}_{v2} + \beta_1 \sigma_{v2} = b_1 \dot{\epsilon}. \tag{5.31}$$

As shown in Chapter 2, when low-order viscoelastic models are used the values of the viscoelastic parameters, a_j, α_j, b_l, and β_l, should be functions of the strain rates $\dot{\epsilon}(t)$.

For a seat-occupant system with $w+r$ elements, there will be $2(w+r)$ differential equations like Equations (5.30) and (5.31) that have to be solved in conjunction with the second-order differential equations represented in matrix form by Equation (5.26). Therefore, if viscoelastic effects are considered, as the number of springs used to represent the foam increases the number of second-order differential equations to be solved also increases. This results in a significant increase in the computational time required to numerically integrate these equations.

The elements of the Jacobian matrix B are given by:

$$\begin{aligned}
B_{11} &= -1, \\
B_{21} &= \frac{a\sin(\beta)}{(l_q+\zeta+(l_3+l_4)\sin(\theta_2)+(l_5+l_6)\sin(\theta_3))^2} + \cot(\beta), \\
B_{31} &= 0, \\
B_{41} &= \frac{a\sin(\beta)(l_3+l_4)\cos(\theta_2)}{(l_q+\zeta+(l_3+l_4)\sin(\theta_2)+(l_5+l_6)\sin(\theta_3))^2} + (l_3+l_4)\cos(\theta_2)\cot(\beta) \\
&\quad +(l_3+l_4)\sin(\theta_2), \\
B_{51} &= \frac{a\sin(\beta)(l_5+l_6)\cos(\theta_3)}{(l_q+\zeta+(l_3+l_4)\sin(\theta_2)+(l_5+l_6)\sin(\theta_3))^2} + (l_5+l_6)\cos(\theta_3)\cot(\beta) \\
&\quad +(l_5+l_6)\sin(\theta_3), \\
B_{61} &= 0.
\end{aligned} \tag{5.32}$$

The above equations have been derived for the seat-occupant system considering no friction at the floor pan interface (see Figure 5.1). The incorporation of friction at the floor pan interface is discussed in the following subsection.

5.3 Governing Equations of the Improved Seat-Occupant Model

In the previous section, the governing equations of the seat-occupant model was derived. The current seat-occupant model can be improved by incorporating the friction at the foot and floor interface as well as by including seat back flexibility. The friction at the foot rest directly affects the final steady state position of the shin, the final angle of the femur and the interfacial pressure distribution at the seat bottom. Also the seat back flexibility affects the steady state dynamic response of the occupant, e.g. when the system is subjected to base excitation. The governing equations of the improved seat-occupant model are derived in this section.

5.3.1 Incorporating Friction at the Foot-Floor Interface in the Seat-Occupant Model

The constraint that the foot slide along the floor pan is imposed by the constraint equation (Equation (5.23)). Friction forces at the foot pan interface can be incorporated into the seat-occupant model by modifying Equation (5.20) to include generalized forces due to friction at the foot. The generalized forces due to friction at the foot can be calculated by computing the virtual work done by the friction force at the foot. The friction force at the foot acts along the floor pan in a direction tangential to the floor pan which is shaped like a hyperbola (See Equation (5.24) and Figure 5.7). The angle θ_{sl} defines the angle at which the friction force acts. Also, the Lagrange multiplier λ is the normal force at the point where the constraint is enforced. Therefore, the friction force at the foot, F_{foot} is given by $F_{foot} = \mu_{foot}\lambda$. This friction force acts at an angle θ_{sl} to the horizontal and in a direction that opposes the motion of the foot along the floor pan. Note that θ_{sl} is given by:

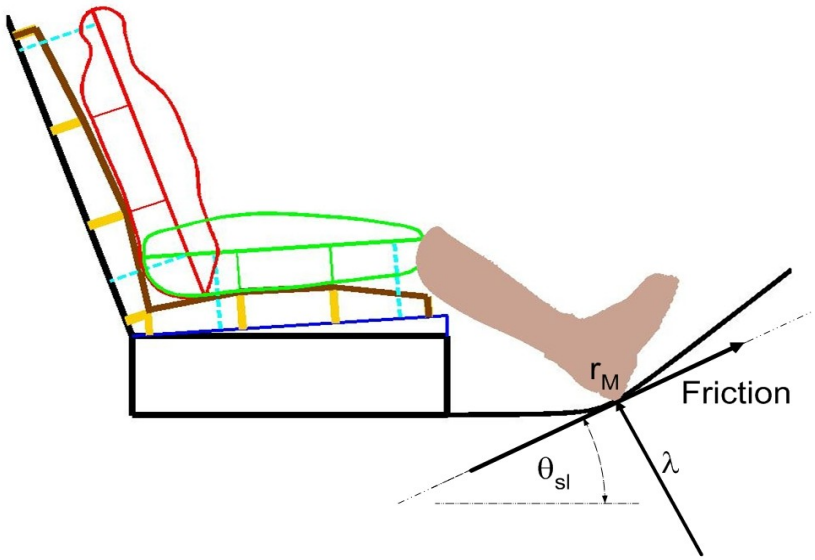

Figure 5.7. Friction force and normal reaction (λ) at the foot seat-rail interface.

$$\theta_{sl} = \arctan\left(\left(\frac{dx_f}{dz_f}\right)^{-1}\right), \tag{5.33}$$

where

$$\frac{dx_f}{dz_f} = a\frac{sin(\beta)}{z_f^2} + \cot(\beta), \tag{5.34}$$

and z_f is given by Equation (5.25).

The virtual work done by the friction force at the foot can be computed by using:

$$\delta W = \mathbf{F}_{foot}.\delta\mathbf{r}_M = \mathbf{F}_{foot}.\sum_{i=1}^{n}\frac{\partial\mathbf{r}_M}{\partial q_i}\delta q_i, \tag{5.35}$$

where $\mathbf{r}_M$ is the position vector of the foot and is given by:

$$\begin{aligned}\mathbf{r}_M &= (\xi(t) + (l_3 + l_4)\cos(\theta_2(t)) + (l_5 + l_6)\cos(\theta_3(t)))\,\vec{i} \\ &\quad + (\zeta(t) + (l_3 + l_4)\sin(\theta_2(t)) + (l_5 + l_6)\sin(\theta_3(t)))\,\vec{k}.\end{aligned} \tag{5.36}$$

The friction force at the foot is given by:

$$\mathbf{F}_{foot} = \mu_{foot}\lambda\left(\cos(\theta_{sl})\vec{i} + \sin(\theta_{sl})\vec{k}\right), \tag{5.37}$$

where μ_{foot} can be defined by the expression:

$$\mu_{foot} = \mu_f\frac{\arctan[10^{10}(\dot{x}_f\cos(\theta_{sl}) + \dot{z}_f\sin(\theta_{sl}))]}{\pi/2}, \tag{5.38}$$

with x_f given by Equation (5.24) and z_f given by Equation (5.25). μ_f is the coefficient of friction for the foot-rail interface and $\dot{x}_f\cos(\theta_{sl}) + \dot{z}_f\sin(\theta_{sl})$ is the velocity of the foot along the floor pan. The value of μ_{foot} computed by using Equation (5.38) is μ_f if the foot is sliding down the floor pan and is $-\mu_f$ if the foot is sliding up the floor pan. Therefore, the purpose of Equation (5.38) is to define the value of μ_{foot} so that the friction force at the foot always opposes the motion of the foot along the floor pan. Now by substituting Equations (5.37) and (5.36) into Equation (5.35), the virtual work terms corresponding to the friction force at the foot can be obtained. The modified equations of motion with the friction force incorporated at the foot are given by:

$$\begin{bmatrix} M_1 & 0 & A_1 & A_2 & A_3 & 0 \\ 0 & M_1 & B_1 & B_2 & B_3 & M_1 \\ C_1 & C_2 & M_7 & 0 & 0 & M_2 cos(\theta_1) \\ D_1 & D_2 & 0 & M_8 & D_3 & (M_3 + M_4) cos(\theta_2) \\ E_1 & E_2 & 0 & E_3 & M_9 & M_5 cos(\theta_3) \\ 0 & 0 & 0 & 0 & 0 & 1 \end{bmatrix} \begin{Bmatrix} \ddot{\xi} \\ \ddot{\zeta} \\ \ddot{\theta}_1 \\ \ddot{\theta}_2 \\ \ddot{\theta}_3 \\ \ddot{z} \end{Bmatrix}$$

$$= \begin{Bmatrix} -A_4 \\ -B_4 \\ -C_3 \\ -D_4 \\ -E_4 \\ -\omega^2 z \end{Bmatrix} - \lambda \begin{Bmatrix} B_{11} \\ B_{21} \\ B_{31} \\ B_{41} \\ B_{51} \\ B_{61} \end{Bmatrix} + \lambda \mu_{foot} \begin{Bmatrix} C_{11} \\ C_{21} \\ C_{31} \\ C_{41} \\ C_{51} \\ C_{61} \end{Bmatrix}. \tag{5.39}$$

The elements $C_{11}...C_{61}$ of the matrix [C] are given by:

$$\begin{aligned} C_{11} &= \cos(\theta_{sl}), \\ C_{21} &= \sin(\theta_{sl}), \\ C_{31} &= 0, \\ C_{41} &= (l_3 + l_4)\sin(\theta_{sl} - \theta_2), \\ C_{51} &= (l_5 + l_6)\sin(\theta_{sl} - \theta_3), \\ C_{61} &= 0. \end{aligned} \tag{5.40}$$

To obtain the response of the seated occupant to applied excitation, i.e., the values of the generalized coordinates that describe the system, Equation (5.39) along with $2(w + r)$ equations of the form given in Equations (5.30) and (5.31) (to consider viscoelasticity of the foam) have to be solved in conjunction with the constraint equation (Equation (5.23)).

5.3.2 Including Seat Back Flexibility in the Seat-Occupant Model

The equations of motion given in matrix form in Equation (5.39) have 6 generalized coordinates, namely the horizontal and vertical positions of the H-point, the angular positions of the torso, femur and shin, and the base excitation applied. If the seat back is allowed to move relative to the seat frame, a degree of freedom, θ_s is added to the system. In this section, the equations of motion are derived for this case. The additional generalized coordinate is θ_s, the angular position of the seat back with respect to the seat frame. The joint between the seat back and the frame is modeled by a very stiff torsional spring, k_s.

The kinetic energy expression given in Equation (5.18) now includes the kinetic energy of the seat. Thus, the expression for the kinetic energy now changes to:

$$T = \frac{1}{2}\sum_{i=1}^{3} m_i(\dot{x}_i^2 + \dot{y}_i^2) + \frac{1}{2}\sum_{i=1}^{3} I_i\dot{\theta}_i^2 + \frac{1}{2}I_s\dot{\theta_s}^2 + \frac{1}{2}m_s l_s^2\dot{\theta_s}^2. \tag{5.41}$$

The expression for potential energy given in Equation (5.19) is also changed to:

$$U = g\sum_{i=1}^{3} m_i y_i + g m_s l_s \sin(\theta_s) + \frac{1}{2}k_s(\theta_s - \theta_{s0})^2 + \sum_{i=1}^{w+r} V_i(\delta_i), \tag{5.42}$$

where θ_{s0} is the initial angular position of the seat back with respect to the horizontal.

Thus, the equations of motion now become:

$$\begin{bmatrix} M_1 & 0 & A_1 & A_2 & A_3 & 0 & 0 \\ 0 & M_1 & B_1 & B_2 & B_3 & 0 & M_1 \\ C_1 & C_2 & M_7 & 0 & 0 & 0 & M_2 cos(\theta_1) \\ D_1 & D_2 & 0 & M_8 & D_3 & 0 & (M_3 + M_4) cos(\theta_2) \\ E_1 & E_2 & 0 & E_3 & M_9 & 0 & M_5 cos(\theta_3) \\ 0 & 0 & 0 & 0 & 0 & M_{10} & G_1 \\ 0 & 0 & 0 & 0 & 0 & 0 & 1 \end{bmatrix} \begin{Bmatrix} \ddot{\xi} \\ \ddot{\zeta} \\ \ddot{\theta}_1 \\ \ddot{\theta}_2 \\ \ddot{\theta}_3 \\ \ddot{\theta}_s \\ \ddot{z} \end{Bmatrix}$$

$$= \begin{Bmatrix} -A_4 \\ -B_4 \\ -C_3 \\ -D_4 \\ -E_4 \\ -G_2 \\ -\omega^2 z \end{Bmatrix} - \lambda \begin{Bmatrix} B_{11} \\ B_{21} \\ B_{31} \\ B_{41} \\ B_{51} \\ B_{61} \\ B_{71} \end{Bmatrix} + \lambda\mu_{foot} \begin{Bmatrix} C_{11} \\ C_{21} \\ C_{31} \\ C_{41} \\ C_{51} \\ C_{61} \\ C_{71} \end{Bmatrix}, \tag{5.43}$$

the extra terms being defined as:

$$\begin{aligned} M_{10} &= I_s + m_s l_s^2, \\ G_1 &= m_s l_s \cos(\theta_s), \\ G_2 &= g m_s l_s \cos(\theta_s) + k_s(\theta_s - \theta_{s0}) + \Delta\theta_s, \\ \Delta\theta_s &= \textstyle\sum_{i=1}^{w+r} F(\delta_i) \frac{\partial \delta_i}{\partial \theta_s} + \sum_{i=1}^{u} c_i \dot{\delta}_i \frac{\partial \dot{\delta}_i}{\partial \dot{\theta}_s}. \end{aligned} \tag{5.44}$$

The terms of the $[B]$ matrix, $B_{11}..B_{51}$ are as defined in Equation (C.2) and

$$\begin{aligned} B_{61} &= 0, \\ B_{71} &= 0, \end{aligned} \tag{5.45}$$

as the constraint is unaffected by θ_s and z.

The terms of the $[C]$ matrix, $C_{11}..C_{51}$ are as defined in Equation (C.2) and

$$\begin{aligned} C_{61} &= 0, \\ C_{71} &= 0, \end{aligned} \tag{5.46}$$

as friction force is unaffected by θ_s and z.

5.4 Simplifying the Governing Equation by the Coordinate Reduction Technique

In order to study the response of the seat-occupant system, the system governing equations derived in this chapter need to be solved simultaneously. However, because of the existence of the Lagrange multiplier λ in Equation (5.26), these equations are

not easy to solve. Therefore, in this study the coordinate reduction technique given by Amirouche [113] and Amirouche and Ider [114] is used to eliminate the additional unknown variable λ. The equations of motion for the seat occupant system (Equation (5.26)) can be expressed as:

$$[M][\ddot{q}] = [Q] - \lambda\{[B]^T - \mu_{foot}[C]^T\}, \tag{5.47}$$

where $q = [\xi, \zeta, \theta_1, \theta_2, \theta_3, z]$ and $[.]^T$ denotes the matrix transpose. The objective is to find a matrix $[S]$ that is a $(n-3) \times m$ orthogonal complement of the matrix $\{[B]^T - \mu_{foot}[C]^T\}$. That is:

$$[S]\{[B]^T - \mu_{foot}[C]^T\} = 0, \tag{5.48}$$

or,

$$\{[B] - \mu_{foot}[C]\}[S]^T = 0. \tag{5.49}$$

If $[S]^T$ is in the null space of $\{[B] - \mu_{foot}[C]\}$, or $[S]$ is in the left null space of $\{[B]^T - \mu_{foot}[C]^T\}$, Equations (5.48) and (5.49) are satisfied and $[S]^T$ is the orthogonal complement of $\{[B] - \mu_{foot}[C]\}$. Therefore, given vectors $[B]$ and $[C]$, matrix $[S]$ can be obtained. Then, premultiplying Equation (5.47) with $[S]$ gives:

$$[S][M][\ddot{q}] = [S][Q]. \tag{5.50}$$

Puri [32] has shown that the first time derivative of the equation of constraint, $[B]$, is zero. That is:

$$[B][\dot{q}] = 0. \tag{5.51}$$

Differentiating Equation (5.51) with respect to time and combining the results with Equation (5.50) yields,

$$[A][\ddot{q}] = [D], \tag{5.52}$$

where the matrices $[A]$ and $[D]$ are given by:

$$[A] = \begin{bmatrix} [S][M] \\ [B] \end{bmatrix} \tag{5.53}$$

and

$$[D] = \begin{bmatrix} [S][Q] \\ -[\dot{B}][\dot{q}] \end{bmatrix}. \tag{5.54}$$

It can be seen that if $[A]$ is positive definite, then Equation (5.52) can be expressed as:

$$[\ddot{q}] = [A]^{-1}[D]. \tag{5.55}$$

The set of second-order differential equations represented by Equation (7.1) along with the equations which represent the nonlinear viscoelastic behavior of the seat can be solved numerically to study the dynamic response of the system.

5.5 Chapter Summary

In this chapter the multibody seat-occupant model was reviewed. The model was based on a previously developed model. The previously developed model was fine tuned. The interfacial friction model was improved to be a function of the relative motion between the occupant and the seat. Also the comprehensive foam model described in Chapter 3 was incorporated into the seat-occupant model. A constraint Lagrangian formulation was used to derive the equations of motion for the seat-occupant system. In deriving the equations of motion of the system, the first step was a careful description of the model of the car seat as well as that of the occupant, including the profile of the dummy and the representation of foam by equivalent springs and the interfacial forces. Also, friction at the foot-rail interface and flexible seat back were also incorporated into the model. Finally, a coordinate reduction technique was used to eliminate the Lagrange multiplier term appeared in the governing equations due to the geometric constraint. It was observed that this leads to $2(w+r)+5$ coupled equations (w and r are numbers of elements in the seat back and the seat bottom). These equations will be solved in the next two chapters to estimate transient and steady state responses of the occupant. Note that there are a large number of parameters that need to be specified in the model. The baseline physical and geometric parameters, including the profile polynomial functions, are

given in Appendices D and E. The baseline foam parameters for the various foam models that are used are given in Appendices F, H and I. The occupant being modeled in the simulations presented in subsequent chapters is a mannequin and the seat is Chrylser car seat. The foam model parameters including the strain rate dependencies were derived using the quasi-static compression tests described earlier. While not used in the seat-occupant modeling, the parameter values for the models of the four CONFOR foams are given in Appendix G.

6. SEAT-OCCUPANT MODELING - TRANSIENT RESPONSE PREDICTION

In the previous chapter, a detailed description of the seat-occupant model was given. The dynamic response of a seat-occupant system can be predicted by using many of the multi-body seat-occupant models published in the literature. However, there are only a few models which can successfully predict both the transient response and the settling point, i.e. static response, of the seat-occupant system, see [50]. In this chapter, the multi-body model introduced in Chapter 5 is used to study the transient and static responses of a seat-occupant system. The multi-body occupant model consists of three bodies corresponding to the torso, the femur and the shin of the seated occupant. The seat model incorporates a global nonlinear viscoelastic foam model which was previously developed in Chapter 3. The foam model includes rate-dependent viscoelastic parameters thereby resolving some problems observed in the previous studies, i.e. seat cushion model was only accurate for a particular compression rate. The seat back and the seat bottom are represented by arbitrary numbers of spring elements which makes it possible to track the interfacial pressure distribution along the seat back and the seat bottom. Therefore, with the significant improvement to the foam model and the multi-body model, the updated seat-occupant model has been used to study the mechanical behavior of the seat-occupant system and to predict the H-Point location as well as the pressure distribution at the interfaces. Effects of different factors like number of nonlinear viscoelastic elements in the seat back and the seat bottom model, the seat geometry, the interfacial friction, the occupants weight and etc. on the static responses are studied. The force distribution at the seat-occupant interface was also obtained experimentally and is compared to the model predictions.

6.1 Solving the Governing Equations

The transient response of the seat-occupant system introduced before is obtained by simultaneously solving the system governing equations which consist of set of second-order differential equations represented by Equation (5.55) and the equations which represent the nonlinear viscoelastic behavior of the seat. Note that in this chapter the seat back is stiff, i.e. no flexible seat back. In order to compute the transient response of the system, the base excitation term z in Equation (5.55) is set to zero. Therefore, the seat-occupant dynamic system has 5 generalized coordinates: horizontal displacement of H-Point ξ, vertical displacement of H-Point ζ, angle of torso θ_1, angle of femur θ_2 and angle of shin θ_3. Note that the behavior of each element is modeled by 2 first-order differential equations (see Equations (4.4) and (4.5)). Therefore, assuming N_{bottom} and N_{back} nonlinear viscoelastic elements represent the seat bottom and the seat back, there are $2(N_{bottom} + N_{back}) + 5$ nonlinear differential equations need to be solved to obtain the system responses. These equations can be solved numerically, e.g. time integration, to estimate the 5 generalized coordinates as functions of time. The steady-state response of the system, i.e. setting point of the occupant in the seat, can also be obtained analytically using the algebraic solution of the governing equations by setting all the time dependent terms in the equations to zero. Puri used the latter technique to estimate the settling point of the occupant [32].

In this study, the governing equations are just solved numerically using MATLAB $ODE45$ function. In order to solve the system equations, the system initial conditions need to be specified. For this study these conditions are chosen so that the occupant and the seat are in contact but the seat back and the seat bottom cushions are not compressed. The initial conditions are given in Appendix D and the variables are shown in Figure 6.1. Also, it is assumed that the seat cushion is made of low density Foam 1. The parameters of Foam 1 are given in Appendix F.

Note that as the foot is constrained to slide along the floor pan the initial generalized coordinates are not independent. Therefore, if initial values for four of these generalized coordinates are prescribed then the value of the fifth generalized coordi-

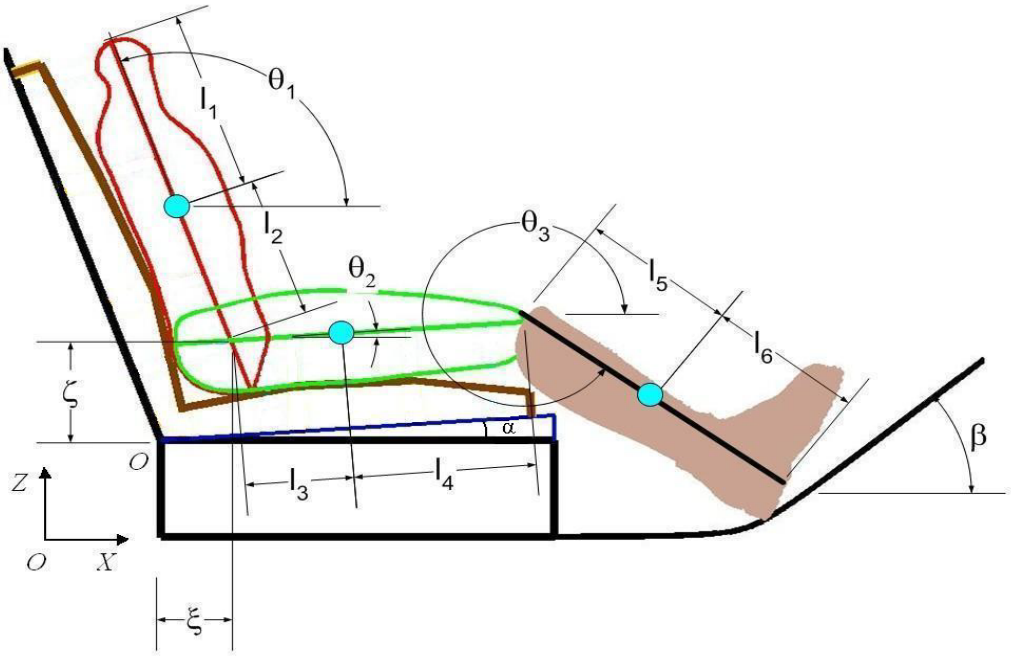

(a)

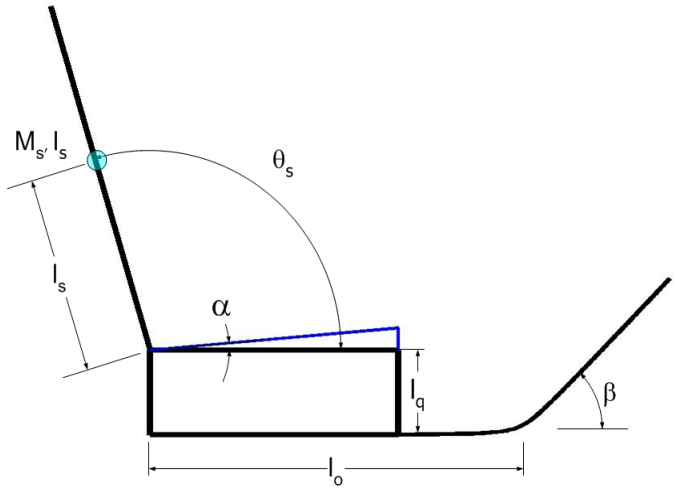

(b)

Figure 6.1. Geometric parameters and variables of the seat-occupant model. (a) geometric parameters of the occupant and (b) geometric variables of the car seat.

nate can be obtained from the constraint equation derived in Chapter 5. Also, it is assumed that the system starts from rest, i.e. all time derivative are zero at $t = 0\ s$.

The angle between the seat back and the seat bottom was chosen to be 110^o based on standard settings for measuring H-Point location. The angle between the seat bottom and the horizontal axis was chosen to be 5^o. Here, it is assumed that the joint between the seat back and the seat bottom is rigid and therefore the angle θ_s stays constant and equal to its initial value. The number of foam elements required to model the seat behavior accurately is also an important parameter which affects the estimated response. In general, if a very few elements are included in the seat-occupant model, the estimated response may be inaccurate, although the computation time decreases significantly. On the other hand, including more elements in the seat back and the bottom increases the estimated pressure distribution resolution, although this comes at a price that the computation time becomes longer. In this study, initially, the seat back and the seat bottom are represented by 40 elements. Later, in this chapter, the effect of numbers of elements on the estimated response of the H-Point is investigated in detail.

As discussed in Section 5.1.2, the total force in each nonlinear viscoelastic element is computed by first computing the total stress in each element and then multiplying the computed stress by the area χ which denotes the area of foam represented by each element. Therefore, area χ for the seat back and the seat bottom are given by,

$$\chi_{back} = \frac{A_{back}}{N_{back}}, \tag{6.1}$$

and,

$$\chi_{bottom} = \frac{A_{bottom}}{N_{bottom}}, \tag{6.2}$$

where A_{back} and A_{bottom} are the areas of the seat back and the bottom and N_{back} and N_{bottom} are the number of springs in the seat back and the seat bottom. Puri [32] measured the area of the seat back and the seat bottom of a 1996 Chrysler LH, which was found to be approximately 9 $in \times 12\ in$ (228.6 $mm \times 304.8\ mm$) for the seat back and 15 $in \times 12\ in$ (381 $mm \times 304.8\ mm$) for the seat bottom. Therefore, if 20

elements are used to model foam behavior at the seat back then the value for χ for the seat back is 5.4 in^2 (3483.86 mm^2). Similarly, if 20 elements are used to model foam behavior at the seat bottom then the value of χ for the seat bottom is 9 in^2 (5806.44 mm^2). Also it is known that the seat in the 1996 Chrysler LH is made of low density polyurethane foam type 1 studied in Chapter 3. Thus the seat back and the seat bottom, or the elements representing the foam in the seat, are characterized by the nonlinear viscoelastic Model 4 with the parameters given in Appendices H and I.

In Chapter 4, it was shown that in order to accurately describe the foam behavior, a linear viscous damping term needs to be added to the hereditary type viscoelastic model of the foam. This viscous damping term $c\dot{x}$ is included in the dynamic model of foam to account for other damping factors, e.g. damping effect caused by air passing through foam at higher frequencies, which are not modeled by viscoelastic damping mechanisms in the foam. It is noted that this is a very simplified model of the effects of this air movement, Patten [115] developed a nonlinear damping model to characterize the effects of air movement in the foam and used it to predict the motion of a mass placed on a car seat undergoing bandlimited ($0 - 20$ Hz) random base excitation. This is especially important as in Chapter 3 the viscoelastic model was estimated using very slow or quasi-static tests. For the results shown in Chapter 4, the value of viscous damper was initially chosen based on the previous experimental studies. But the damping coefficient was later adjusted to match the peak amplitude of the estimated frequency responses with the experimentally measured frequency responses of the foam, for example see Figure 4.13. For the seat-occupant model, the estimated damping coefficient for the single-degree-of-freedom foam-mass system (C_{SDOF} = 10 Ns/m) is adjusted based on the areas of the seat back and the seat bottom. Therefore, the damping coefficient used in the seat-occupant model is computed as,

$$C_{seat-occupant} = \frac{\frac{A_{seat}}{A_{foam}} \times c_{SDOF}}{N}, \tag{6.3}$$

where A_{seat} is the total area of the seat 288 in^2 (0.1858 m^2), A_{foam} is the area of the foam sample cube used in the single-degree-of-freedom foam-mass system experiment 9 in^2 (5806.44 mm^2), C_{SDOF} is the damping coefficient used in simulations described Chapter 4; it was chosen to make the simulation results closer to the experimental results, and N is the number of the viscous dampers in the seat back and the seat bottom. In this research, it is assumed that the number of dampers is equal to the number of elements representing the seat and thus $N = N_{back} + N_{bottom}$. Note that the final equilibrium position and the static force distribution between the seat and the occupant will be independent of the number of dampers or the damping constants. However, these values determine the transient behavior of the system as well as the steady-state response of the system subjected to harmonic input, which will be described in the next chapter.

The position of the H-Point, which is defined by the generalized coordinates ξ and ζ, is shown in Figures 6.2(a)-6.2(b). It is observed that the horizontal and the vertical position of the H-point reach their steady-state values after almost 25 *seconds*. This can be verified further by considering the variation of the generalized velocities with time and these are shown in Figure 6.3. The H-Point velocities become very close to zero within the first 25 *seconds* of integration. Also, in general, the horizontal position of the H-point ξ reaches its steady state position faster than the vertical position of the H-point ζ. This can be explained noting that the only external force acting on the occupant is the occupant weight. The final H-Point location is given by $\xi = 85.8$ mm and $\zeta = 0.124$ mm. Note that the estimated transient time in this study is shorter than the transient time of the same system reported by Puri [32]. This can be explained noting that Puri's seat-occupant model did not include the time dependent viscoelastic terms and the only damping mechanism was the viscous damping.

The posture of the occupant is characterized by three generalized coordinates θ_1, θ_2 and θ_3 and these are shown in Figures 6.4 to 6.6. It is observed that the three angles θ_1, θ_2 and θ_3 reach their steady-state values after almost 20 *seconds*. This

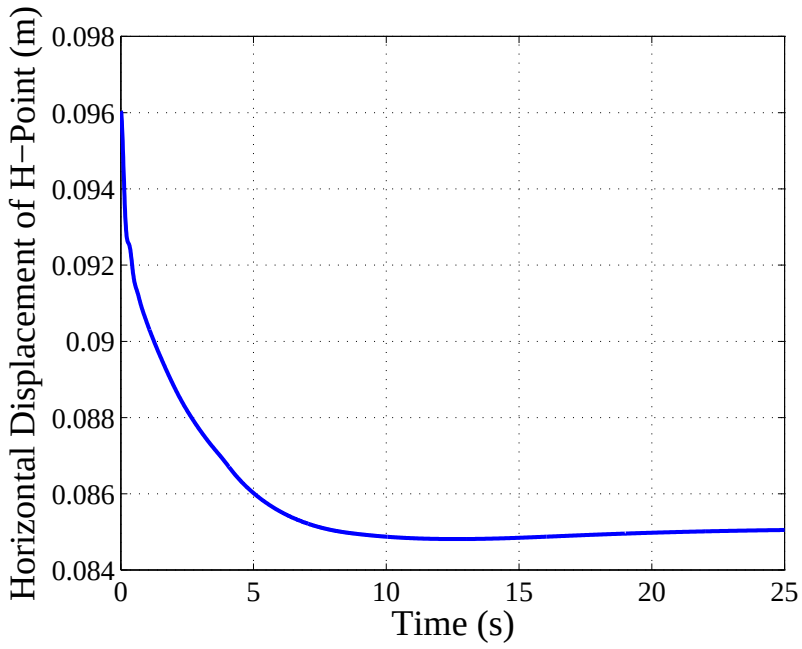

(a)

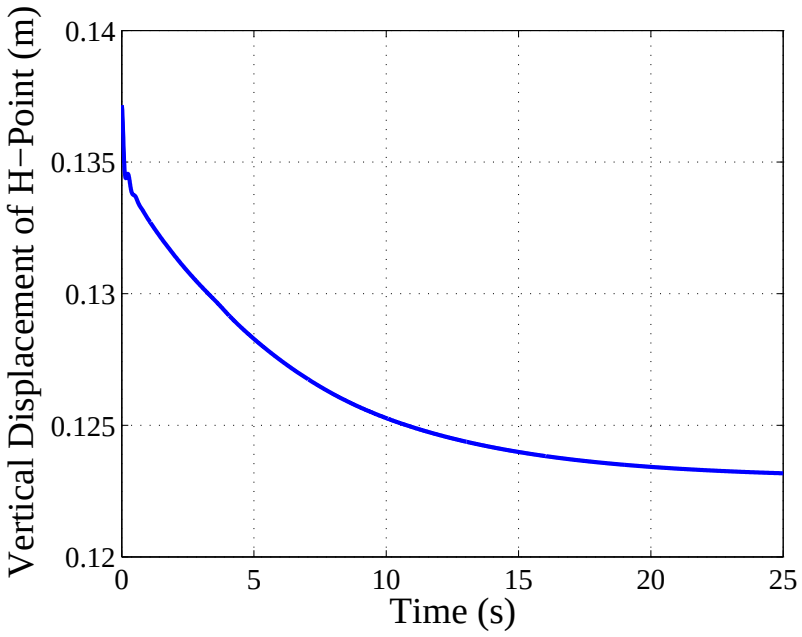

(b)

Figure 6.2. (a) The estimated horizontal position of H-Point ξ and (b) the estimated horizontal position of H-Point ζ.

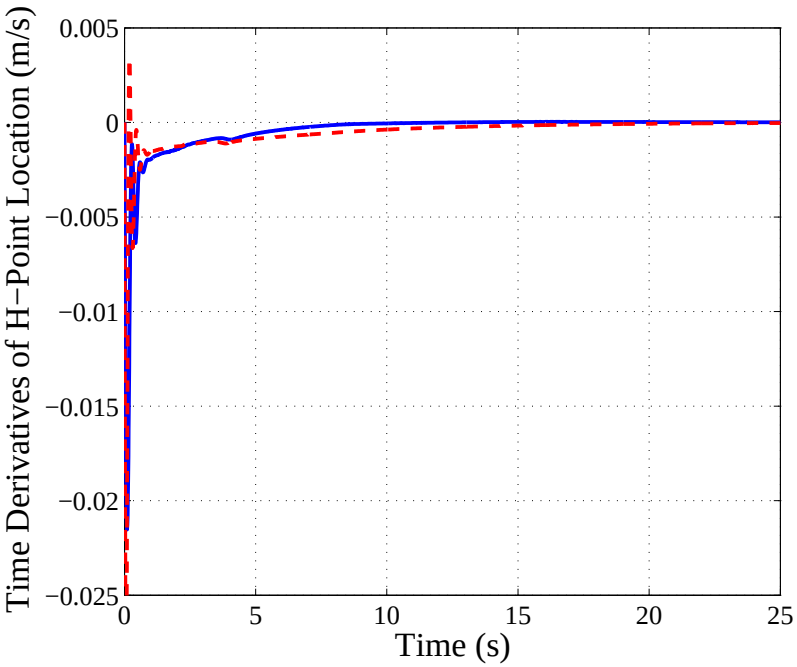

Figure 6.3. The estimated velocity of H-Point. Blue: horizontal velocity of H-Point $\frac{d\xi}{dt}$ and red: vertical velocity of H-Point $\frac{d\zeta}{dt}$.

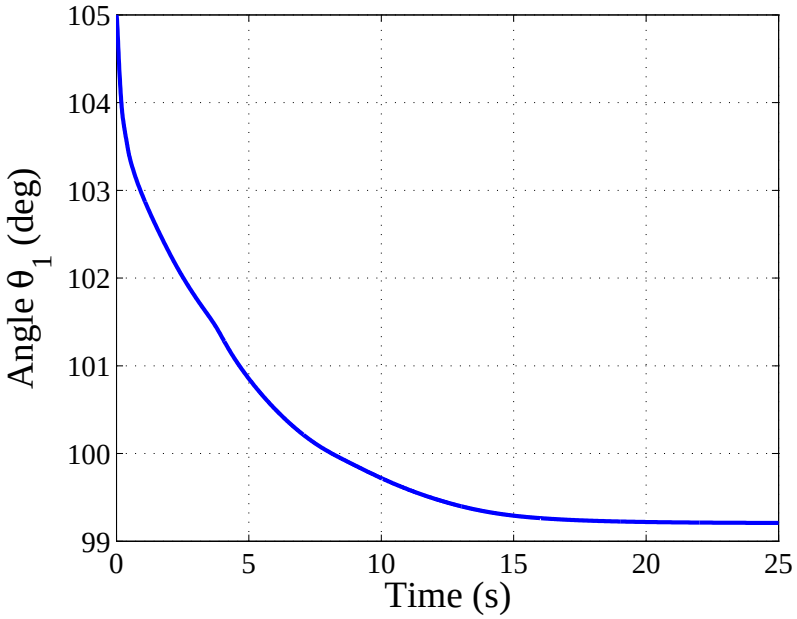

Figure 6.4. The estimated angle of the occupant's shin θ_1.

can be verified further by considering the variation of the angular velocities of the three bodies as shown in Figure 6.7. The angular velocities become very close to zero within the first 20 *seconds* of integration. Also, in general, the femur angle θ_2 reaches its steady state position slower than the other two angles θ_1 and θ_3. The final steady-state angles are given by $\theta_1 = 99.21^o$, $\theta_2 = 9.20^o$ and $\theta_3 = -43.56^o$. The occupant positions at three instants, $t = 0,\ 10$ and 25 *sec* are shown in Figure 6.8.

When the system reaches the steady state, the force in each element attached to the femur can be plotted to obtain a measure of the seat-occupant interface force/pressure at the bottom of the seat. This is shown in Figure 6.9(a). Similarly, the pressure in each element attached to the torso can be plotted to obtain a measure of the seat-occupant interface pressure at the back of the seat. This is shown in Figure 6.9(b).

It can be seen from Figure 6.9(a) that there is a steep dip in the interfacial pressure at around 0.15 m. This can be attributed to the presence of a seam in the foam at the back of the seat. It can also be seen from Figure 6.9(a) that at the seat bottom the

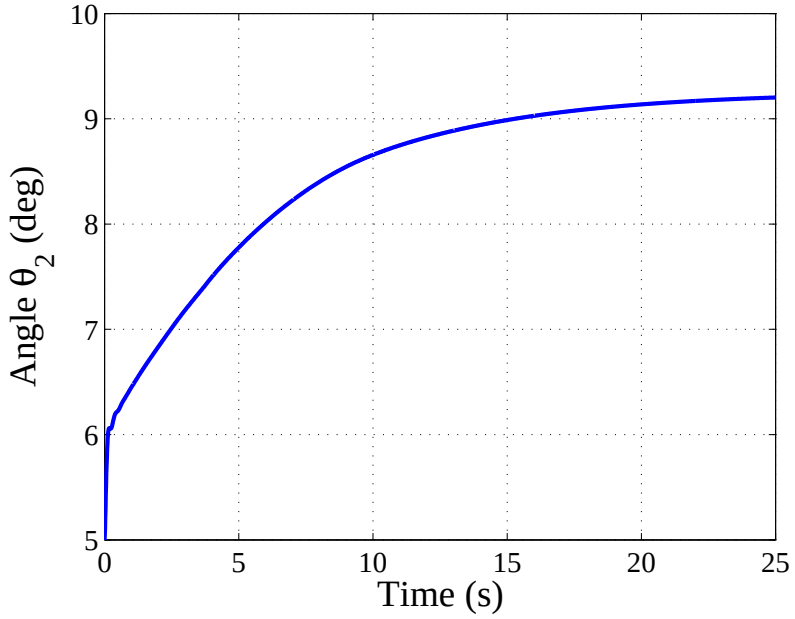

Figure 6.5. The estimated angle of occupant's femur θ_2.

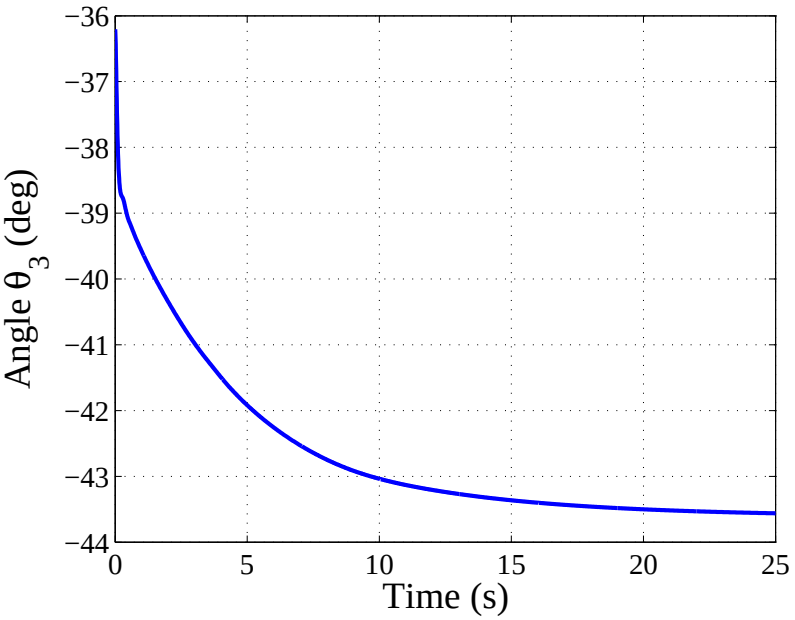

Figure 6.6. The estimated angle of occupant's torso θ_3.

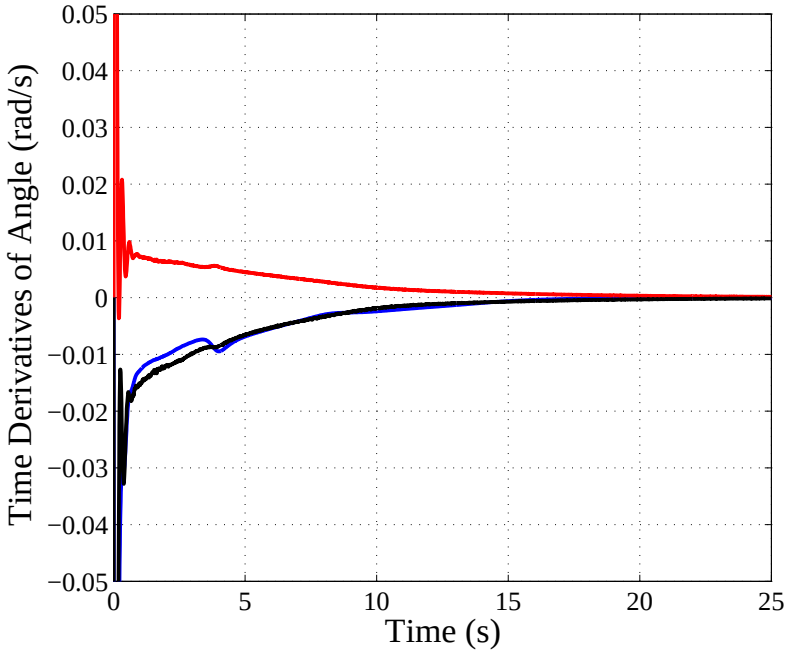

Figure 6.7. The estimated angular velocities of the occupant's torso, femur and shin. Blue: angular velocity of the shin $\frac{d\theta_1}{dt}$, red: angular velocity of the femur $\frac{d\theta_2}{dt}$ and black: angular velocity of the torso $\frac{d\theta_3}{dt}$.

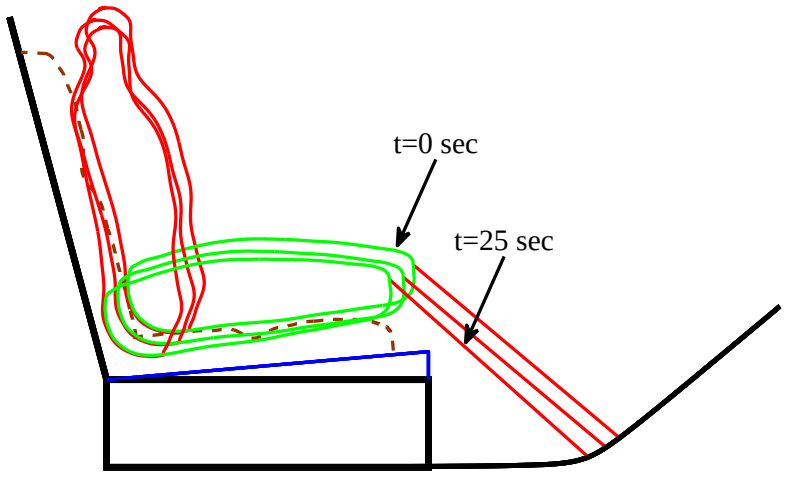

Figure 6.8. The occupant positions at three instants, $t = 0,\ 10,\ 25$ *sec*.

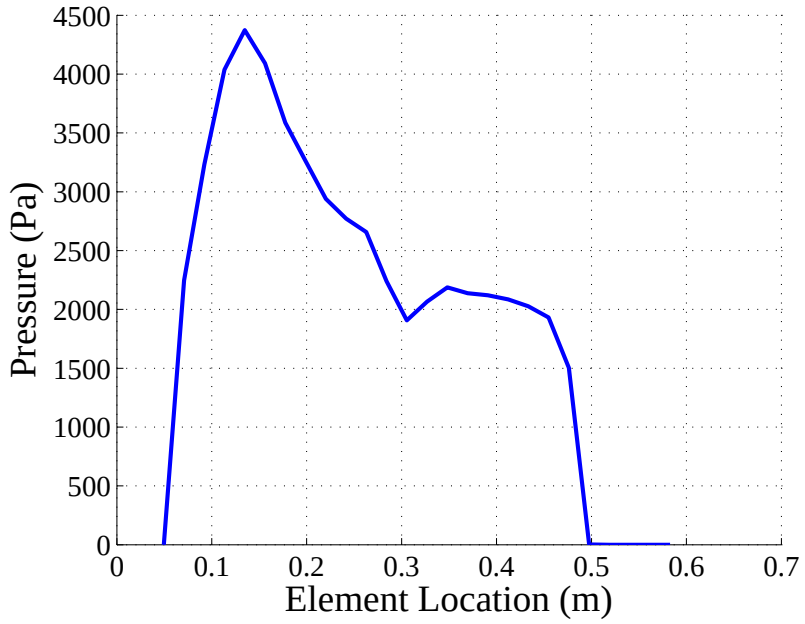

(a)

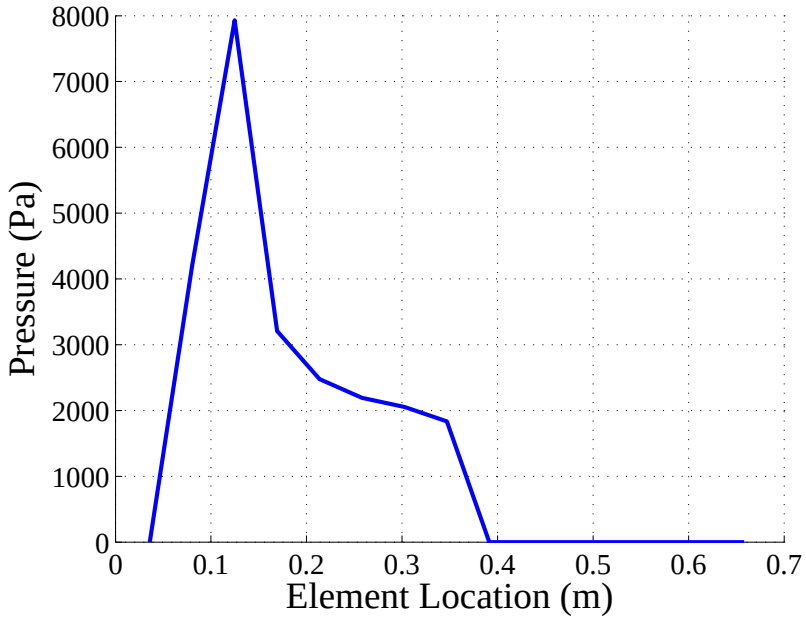

(b)

Figure 6.9. The estimated pressure distribution (a) at the occupant and the seat bottom and (b) at the occupant and the seat back.

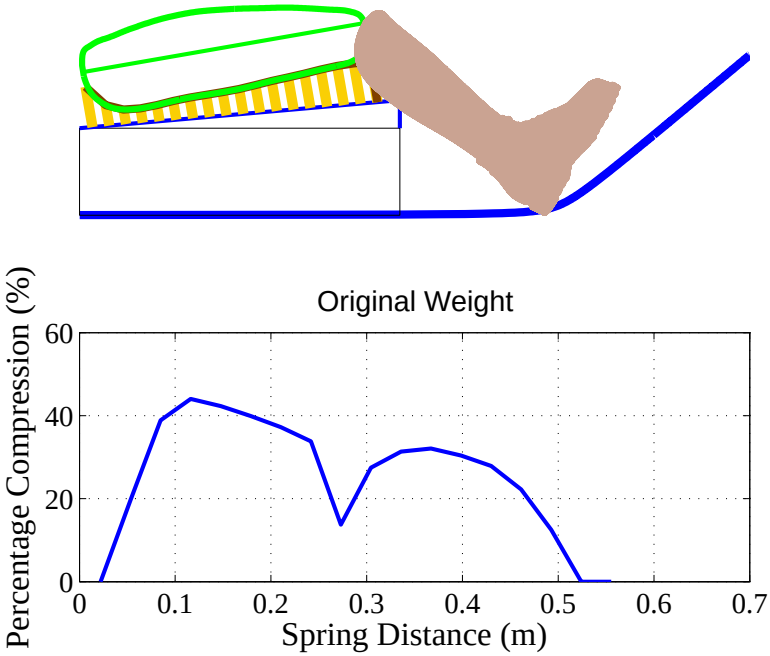

Figure 6.10. The percentage compression in the seat bottom.

maximum force occurs beneath the H-Point. According to [77] this maximum force is known to directly affect static comfort. Ebe [77] had found through subjective testing that the pressure in a 4 $cm \times 4$ cm region beneath the ischial bones varies linearly with occupant static comfort. The final percentage compression along the seat bottom is shown in Figure 6.10. As expected, the maximum compression occurs just below the H-Point where the seat is compressed as much as 45%. The position of the occupant's femur and shin and the nonlinear elements in the seat bottom are also shown in the figure.

It is known that foam exhibits nonlinear viscoelastic behavior which was discussed before. The estimated elastic and viscoelastic stresses in the seat bottom element just below the H-Point are shown in Figure 6.11. It is observed that, in general, the elastic stress is greater than the viscoelastic stress. It can be seen from the figure that the viscoelastic stress in the element reaches the steady-state value within the

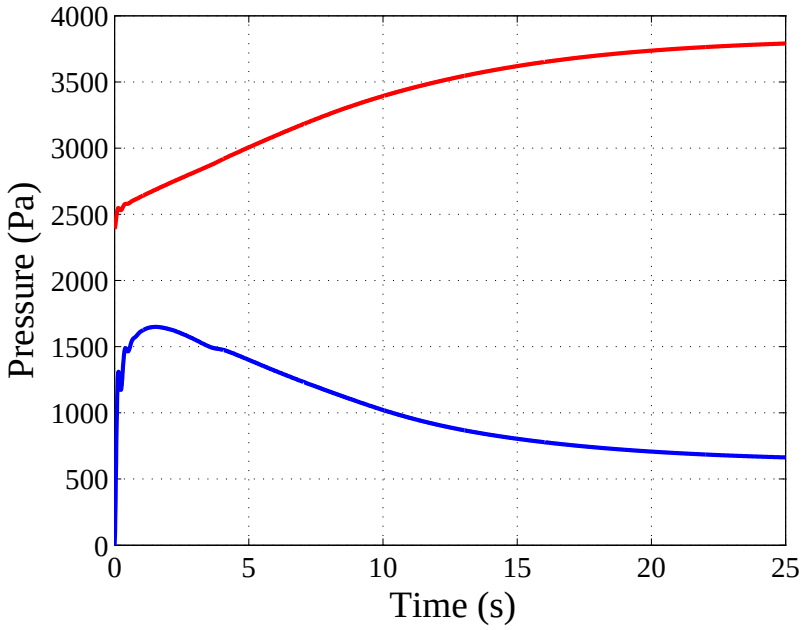

Figure 6.11. The estimated pressure as function of time for the seat bottom element below the H-Point. Red: elastic stress and blue: viscoelastic stress.

first 25 *seconds* of the response, and the steady-state viscoelastic response is not zero. This is not consistent with the previous studies conducted by Puri where the steady-state viscoelastic stress was zero. This is because of the different viscoelastic models used in two studies; Puri used a viscoelastic model that only contained the σ_{v2} term whose input is strain rate, thus at steady state its contributions would be zero. In this study, the input to the first viscoelastic term is the elastic stress (not included in Puri's model) which would contribute to the total stress at steady state. The first viscoelastic term converges to the scaled elastic stress as shown in Equation (4.20).

6.2 Variation of the Model Parameters

As discussed earlier in this thesis, the static comfort of the occupant and the ergonomic functionality are both functions of the car seat geometry and properties. Of primary importance in seat design are the H-Point location (related to ergonomics)

and the seat-occupant interface pressure (related to static comfort). In order to design a car seat, it is very important to study how different components of the seat-occupant system affect these two outcomes when an occupant settlings into a seat. Also, when tuning a model to match measure responses an understanding of how different model parameters affect the outcome is needed. In this section, the effects of variation of different seat-occupant system model parameters on the system response are investigated. The base line parameters of the model are given in Appendices D-F and Appendix I.

6.2.1 Variation in the Number of Elements

The variation in the steady-state values of the horizontal and the vertical position of the occupant H-Point, i.e. ξ_{ss} and ζ_{ss}, with different values of N_{back} and N_{bottom} was studied and the results are shown in Figures 6.12 and 6.13, respectively. The steady-state values are obtained by integrating the governing equations until the occupant has reached the steady state ($T > 25\ Sec$). Initially, the number of elements at the seat back is kept constant at $N_{back} = 15$ while N_{bottom} is varied between 10 and 40 (10, 15, $\cdots$, 40). Next, the number of elements at the seat bottom is kept constant at $N_{bottom} = 15$ while N_{back} is varied between 10 and 40. It can be seen from Figure 6.12 that the values of ξ and ζ are dependent on the number of elements used at the bottom of the seat. Similarly, it can be seen from Figure 6.13(a) that the value of ξ is dependent on the number of springs used at the seat back. However, the value of ζ varies only a small amount with the number of elements used to model the seat back as shown in Figure 6.13(b). From Figures 6.12 and 6.13 it can be observed that if the numbers of elements used to model the seat back and the seat bottom are increased beyond 20 springs, the predictions of the H-Point are almost the same.

The predicted pressure distribution between the seat occupant and the seat bottom when $N_{s,back} = 20$ and $N_{s,bottom} = 20$ is shown in Figure 6.14. The maximum pressure occurs just below the H-Point. There is a dip close to 0.3 m which is due to

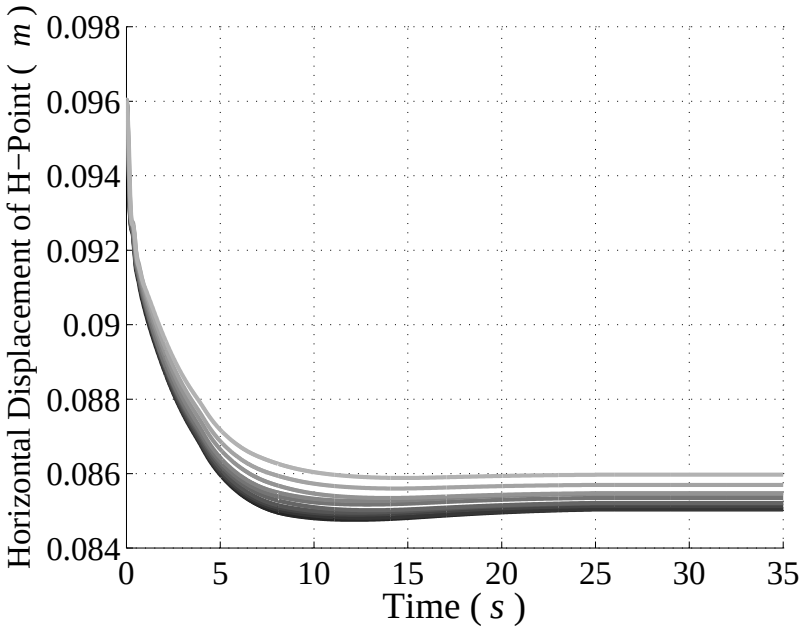

(a)

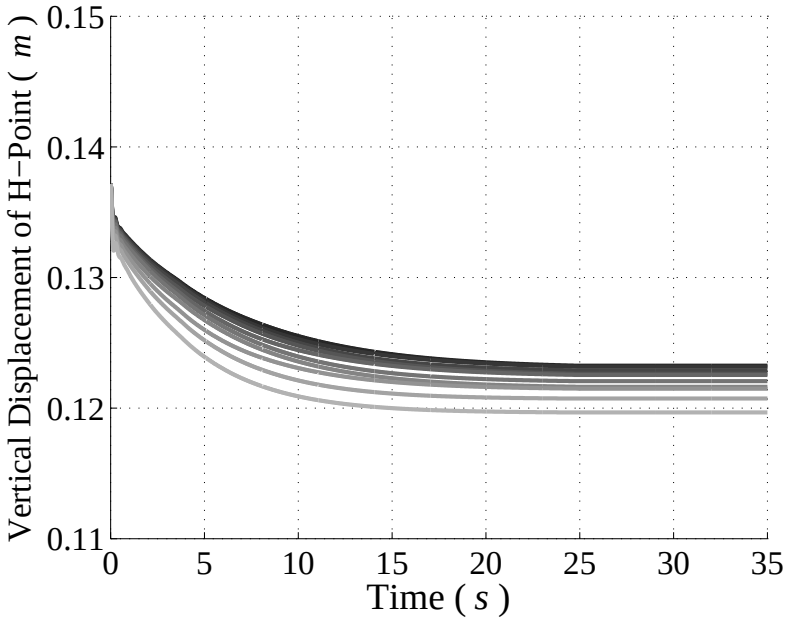

(b)

Figure 6.12. (a) The horizontal location (ξ) and (b) the vertical location (ζ) of the H-Point, when the number of elements at the seat bottom is varied between 10 and 40 in steps of 2 (light gray to black) and the number of elements at the seat back was kept constant at 15. The coefficient of friction μ is 0.25.

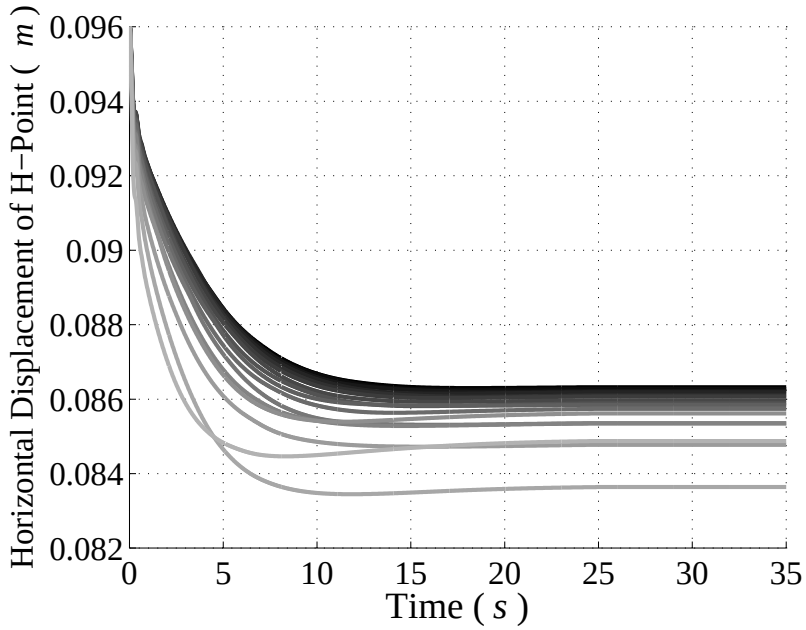

(a)

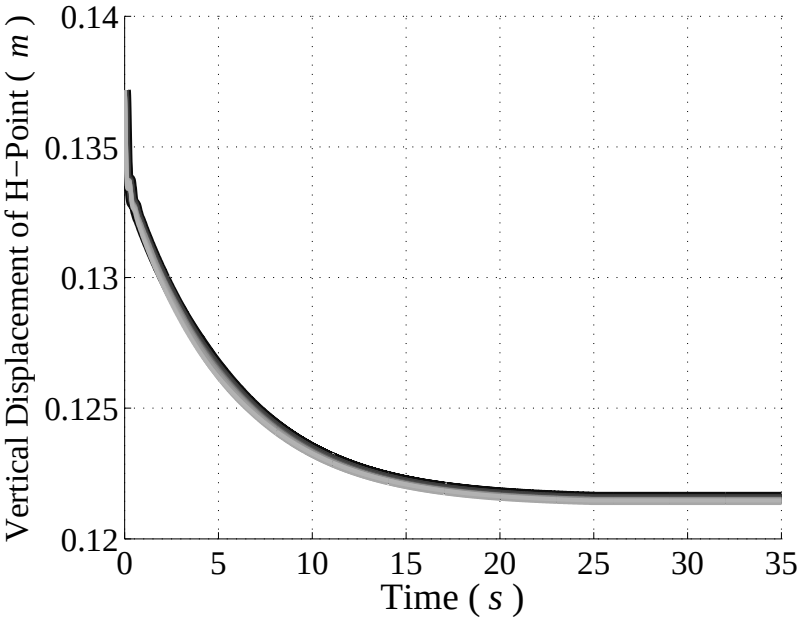

(b)

Figure 6.13. (a) The horizontal location (ξ) and (b) vertical location (ζ) of the H-Point when the number of elements at the seat back is varied between 10 and 40 in steps of 2 (light gray to black) and the number of elements at the seat bottom was kept constant at 15. The coefficient of friction μ is 0.25.

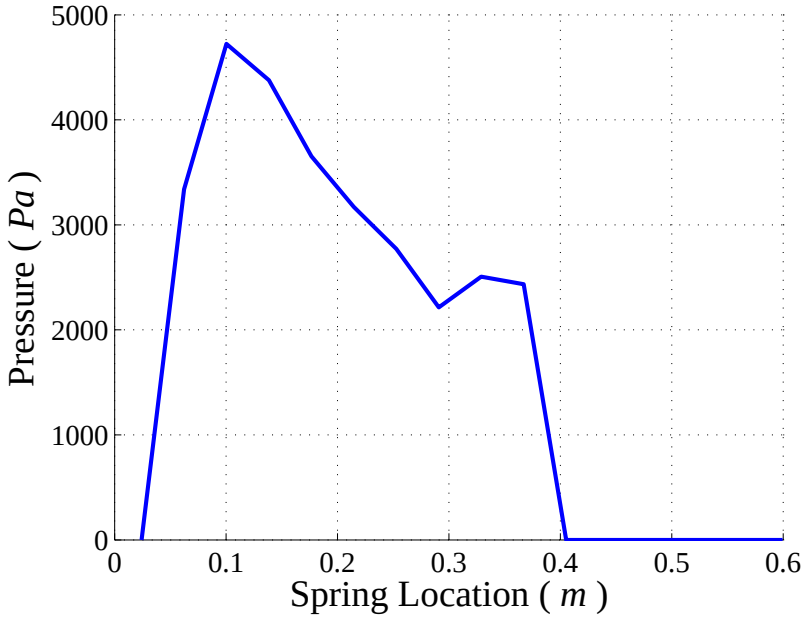

Figure 6.14. The predicted seat-occupant interface pressure between the occupant and the seat bottom as a function of the distance along the seat rail. Twenty elements were used to model the seat bottom and the seat back. The coefficient of friction μ is 0.25.

a stitch seam in the seat cushion. Zero pressure at the end of seat also indicates that there is no contact between the occupant femur and the seat bottom close to the seat back frame and seat bottom frame join and at the seat front.

6.2.2 Variation of the Interfacial Friction Coefficient (μ)

The effect of varying the interfacial friction coefficient on the steady state H-Point location was studied. It was previously observed that if the coefficient of friction is less than 0.15, the occupant can slip out of the seat [32]. For these studies $N_{back} = N_{bottom} = 20$. The horizontal and vertical locations of the H-Point for different values of the friction coefficient (μ) are shown in Figures 6.15. The coefficient of friction is varied between 0.20 and 0.45 in 0.05 increments. For the smallest value of the coefficient of friction $\mu = 0.20$, it can be seen from their initial position that

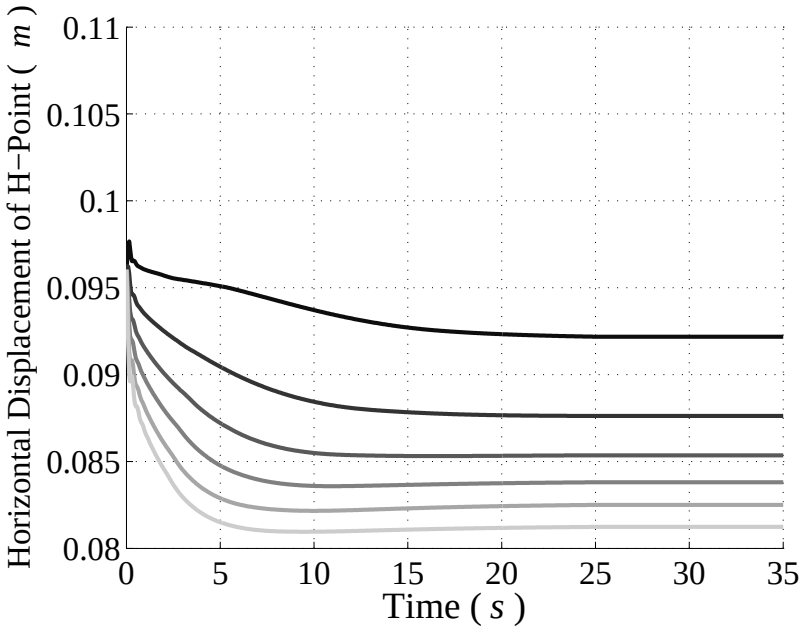

(a)

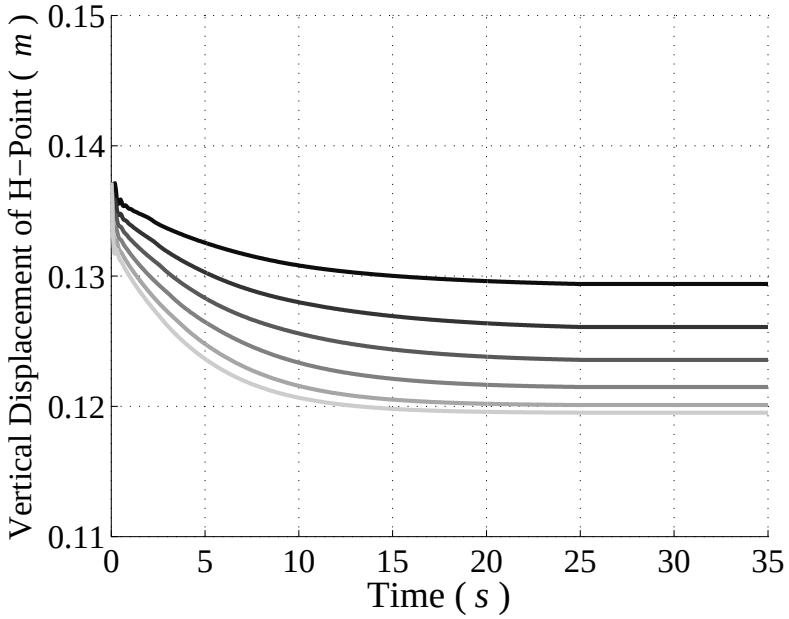

(b)

Figure 6.15. (a) The horizontal location of the H-Point ξ; (b) the vertical location of the H-Point ζ, when the coefficient varies between 0.20 to 0.45 (light black to dark black). The number of springs in the seat back and the seat bottom is equal to 20.

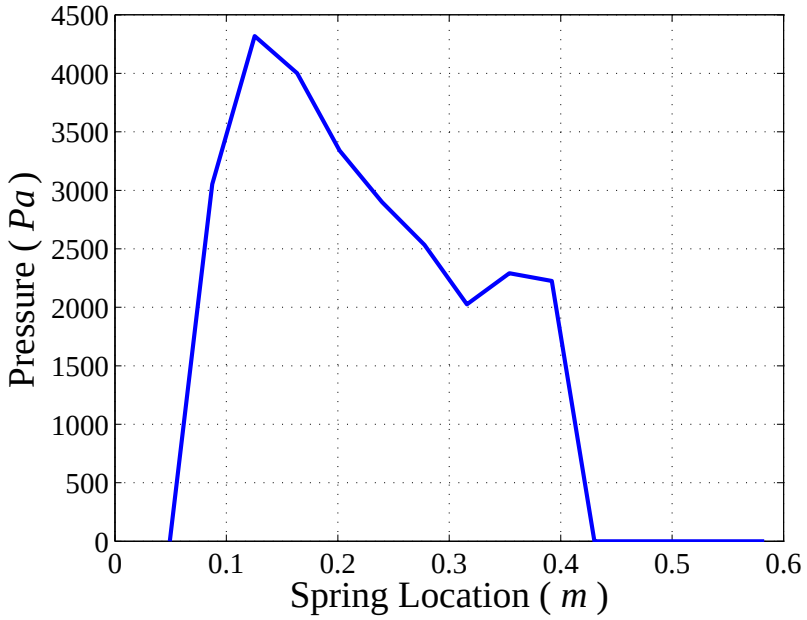

Figure 6.16. The pressure distribution at the occupant and the seat bottom interface as a function of the distance along the seat bottom. The coefficient of friction μ is equal to 0.4.

the vertical and the horizontal displacements of the H-Point are maximum. As the coefficient of friction is increased, the horizontal and the vertical displacements of the H-Point change by smaller amounts from the initial position and this change is smallest (in this study) when the coefficient of friction is set to $\mu = 0.4$. This is mostly due to the fact that the friction force opposes the relative motion between the occupant and the seat.

Shown in Figure 6.16 is the predicted pressure distribution at the seat bottom when each of the seat bottom and the seat back were modeled by 20 elements and the coefficient of friction was set to 0.4. The pressure distribution profile shown in Figure 6.16 is similar to the one presented earlier in Figure 6.14. However, the maximum pressure reduces by as much as 450 Pa which is due to the lower compression in the foam in the former case (see Figure 6.15).

6.2.3 Variation of the Foam Stiffness

The effect of varying the foam stiffness on the steady state H-Point location was studied. Here the foam stiffness was varied between 0.9 to 1.3 (in steps of 0.05) times the actual stiffness estimated for low density foam 1. The vertical displacement of H-Point as the stiffness was varied is shown in Figure 6.17. It is clear that as the foam becomes stiffer, the total displacement of the H-point decreases, see the black curve. Here the coefficient of friction μ is 0.35. Later in this chapter it is shown that this coefficient of friction gives the best pressure distribution prediction compared to the experimental measurements. The predicted pressure distribution between the occupant and the seat bottom and when the foam stiffness is varied is shown in Figure 6.18. It is shown that as the foam becomes stiffer (darker curves), the pressure distribution becomes smoother and the peak pressure reduces from 5000 Pa to 3500 Pa just below the H-Point.

6.2.4 Variation of the Occupant's Weight

One of the main advantages of the current seat-occupant model is that the model is at the subsystem level that can be varied. The foam model incorporated into the seat cushion model, is nonlinear and describes large strain behaviors of polyurethane foam. Incorporating such a nonlinear foam model is important as it enables the seat-occupant model to accurately predict the system responses with different occupants with different body masses and weights. Therefore, unlike some other system level seat-occupant models where the models are functions of the occupant weight, that is, different seat-occupant models are estimated depending on the occupant weight. Here, a comprehensive model can be used to describe the seat-occupant responses for a range of seats and a range of occupants. Therefore, a unique model is used to estimated the system responses even if the occupants have different weights. It is shown in Figure 6.19(a) the vertical displacement of the H-Point when the occupant's weight was varied between 0.9 to 1.5 (in steps of 0.1) of its baseline weight 60 kg. It

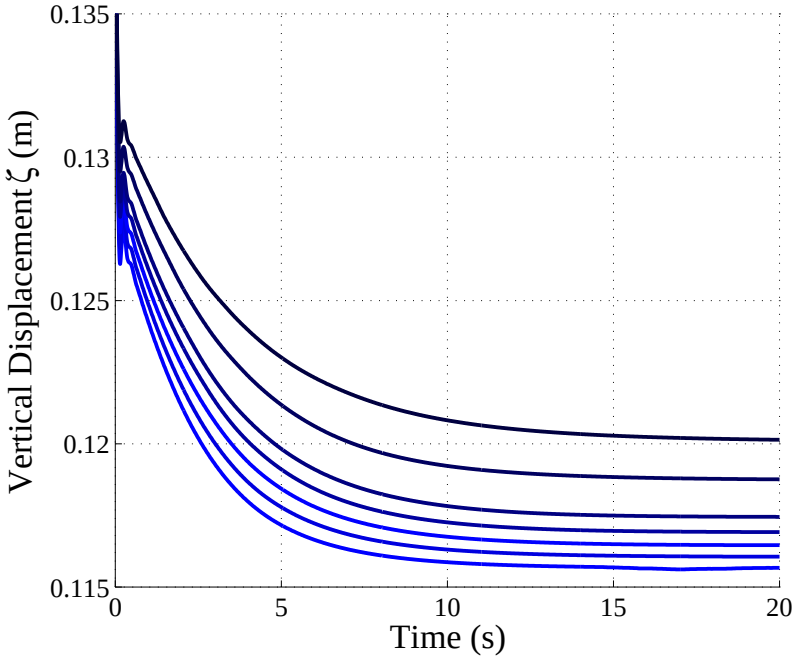

Figure 6.17. The vertical location (ζ) of the H-Point when the seat stiffness is varied between 0.9 to 1.3 times (light blue to black) the actual foam stiffness. The coefficient of friction μ is 0.35.

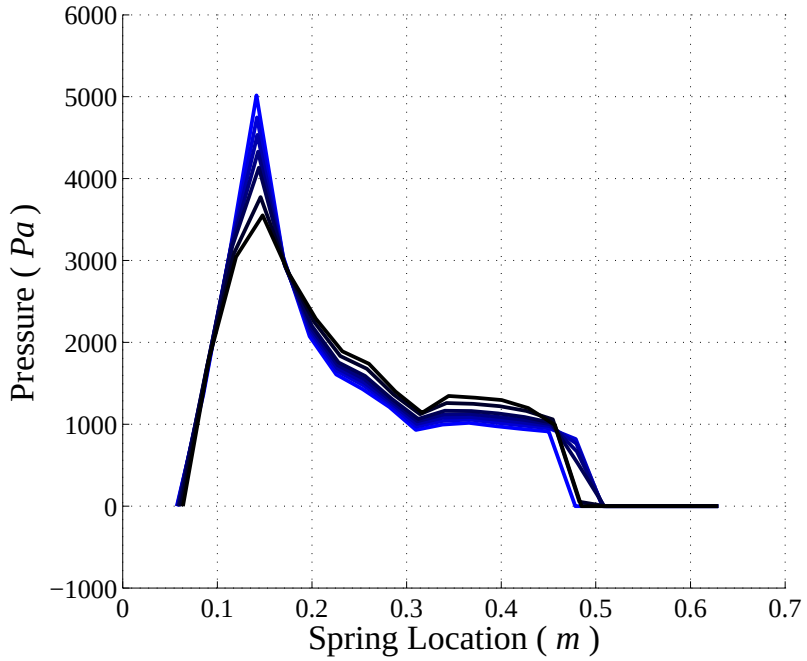

Figure 6.18. The interfacial pressure distribution at the seat bottom when the seat stiffness is varied between 0.9 to 1.3 times (light blue to black) the actual foam stiffness. The coefficient of friction μ is 0.35.

is seen that as the occupant's weight increases the total displacement of the H-point increases as well.

The percentage compression in the cushion along the seat bottom when the occupant's weight was varied is shown in Figure 6.19(b). As expected, the maximum compression in the cushion increases when the occupant becomes heavier. The final positions of different occupants with different body masses are also shown in Figure 6.20. The predicted pressure distribution between the occupant and the seat bottom when the occupant's weight was varied is shown in Figure 6.21. It is observed that the variation in the pressure distribution is smoother for lighter occupants (blue curves). However, for heavier occupants the maximum pressure increases significantly compared to the peak pressure (around 4500 Pa) for the baseline occupant.

6.2.5 Variation of the Friction at the Foot

The initial position of the foot is important factor which directly affect the predicted pressure distribution at the seat bottom. The coefficient of friction between the foot and foot rest determines the final angles of the shin, the femur and the interfacial pressure distribution. Figure 6.22 depicts the initial position and the final position of the shin and the femur center lines when the coefficient of friction between the foot and foot rest was varied. Here the initial position of the foot is shown by the dashed line. The black line is the final position of foot when the coefficient of friction $\mu_{foot} = 2.5$ and the red line is the final position of foot when the coefficient of friction $\mu_{foot} = 0.45$. Clearly the overall displacement of the foot decreases as the coefficient of friction in increased from 0.45 to 2.5. Also it is clear that the coefficient of friction affects the angle of femur: for the lower coefficient of friction, the femur angle θ_2 is larger.

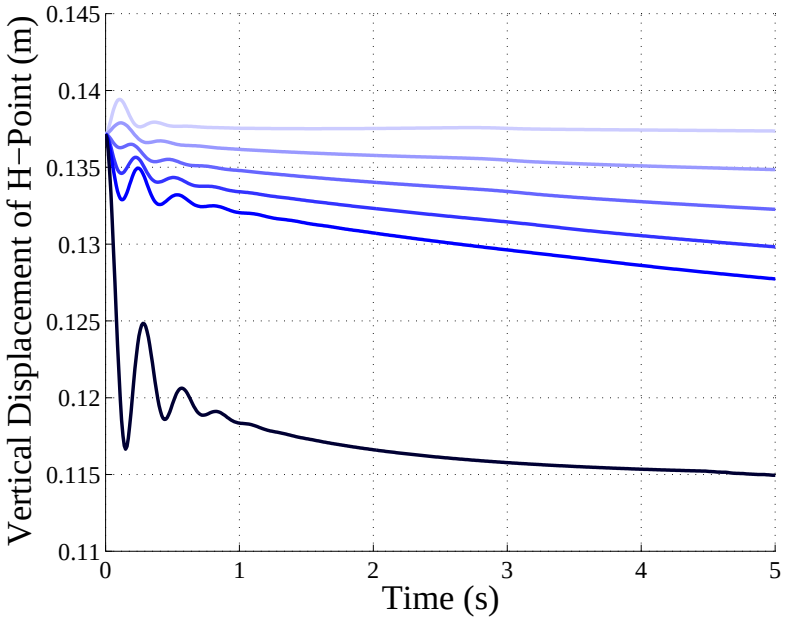

(a)

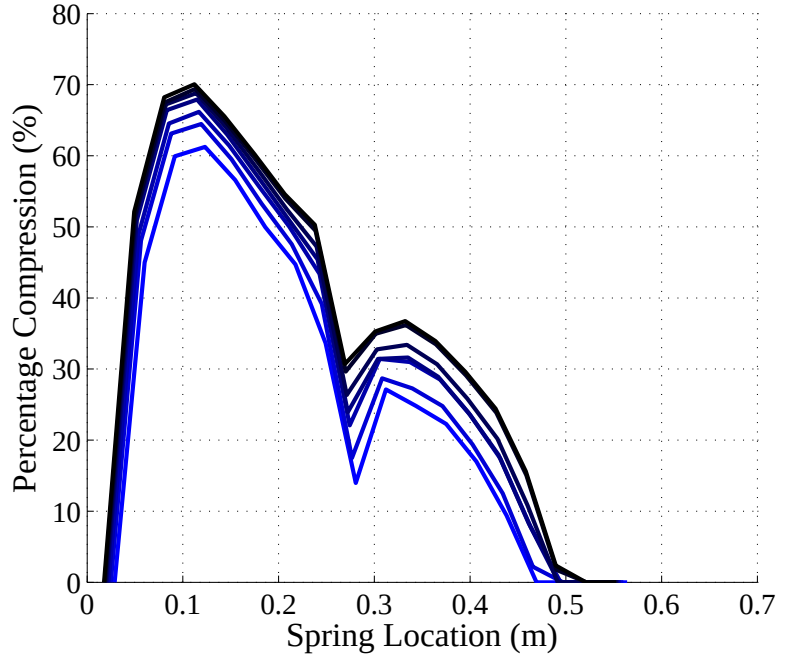

(b)

Figure 6.19. (a) The vertical location of the H-Point ζ (b) the percentage compression along the seat bottom, when the occupant's weight was varied between 0.9 to 1.5 (light black to dark black) of its baseline weight 60 kg in the steps of 0.1.

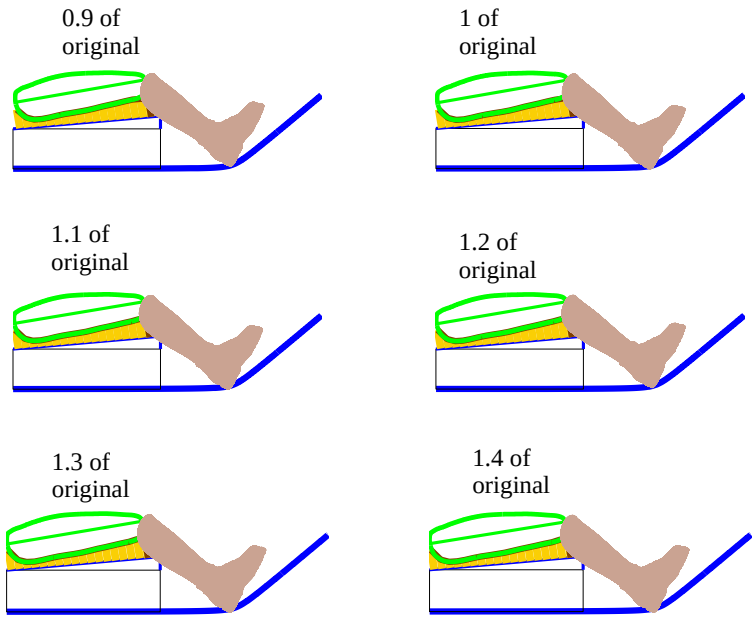

Figure 6.20. The final settling points of the occupants when the occupant's weight was varied between 0.9 to 1.5 of its baseline weight 60 kg in the steps of 0.1.

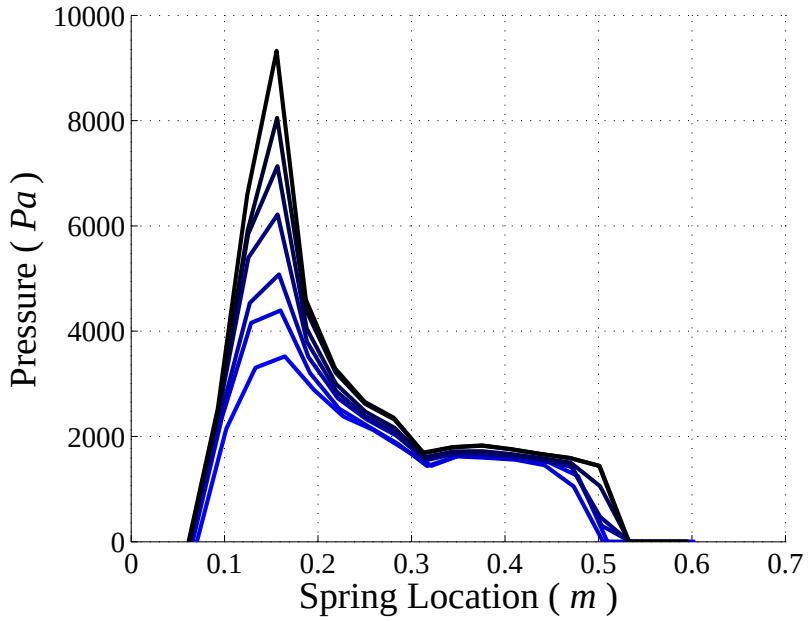

Figure 6.21. The predicted pressure distribution between the occupant and the seat at the seat bottom when the occupant's weight was varied between 0.9 to 1.5 (light black to dark black) of its baseline weight 60 kg in the steps of 0.1.

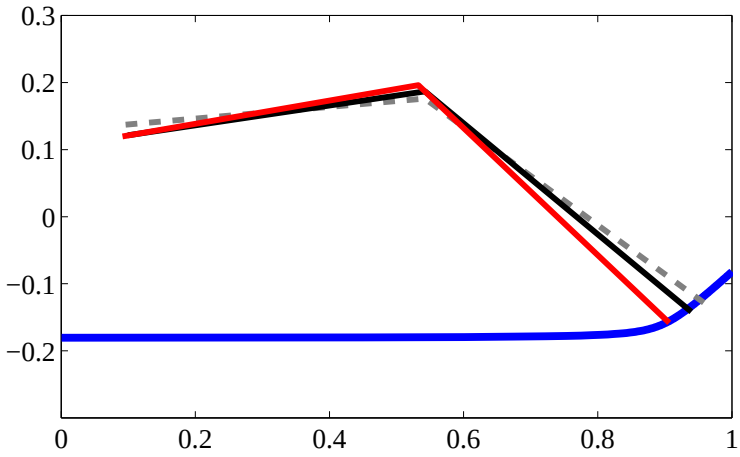

Figure 6.22. Initial position (dashed gray) and the final position of the sheen and femur, red: μ_{foot}=0.45; black: $\mu_{foot} = 2.5$ foot friction.

6.2.6 Variation of the Seat Material

A variety of foams are used in car seats. The effect of varying the seat material on the steady state H-Point location was studied. Two types of foams were incorporated in the seat-occupant system. Both foam types, foam 1 and foam 2, are low density polyurethane foams; the characteristics of these foams were described in Chapter 3. The measured experimental stress-time responses of foam 1 and foam 2 subjected to large strain compression at different rates are shown in Figure 6.23. It is clear that foam 2 is in general stiffer than foam 1. The horizontal and vertical displacements of the H-Point when the seat is made of two different foam types are shown in Figures 6.24. It is seen that the total displacement of the H-Point is smaller when the seat is made of the stiffer foam 2. Also when the seat is made of the stiffer foam 2, the transient response duration becomes longer. It is shown in Figure 6.25 the predicted pressure distribution between the occupant and the seat bottom when the seat is made of foam 1 and foam 2. It is seen that when the seat is made of the stiffer foam 2, the pressure distribution is smoother and the peak pressure decreases.

6.3 Experiments: Pressure Distribution at the Seat-Occupant Interface

The pressure distribution at the seat-occupant interface directly affects the static comfort of the seat occupant. In the present study experiments were conducted to measure the pressure distribution at the seat-occupant interface. These results help to choose a proper value for the interfacial coefficient of friction and later is used to validate the analytical results. The details regarding the experiment and the experimental results obtained are presented here. They were conducted by Ippili, Widdle and Puri [32].

6.3.1 Experimental Setup

The measurement of force distribution at the seat-occupant interface was performed using a flexible grid of closely spaced sensors. These sensors are part of a Body

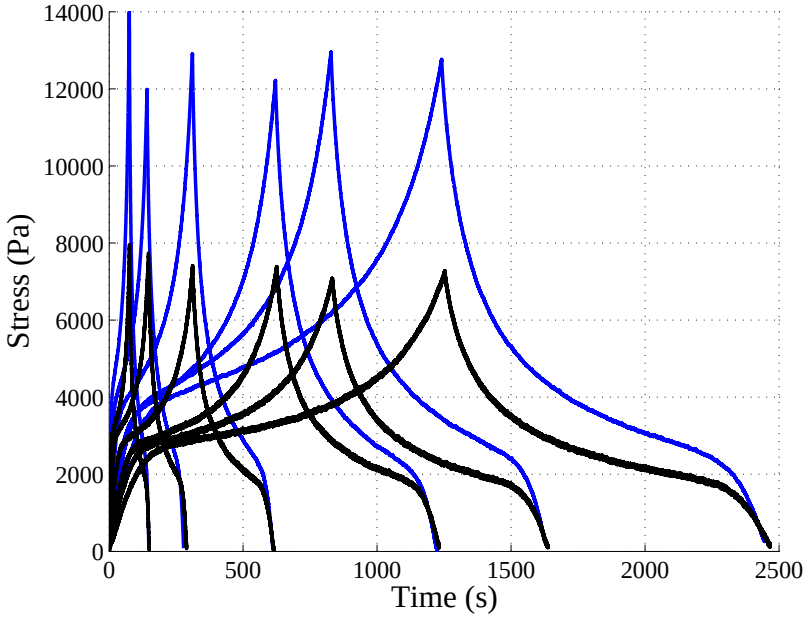

Figure 6.23. Measured stress-time responses of foam 1 (black) and foam 2 (black) for tests performed at different compression rates.

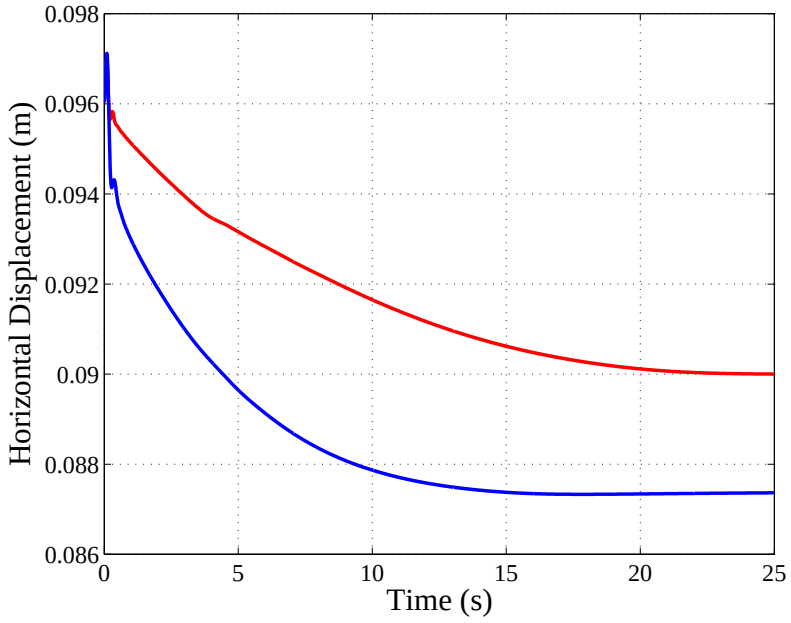

(a)

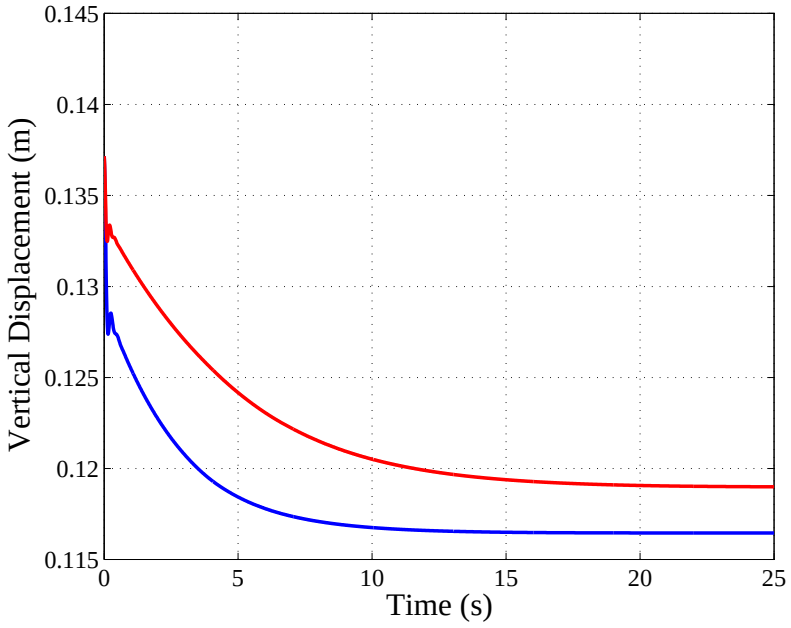

(b)

Figure 6.24. (a) the horizontal displacement of the H-Point ξ; (b) the vertical displacement of the H-Point ζ. Blue: foam 1 and red: foam 2.

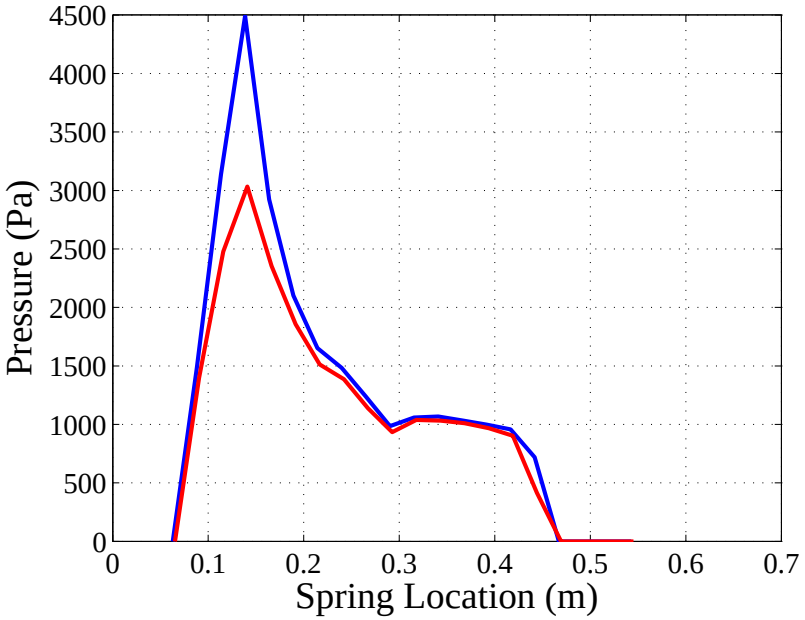

Figure 6.25. Predicted pressure distribution at the seat bottom interface. Blue: foam 1 and red: foam 2.

Pressure Measurement System (BPMS) manufactured by Tekscan (BPMSTM Body Pressure Measurement System, User Manual, Version 5.23, 2003). The output of the system is an array of force measurements.

The hardware for acquiring force data consists of an ultra thin sensor mat having a grid of 48×42 resistive sensors. The physical dimensions of this mat are 21.6 in$\times$ 19.6 in (548.64 mm$\times$ 497.84 mm). Each sensor in the grid behaves like a variable resistor. The sensor has a very high resistance when it is unloaded and its resistance decreases with increasing load. The resistance of each sensor is measured and is then converted to a digital value in the range of 0 to 255 (8 bit integer). Force measurements from the sensor mat are output in the form of a matrix having 48 rows and 42 columns. Each element in the matrix denotes the corresponding sensor in the sensor mat and has a value between 0 to 255. To calculate the actual force the sensor mat can be calibrated by loading the senor mat with standard weights. It is worth mentioning that resistive sensor mats are designed primarily for measuring the force in the vertical direction. Shear forces acting on the mat may however lead to some deformation of the sensors and this may lead to errors in the measured force.

A schematic diagram of the experimental setup for measuring force distribution at the seat-occupant interface is shown in Figure 6.26. For the present experiment two sensing mats were used. The first sensing mat was used at the bottom of the seat and is aligned so that the side having 48 sensors aligned along the length of the seat bottom. The second sensing mat was used at the back of the seat and is aligned so that the side having 42 sensors aligned along the length of the seat back. Signals from both the sensing mats are passed through the Tekscan Handle (a connector) which passes the signals to the computer for further analysis. It is worth mentioning that the odd orientation of the sensing mat used at the seat back was due to the peculiar orientation of the handle into which signals from both the sensing mats had to be input.

To measure the force distribution at the seat-occupant interface an experiment was conducted with a mannequin whose characteristics are given in Appendix E. For

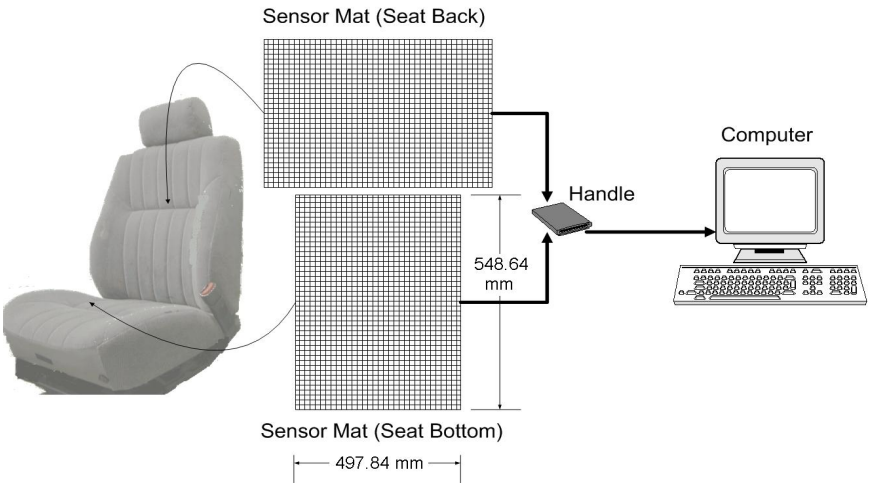

Figure 6.26. Schematic of the experimental setup for measuring force distribution at the seat-occupant interface.

reasons explained earlier (an unreliable neck joint) the head was removed for the base excitation experiments reported in the next chapter. Thus it was removed in the modeling and in this experiment. The dummy was carefully lowered onto the seat so as to minimize the effects of sudden impact forces on the seat foam. Furthermore, the dummy was placed in the seat so that it maintained a side-to-side balanced sitting posture. The dummy was allowed to settle into the seat for 60 minutes and after settling was complete the data obtained from the sensor mat at the bottom of the seat was collected. Data from the sensor mat used at the back of the seat was not analyzed in this study.

6.3.2 Experimental Results

The data obtained from the sensor mat was used to compute the pressure distribution between the occupant femur and the seat bottom. The measured pressure distribution along the length of the seat bottom (along the longitudinal direction) is shown in Figure 6.27 in red. By comparing the analytical and the experimental results it was found that the model with the coefficient of friction between the seat

and the occupant ($\mu_{interfacial}$) equal to 0.35 produced the closest match to the experiment: the peak values of the pressure at the seat bottom are very close. The maximum pressure occurs at 0.15 m which is below the final position of the H-Point. Also, the results from the analytical model show a dip at 0.3 m which is due to the presence of a seam in the seat bottom and is consistent with the results obtained from the experiment, though it is to the right of where it occurs in the experiment. However, the predicted pressure distribution after the dip is much larger than in the experimental results. This may be partially be attributed to practical difficulties in matching the initial position of the mannequin on the seat and the initial conditions in the simulation. The initial position of the foot greatly affects the pressure distribution close to the occupant knee and this was not well controlled in this experiment, unlike in the base excitation experiments described in the next chapter. In general, this requires further investigation both from measurement and modeling perspectives. However, there are qualitative similarities between the analytically computed results and the experimental results.

6.4 Chapter Summary

In this chapter the multi-body seat-occupant model introduced in Chapter 5 was used to study the dynamic responses of the seat-occupant system. The system governing equations were solved by using the numerical time integration to obtain the occupant's response. The steady-state responses were used to obtain the H-Point location and the pressure distribution at the seat-occupant interface. Variations in the H-Point location and the seat-occupant pressure distribution with changes in the seat-occupant parameters, including the number of springs in the seat back, the seat bottom, the coefficient of friction, the foam stiffness, the seat material and the occupant weight were studied. Results showed that at least 40 elements, 20 in the seat back and the seat bottom, are required to reasonably capture the response. Inclusion of more elements beyond this didn't change the predictions significantly. It was

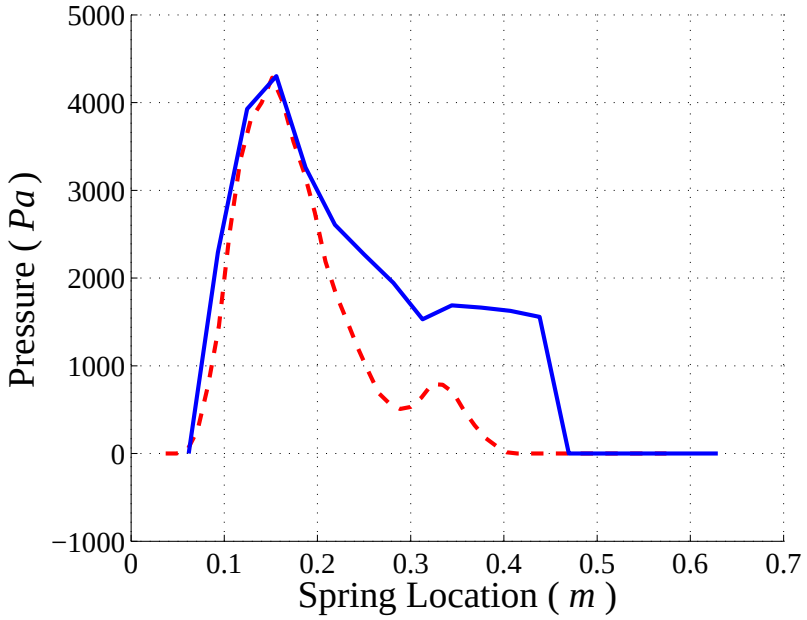

Figure 6.27. The predicted (blue line) and the measured (dashed red line) experimental pressure distribution at the seat bottom.

also observed that the coefficients of friction used to model the interfacial behavior between the occupant and the seat and the foot and the foot rest (floor pan) play a strong role in the final position of the occupant in the seat. Finally, previous experimental measurements were used to verify the predicted pressure distribution at the seat-occupant interface. It was observed that if the coefficient of friction was adjusted, the analytical and the experimental results are in qualitative agreement.

7. SEAT-OCCUPANT MODELING - STEADY-STATE RESPONSE PREDICTION

In the previous chapter, the multi-body seat-occupant model, introduced earlier in Chapter 5, was used to study the dynamic transient response of the seat-occupant system. The predicted responses were used to study how the occupant settles in a seat and to estimate a series of metrics used to evaluate static comfort and seat functionality, such as H-Point location and pressure distribution. As discussed earlier, vibration transmissibility is an important factor which is directly related to comfort perception by occupants, e.g. dynamic comfort. Earlier in Chapter 4, a single-degree-of-freedom foam-mass system which can be thought of as the simplest seat-occupant model was used to study how the harmonic vibration is transmitted from the system base to the mass. The multi-body seat occupant model can also be used to study how vibrations are transmitted to the occupant. The latter model has many advantages over the single-degree-of-freedom foam-mass model. For example, the occupant model shapes can now be predicted. To study seat transmissibility, the seat-occupant system is subjected to harmonic base excitations and the occupant response is predicted.

Joshi [47] used an earlier version of the multi-body seat-occupant model described in the previous chapters to examine the dynamic response of a seat-occupant system when it is subjected to harmonic base excitations. In her model, the cushion is replaced by a number of nonlinear viscoelastic elements represented by a foam model that is similar to Model 2 described in Chapter 3 and the foam model parameters were estimated by fitting the model to a single uniaxial compression test data at a low compression rate. Time integration of the governing equations of the seat-occupant model was used to estimate the seat-occupant steady state harmonic response. It was observed that direct time integration of the governing equations is a time-consuming process even for a relatively small frequency range and the computation time became

even more of an issue for higher levels of excitation where nonlinearities are playing a stronger role. With the increased complexity of foam Model 4 (over Model 2) and with strain-rate dependent parameters, or higher order kernels, computation time becomes an impediment to performing parameter variations studies, an important component of virtual seat design.

Incremental harmonic balance (IHB) is an alternative approach to determining the steady-state response of the seat-occupant system subjected to harmonic excitations. As shown in Chapter 4, the incremental harmonic balance method is an iterative method, based on the harmonic balance method that improves on an initial guess of the harmonic balance solution. When solving for steady-state solutions over a range of frequencies, the solution at a nearby frequency can serve as a good initial guess for the solution at the new excitation frequency, reducing the number of iterations required to obtain an accurate solution and thus speeding up computations. In the incremental harmonic balance method the steady-state response of the system is estimated directly and does not suffer from the problems of time-integration where the transient response has to die away before the steady-state response can be determined.

In this chapter, use of the incremental harmonic balance method is used to determine the steady-state behavior of the seat-occupant system subjected to vertical base excitations at different frequencies is described. The reductions in computation times over those for time-integration to obtain steady-state responses are described. Some examples of its use are given and the frequency response of the system is represented in terms of the displacement of the H-point in the horizontal and vertical direction. Effects of different factors like number of nonlinear viscoelastic elements in the seat back and the seat bottom model, the seat geometry, the seat material, the occupant's weight on the steady state responses and the estimated frequency responses are shown.

7.1 Incremental Harmonic Balance Solution of the Governing Equations

The steady-state response of the seat-occupant system subjected to base excitation is obtained by simultaneously solving the system governing equations derived in Chapter 5. The governing equations consist of a set of second-order differential equations represented by Equations given by (5.55) and the equations which represent the nonlinear viscoelastic behavior of the seat given in Chapter 5. The seat-occupant dynamic system has 6 generalized coordinates: horizontal displacement of H-Point ξ, vertical displacement of H-Point ζ, angle of torso θ_1, angle of femur θ_2, angle of shin θ_3 and the base excitation z. Assuming N_{bottom} and N_{back} nonlinear viscoelastic elements represent the seat bottom and the seat back, there are $2(N_{bottom}+N_{back})+6$ nonlinear differential equations need to be solved to obtain the system response. Note that the nonlinear viscoelastic elements are represented by foam Model 4 with strain rate-dependent viscoelastic parameters. The baseline set of parameters for this model are given in Appendices E and I.

In Chapter 4, incremental harmonic balance was used to obtain the steady-state response if a single-degree-of-freedom foam-mass system. However, here, there are more governing equations and each is more complex, e.g. if the seat is modeled by 30 elements, 66 nonlinear equations need to be solved simultaneously.

In this model, the seat-occupant motion is governed by Equation (5.55) as,

$$[A][\ddot{q}] = [D], \tag{7.1}$$

where $\ddot{q}$ is the second derivative of the system generalized coordinate vector that contains (in order): horizontal acceleration of the H-Point $\ddot{\xi}$, the vertical acceleration of the H-Point $\ddot{\zeta}$, the angular acceleration of the torso $\ddot{\theta}_1$, the angular acceleration of the femur $\ddot{\theta}_2$, and the angular acceleration of the shin $\ddot{\theta}_3$ and the base acceleration $\ddot{z}$. Matrices $[A]$ and $[D]$ are functions of the generalized coordinates and their derivative and are given in Sections 5.2 and 5.3. The time variable in Equation (7.1) is rescaled based on the frequency of the harmonic base excitation. Thus, for base excitation, $z(t) = Zsin(\omega t)$, a new variable τ is defined as $\tau = \omega t$. Therefore, derivatives with

respect to t can be updated according to the new variable, e.g. $\frac{\partial}{\partial t} = \frac{\partial}{\partial \tau}\frac{\partial \tau}{\partial t} = \omega\frac{\partial}{\partial \tau}$. Thus, Equation (7.1) become,

$$\omega^2[A][q''] = [D]. \tag{7.2}$$

where $'$ denote a derivative with respect to τ. The system variables are perturbed around a given solution:

$$\begin{aligned} [q] &:= [q] + [\Delta q], \\ [q'] &:= [q'] + [\Delta q'], \\ [q''] &:= [q''] + [\Delta q''] \\ \omega &:= \omega + \Delta\omega. \end{aligned} \tag{7.3}$$

Substituting Equation (7.3) into Equation (7.2) and linearizing around the solution $(\omega,\ q,\ ,q',\ q'')$, Equation (7.2) can be expressed as,

$$\begin{aligned} \omega^2 A q'' \ &+\ \omega^2\frac{\partial A}{\partial q}q''\Delta q + \omega^2\frac{\partial A}{\partial q'}q''\Delta q' + \omega^2\frac{\partial A}{\partial q''}q''\Delta q'' \\ +\omega^2 A\Delta q'' \ &+\ 2\omega A q''\Delta\omega - D - \frac{\partial D}{\partial q}\Delta q - \frac{\partial D}{\partial q'}\Delta q' - \frac{\partial D}{\partial q''}\Delta q'' \\ &\quad -\frac{\partial D}{\partial \omega}\Delta\omega = 0. \end{aligned} \tag{7.4}$$

Here, the vector-matrix notation is dropped and scalars and vectors are recognized based on context. Noting that matrix A is just a function of q and vector D is just functions of q and q',

$$\begin{aligned} \frac{\partial A}{\partial q'} &= 0, \\ \frac{\partial A}{\partial q''} &= 0, \\ \frac{\partial D}{\partial q''} &= 0. \end{aligned} \tag{7.5}$$

Then, Equation (7.4) can be simplified as,

$$\begin{aligned} &\omega^2 A\Delta q'' - \frac{\partial D}{\partial q'}\Delta q' + \left[\omega^2\frac{\partial A}{\partial q}q'' - \frac{\partial D}{\partial q}\right]\Delta q - \left[\frac{\partial D}{\partial \omega} - \right. = 0, \\ &\left. 2\omega A q''\right]\Delta\omega + \omega^2 A q'' - D = 0. \end{aligned} \tag{7.6}$$

and this equation can simply be expressed as,

$$[M(q)]\,[\Delta q'']+[c(q,q')]\,[\Delta q']+[K(q,q',q'')]\,[\Delta q]+\Omega\Delta\omega+[R]=0. \tag{7.7}$$

In Equation (7.7), R is the error term that goes to zero as q converges to the actual solution. If the base excitation is periodic, the steady-state responses are periodic with period 2π and the j^{th} term of q and Δq can be approximated by the following NT-term harmonic expansion,

$$\begin{aligned} q_j &= a_{j,0}+\sum_{l=1}^{NT}[a_{j,l}cos(l\tau)+b_{j,l}sin(l\tau)], \\ \Delta q_j &= \Delta a_{j,0}+\sum_{l=1}^{NT}[\Delta a_{j,l}cos(l\tau)+\Delta b_{j,l}sin(l\tau)], \end{aligned} \tag{7.8}$$

where $\Delta a_{i,j}$ and $\Delta b_{i,j}$ are unknown and need to be identified. Remembering that $[\mu]$, $[c]$ and $[K]$ in Equation (7.7) are matrices, by substituting Equation (7.8) into equation (7.7), the p^{th} row of $[\mu]$, $[c]$ and $[K]$ can be expressed as

$$\begin{aligned} -\mu_{p,j}[\sum_{l=1}^{NT}[\Delta a_{j,l}l^2cos(l\tau)+\Delta b_{j,l}l^2sin(l\tau)]] \\ +c_{p,j}[\sum_{l=1}^{NT}[-\Delta a_{j,l}lsin(l\tau)+\Delta b_{j,l}lcos(l\tau)]] \\ +K_{p,j}[\Delta a_{j,0}+\sum_{l=1}^{NT}[\Delta a_{j,l}cos(l\tau)+\Delta b_{j,l}sin(l\tau)]] \\ +\Omega_p\Delta\omega+R_p=0. \end{aligned} \tag{7.9}$$

Applying Galerkin's method,

$$\begin{aligned} \int_0^{2\pi}[-\mu_{p,j}[\sum_{l=1}^{NT}[\Delta a_{j,l}l^2cos(l\tau)+\Delta b_{j,l}l^2sin(l\tau)]] \\ +c_{p,j}[\sum_{l=1}^{NT}[-\Delta a_{j,l}lsin(l\tau)+\Delta b_{j,l}lcos(l\tau)]] \\ +K_{p,j}[\Delta a_{j,0}+\sum_{l=1}^{NT}[\Delta a_{j,l}cos(l\tau)+\Delta b_{j,l}sin(l\tau)]] \\ +\Omega_p\Delta\omega+R_p]Xd\tau=0, \end{aligned} \tag{7.10}$$

where

$$[X] = [1, cos(\tau), \cdots, cos(NT\tau), sin(\tau), \cdots, sin(NT\tau)]^T. \tag{7.11}$$

Note that the result of the integral given by Equation (7.10) is a $NT \times 1$ vector. The h^{th} row of Equation (7.10) is

$$\int_0^{2\pi} [A^0_{p,j,h}\Delta a_{j,0} + \sum_{l=1}^{NT}[A^{(lc)}_{p,j,h}\Delta a_{j,l} + A^{(ls)}_{p,j,h}\Delta b_{j,l}] + B_{p,h}\Delta\omega + R_{p,h}]d\tau = 0, \tag{7.12}$$

where

$$\begin{aligned} A^{(0)}_{p,j,h} &= K_{p,j}X_h, \\ A^{(lc)}_{p,j,h} &= [-\mu_{p,j}l^2 cos(l\tau) - c_{p,j}lsin(l\tau) + K_{p,j}cos(l\tau)]X_h, \\ A^{(ls)}_{p,j,h} &= [-\mu_{p,j}l^2 sin(l\tau) + c_{p,j}lcos(l\tau) + K_{p,j}sin(l\tau)]X_h, \\ B_{p,h} &= \Omega_p X_h, \\ P_{p,h} &= R_p X_h. \end{aligned} \tag{7.13}$$

$A^{(0)}_{p,j,h}$, $A^{(lc)}_{p,j,h}$, $A^{(ls)}_{p,j,h}$, $B_{p,h}$ and $P_{p,h}$ are periodic because $\mu_{p,j}$, $c_{p,j}$, $K_{p,j}$ and $R_{p,j}$ are functions of $[q]$ and $[q']$ which are harmonic. Therefore, $A^{(0)}_{p,j,h}$, $A^{(lc)}_{p,j,h}$, $A^{(ls)}_{p,j,h}$, $B_{p,h}$ and $P_{p,h}$ can be expressed as harmonic expansions. Integrating Equation (7.12) over one period, it is clear that all terms are zero except the constant terms of the harmonic expansion of this integrand. Therefore,

$$C^{(0)}_{p,j,h}\Delta a_{j,0} + \sum_{l=1}^{NT}[C^{(lc)}_{p,j,h}\Delta a_{j,l} + C^{(ls)}_{p,j,h}\Delta b_{j,l}] + C^{(\omega)}_{p,j,h}\Delta\omega + C^{(R)}_{p,j,h} = 0, \tag{7.14}$$

where $C^{(0)}_{p,j,h}$, $C^{(lc)}_{p,j,h}$, $C^{(ls)}_{p,j,h}$, $C^{(\omega)}_{p,j,h}$, $C^{(R)}_{p,j,h}$ are the constant terms and can be estimated by using a Fourier Series analysis of each of $A^{(0)}_{p,j,h}$, $A^{(lc)}_{p,j,h}$, $A^{(ls)}_{p,j,h}$, $B_{p,h}$ and $P_{p,h}$. Finally, Equation (7.14) can be expressed in matrix form as

$$[\Pi]\Delta V + [\Phi]\Delta\omega + [\Psi] = 0, \tag{7.15}$$

where $\Delta V = [\Delta a_{i,j}, \Delta b_{i,j}]^T$. If the excitation is at a single frequency (i.e. $\Delta\omega = 0$), this equation can be solved iteratively by using the Newton-Raphson method. If

a solution path is of interest, Equation (7.15) can be augmented by coupling the solution with an arc-length continuation method to track the solution path. This is done by introducing a path parameter (η), and defining,

$$g(\nu) - \eta = 0, \tag{7.16}$$

where $\nu = [V, \omega]$ [101]. $g = \nu^T \nu$ is often used which is related to the length of the arc of the solution path. Perturbing η as $\eta + \Delta\eta$ and linearizing Equation (7.16) about the η, yields,

$$\frac{\partial g}{\partial V}\Delta V + \frac{\partial g}{\partial \omega}\Delta\omega - \Delta\eta + g - \eta = 0. \tag{7.17}$$

Note that η is the distance along the solution path and $\Delta\eta$ determines the position of the next point on the solution path that needs to be calculated. This equation is combined with Equation (7.15), $\Delta\eta$ is specified and $\Delta\omega$ and ΔV are solved for simultaneously. When solutions for a range of frequencies are required, the solution to the linearized system is used as an initial guess for the first solution. This solution at the starting frequency is then used as an initial guess for the next point which should be close to the previous point. The process is repeated until the full solution path is obtained.

In the next section, the incremental harmonic balance method will be applied to the equations derived for the seat-occupant system.

7.2 Results

In this section the incremental harmonic balance method is applied to determine the steady-state response of the seat-occupant system when subjected to harmonic base excitation.

The time responses of the horizontal and the vertical displacement of the H-Point of the seat-occupant system when it is subjected to 0.01 g base acceleration at 10 Hz are shown in Figures 7.1(a) and 7.1(b). The blue line solution was generated via time integration (ode45 in MatLab with a step size of 0.001 *seconds*) and the dashed

red line is the harmonic balance steady-state solution. It is observed that for the responses obtained by time integration, it takes almost 5 s until the system reaches its steady state. However, after the responses reach the steady state, the predicted responses from time integration (blue) and incremental harmonic balance (dashed red) are almost identical. Also it is observed that as the input base acceleration is in the vertical direction, the amplitude of the vertical displacement of H-Point is much greater than the amplitude of the estimated horizontal response of the H-Point.

The incremental harmonic balance method can also be applied to obtain the response amplitude (and phase) for a range of frequencies of excitation. Here, this type of plot is referred to as the frequency response of the seat-occupant system. The response at the excitation frequency or multiples of the excitation frequencies (harmonics) may be plotted. The frequency response of the seat-occupant system is represented by the amplitude of the horizontal and vertical H-Point response. Here thirty harmonics ($NT = 30$) are assumed in the solutions and, unless stated otherwise, the first harmonic amplitude (the magnitude of the response at the base excitation frequency) is plotted. The harmonic amplitudes are calculated by using:

$$H_{j,n} = (a_{j,n}^2 + b_{j,n}^2)^{\frac{1}{2}}, \tag{7.18}$$

where $H_{j,n}$ is the n^{th} harmonic and $a_{j,n}$ and $b_{j,n}$ are given in Equation (7.8). For lower level base excitation levels, it is likely that higher harmonics will play only a very small role in the solution and only the first harmonic is significant. However, to be consistent with the solution approach at higher excitations levels, higher harmonics are still included in the solution here.

Vertical base excitations of accelerations 0.1 g are applied to the seat rail and the magnitude of the frequency response of the vertical and horizontal displacements of the H-Point at the frequency of excitation are shown Figure 7.2. The vertical displacement steady-state responses were also determined using time-integration at a few frequencies and are shown by black circles along with the incremental harmonic balance. In Figure 7.2, it can be seen that the resonances in the two directions are located at slightly different frequencies: 7.6 Hz and 7.3 Hz for vertical and horizontal

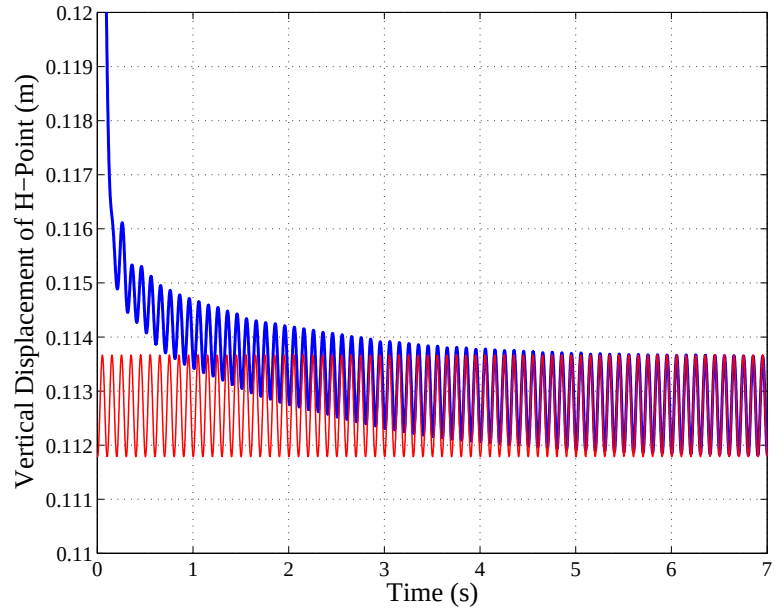

(a)

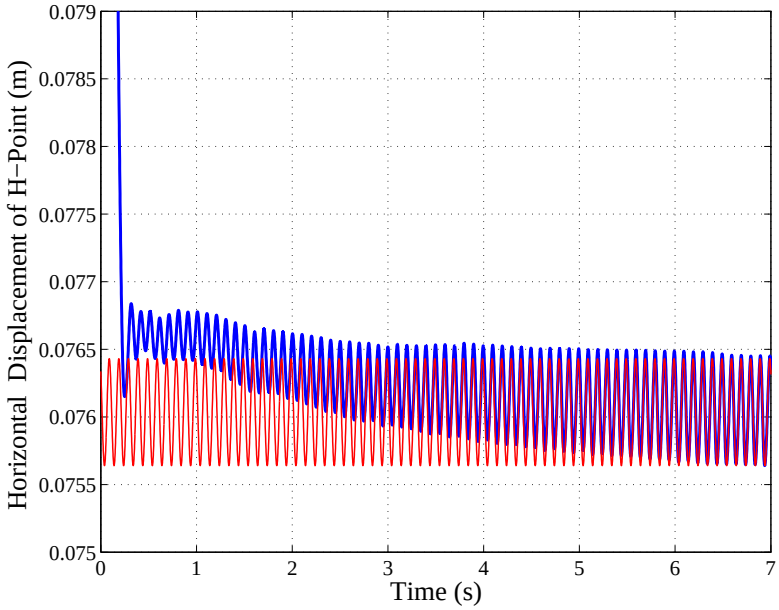

(b)

Figure 7.1. The vertical and the horizontal responses of the H-Point. (a) Vertical response and (b) horizontal response. Base acceleration is 0.01 g at 10 Hz. Blue: estimated response from time integration and red: estimated response from incremental harmonic balance.

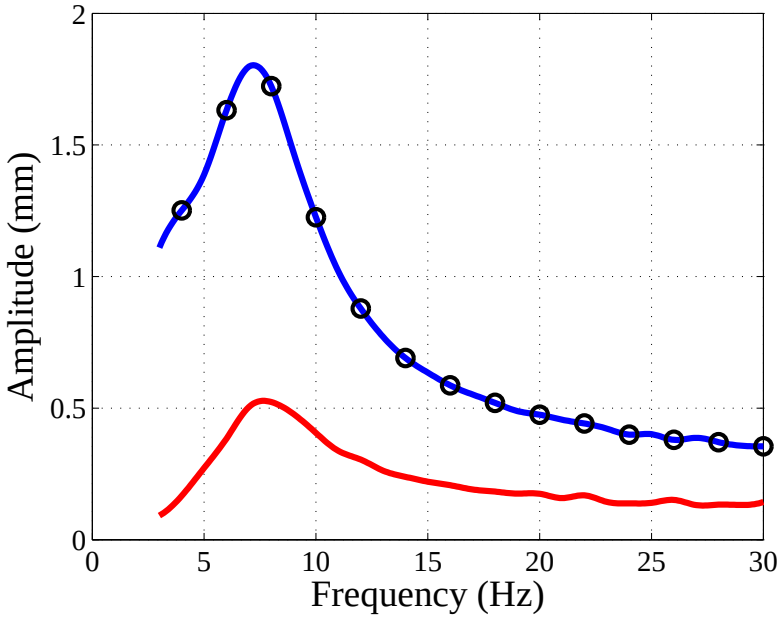

Figure 7.2. Frequency response of the model subjected to 0.1 g vertical base excitation; blue line is the vertical displacement of H-Point, red line is the horizontal displacement of H-Point and black dots are the results from time integration.

displacement of the hip joint, respectively. The results shown are in good agreement with the steady-state responses obtained by direct-time integration of the governing equations (black dots). When comparing the estimated frequency response with the experimental frequency response measured by White [106], it is observed that the model prediction of the resonance frequency (peak frequency at 7.6 Hz) matches the experimental measurements (peak frequency at 7.8 Hz).

The deflection shapes of the occupant at three different frequencies (4, 8 and 20 Hz) for 0.1 g base accelerations are shown in Figures 7.3(a), 7.3(b) and 7.3(c), respectively. The deflection shape at 4 Hz and 0.01 g base acceleration is seen to contain mainly vertical motion (bounce mode) (Figure 7.3(a)). The torso, hip, knee and foot have an almost entirely vertical motion, with the hip and knee having maximum displacement. Also it is observed that the femur has a vertical motion too. The occupant's torso also slides along the seat back.

The deflection shape at 8 Hz and 0.1 g base acceleration is seen to contain mainly vertical motion (bounce mode) (Figure 7.3(b)). Note that this frequency is very close to the resonance frequency observed in Figure 7.2. The torso, hip, knee and foot have an almost entirely vertical motion, with the hip having maximum displacement. It is observed that the femur has a vertical motion as well as a pitch mode. The occupant's torso also slides along the seat back.

The deflection shape at 20 Hz and 0.01 g base acceleration is seen to contain combination of vertical and horizontal motions (bounce and fort-and-aft modes). Note that this frequency is well above the resonance frequency observed in Figure L.3. Here the torso and foot have an almost entirely vertical motion. However, the hip has both vertical and horizontal motion. Although the vertical motion is more dominant. It is observed that the femur has a much stronger rotation than at the other two frequencies. Also, unlike the previous two cases, the motion of the torso is mostly normal to the seat back.

In Table 7.1 is shown the CPU time used to obtain solutions by the incremental harmonic balance and by direct-time integration. Results are reported for the base

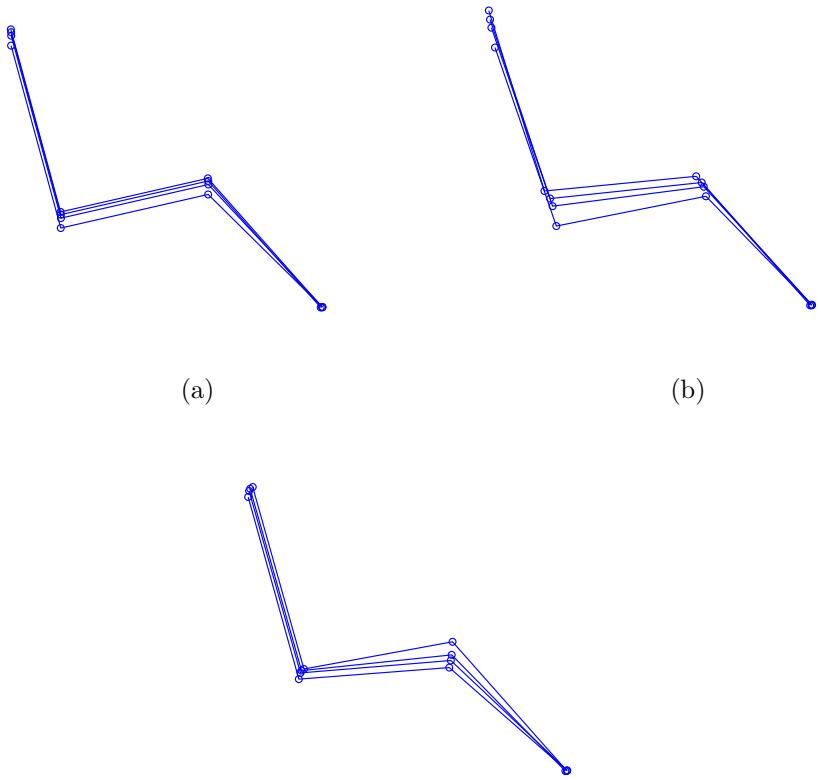

(a) (b)

(c)

Figure 7.3. Deflection shapes of the occupant at (a) 4 Hz, (b) 8 Hz, and (c) 20 Hz for 0.1 g base acceleration (times 50). Deflections are magnified 50 times in (a) and (b) and by 150 times in (c) for clear observation.

acceleration $0.1g$ for a single base excitation frequency, 8 Hz. The CPU time used to generate the complete response curve (300 frequency points) is also reported as well. It is clearly shown that application of incremental harmonic balance saves a significant amount of computational time compared to time taken to do direct-time integration. This facilitates detailed exploration of the behavior of different models and how the characteristics of different components in the model affect the system response. Such detailed explorations are needed to improve the seat-occupant models and also to optimize seat design.

Table 7.1. CPU time used by incremental harmonic balance and direct time integration of the seat-occupant model governing equations for 0.1 g base acceleration.

Excitation Frequency	Incremental Harmonic Balance	Direct Time Integration
8 Hz	20 *seconds*	500 *seconds*
Complete Path (300 pts)	1000 *seconds*	40 hr

7.3 Variation of the Model Parameters

The dynamic comfort of a car seat occupant is affected by many factors. Metrics like the Seat-to-Head-Transmissibility metric [48] are functions of the response acceleration of the occupant over a range of low frequencies, thus the frequency response of the occupant is an important characteristic affecting dynamic comfort. In this

section, the effects of variation in different seat-occupant system model parameters on the system's frequency response are shown.

7.3.1 Variation in the Number of Elements

The variation in the frequency responses of the horizontal and the vertical displacement of the occupant H-Point at the excitation frequency with different values of N_{back} and N_{bottom} was studied and the results are shown in Figure 7.4. Here the seat-occupant system is subjected to 0.05 g vertical base excitation and all the parameters are set to their baseline values and the foam parameters are scaled where needed by the number of elements used. The frequency responses are obtained by solving the governing equations using the incremental harmonic balance method. It is assumed that the number of elements at the seat back N_{back} and the seat bottom N_{bottom} are equal. The number of elements at the seat back N_{back} and the seat bottom N_{bottom} were chosen to be 30, 50 and 60 elements.

It can be seen from Figure 7.4 that the estimated frequency responses are not strongly dependent on the number of elements used at the bottom and back. However, it should be noted there is convergence problems when there are less than 12 elements in the seat back and the seat bottom. Especially, it is observed that the frequency responses of the horizontal displacement of the seat-occupant model are not very sensitive to the number of elements. By increasing the number of elements from 30 to 60, the frequency responses of the horizontal displacement of the model slightly move to the left by 7%.

7.3.2 Variation in the Level of Base Acceleration

The variation in the frequency responses, at the frequencies of excitation, of the horizontal and the vertical displacement of the occupant H-Point with different levels of the base acceleration was studied and the results are shown in Figures 7.5 to 7.9. Note that the response amplitude is normalized by the excitation acceleration. Here

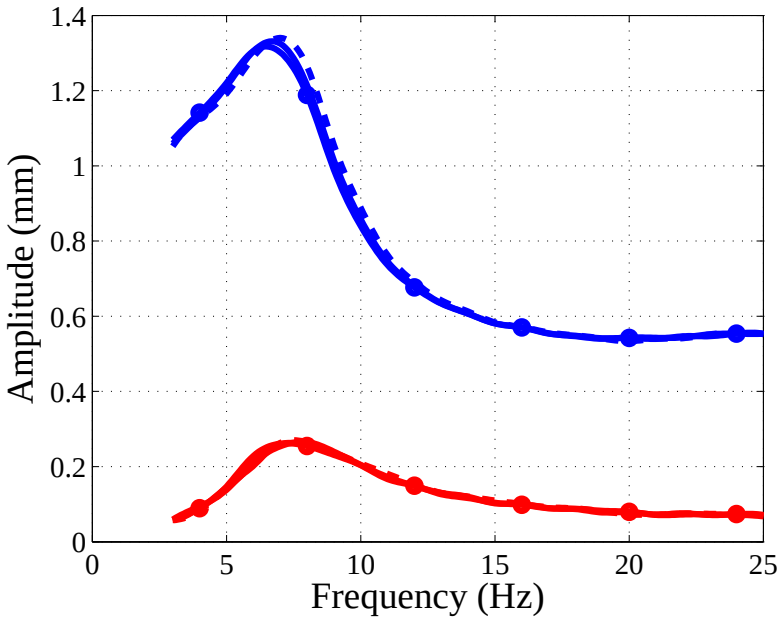

Figure 7.4. Frequency response of the occupant's H-point at the excitation frequency. The system was subjected to 0.05 g vertical base (seat rail) excitation. The blue line is the vertical displacement of H-Point, and the red line is the horizontal displacement of H-Point. Solid line (circle marker): 30 elements in the seat back and the seat bottom ($N_{back} = N_{bottom} = 15$), solid line: 50 elements in the seat back and the seat bottom ($N_{back} = N_{bottom} = 25$) and dashed line: 60 elements in the seat back and the seat bottom ($N_{back} = N_{bottom} = 30$).

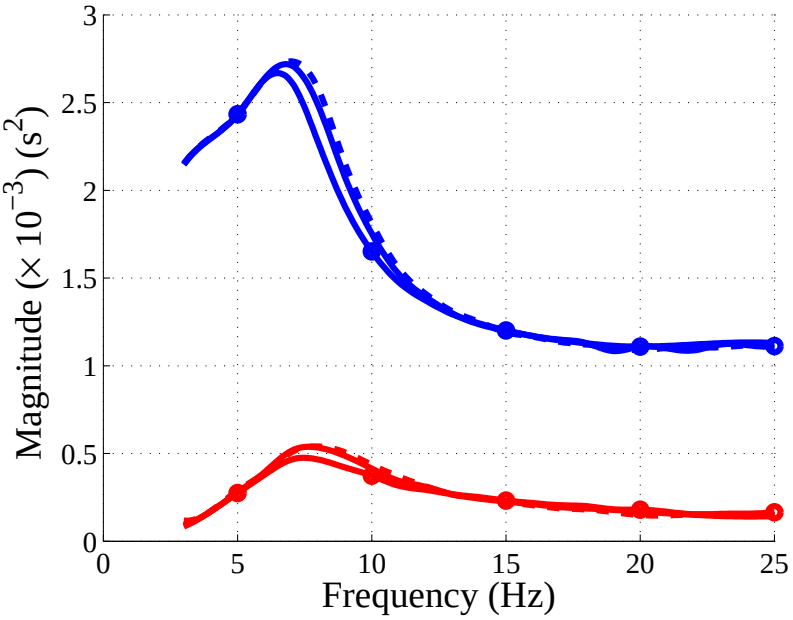

Figure 7.5. Magnitude of the frequency response normalized by the input base excitation. Solid line (circle marker): base excitation 0.2 g, solid line: base excitation 0.1 g and dashed line: base excitation 0.05 g. Blue line is the vertical displacement of H-Point, red line is the horizontal displacement of H-Point. 30 elements in the seat back and the seat bottom ($N_{back} = N_{bottom} = 15$).

the seat back and the seat bottom are represented by 30 elements, i.e. $N_{back} = N_{bottom} = 15$ and the other variables are set to the baseline values. The frequency responses shown in Figure 7.5 are obtained by solving the governing equations using the incremental harmonic balance. The base acceleration was varied between 0.05 g, 0.1 g and 0.2 g.

The normalized frequency response amplitudes at the two lowest base accelerations are very similar, and the responses at harmonics of the excitation frequencies (not shown) were very small, thus it is concluded that the system behavior is almost linear at these excitation levels. However, as the base acceleration was increased to 0.2 g, the normalized frequency response changes and the responses at harmonics of the excitation frequencies are larger, both providing evidence that the system is

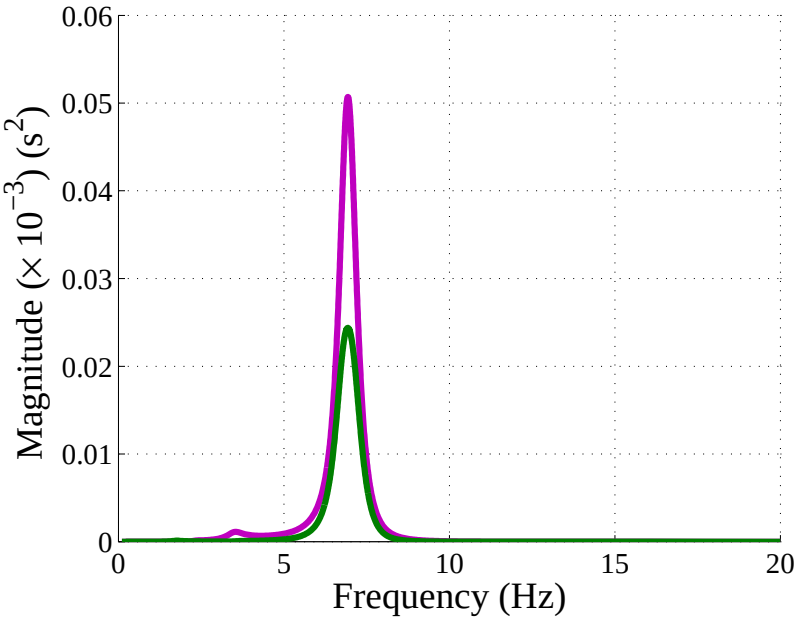

Figure 7.6. The magnitude of the responses at the second and the third harmonics of the excitation frequencies normalized by the input base excitation when system is subjected to a 0.2 g vertical base excitation. Purple: second harmonic, and green: third harmonic.

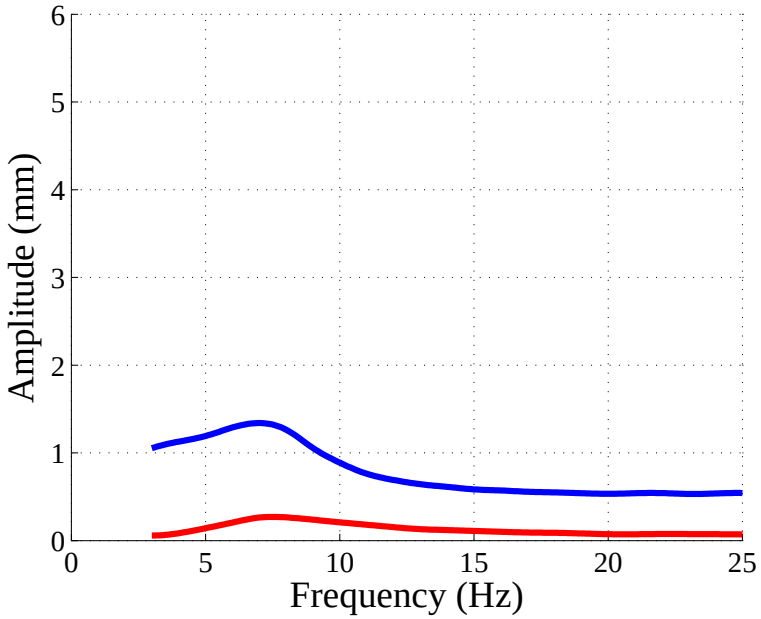

Figure 7.7. Frequency response of the model, at the excitation frequencies, when system is subjected to a 0.05 g vertical base excitation; blue line is the vertical displacement of H-Point, red line is the horizontal displacement of H-Point. 30 elements in the seat back and the seat bottom ($N_{back} = N_{bottom} = 15$).

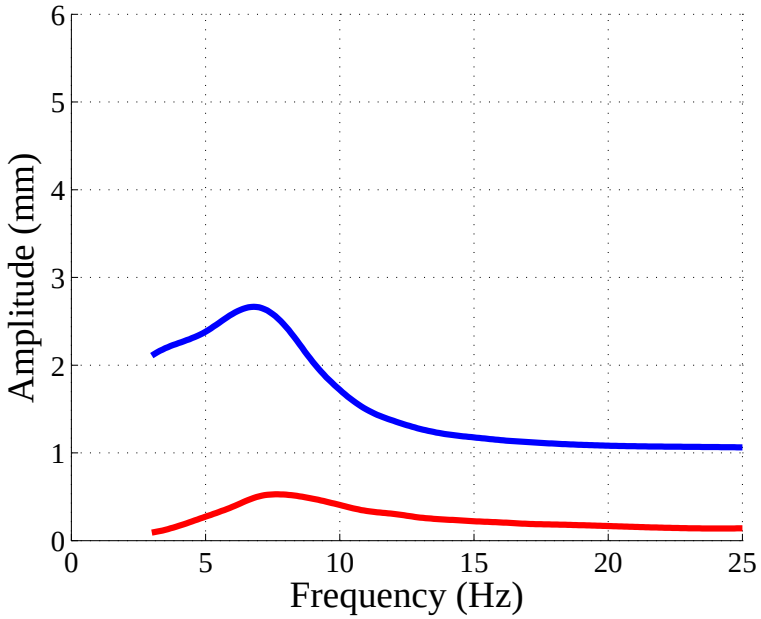

Figure 7.8. Frequency response of the model, at the excitation frequencies, when system is subjected to a 0.1 g vertical base excitation; blue line is the vertical displacement of H-Point, red line is the horizontal displacement of H-Point. 30 elements in the seat back and the seat bottom ($N_{back} = N_{bottom} = 15$).

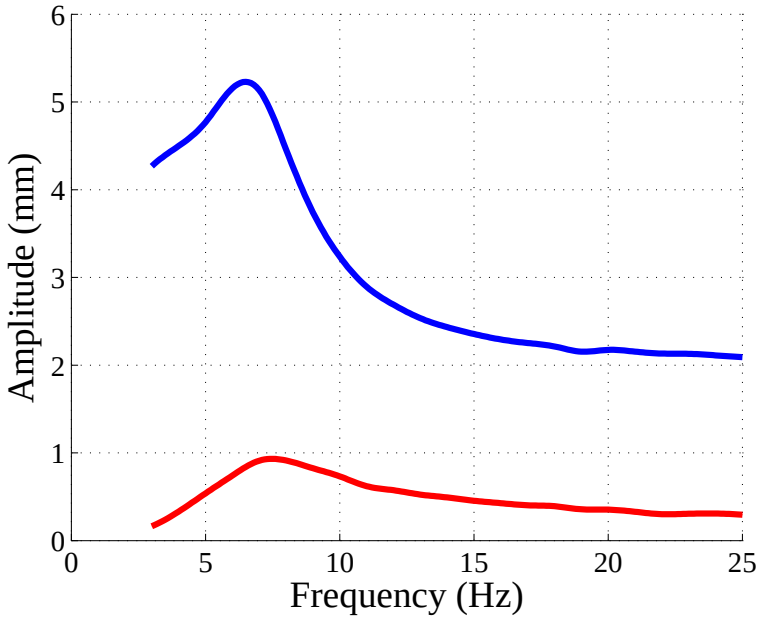

Figure 7.9. Frequency response of the model, at the excitation frequencies, when system is subjected to a 0.2 g vertical base excitation; blue line is the vertical displacement of H-Point, red line is the horizontal displacement of H-Point. 30 elements in the seat back and the seat bottom ($N_{back} = N_{bottom} = 15$).

behaving nonlinearly at this excitation level. The responses at the second and the third harmonics of the excitation frequencies when the base acceleration is 0.2 g are also shown in Figure 7.6. The responses at higher harmonics were small.

The corresponding predicted response amplitudes at the frequencies of excitation (i.e., not normalized responses) are shown in Figures 7.7, 7.8 and 7.9, respectively. It is seen that as the base acceleration is increased, the amplitude of the estimated frequency responses increase as well.

7.3.3 Variation of the Angle of Seat Back

The variation in the frequency responses of the horizontal and the vertical displacement of the occupant H-Point with different seat back angles was studied and the results are shown in Figure 7.10. Here the seat back and the seat bottom are represented by 30 elements, i.e. $N_{back} = N_{bottom} = 15$. The frequency responses are obtained by solving the governing equations using the incremental harmonic balance. The base acceleration was set to 0.05 g.

The estimated frequency responses for three seat back angles 100^o, 105^o and 110^o are shown in Figure 7.10. Note that in the baseline seat-occupant model the seat back angle is 110^o. It is seen that as the seat back angle is increased from 100^o to 110^o, the amplitude of the estimated frequency responses of the horizontal displacement remain almost constant with an exception of the frequency response of the horizontal displacement of the H-Point when the angle is 100^o. However, as the seat back angle is decreased, the amplitude of the estimated frequency responses of the vertical displacement increases. Also the resonance frequency of the system slightly increases (by almost 15%) as the seat back angle is decreased.

7.3.4 Variation of the Occupant's Weight

As mentioned earlier, one of the main advantages of the current seat-occupant model is that the model consists of models of sub-systems that have a direct phys-

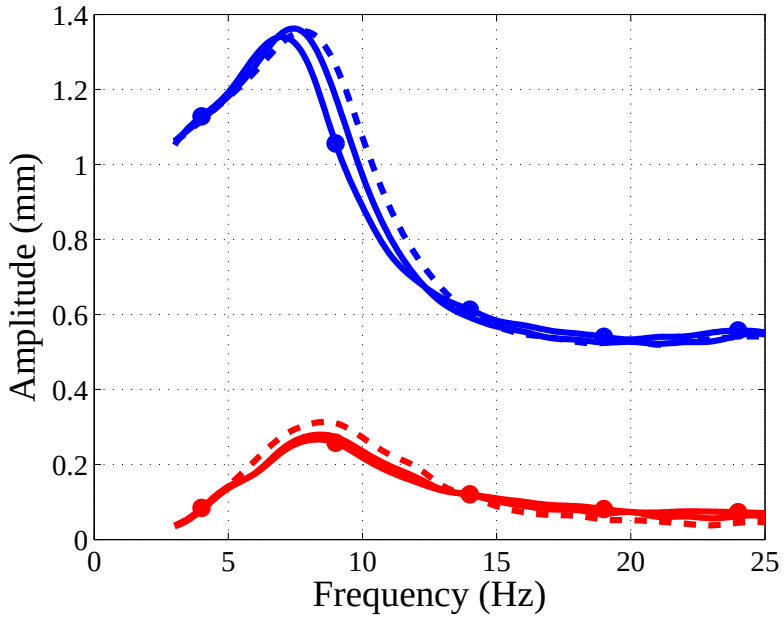

Figure 7.10. Frequency response of the model, at the excitation frequencies, subjected to 0.05 g vertical base excitation. Blue line is the vertical displacement of H-Point, red line is the horizontal displacement of H-Point. Solid line (circle marker): seat back angle $\theta_s = 110^o$, solid line: seat back angle $\theta_s = 105^o$ and dashed line: seat back angle $\theta_s = 100^o$. 30 elements in the seat back and the seat bottom ($N_{back} = N_{bottom} = 15$).

ical relationship to the seat-occupant system components. The foam model, i.e. seat cushion model, is nonlinear and capable of describing large strain behaviors of polyurethane foam. Incorporating such a nonlinear foam model is important as it enables the seat-occupant model to accurately predict the system responses with different occupants of different body masses and weights. Therefore, unlike some other system level seat-occupant models where the models are functions of the occupant weight, e.g. different seat-occupant models are estimated depending on the occupant weight, here, a comprehensive model describes the seat-occupant responses, even if the occupants have different weights. The variation in the frequency responses of the horizontal and the vertical displacement of the H-Point of different occupants with different body masses was studied and the results are shown in Figure 7.11. Here the seat back and the seat bottom are represented by 30 elements, i.e. $N_{back} = N_{bottom} = 15$. The frequency responses are obtained by solving the governing equations using the incremental harmonic balance. Also the base acceleration was set to 0.05 g. The baseline model parameters were used except for the weight which was varied from its baseline value of 60 Kg.

The predicted frequency response magnitudes (magnitude of the responses at the excitation frequencies) when the occupant weight was varied between 45 kg and 60 kg (all three bodies scaled equally) are shown in Figure 7.11. As the occupant weight is decreased from 60 Kg the maximum amplitude of the estimated frequency response decreases as does the location of the maximum amplitude in the frequency response (goes from 7.5 Hz to 6 Hz). This decreases in resonance frequency with a decrease in mass may seem counter intuitive until the changing stiffness with foam compression under the occupant H-Point is considered. With the heavier occupant, the foam under the H-Point is compressed so that it is in Region III of the stress-strain curve shown in Figure 3.2 in Chapter 3, and the foam is much stiffer than it is in Region II.

For the lighter occupants, the foam under the H-point location is much softer because the foam is now in Region II of the stress-strain curve, thus leading to the decrease in resonance frequency associated with the up-and-down, bounce mode of the

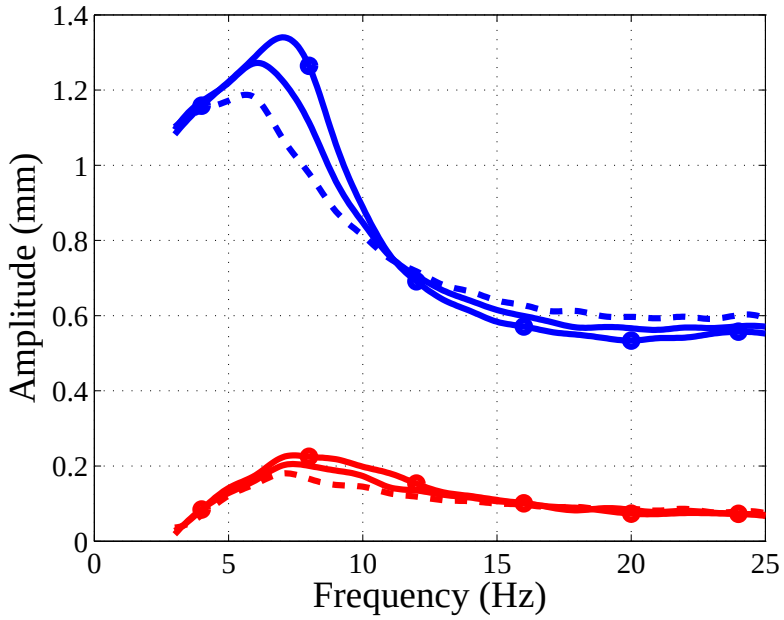

Figure 7.11. Frequency response of the model subjected to 0.05 g vertical base excitation. Blue line is the vertical displacement of H-Point, red line is the horizontal displacement of H-Point. Solid line (circle marker): 60 kg occupant, solid line: 55 kg occupant and dashed line: 45 kg occupant. 30 elements in the seat back and the seat bottom ($N_{back} = N_{bottom} = 15$).

occupant, the dominant feature in the frequency response curves. Similar behavior was observed before in [80].

7.3.5 Variation of the Seat Material

Car seats can be made of different types of polyurethane foams. The effects of varying the seat material on the frequency responses of the H-Point displacement, predicted by using incremental harmonic balance were investigated. Two types of foams were examined. Both foam types, Foam 1 and Foam 2, are low density polyurethane foams which are described in Chapter 3, where the influence of the foam properties on the foam-mass system response is shown. Foam 1 is the baseline foam used in

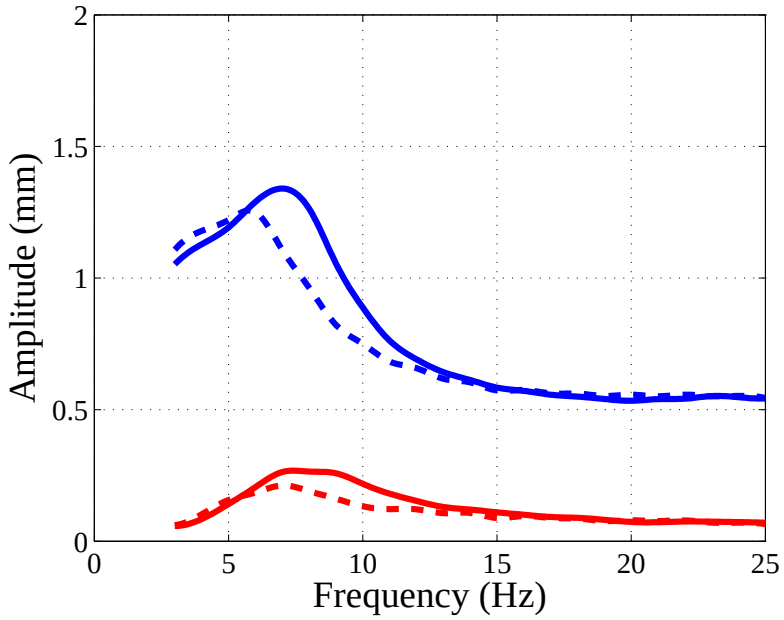

Figure 7.12. Frequency response of the model subjected to 0.05 g vertical base excitation. Blue lines are the vertical displacement of H-Point and the red lines are the horizontal displacement of H-Point. Solid line: low density foam 1 and dashed line: low density foam 2 (stiffer foam). 30 elements in the seat back and the seat bottom ($N_{back} = N_{bottom} = 15$).

the simulations above. Again, for other variables the baseline values are used in the simulations and $N_{back} = N_{bottom} = 15$. The base acceleration was again set to 0.05 g.

The estimated frequency responses when the seat cushions are made of two different types of foams are shown in Figure 7.12. It is seen that when the foam is softer (foam 1), the amplitude of the estimated frequency response is higher and the location of the resonance is higher. The compression of the foam under the H-point strongly affects this, predominantly, bounce mode behavior. With the stiffer foam (foam 2), the compression is less than with the softer foam, so again, the nonlinear elastic behavior of the foam means that the stiffness of (the generally stiffer) foam 2 under the H-point is lower than the stiffness of (the generally softer) foam 1 in this region of the seat bottom, because foam 1 is more highly compacted.

7.3.6 Variation of the Viscous Damping Coefficient

The effect of the viscous damping coefficient on the frequency responses of the horizontal and the vertical displacement of the occupant H-Point, as predicted by using incremental harmonic balance, was studied. As discussed before, the viscous dampers were added to the system to account for other damping factors which are not modeled by viscoelastic damping mechanisms in the foam and thus may not be contributing in very slow or quasi-static tests. The viscous damping coefficient for the seat-occupant system is chosen to be the value estimated for the single-degree-of-freedom foam-mass system model described in Chapter 4.

Recall that the viscous damping coefficient was chosen to make the foam-mass system's predicted frequency response match the measured frequency response (see Section 4.5). The baseline values were used for all other parameters. The estimated frequency responses when the viscous damping coefficient is 0.8, 1 and 1.2 times its baseline value of $c = 2000\ Ns/m$ are shown in Figure 7.13. As expected, as the damping coefficient is increased, the amplitude of the predicted frequency responses decreases. Note that the resonance frequency location in the horizontal frequency response decreases as damping is lowered.

7.4 Including the Seat Back Flexibility in the Model

In practice the connection between the seat back frame and the seat bottom frame is not rigid. Here this flexibility is modeled as a pin joint with a stiff torsional spring attached. The equations of motion for this system are also given in Chaper 5. The flexibility in the seat back introduces another generalized coordinate into the equations: of motion: the angular motion of the seat back with respect to the seat frame. The baseline value of the torsional spring coefficient is $20,000\ N/rad$. This value is similar to that used in the model developed by Kim, White, Bajaj and Davies [106] ($k_s = 21,584.8\ N/rad$) that produced the prediction that best matched measured frequency responses of the seat-occupant system. The vertical

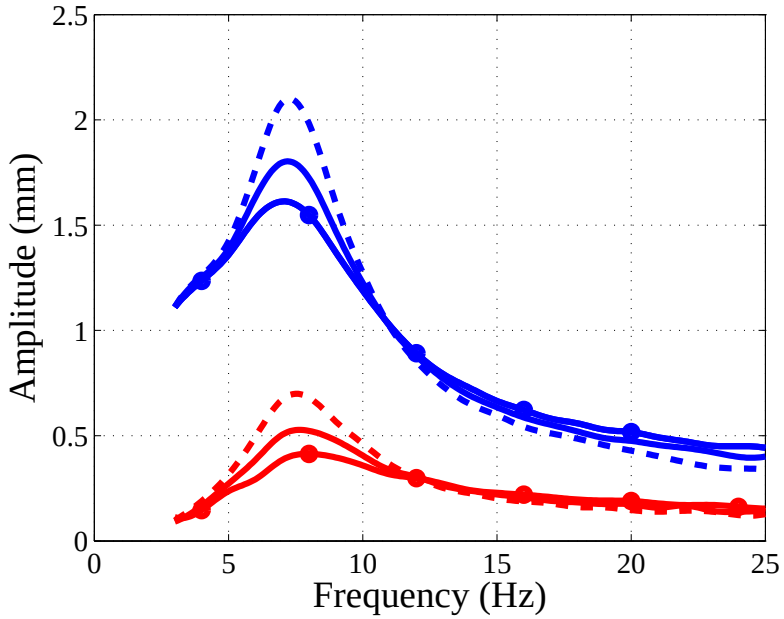

Figure 7.13. The magnitude of the frequency response at the frequencies of excitation of the seat-occupant model subjected to 0.05 g vertical base excitation. Blue lines are the vertical displacement of H-Point, red lines are the horizontal displacement of H-Point. Solid line (circle marker): viscous damping coefficient, $c = 1.2 \times 2000\ Ns/m$, solid line: $c = 1 \times 2000\ Ns/m$ and dashed line: $c = 0.8 \times 2000\ Ns/m$. Baseline values used for all other parameters.

base excitation acceleration level for the results shown below is 0.1 g and the seat is modeled by 30 elements ($N_{back} = N_{bottom} = 15$). All other parameters are at their baseline values.

The predicted frequency response magnitudes of the horizontal displacement and the vertical displacement of the H-Point are shown in Figure 7.14 for the rigid and the flexible seat frame models. It is observed that the frequency of the vertical frequency response resonances is slightly moved to the right from 7.4 Hz to 7.7 Hz. Also another peak appears in the response at 3 Hz. These results are similar to the experimental frequency responses measured by White [106] though in his responses there is just one peak at 7.9 Hz. The resonance around 7.3 Hz in the horizontal motion frequency response does not change very much when the seat-back flexibility is introduced but a new peak appears in the response at around 12 Hz. This is also consistent with experimental frequency responses measured by White [106] which contained two peaks at 7.5 Hz and 11 Hz.

The variation in the frequency responses of the horizontal displacement and the vertical displacement of the occupant H-Point with different seat back spring stiffness coefficients was studied and the results are shown in Figure 7.15. The estimated frequency responses when the torsional stiffness coefficient is varied between 0.8 to 1.2 times its baseline value are shown in Figure 7.15. As the torsional stiffness coefficient is increased, the estimated frequency response of the vertical displacement changes very little but the second resonance in the horizontal displacement frequency response changes significantly. As the torsional stiffness coefficient is decreased, the second resonance appears at a lower frequency and the amplitude increases; this is consistent with the softer torsional spring providing less resistance to fore-aft motion.

7.5 Chapter Summary

The multi-body seat-occupant model, described and used earlier for transient response and settling point prediction, was used again to study the dynamic response

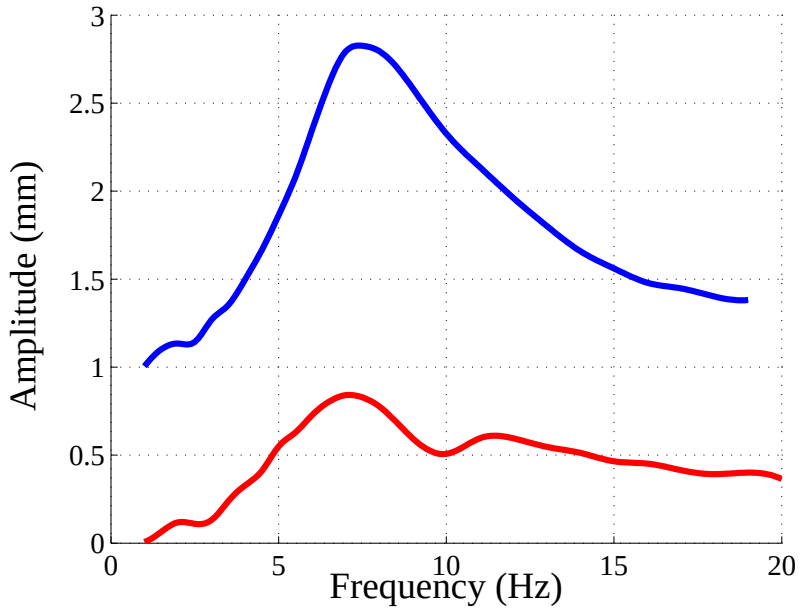

Figure 7.14. Frequency response of the model subjected to 0.2 g vertical base excitation when the seat back spring is included, $K_s = 20,000\ N/rad$. Blue line is the vertical displacement of H-Point, red line is the horizontal displacement of H-Point. 30 elements in the seat back and the seat bottom ($N_{back} = N_{bottom} = 15$).

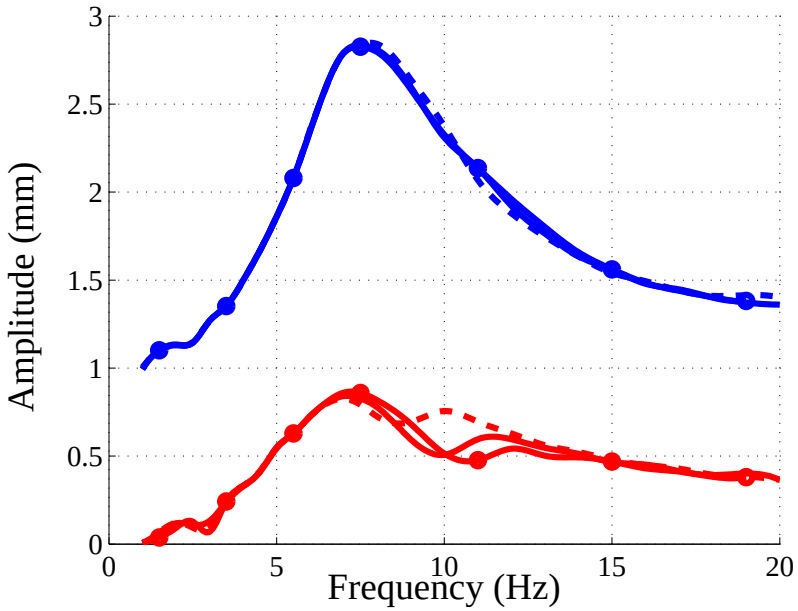

Figure 7.15. Predicted frequency response with 0.1 g vertical base excitation when the seat back spring is included in the model. Blue lines are the vertical displacement of H-Point and the red lines are the horizontal displacement of H-Point. Solid line (circle marker): seat back torsional stiffness coefficient is set to $1.2 \times 20,000\ N/rad$, solid line: seat back torsional stiffness coefficient is set to baseline value $20,000\ N/rad$ and dashed line: seat back torsional stiffness coefficient set to $0.8 \times 20000\ N/rad$. 30 elements in the seat back and the seat bottom ($N_{back} = N_{bottom} = 15$).

of the seat-occupant system when the system was subjected to vertical harmonic base excitation at different frequencies. A modified incremental harmonic balance method was applied to the system of equations to determine the steady-state response of the system. Application of the incremental harmonic balance method significantly reduces the time required to compute the steady-state response over that required when using time-integration; this makes extensive parameter variation studies more feasible. The frequency responses of the H-Point motion were predicted over a range of frequencies by incorporating incremental harmonic balance and continuation simultaneously. Deflection shapes were also studied.

Different parameters of the model, such as occupant weight, foam type used in the cushion, seat back angle and seat back frame stiffness were varied and their effects on the system responses were studied. While some of the results were consistent with simple intuitive explanations, e.g., lower spring stiffness for seat-back frame leading to lower frequency resonances, some results were different to what might be expected, unless one considered the nonlinear behavior of the foam. For example, a higher occupant mass leads to more foam compression, to a region where the foam is compacted and much stiffer than it is when compressed less, thus leading to a higher frequency resonance with increased occupant mass. While there were similarities between the predictions of the model and frequency responses measured in experiments, the amplitudes of the responses were different. The damping model due to air motion, currently a simple viscous damping model, may need to be improved because the value that worked best for the foam-mass model appeared to be too high for this model (predicted frequency response amplitudes were lower than those from the experiment).

8. SUMMARY, CONCLUSION AND FUTURE WORK

One objective of this research was to improve traditional models of foam behavior that describe a large range of compressive strain behavior of polyurethane foams. The existing foam models, in general, fall into two categories: models that are simple but have limited application range, and models which are more complex but have much wider application range. The foam model should be an integral part of a seat-occupant model. In this application the compression of the foam in different parts of the seat varies significantly and this compression changes with occupant weight and posture. As compression levels change so does the stiffness of the foam, and so a series of simple models would be required to model different occupants' responses and some strategy would need to be developed to transition between model. The complex models, e.g. finite element models, may be too computationally costly to be incorporated into the seat-occupant system making them cumbersome to use for exploratory seat design. In this research, phenomenological foam models were developed. The form of the models was based on previously developed hereditary-type nonlinear viscoelastic foam models, but they have a much wider application range so that when incorporated into seat-occupant models, it is possible with the one model to predict both the settling point of the occupant and compression of the foam across the seat and the dynamic response of the occupant around that settling point. The developed model is still relatively simple when compared to more complex models.

The improved foam model helped in achievement of the second objective of the research, which was to extend an existing seat-occupant model [33, 51] so that it produced improved estimates of seat occupants' dynamic responses, which could then be used to predict comfort metrics and related quantities such as the H-Point location, the seat-occupant interfacial pressure distribution, and the steady-state response of the occupant over a frequency range when the base of the seat is subject to harmonic

motion. To accelerate calculation of these frequency responses, a modified incremental harmonic balance technique was developed, which provides between a 25 times and a 144 times reduction in computation time over using time integration techniques to extract steady-state harmonic response behavior.

In this chapter a summary of the research described in this thesis is presented, followed by conclusions and recommendations for future work.

8.1 Summary

Over the course of this research, the objectives of this research given in Chapter 1 were met. A method to construct nonlinear viscoelastic model for predicting the uniaxial response of flexible polyurethane foams under large range of compressive strains were developed. The models' structure combines features of many previously developed models. It differs from those models in that the identified model for a particular foam can be used to make accurate predictions of responses measured in a series of large strain cyclic experiments where strain rates were varied. As part of this model identification, procedures were developed to estimate the proposed model parameters. It was shown that the estimated parameters of low-order viscoelastic hereditary kernels are functions of the input strain rates used in the quasi-static compression tests. Two types of models were constructed:

- a model with low order hereditary kernels in the viscoelastic part of the model and the viscoelastic parameters are simple functions of the strain rates,
- a model with higher order hereditary kernels in the viscoelastic part of the model where the estimated viscoelastic parameters are not functions of strain rate.

In the first case the model is very simple, i.e. total of four viscoelastic parameters are required, which is easily incorporated into the seat-occupant model adding only two second-order differential equations for each foam element. The second method

requires more computation because the viscoelastic kernels have many more terms. The performance of the proposed models was verified by comparing the predictions of the responses to the measured responses from experiments on five different foam samples: two types of low density foams used in car seats, and three types of high density CONFOR foams.

A methodology was developed to predict the uniaxial responses of a two-layer foam system. In the method the foam models with the strain rate dependent parameters, estimated from experimental data on the individual foams in the layers, are used together with continuity equations at the boundary between the two layers. It was observed that although the layered system is compressed at a constant strain rate, foams in the two layers are compressed at different rates. It is observed that the predicted stress responses of the layer system is in agreement with the measured responses from experiments conducted on two-layer foam systems.

The foam models were then incorporated into a single-degree-of-freedom foam-mass system subjected to harmonic base excitation and the responses predictions were compared to responses measured in the experiment. This study was helpful in two ways:

- it increased understanding of how the estimated foam model behaves at much higher strain rates,
- the single-degree-of-freedom foam-mass system can be thought of as the simplest model of a seat-occupant system and this study increased understanding of how the foam seat and the occupant interact in the vertical direction.

The incremental harmonic balance method was used to find steady-state periodic responses of the system and this significantly reduced computation time over using time integration to determine steady-state responses. The system frequency response curves were predicted for 2 riding masses, 3 base excitation levels, and three different hereditary-type viscoelastic models. Predictions from system models with different viscoelastic model forms (foam Models 2-4) resulted in different frequency response

curves with different frequency locations for peak responses, even though all three models' system parameters were estimated from the same compression test data and in each case produced reasonably accurate predictions of the stresses in the foam during the compression tests. These differences in response predictions persisted even when the strain rate dependence of the parameters was included in the model. A set of data of data from experiments conducted by Sundaram [80] was used to examine the accuracy of the three foam-mass models' predictions. It was shown that foam Model 4 with the strain-rate dependent parameters produced predictions that were most closely aligned with experimental results but it was also necessary to include a viscous damping term to align the predictions with the experimental results.

The multibody seat-occupant model described in Puri and Joshi [32, 47] for calculating the dynamic response of the seated occupant was modified. The strain rate dependent foam model 4 was incorporated into the seat-occupant model. For transient responses the magnitude of the strain rate was used in the parameter models and for the harmonic responses, the root mean square (rms) value of the strain rate was used. Other improvements included a more realistic interfacial model and a better geometric constraint at interfaces.

The multi-body seat-occupant model was used to study the transient dynamic responses of the seat-occupant system. Following the same procedures as Puri [32], the system governing equations were solved by using the numerical time integration to obtain the occupant's transient dynamic response and the static equilibrium position. From this, the H-Point location and the pressure distribution at the seat-occupant interface, two important factors in occupant comfort. Variations in the H-Point location and the seat-occupant pressure distribution with changes in the seat-occupant parameters, including the number of springs in the seat back, the seat bottom, the coefficient of friction, the foam stiffness, the seat material and the occupant weight were studied. Previously taken experimental measurements were used to verify the predicted pressure distribution at the seat-occupant interface. The coefficient of fric-

tion needed to be adjusted so that the analytical and the experimental results are in good qualitative agreement.

The multi-body seat-occupant model was also used to study the dynamic response of the seat-occupant system when the system was subjected to vertical harmonic base excitation at different frequencies. A modified incremental harmonic balance method was applied to the system of equations to determine the steady-state response of the seat-occupant system. Application of the incremental harmonic balance method significantly reduced the time required to find the steady-state response. Direct-time integration of the governing equations to find the steady-state responses was computationally inefficient, making a large number parameter variation studies infeasible when using this approach. Frequency responses of the H-Point as functions of the input frequency were predicted by incorporating the incremental harmonic balance and continuation simultaneously and from the results occupant deflection shapes could also be generated. Also different parameters of the model, such as occupant's weight, foam type used in the cushion, seat back angle were varied and their effects on the system responses were studied. The predicted frequency responses were compared with those from a previously conducted experiment and while there were differences, resonances were at similar locations and introduction of a flexible seat-back frame further improved the agreement between the experimental and analytical results.

The development of the comprehensive foam Model 4 with strain-rate dependent parameters (or the foam Model 4 higher order fixed parameter models) has lead to a very significant improvement in the seat-occupant model. It means that occupant response predictions that are known to affect occupant ergonomics and static and dynamic comfort (the settling point, pressure distributions and frequency responses) can be made from a single model, and the responses of different occupants can easily be predicted from this same model. Together with the computational improvements in the frequency response calculations this advance sets the stage for more realistic virtual seat design.

8.2 Recommendations for Future Work

Although significant advances have been made in the course of this research, certain issues need to be addressed to further improve the models. These are described below.

1. The present model is a uniaxial model and describes the foam behavior under compression. The utility of developing a more comprehensive model which describes the foam behavior under shear and tension needs to be investigated in the future.

2. The functions which govern the relationships between the viscoelastic parameters and the input strain rate, were just estimated using a few slow compression tests. In the future, it is necessary to perform more tests on the polyurethane foam at much faster strain rates to verify, or improve, the models of the strain-rate dependence of the model parameters. The accuracy of the higher order viscoelastic models (without strain rate dependencies in the parameters) should also be examined with this additional data.

3. Currently the estimated elastic component of the foam model is a function of the input strain rate (although this variation was not incorporated into the comprehensive models described in this thesis). It was observe that the elastic component predictions varied from their average values by up to 10% depending on the input strain rate. This problem needs to be investigated in the future.

4. From previous studies, it is well known that when the foam is subjected to cyclic compression tests, the foam response reaches a steady-state response after a few cycles. In this study, the foam model was just fitted to the first cycle of the response. The foam model should also be fitted to the steady-state stress-strain response to study how the new estimated models are different from the current model. Ideally, one model that predicts all cycles of the response would be desirable because it would be appropriate for both transient and steady state harmonic responses.

5. In this study, the methodology, to predict the characteristic behavior of layered foam systems from the characteristic behavior of its individual layers, was just tested on a 2-layer system at 2 different strain rates. The same methodology can be verified by using uniaxial compression data from different strain-rate experiments conducted on more complex systems consisting of several layers of nonlinear viscoelastic materials.

6. The application range of the estimated comprehensive model was tested using slow quasi-static tests as well as fast harmonic base excitation tests. It is important to examine if the current comprehensive model can predict the foam responses when it is subjected to very fast impulsive inputs. High density viscoelastic foams like CONFOR foams are used for shock isolation, so the ability to model foam behavior when responding to impulsive excitation would be helpful in the design of isolation systems incorporating these types of foams.

7. At present, the model of occupant in the seat-occupant model is rigid and two-dimensional. In the future, with recent advances in digital modeling of human subjects, more realistic 3D models of the occupant can be incorporated in the seat-occupant model. Also, the occupant model needs to be improved by incorporating the mechanical behavior of the body tissues in the occupant model. The developed methodology for the layered-foam materials could be helpful to study the mechanical behavior of a layered system consisting of the body-tissue and the foam.

8. At present a simple model has been used to model the interfacial friction forces between the seat and occupant. An improved model for these forces, that includes the shear effects in foam has to be developed and incorporated into the system model. As shown in the parameter variation studies, these interfacial forces can have a large impact on the occupant's responses.

9. The seat-occupant simulation results presented in this research have to be validated by comparison with more experimental data. Such data will also be

useful in refining the model to address current deficiencies in the model such as the non-viscoelastic damping that is apparent in the harmonic testing, and currently modeled by a simple viscous damping term.

10. In the current seat-occupant model, the seat is simplify represented by a frame and a cushion. Other effective components of the seat such as the suspension system and the seat cover should be incorporated into the seat-occupant model.

LIST OF REFERENCES

LIST OF REFERENCES

[1] L. J. Gibson and M. F. Ashby. *Cellular Solids: Structure and Properties*. Cambridge University Press, 2nd edition, 1997.

[2] R. Widdle. *Measurement and Modeling of the Mechanical Properties of Polyurethane Foam*. PhD Thesis, Purdue University, West Lafayette, IN, USA, 2005.

[3] Y. Deshmukh. *Measurement of Foam Properties and Modeling of Layered Foam Systems*. Masters Thesis, Purdue University, West Lafayette, IN, 2010.

[4] W. E. Warren and A. M. Kraynik. The linear elastic properties of open-cell foams. *Journal of Applied Mechanics*, 55(2):341–346, 1988.

[5] W. E. Warren and A. M. Kraynik. The nonlinear elastic behavior of open-cell foams. *Journal of Applied Mechanics*, 58(2):376–381, 1991.

[6] W. E. Warren and A. M. Kraynik. Linear elastic behavior of a low-density kelvin foam with open cells. *Journal of Applied Mechanics*, 64(4):787–794, 1997.

[7] H. X. Zhu, N. J. Mills, and J. F. Knott. Analysis of the high strain compression of open-cell foams. *Journal of the Mechanics and Physics of Solids*, 45(11):1875–1904, 1997.

[8] M. J. Silva, W. C. Hayes, and L. J. Gibson. The effects of non-periodic microstructure on the elastic properties of two-dimensional cellular solids. *International Journal of Mechanical Sciences*, 37(11):1161–1177, 1995.

[9] M. W. D. Van der Burg, V. Shulmeister, E. Van der Geissen, and R. Marissen. On the linear elastic properties of regular and random open-cell foam models. *Journal of Cellular Plastics*, 33(1):31–54, 1997.

[10] V. Shulmeister, M. W. D. Van der Burg, E. Van der Giessen, and R. Marissen. A numerical study of large deformations of low-density elastomeric open-cell foams. *Mechanics of Materials*, 30(3):125–140, 1998.

[11] H. X. Zhu, J. R. Hobdell, and A. H. Windel. Effects of cell irregularity on the elastic properties of open-cell foams. *Acta Materialia*, 48(20):4893–4900, 2000.

[12] H. X. Zhu, J. R. Hobdell, and A. H. Windle. Effects of cell irregularity on the elastic properties of 2d voronoi honeycombs. *Journal of the Mechanics and Physics of Solids*, 49(4):857–870, 2001.

[13] H. X. Zhu and A. H. Windle. Effects of cell irregularity on the high strain compression of open-cell foams. *Acta Materialia*, 50(5):1041–1052, 2002.

[14] C. Chen, T. J. Lu, and N. A. Fleck. Effect of imperfections on the yielding of two-dimensional foams. *Journal of the Mechanics and Physics of Solids*, 47(11):2235–2272, 1999.

[15] E. W. Andrews and L. J. Gibson. The role of cellular structure in creep of two-dimensional cellular solids. *Materials Science and Engineering*, A303(3):120–126, 2001.

[16] J. S. Huang and L. J. Gibson. Creep of open-cell Voronoi foams. *Material Science and Engineering*, A339(1):220–226, 2003.

[17] R. M. Christensen. *Theory of Viscoelasticity: An Introduction*. Academic Press, New York, 2nd edition, 1982.

[18] R. L. Bagley and P. J. Torvik. A theoretical basis for the application of fractional calculus to viscoelasticity. *Journal of Rheology*, 27(3):201–210, 1983.

[19] R. Bloch, W. V. Chang, and N. W. Tschoegl. The behavior of rubberlike materials in moderately large deformations. *Journal of Rheology*, 22(1):1–32, 1978.

[20] H. T. Banks, L. K. Potter, and Y. Zhang. Stress-strain laws for carbon black and silicon filled elastomers. *Proceedings of the 36th IEEE Conference on Decision and Control*, December 1997. San Diego, California USA.

[21] H. T. Banks. Modeling of quasi-static and dynamic load responses of filled viscoelastic materials. *Technical Report, Center for Research in Scientific Computation, North Carolina State University*, CRSC-TR98-48, 1998.

[22] H. T. Banks, G. A. Pinter, L. K. Potter, M. J. Gaitens, and L. C. Yanyo. Modeling of nonlinear hysteresis in elastomers under uniaxial tension. *Journal of Intelligent Materials Systems and Structures*, 10(2):116–134, 1999.

[23] J. S. Bergström and M. C. Boyce. Constitutive modeling of the large strain time-dependent behavior of elastomers. *Journal of the Mechanics and Physics of Solids*, 46(5):931–954, 1998.

[24] J. V. Suvorova, N. G. Ohlson, and S. I. Alexeeva. An approach to the description of time-dependent materials. *Materials & Design*, 24(4):293–297, 2003.

[25] L. M. Yang and V. P. W. Shim. A visco-hyperelastic constitutive description of elastomeric foam. *International Journal of Impact Engineering*, 30(8):1099–1110, 2004.

[26] Y. Anani and Y. Alizadeh. Visco-hyperelastic constitutive law for modeling of foam's behavior. *Materials & Design*, 32(5):2940–2948, 2011.

[27] L. M. Yang, V. P. W. Shim, and C. T. Lim. A visco-hyperelastic approach to modeling the constitutive behavior of rubber. *International Journal of Impact Engineering*, 24(6):545–560, 2000.

[28] S. W. White, S. K. Kim, A. K. Bajaj, P. Davies, D. K. Showers, and P. E. Liedtke. Experimental techniques and identification of nonlinear and viscoelastic properties of flexible polyurethane foam. *Nonlinear Dynamics*, 22(3):281–313, 2000.

[29] R. Singh. *Dynamic Modeling of Polyurethane Foam and Development of System Identification Methodologies.* Masters Thesis, Purdue University, West Lafayette, IN, USA, 2001.

[30] R. Singh, P. Davies, and A. K. Bajaj. Nonlinear modeling and identification of the dynamic behavior of polyurethane foam. *ASME Design Engineering Technical Conference*, September 2012, Pittsburgh, PA, USA.

[31] R. Deng, A. K. Bajaj, and P. Davies. Flexible polyurethane foam modeling and identification of viscoelastic parameters for automotive seating applications. *Journal of Sound and Vibration*, 262(3):391–417, 2003.

[32] T. Puri. *Seat-Occupant Modeling and Experiment Verification for H-Point Prediction in All-Foam Seats.* Masters Thesis, Purdue University, West Lafayette, IN, USA, 2004.

[33] R. Fosdick, Y. Ketema, and J.-H. Yu. Vibration damping through the use of materials with memory. *International Journal of Solids and Structures*, 35(5-6):403–420, 1998.

[34] M. J. Griffin. *Handbook of Human Vibration.* Academic Press, San Diego, CA, USA, 2012.

[35] J. Pang, M. Qatu, R. Dukipatti, G. Sheng, and W. Patten. Model identification for nonlinear automotive seat cushion structure. *International Journal of Vehicle Noise and Vibration*, 1(1):142–157, 2004.

[36] S. Rakheja, I. Stiharu, H. Zhang, and P.E. Boileau. Seated occupant interactions with seat backrest and pan, and biodynamic responses under vertical vibration. *Journal of Sound and Vibration*, 298(3):651–671, 2006.

[37] L. Wei and M.J. Griffin. Mathematical models for the apparent mass of the seated human body exposed to vertical vibration. *Journal of Sound and Vibration*, 212(5):855–874, 1998.

[38] T. Fairley and M.J. Griffin. The apparent mass of the seated human body: vertical vibration. *Journal of Biomechanics*, 22(3):81–94, 1989.

[39] J. Rosen and M. Arcan. Modeling the human body/seat system in a vibration environment. *Journal of Biomechanical Engineering*, 125(2):223–231, 2003.

[40] W. Qassem, M.O. Othman, and S. Abdul-Majeed. The effects of vertical and horizontal vibrations on the human body. *Medical Engineering Physics*, 16(2):151–160, 1994.

[41] R. Muksian and C. D. A Nash. A model for the response of seated humans to sinusoidal displacements of the seat. *Journal of Biomechanics*, 7(3):209–215, 1982.

[42] J. Mizrahi and Z. Susak. *In vivo* elastic and damping response of the human leg to impact forces. *Journal of Biomechanical Engineering*, 104(4):63–66, 1982.

[43] S.P. Nigam and M. Malik. A study on a vibratory model of a human body. *Journal of Biomechanical Engineering*, 109(2):148–153, 1987.

[44] M.K. Patil, M.S. Palanichamy, and D.N. Ghista. Man-tractor system dynamics: Towards a better suspension system for human ride comfort. *Journal of Biomechanics*, 11(8):397–406, 1978.

[45] S. D. Smith. Nonlinear resonance behavior in the human body exposed to whole body vibration. *Shock and Vibration*, 1(5):439–450, 1994.

[46] S. D. Smith. Modeling differences in the vibration response characteristics of the human body. *Journal of Biomechanics*, 33(3):1513–1516, 2000.

[47] G. Joshi. *Planar Whole-Body Vibratory Response of a Nonlinear Multi-Body Model of a Seat-Occupant System with Polyurethane Foam.* Masters Thesis, Purdue University, West Lafayette, IN, USA, 2010.

[48] P. B. Kumbhar, P. Xu, and J. J. Yang. A literature survey of biodynamic models for whole body vibration and vehicle ride comfort. *ASME 2012 International Design Engineering Technical Conferences and Computers and Information in Engineering Conference*, August 2012. Chicago, IL, USA.

[49] C. C. Chiang and C. F. Liang. A study on biodynamic models of seated human subjects exposed to vertical vibration. *International Journal of Industrial Ergonomics*, 36(3):869–890, 2006.

[50] A. Siefert, S. Pankoke, and H. P. Wölfel. Virtual optimisation of car passenger seats: simulation of static and dynamic effects on drivers seating comfort. *International Journal of Industrial Ergonomics*, 38(5):410–424, 2008.

[51] R. H. Setyabudhy, A. Ali, R. P. Hubbard, C. Beckett, and R. C. Averill. Measuring and modeling of human soft tissue and seat interaction. *SAE International Journal of Passenger Cars*, 106(6):1058–1065, 1997.

[52] M. Verver, R. de Lange, P. van Hoof, and J.S.H.M. Wismans. Aspects of seat modeling for seating comfort analysis. *Applied Ergonomics*, 36(4):33–42, 2005.

[53] R. Satyabudhy, A. Ali, R. Hubbard, C. Beckett, and R. Averill. Measuring and modeling of human soft tissue and seat interaction. *SAE International Journal of Passenger Cars*, 106(6):1–10, 1997.

[54] M. Verver and P. van Hoof. Development of a FEM pelvis model for analysis of pressure distributions. *SAE Journal of Passenger Cars*, 112(7):20–29, 2003.

[55] T. Kondo and Y. Ito. Predicting ride comfort on seat using explicit FEM code. *SAE World Congress*, April 2002, Detroit, MI, USA.

[56] A. Siefert, S. Pankoke, and H.P. Wölfel. Virtual optimization of car passenger seats: Simulation of static and dynamic effects on drivers seating comfort. *International Journal of Industrial Ergonomics*, 38(2):410–424, 2008.

[57] A. Siefert, C. Delavoye, and M. Cakmak. Casimir: Human finite-element model for static and dynamic assessment of seating comfort. *IEA International conference*, November 2006. Washington, DC, USA.

[58] Y. Matsumoto and M. J. Griffin. Modeling the dynamic mechanisms associated with the principal resonance of the seated human body. *Clinical Biomechanics*, 16(1):31–44, 2001.

[59] T. Yoshimura, K. Nakai, and G. Tamaoki. Multi-body dynamics modelling of seated human body under exposure to whole-body vibration. *Industrial Health*, 43(3):441–447, 2005.

[60] Y. Cho and Y. S. Yoon. Biomechanical model of human on seat with backrest for evaluating ride quality. *International Journal of Industrial Ergonomics*, 27(5):331–345, 2001.

[61] Y. Cho, Y. S. Yoon, and S.J. Park. Determination of seat sponge properties with estimated biodynamic model. *SAE International Congress*, April 2000. Detroit, MI, USA.

[62] S.J. Park, S.C. Park, J.H. Kim, and C.B. Kim. Biomechanical parameters on body segments of korean adults. *International Journal of Industrial Ergonomics*, 23(2):23–31, 1999.

[63] I. Kaleps and J. Whitestone. Hybrid III geometrical and inertial properties. *SAE Paper No. 880638*, 1988.

[64] M.M. Panjabi, G. Andersson, L. Jorneus, E. Hult, and L. Mattsson. In vivo measurements of spine column vibrations. *Journal of Bone and Joint Surgery*, 68(5):695702, 1986.

[65] B. Hinz and H. Seidel. The non-linearity of human body's response during sinusoidal whole body vibration. *Industrial Health*, 25(5):169–181, 1987.

[66] International Standard/DIS 5982. Mechanical vibration and of idealized values to characterize seated body biodynamic response under vertical vibration, 2000.

[67] M. Verver, J. van Hoof, C. Oomens, N. van de Wouw, and J. Wismans. Estimation of spinal loading in vertical vibrations by numerical simulation. *Clinical Biomechanics*, 18(9):800–811, 2003.

[68] R. K. Ippili, P. Davies, A. K. Bajaj, and L. Hagenmeyer. Nonlinear multibody dynamic modeling of seat–occupant system with polyurethane seat and h-point prediction. *International Journal of Industrial Ergonomics*, 38(5):368–383, 2008.

[69] Y. Azizi, A. K. Bajaj, and P. Davies. Predicting the response of a seat-occupant model by using incremental harmonic balance. *SAE 2013 World Congress and Exhibition*, April 2013, Detroit, MI, USA.

[70] S. K. Kim, S. W. White, A. K. Bajaj, and P. Davies. Simplified models of the vibration of mannequins in car seats. *Journal of Sound and Vibration*, 264(1):49–90, 2003.

[71] M. Demi and J. Luki. Investigation of the transmission of fore and aft vibration through the human body. *Applied Ergonomics*, 40(4):622–629, 2009.

[72] M. Bovenzi and C. T. J. Hulshof. An updated review of epidemiologic studies on the relationship between exposure to whole-body vibration and low back pain. *Journal of Sound and Vibration*, 215(4):595–611, 1998.

[73] Z. Zhou and M. J. Griffin. Response of the seated human body to whole-body vertical vibration: biodynamic responses to sinusoidal and random vibration. *Ergonomics*, 57(5):693–713, 2014.

[74] G. S. Paddan, N. J. Mansfield, C. I. Arrowsmith, A. N. Rimell, S. K. King, and S. R. Holmes. The influence of seat backrest angle on perceived discomfort during exposure to vertical whole-body vibration. *Ergonomics*, 55(8):923–936, 2012.

[75] K. Ebe and M. J. Griffin. Qualitative models of seat discomfort including static and dynamic factors. *Ergonomics*, 43(6):771–790, 2000.

[76] B. Basri and M. J. Griffin. Predicting discomfort from whole-body vertical vibration when sitting with an inclined backrest. *Applied Ergonomics*, 44(3):423–434, 2013.

[77] K. Ebe and M. J. Griffin. Factors affecting static seat cushion comfort. *Ergonomics*, 44(10):901–921, 2001.

[78] H. Dupuis and G. Zerlett. Whole-body vibration and disorders of the spine. *International Archives of Occupational and Environmental Health*, 59(4):323–336, 1987.

[79] E. B. Magid and R. Coermann. The reaction of the human body to extreme vibrations. *Processing of Institute of Environmental Science*, pages 135–155, 1960.

[80] V. Sundaram. *Measurement of Experimental Responses of Polyurethane and CONFOR Foams and Development of System Identification to Estimate Polyurethane Foam Parameters from Experimental Impulse Responses*. Masters Thesis, Purdue University, West Lafayette, IN, 2014.

[81] R. D. Widdle, A. K. Bajaj, and P. Davies. Measurement of the poissons ratio of flexible polyurethane foam and its influence on a uniaxial compression model. *International Journal of Engineering Science*, 46(1):31–49, 2008.

[82] L. Ljung. *System Identification: Theory For the User*. John Wiley & Sons, Inc., 2^{nd} edition, 1999.

[83] R. J. Schilling and S. L. Harris. *Fundamentals of Digital Signal Processing Using MATLAB*. CL-Engineering, 2004.

[84] Y. Azizi, P. Davies, and A. K. Bajaj. Identification of nonlinear viscoelastic models of flexible polyurethane foam from uniaxial compression data. *ASME International Congress and Exposition*, November 2012, Houston, TX, USA.

[85] J. Yamaguchi, A. Takanishi, and I. Kato. Experimental development of a foot mechanism with shock absorbing material for acquisition of landing surface position information and stabilization of dynamic biped walking. *IEEE International Conference on Robotics and Automation*, May 1995, Nagoya, Japan.

[86] A. Akiyama, S. Yoshida, T. Matsuhashi, N. Rangarajan, T. Shams, H. Ishikawa, and A. Konosu. Development of simulation model and pedestrian dummy. *SAE International Congress and Exposition*, March 1999. Detroit, MI.

[87] D. J. Whiteside. A comprehensive overview of the pedestrian protection requirements and test methodology. *SAE International Congress and Exposition*, April 2010. Detroit, MI.

[88] L. Yoo, J. Reed, A. Shin, J. Kung, J. K. Gimzewski, V. Poukens, R. A. Goldberg, R. Mancini, M. Taban, and R. Moy. Characterization of ocular tissues using microindentation and hertzian viscoelastic models. *Investigative Ophthalmology and Visual Science*, 52(6):3475–3482, 2011.

[89] O. L. Davies and N. J. Mills. The rate dependence of confor polyurethane foams. *Cellular Polymers*, 18(2):117–136, 1999.

[90] Y. Matsui. Effect of humidity on quasi-static characteristics of foam CF-45 for TRL pedestrian legform impactor. *International Journal of Vehicle Safety*, 7(3):440–449, 2014.

[91] C. K. Thorbole, H. M. Lankarani, and T. Costello. Temperature effect on the dynamic characteristic of the aircraft seat cushion. *ASME International Mechanical Engineering Congress and Exposition*, November 2009. Lake Buena Vista, Florida, USA.

[92] A. L. Desbiens and M. R. Cutkosky. Landing and perching on vertical surfaces with microspines for small unmanned air vehicles. *International Symposium on Unmanned Aerial Vehicles*, June 2009. Reno, Nevada, USA.

[93] N. Cappetti, A. Donnarumma, A. Naddeo, and L. Russo. Design of experiment about foam cf45 for pedestrian safety in car design. *Journal of Materials Processing Technology*, 175(1):77–82, 2006.

[94] A. Janssen. *Strain Rate Dependency of CONFOR Foam*. Masters Thesis, Eindhoven University of Technology, Eindhoven, Netherlands, 1999.

[95] Y. Azizi, P. Davies, and A. K. Bajaj. Identification of nonlinear viscoelastic models of flexible polyurethane foam from uniaxial compression data. *Submitted to Journal of Engineering Materials and Technology*, 2014.

[96] R. Deng. *Modeling and Characterization of Flexible Polyurethane Foam*. PhD Thesis, Purdue University, West Lafayette, IN, USA, 2004.

[97] R. Singh. *Dynamic Modeling of Polyurethane Foam and Development of System Identification Methodologies*. Masters Thesis, Purdue University, West Lafayette, IN, USA, 2001.

[98] Y. Azizi, A. K. Bajaj, and P. Davies. Prediction and verification of the periodic response of a single-degree-of-freedom foam-mass system by using incremental harmonic balance. *Submitted to Nonlinear Dynamic*, 2014.

[99] Y. Azizi, A. K. Bajaj, and P. Davies. Periodic response of a single-degree-of-freedom foam-mass-system by using incremental harmonic balance method. *ASME International Congress and Exposition*, November 2012, Houston, TX, USA.

[100] G. Joshi, A. K. Bajaj, and P. Davies. Whole-body vibratory response study using a nonlinear multi-body model of seat-occupant system with viscoelastic flexible polyurethane foam. *Industrial Health*, 48(5):663–674, 2010.

[101] A. Y. T. Leung and S. K. Chuir. Non-linear vibration of coupled duffing oscillators by an improved incremental harmonic balance method. *Journal of Sound and Vibration*, 181(4):619–633, 1995.

[102] E. L. Allgower and K. Georg. *Introduction To Numerical Continuation Methods.* Society for Industrial Mathematics, 2003.

[103] E. L. Allgower and K. Georg. Continuation and path following. *Acta Numerica*, 2(1):1–64, 1993.

[104] A. Y. T. Leung. Nonlinear natural vibration analysis of beams by selective coefficient increment. *Computational Mechanics*, 5(1):73–80, 1989.

[105] Y. K. Cheung, S. H. Chen, and S. L. Lau. Application of the incremental harmonic balance method to cubic non-linearity systems. *Journal of Sound and Vibration*, 140(2):273–286, 1990.

[106] S. W. White, S. K. Kim, A. K. Bajaj, P. Davies, D. K. Showers, and P. E. Liedtke. Experimental techniques and identification of nonlinear and viscoelastic properties of flexible polyurethane foam. *Nonlinear Dynamics*, 22(3):281–313, 2000.

[107] S. Nishiyama. Vertical and lateral vibration analysis of vehicle-occupant dynamic interaction with simulation system. *Transactions of the Japan Society of Mechanical Engineers*, 59(567):3239–3246, 1993.

[108] S. Nishiyama. Development of simulation system on vehicle-occupant dynamic interaction. First report: Theoretical analysis and system verification. *Transactions of the Japan Society of Mechanical Engineers*, 59(568):3613–3621, 1993.

[109] S. Nishiyama. Development of simulation system on vehicle-occupant dynamic interaction. Second report: Influence of sitting posture on human comfort. *Transactions of the Japan Society of Mechanical Engineers*, 59(568):3622–3629, 1993.

[110] R. K. Ippili, P. Davies, A. K. Bajaj, and L. Hagenmeyer. Nonlinear multibody dynamic modeling of seat-occupant system with polyurethane seat and H-Point prediction. *International Journal of Industrial Ergonomics*, 38(5):368–383, 2008.

[111] R. Ippili. *System Identification of Quasi-static Foam Behavior and Its Application in the Prediciton of Static Equilibrium Position of a Car Sseat Occupant.* Master's thesis, Purdue University, West Lafayette, IN, USA, 2003.

[112] D.T. Greenwood. *Principles of Dynamics.* Prentice-Hall, Englewood Cliffs, NJ, USA, 1965.

[113] F. M. L. Amirouche. *Computational Methods in Multibody Dynamics.* Prentice Hall, Englewood Cliffs, New Jersey, 1992.

[114] F. M. L. Amirouche and S. K. Ider. Simulation and analysis of a biodynamic human model subjected to low accelerations- a correlation study. *Journal of Sound and Vibration*, 123(2):281–292, 1988.

[115] W. N. Patten, S. Sha, and C. Mo. A vibration model of open celled polyurethane foam automotive seat cushion. *Journal of Sound and Vibration*, 217(1):145–161, 1998.

APPENDICES

Appendix A. Parameter Estimation for Foam Model 1

In Chapter 2 of this thesis, 4 different nonlinear foam models were reviewed. The models were given in Table 3.2. In this section, procedures for estimating the parameters of Model 1, given the values for N and M_2, and the stress-strain test data, are described. The foam model 1 is given by

$$\sigma = \sigma_e + \sigma_{v2} = \sum_{i=1}^{N} k_i \epsilon^i(t) + \int_0^t \sum_{l=1}^{M_2} b_l e^{-\beta_l (t-\tau)} \dot{\epsilon}(\tau) d\tau. \tag{A.1}$$

The full description of the model was given in Chapter 2.

The first step is to transform the differential equation form of the model into a discrete-time model by using an impulse invariant mapping of the hereditary kernels [82, 83]. Consider the second viscoelastic term σ_{v2}:

$$\sigma_{v2}(t) = \sum_{l=1}^{M_2} b_l e^{-\beta_l t} * \dot{\epsilon}(t), \tag{A.2}$$

where $(*)$ represents convolution. The impulse response of this system relating $\dot{\epsilon}(t)$ to $\sigma_{v2}(t)$ can be expressed as,

$$g(t) = \sum_{l=1}^{M_2} b_l e^{-\beta_l t}. \tag{A.3}$$

Sampling the impulse response at the sampling frequency f_s (Hz), yields:

$$g(n\Delta) = g_n = \Delta \sum_{l=1}^{M_2} b_l e^{-\beta_l n\Delta}, \tag{A.4}$$

where Δ is the sampling interval in seconds which is the inverse of sampling frequency (f_s). Taking z-transform of Equation (A.4) gives,

$$G(z) = \Delta \sum_{l=1}^{M_2} \frac{b_l}{1 - e^{-\beta_l \Delta} z^{-1}}. \tag{A.5}$$

This can be rewritten as,

$$G(z) = 1 + \frac{F_0 + F_1 z^{-1} + \cdots + F_{M_2-1} z^{-(M_2-1)}}{1 + E_1 z^{-1} + \cdots + E_{M_2} z^{-M_2}}. \tag{A.6}$$

If u_n is the input to this filter and v_n is the output, then the difference equation can be written as:

$$v_n = -E_1 v_{n-1} - \cdots - E_{M_2} v_{n-M_2} + F_0 u_n + \cdots + F_{M_2-1} u_{n-M_2+1}. \tag{A.7}$$

Here, $u_n = \dot{\epsilon}(n\Delta)$ and $v_n = \sigma_{v2}(n\Delta)$. This is an $ARMA$ filter. Note that, above equation can also be written in terms of a system relating $\epsilon(n\Delta)$ to $\sigma_{v2}(n\Delta)$. However, if $\dot{\epsilon}(n\Delta)$ is used, i.e. Equation (A.7), a digital differentiator needs to be designed to generate this signal from recorded $\epsilon(n\Delta)$. For example the program $firpm$ in $Matlab$ can be used to design this differentiator. In this work, $\epsilon(t)$ are simple ramps, so estimating $\dot{\epsilon}(t)$ at $t = n\Delta$ is straight forward. Finally, given the input u_n (or $\dot{\epsilon}(n\Delta)$) and the output v_n (or $\sigma_{v2}(n\Delta)$), Equation (A.7) can be used to develop a system of equations:

$$\begin{bmatrix} v_{M_2+1} \\ \vdots \\ v_{n_{end}} \end{bmatrix} = \begin{bmatrix} v_{M_2} & \cdots & v_1 & u_{M_2+1} & \cdots & u_2 \\ & & \ddots & & & \\ v_{n_{end}-1} & \cdots & v_{n_{end}-M_2} & u_{n_{end}} & \cdots & u_{n_{end}-M_2+1} \end{bmatrix} \begin{bmatrix} E_1 \\ \vdots \\ E_{M_2} \\ F_0 \\ \vdots \\ F_{M_2-1}. \end{bmatrix}. \tag{A.8}$$

This system of equations can be solved to obtain the unknowns E_l and F_l. Then, the partial fraction decomposition of Equation (A.6) is used to identify b_l and β_l in Equation (A.5).

The iterative process has four steps as follows:

- Step 1: first, form initial estimates for k_i by fitting a N^{th} order polynomial to the average of loading and unloading stress-strain curves. Then, knowing k_i, the elastic component Σ_e is constructed,
- Step 2: subtract the measured total, e.g. from experiment, from the estimated elastic stress to form initial guess for σ_{v2} as $\sigma_{v2} = \sigma - \sigma_e$,

- Step 3: b's and β's are estimated by solving Equation (A.8) and σ_{v2} is reconstructed,
- Step 4: Subtract the measured total stress, e.g. from experiment, from the estimated viscoelastic stress σ_{v2} to form initial guess for σ_e as $\sigma_e = \sigma - \sigma_{v2}$.

Steps 2 to 4 are repeated until convergence in the viscoelastic parameters and the elastic component is observed.

Appendix B. Parameter Estimation for Foam Model 3

In chapter 2 of this thesis, 4 different nonlinear foam models were reviewed. The models were given in Table 3.2. In this section, procedures for estimating the parameters of Model 3, given the values for N and M_1, and the stress-strain test data, are described. Note that Foam model 2 is a especial case of model 3. Therefore, the process of estimating the parameters of model 2 is very similar to the procedures discussed below. The foam model 3 is given by

$$\sigma = \sigma_e + \sigma_{v1} = \sum_{i=1}^{N} k_i \epsilon^i(t) + \int_0^t \sum_{j=1}^{M_1} a_j e^{-\alpha_j (t-\tau)} \sum_{i=1}^{N} k_i \epsilon^i(\tau) d\tau. \tag{B.1}$$

The full description of the model was given in Chapter 2.

The first step is to transform the differential equation form of the model into a discrete-time model by using an impulse invariant mapping of the hereditary kernels [82, 83]. Consider Model 3 as,

$$\sigma(t) \equiv \sigma_e(t) + \sigma_{v1}(t) = \sigma_e(t) + \sum_{j=1}^{M_1} a_j e^{-\alpha_j t} * \sigma_e(t) = \sigma_e(t) * \{\delta(t) + \sum_{j=1}^{M_1} a_j e^{-\alpha_j t}\}. \tag{B.2}$$

The impulse response of this system relating $\sigma_e(t)$ to $\sigma(t)$ can be expressed as,

$$h(t) = \delta(t) + \sum_{j=1}^{M_1} a_j e^{-\alpha_j t}, \tag{B.3}$$

where $\delta(t)$ represents unit impulse function. Sampling the impulse response at the sampling frequency f_s (Hz), yields:

$$h(n\Delta) = h_n = \Delta[\delta_n + \sum_{j=1}^{M_1} a_j e^{-\alpha_j n\Delta}], \tag{B.4}$$

where Δ is the sampling interval in seconds which is the inverse of sampling frequency (f_s), $\delta_n = 1$ for $n = 0$ and $\delta_n = 0$ if $n \neq 0$. Taking z-transform of Equation (B.4) gives,

$$H(z) = \Delta \left[1 + \sum_{j=1}^{M_1} \frac{a_j}{1 - e^{-\alpha_j \Delta} z^{-1}} \right]. \tag{B.5}$$

This can be rewritten as,

$$\begin{aligned} H(z) &= 1 + \frac{B_0 + B_1 z^{-1} + \cdots + B_{M_1-1} z^{-(M_1-1)}}{1 + A_1 z^{-1} + \cdots + A_{M_1} z^{-M_1}} \\ &= \frac{(1 + B_0) + (B_1 + A_1) z^{-1} + \cdots + a_{M_1} z^{-M_1}}{1 + A_1 z^{-1} + \cdots + A_{M_1} z^{-M_1}}. \end{aligned} \tag{B.6}$$

This can be further simplified as,

$$H(z) = \frac{D_0 + D_1 z^{-1} + \cdots + D_{M_1} z^{-M_1}}{1 + C_1 z^{-1} + \cdots + C_{M_1} z^{-M_1}}. \tag{B.7}$$

If x_n is the input to this filter and y_n is the output, then the difference equation can be written as,

$$y_n = -C_1 y_{n-1} - \cdots - C_{M_1} y_{n-M_1} + D_0 x_n + \cdots + D_{M_1} x_{n-M_1}. \tag{B.8}$$

Here, $x_n = \sigma_e(n\Delta)$ and $y_n = \sigma(n\Delta)$. Note that this is a (M_1, M_1) $NARMAX$ filter. If $\sigma_e(n\Delta)$ and $\sigma(n\Delta)$ are known, Equation (B.8) can be used to develop the following set of equations:

$$\begin{bmatrix} y_{M_1+1} \\ y_{M_1+2} \\ \vdots \\ y_{n_{end}} \end{bmatrix} = \begin{bmatrix} y_{M_1} & \cdots & y_1 & x_{M_1+1} & \cdots & x_1 \\ & & \ddots & & & \\ y_{n_{end}-1} & \cdots & y_{n_{end}-M_1} & x_{n_{end}} & \cdots & x_{n_{end}-M_1} \end{bmatrix} \begin{bmatrix} C_1 \\ \vdots \\ C_{M_1} \\ D_0 \\ \vdots \\ D_{M_1}. \end{bmatrix}, \tag{B.9}$$

where n_{end} is the last sample. The system of equations can be solved to identify C_j and D_j (or A_j and B_j). Then, the partial fraction decomposition of Equation (B.7) is used to identify the viscoelastic parameters a's and α's.

Recall that $\sigma_e(n\Delta) = \sum_{i=1}^{N} k_i \epsilon^i(n\Delta)$. Using this, Equation (B.8) can be expanded and reorganized as follows:

$$\begin{aligned} \rho_n &\equiv y_n + C_1 y_{n-1} + \cdots + C_{M_1} y_{n-M_1} \\ &= k_1(D_0\epsilon_n + \cdots + D_{M_1}\epsilon_{n-M_1}) + \cdots + k_N(D_0\epsilon_n^N + \cdots + D_{M_1}\epsilon_{n-M_1}^N). \end{aligned} \tag{B.10}$$

If C_j and D_j are known along with ϵ_n and $y_n = \sigma(n\Delta)$, then Equation (B.10) can be used to construct the following system of equations:

$$\begin{bmatrix} \rho_{M_1+1} \\ \vdots \\ \rho_{n_{end}} \end{bmatrix} = \begin{bmatrix} D_0\epsilon_{M_1+1} + \cdots + D_{M_1}\epsilon_1 & \cdots & D_0\epsilon_{M_1+1}^N + \cdots + D_{M_1}^N\epsilon_1 \\ & \ddots & \\ D_0\epsilon_{n_{end}} + \cdots + D_{M_1}\epsilon_{n_{end}-M_1} & \cdots & D_0\epsilon_{n_{end}}^N + \cdots + D_{M_1}^N\epsilon_{n_{end}-M_1} \end{bmatrix} \left[C_1, \cdots, C_{M_1}, D_0, \cdots, D_{M_1}\right]^T. \tag{B.11}$$

Finally, the linear regression can be used to estimate the polynomial coefficients k_i.

The iterative process has three steps as follows:

- Step 1: first, form initial estimates for k_i by fitting a N^{th} order polynomial to the average of loading and unloading stress-strain curves. Then, knowing k_i, the elastic component Σ_e is constructed,
- Step 2: solve Equation (B.9) to estimate the viscoelastic parameters a's and α's and σ_{v1} is constructed,
- Step 3: solve Equation (B.11) to estimate the elastic parameters k's and σ_e is constructed.

Steps 2 to 3 are repeated until convergence in the viscoelastic parameters and the elastic component is observed.

Appendix C. Governing Equations Used to Estimate the Transient Response of the Seat-Occupant System

The constrained Lagrangian formulation is used to derive the governing equations of the seat-occupant system. A holonomic constraint is imposed on the motion as the occupant's foot is constrained to slide along the floor pan. Equations of motion are then modified by incorporating constraint forces which are expressed in terms of the Lagrange multiplier λ. Puri [32] has shown that the equations of motion can be expressed as,

$$\begin{bmatrix} M_1 & 0 & A_1 & A_2 & A_3 & 0 \\ 0 & M_1 & B_1 & B_2 & B_3 & 0 \\ C_1 & C_2 & M_7 & 0 & 0 & 0 \\ D_1 & D_2 & 0 & M_8 & D_3 & 0 \\ E_1 & E_2 & 0 & E_3 & M_9 & 0 \end{bmatrix} \begin{Bmatrix} \ddot{\xi} \\ \ddot{\zeta} \\ \ddot{\theta}_1 \\ \ddot{\theta}_2 \\ \ddot{\theta}_3 \end{Bmatrix} = \begin{Bmatrix} -A_4 \\ -B_4 \\ -C_4 \\ -D_4 \\ -E_4 \end{Bmatrix} - \lambda \begin{Bmatrix} B_{11} \\ B_{21} \\ B_{31} \\ B_{41} \\ B_{51} \end{Bmatrix} + \lambda\mu_{foot} \begin{Bmatrix} C_{11} \\ C_{21} \\ C_{31} \\ C_{41} \\ C_{51} \end{Bmatrix}, \tag{C.1}$$

where ξ is the horizontal displacement of the hip joint, ζ is the vertical displacement of the hip joint, and θ_1, θ_2, and θ_3 are the rotations of the torso, femur and shin, respectively. The variables on the left side of the equation are given by:

$$\begin{aligned} M_1 &= m_1 + m_2 + m_3, & A_1 &= -m_1 l_2 \sin(\theta_1), \\ A_2 &= -\sin(\theta_2)(m_2 l_3 + m_3 l_3 + m_3 l_4), & A_3 &= -m_3 l_5 \sin(\theta_3), \\ B_1 &= m_1 l_2 \cos(\theta_1), & B_2 &= \cos(\theta_2)(m_2 l_3 + m_3 l_3 + m_3 l_4), \\ B_3 &= m_3 l_5 \cos(\theta_3), & C_1 &= -m_1 l_2 \sin(\theta_1), \\ C_2 &= m_1 l_2 \cos(\theta_1), & M_7 &= I_1 + m_1 l_2^2, \\ D_1 &= -\sin(\theta_2)(m_2 l_3 + m_3 l_3 + m_3 l_4), & D_2 &= \cos(\theta_2)(m_2 l_3 + m_3 l_3 + m_3 l_4), \\ M_8 &= m_3(l_3 + l_4)^2 + m_2 l_3^2 + I_2, & D_3 &= m_3 l_5 (l_3 + l_4)\cos(\theta_2 - \theta_3), \\ E_1 &= -m_3 l_5 \sin(\theta_3), & E_2 &= m_3 l_5 \cos(\theta_3), \\ E_3 &= m_3 l_5 (l_3 + l_4)\cos(\theta_3 - \theta_2), & M_9 &= I_3 + m_3 l_5^2, \end{aligned}$$

where the variables are shown in Figure 6.1. The variables on the right side Equation (C.1) are given by:

$$\begin{aligned}
A_4 &= -m_1 l_2 \cos(\theta_1)\dot{\theta_1}(t)^2 - \cos(\theta_2)\dot{\theta_2}(t)^2(m_2 l_3 + + m_3 l_3 + m_3 l_4), \\
&\quad -m_3 l_5 \cos(\theta_3)\theta_3\dot{(t)}^2 + \cos(\theta_1)\textstyle\sum_{j=1}^{r} F_j^{interface,torso} \\
&\quad + \cos(\theta_2)\textstyle\sum_{j=1}^{w} F_j^{interface,femur} + \Delta_\xi, \\
B_4 &= -m_1 l_2 \sin(\theta_1)\dot{\theta_1}(t)^2 - \sin(\theta_2)\dot{\theta_2}(t)^2(m_2 l_3 + + m_3 l_3 + m_3 l_4), \\
&\quad -m_3 l_5 \sin(\theta_3)\theta_3\dot{(t)}^2 + g(m_1 + m_2 + m_3) \\
&\quad - \sin(\theta_1)\textstyle\sum_{j=r}^{w} F_j^{interface,torso} + \sin(\theta_2)\sum_{j=1}^{w} F_j^{interface,femur} + \Delta_\zeta, \\
C_4 &= g m_1 l_2 \cos(\theta_1) + \Delta_{\theta_1}, \\
D_4 &= g\cos(\theta_2)(m_2 l_3 + m_3 l_3 + m_3 l_4) + m_3(l_3 l_5 + l_5 l_4)\sin(\theta_2 - \theta_3)(\dot{\theta_3})^2 + \Delta_{\theta_2}, \\
E_4 &= g m_3 l_5 \cos(\theta_3) + m_3(l_3 l_5 + l_5 l_4)\sin(\theta_3 - \theta_2)(\dot{\theta_2})^2.
\end{aligned}$$

The Δ terms in the above expressions are given by:

$$\begin{aligned}
\Delta_\xi &= \textstyle\sum_{i=1}^{w+r} F(\delta_i)\frac{\partial \delta_i}{\partial \xi} + \sum_{i=1}^{u} c_i\dot{\delta}_i\frac{\partial \dot{\delta}_i}{\partial \dot{\xi}}, & \Delta_\zeta &= \textstyle\sum_{i=1}^{w+r} F(\delta_i)\frac{\partial \delta_i}{\partial \zeta} + \sum_{i=1}^{u} c_i\dot{\delta}_i\frac{\partial \dot{\delta}_i}{\partial \dot{\zeta}}, \\
\Delta_{\theta_1} &= \textstyle\sum_{i=1}^{w+r} F(\delta_i)\frac{\partial \delta_i}{\partial \theta_1} + \sum_{i=1}^{u} c_i\dot{\delta}_i\frac{\partial \dot{\delta}_i}{\partial \dot{\theta}_1}, & \Delta_{\theta_2} &= \textstyle\sum_{i=1}^{w+r} F(\delta_i)\frac{\partial \delta_i}{\partial \theta_2} + \sum_{i=1}^{u} c_i\dot{\delta}_i\frac{\partial \dot{\delta}_i}{\partial \dot{\theta}_2},
\end{aligned}$$

The elements of the Jacobian matrix $[B]$ are given by:

$$\begin{aligned}
B_{11} &= -1, \\
B_{21} &= \tfrac{a\sin(\beta)}{(l_q+\zeta+(l_3+l_4)\sin(\theta_2)+(l_5+l_6)\sin(\theta_3))^2} + \cot(\beta), \\
B_{31} &= 0, \\
B_{41} &= \tfrac{a\sin(\beta)(l_3+l_4)\cos(\theta_2)}{(l_q+\zeta+(l_3+l_4)\sin(\theta_2)+(l_5+l_6)\sin(\theta_3))^2} + (l_3+l_4)\cos(\theta_2)\cot(\beta) \\
&\quad +(l_3+l_4)\sin(\theta_2), \\
B_{51} &= \tfrac{a\sin(\beta)(l_5+l_6)\cos(\theta_3)}{(l_q+\zeta+(l_3+l_4)\sin(\theta_2)+(l_5+l_6)\sin(\theta_3))^2} + (l_5+l_6)\cos(\theta_3)\cot(\beta) \\
&\quad +(l_5+l_6)\sin(\theta_3).
\end{aligned}$$

The elements of the matrix $[C]$ are given by:

$$\begin{aligned}
C_{11} &= \cos(\theta_{sl}), \\
C_{21} &= \sin(\theta_{sl}), \\
C_{31} &= 0, \\
C_{41} &= (l_3+l_4)\sin(\theta_{sl}-\theta_2), \\
C_{51} &= (l_5+l_6)\sin(\theta_{sl}-\theta_3).
\end{aligned}$$

In the above Equations ξ, ζ, θ_1, θ_2, and θ_3 are the generalized coordinates which are shown in Figure 5.4. δ_i is the compression in each spring element. l_i are the distances from the centers of mass measured from the joints. The force $F(\delta_i)$ is the spring force.

Appendix D. The Initial Conditions Used to Solve the Seat-Occupant System Governing Equations

In simulations in Chapters 6 and 7, the occupant was placed so that the occupant's bodies are just in contact with the seat. The initial conditions corresponding to this for the mannequin modeled in this research is given in Table D.1.

Table D.1. The initial conditions used to solve the system governing equations.

ξ (m)	+ 0.125
ζ (m)	+ 0.173
θ_1 $(degree)$	+105
θ_2 $(degree)$	+5
θ_3 $(degree)$	−40

Appendix E. Model Parameters for the Baseline Seat-Occupant System

In the following tables various parameter values of the seat-occupant system that are used in the simulations described in Chapter 6 are presented.

Table E.1. Seat parameter values used in the simulations.

Parameter	*Symbol*	*Value*
Angle of the seat rail (°)	α	5.0
Angle of the seat back (°)	θ_s	110.0
Distance from seat corner to base of foot rest (m)	l_0	0.899
Distance from seat rail to seat cushion (m)	l_q	0.163
Number of springs at the back of the seat	N_{back}	
Chapter 6		20
Chapter 7		15
Number of springs at the bottom of the seat	N_{bottom}	
Chapter 6		20
Chapter 7		15
Contact area at the seat back for a Chrysler LH seat		9 in×12 in
Contact area at the seat bottom for a Chrysler LH seat		15 in×12 in
Friction coefficient at the foot-rail interface	μ_f	0.4
Friction coefficient at the torso-seat back interface	μ_{back}	0.35
Friction coefficient at the femur-seat bottom interface	μ_{bottom}	0.35

Table E.2. The inertial properties of the seat occupant (dummy) used in the simulations.

Parameter	*Symbol*	*Value*
Mass of torso, neck, pelvis and arms (kg)	m_1	34.138
Mass of femur (kg)	m_2	17.844
Mass of shin (kg)	m_3	7.948
Mass moment of inertia of torso, neck, pelvis and arms (kgm^2)	I_1	1.3927
Mass moment of inertia of femur (kgm^2)	I_2	0.3352
Mass moment of inertia of shin (kgm^2)	I_3	0.1973
Length of torso and pelvis (m)		0.6223
Length of femur (m)		0.5334
Length of shin (m)		0.4572

Appendix F. Estimated Parameters for Low Density Foam 1 and Foam 2

The estimated viscoelastic parameters for low density Foam 1 are given in Tables F.1 and F.2. Also, the estimated viscoelastic parameters for low density Foam 2 are given in Tables F.3. The parameters were estimated by fitting foam Model 4 to the experimental data using the parameter estimation process explained in Chapter 3. The estimated parameters given in the table were also used in Chapter 3 to estimate the foam responses at different rates.

Table F.1. Estimates of the viscoelastic parameters in Model 4. Estimates were calculated using data from the first four tests (T_1, T_2, T_3, and T_4). To obtain similar prediction accuracy in the longer duration tests more viscoelastic terms are needed (see Table 3.5). $\pm$ represents the standard deviation of the estimates given in Figs. 3.8 and 3.9.

	α_1	β_1	a_1	b_1
T_1	1.48±0.06	0.55±0.02	-0.103±0.004	38810±970
T_2	0.96±0.01	0.38±0.01	-0.083±0.002	49750±1500
T_3	0.542±0.008	0.267±0.005	-0.0451±0.0005	65523±1310
T_4	0.319±0.003	0.166±0.002	-0.0281±0.0003	78939 ±790

Table F.2. Estimated viscoelastic parameters for Model 4 for tests T_5 and T_6 where $N = 10$, $M_1 = 1$, and $M_2 = 5$. $\pm$ represents the standard deviation of the estimates given in Figs. 3.8 and 3.9.

	α_1	$\beta_1,\cdots,\beta_5$	a_1	$b_1,\cdots,b_5$
T_5	1.40	0.051 2.20±6.96i 2.48±13.00i	-0.152	3.34 -3.25±1.53 2.53±6.52
T_6	1.07	0.041 1.89±5.76i 2.27±10.91i	-0.123	38720 -98550±16410 130750±105620

Table F.3. Estimates of the viscoelastic parameters in Model 4 when one viscoelastic term is included in each viscoelastic component. Estimates were calculated using data from the first four tests (T_1, T_2, T_3, and T_4).

	α_1	β_1	a_1	b_1
T_1	3.55±0.05	0.75±0.02	-0.103±0.004	40001±970
T_2	0.88±0.03	0.45±0.01	-0.067±0.002	51025±1500
T_3	0.566±0.008	0.345±0.005	-0.456±0.0005	78523±1310
T_4	0.519±0.003	0.234±0.002	-0.0333±0.0003	92015 ±790

Appendix G. Estimated Parameters of CONFOR Foams

The estimated viscoelastic parameters for three types of CONFOR foams are given in Tables G.1 to G.3. The CONFOR foam properties are given in Table 3.6. The parameters were estimated by fitting foam Model 4 to the experimental data using the parameter estimation process explained in Chapter 3. The estimated parameters given in the table were also used in Chapter 3 to estimate the responses of CONFOR foams at different rates.

Table G.1. Estimates of the viscoelastic parameters of Foam 1. ± represents the standard deviation of the estimates.

input strain rate	α_1	β_1
$0.00438/s$	0.431±0.001	0.442±0.007
$0.00109/s$	0.1541±0.0008	0.2069±0.002
$0.00052/s$	0.0943±0.0003	0.145±0.001
$0.00026/s$	0.0603±0.0002	0.0945±0.0004
input strain rate	a_1	b_1
$0.00438/s$	-0.2680±0.0008	37941±639
$0.00109/s$	-0.0830±0.0004	51216±486
$0.00052/s$	-0.0507±0.0001	61782±335
$0.00026/s$	-0.0319±0.0001	78941.06±334

Table G.2. Estimates of the viscoelastic parameters of Foam 2. ± represents the standard deviation of the estimates.

input strain rate	α_1	β_1	a_1	b_1
$0.00438/s$	0.3539±0.002	0.301±0.006	-0.1988±0.0008	2237±101
$0.00109/s$	0.08±0.01	0.085±0.002	-0.0355±0.0005	2919±84
$0.00052/s$	0.0366±0.0003	0.066±0.001	-0.0154±0.0003	4348±102
$0.00026/s$	0.0167±0.0003	0.0200±0.0005	-0.0063±0.0003	6042±55

Table G.3. Estimates of the viscoelastic parameters of Foam 3. ± represents the standard deviation of the estimates.

input strain rate	α_1	β_1	a_1	b_1
$0.00438/s$	0.280±0.003	0.224±0.009	-0.152±0.001	6303±59
$0.00109/s$	0.0657±0.0005	0.061±0.001	-0.0300±0.0004	9460±408
$0.00052/s$	0.0342±0.0004	0.0309±0.0009	-0.0142±0.0003	11062±236
$0.00026/s$	0.0135±0.0003	0.0136±0.0006	-0.0048±0.0005	16418±334

Appendix H. Estimated Parameters of Foam Model 1, Foam Model 3 and Foam Model 4

The viscoelastic parameters estimated for foam Model 1, and Model 3 and Model 4 are given in Table H.1. The parameters were estimated by fitting the foam models to the experimental data from conducting a compression test (strain rate equals to $88 \times 10^{-4}\ s^{-1}$) on the low density Foam 1. The parameters were used in Chapter 4 to characterize the mechanical behavior of foam used in the single-degree-of-freedom foam-mass system. Note that estimated parameters of foam Model 4 is the same as the ones presented in Table F.1 after some scaling.

Table H.1. Model parameters estimated from model fits to quasi-static compression test data.

	Model 1	Model 3	Model 4
$k_1\ (N/m)$	3.23×10^3	4.68×10^3	3.40×10^3
$k_2\ (N/m^2)$	-2.70×10^5	-3.63×10^5	-2.76×10^5
$k_3\ (N/m^3)$	1.12×10^7	1.52×10^7	1.12×10^7
$k_4\ (N/m^4)$	-2.23×10^8	-3.01×10^8	-2.17×10^8
$k_5\ (N/m^5)$	1.72×10^9	2.33×10^9	1.68×10^9
$a_1\ (1/s)$	-	-0.037	-0.104
$b_1\ (N/m)$	2.28×10^3	-	2.96×10^3
$b_2\ (N/m)$	1.11×10^3	-	-
$\alpha_1\ (1/s)$	-	0.084	1.44
$\beta_1\ (1/s)$	1.00	-	0.553
$\beta_2\ (1/s)$	0.325	-	-

Appendix I. Strain-Rate Dependant Foam Model Parameters

In Chapter 3, simple functions were identified which govern the relationships between estimated viscoelastic parameters of foam Model 4 and the input strain rate. The estimated functions are given by Equation (I.1). Foam Model 4 with strain rate dependent viscoelastic parameters given by Equation (I.1) were used in Chapters 4, 6 and 7 to characterize the mechanical behavior of foam in the single-degree-of-freedom foam-mass system (Chapter 4) and in the seat-occupant model (Chapters 6 and 7).

$$\begin{aligned} a_1(|\dot{\epsilon}|) &= -9.2|\dot{\epsilon}| - 0.027, \\ \alpha_1(|\dot{\epsilon}|) &= 147.1|\dot{\epsilon}| + 0.21, \\ b_1(|\dot{\epsilon}|) &= \frac{1}{1.6 \times 10^{-3}|\dot{\epsilon}| + 1.16 \times 10^{-5}}, \\ \beta_1(|\dot{\epsilon}|) &= 47.2|\dot{\epsilon}| + 0.14, \end{aligned} \tag{I.1}$$

where $\dot{\epsilon}$ is the input strain rate.

Appendix J. Estimating Equivalent Local Parameters for CONFOR Foams

The mechanical behavior of CONFOR foams were studied and the results of the studies were reported in Chapter 3. For each foam type, two types of models, a low order model with strain rate dependent parameters and a high order model with strain rate independent parameters, were identified, which describe the large strain behavior of the foam at different rates. In practice CONFOR foams, used for cushioning, vibration/noise and shock isolation, are usually precompressed to a certain level and then subjected to low amplitude oscillatory inputs. Due to strong nonlinear viscoelastic behavior of these materials, their local mechanical behaviors such as local damping and local stiffness behavior, are greatly affected by the level of precompression, amplitude and frequency of the excitation. For these applications simpler models can be estimated, which characterize the local linear behavior of CONFOR foams. In this section, the local linear dynamic behaviors of CONFOR foams are described. By using the identified comprehensive nonlinear viscoelastic foam models, foam responses are constructed when the foam is subjected to oscillatory inputs about different precompression levels. The predicted harmonic responses are then used to identify linear quantities which characterize the local and linear damping and dynamic stiffness of CONFOR foams. It is observed that the local dynamic behavior of foams are different for different CONFOR foam types and vary when the foams are compressed to different precompression levels and for different excitation frequencies

In order to characterize the linear dynamic behavior of materials, different methods can be adopted. In one approach, the material is compressed to a certain level and then is subjected to an impulse. Then the logarithmic decrement method is used to estimate the linear damping coefficient from the system transient response, or a Prony Series is fitted to the data and the exponential decay and natural frequencies can be used to determine the damping ratio and the stiffness. In another approach, the material is subjected to a harmonic input and the resultant force-displacement curves are used to estimate the damping coefficient and the dynamic stiffness coeffi-

cient. In this study the second estimation approach is used. The input displacement is defined as

$$S = S_{average} + \Delta S sin(2\pi f t), \tag{J.1}$$

where $S_{average}$, ΔS and f are precompression, amplitude and frequency, respectively. Note that the input strain Equation (J.1) can be converted to displacement by multiplying the strain by the foam thickness. Due to foam's high damping property, the foam response quickly reaches steady-state. Here, the estimated foam model with strain rate dependent parameters (see section 3.6.4) was used to predict the Foam 1 response to the input given by Equation (J.1) with $S_{average} = 57\ mm$ (corresponding to 75% precompression in foam), $\Delta S = 0.76\ mm$ (corresponding to 1% of the foam thickness) and $f = 0.01\ Hz$. A sample force-displacement result is shown in Figure J.1. It is clear that the response reaches steady-state quickly, after just one cycle. Here, to ensure the response reaches the steady state, the total time of the test is set to $t = \frac{1}{f}$ i.e. 10 cycles.

In general foam response subjected to the input given in Equation (J.1) is nonlinear. The force-displacement responses for different input amplitude values are shown in Figure J.2. It is clear that for larger input amplitude the response exhibits nonlinear behavior. However, if the input amplitude is small enough, the foam response is close to linear. The foam steady state responses to harmonic input at different precompression levels when $\Delta S = 0.76\ mm$ (corresponding to 1% of the foam thickness) and $f = 0.01\ Hz$ are shown in Figure J.3(a).

The area of the hysteresis loop shown in Figure J.1 can be measured and it is denoted as A_{loss}.Using Green theorem,

$$A_{loss} = \frac{1}{2} \oint_C \left(SdF - FdS \right), \tag{J.2}$$

where C is the contour of the hysteresis loop shown in Figure J.1 and F and S are force and displacement, respectively. Recalling that F and S are functions of time t and integrating over one period, Equation (J.2) is expressed as

$$A_{loss} = \frac{1}{2} \int_t^{t+T} \left(S\frac{dF}{dt} - F\frac{dS}{dt} \right) dt, \tag{J.3}$$

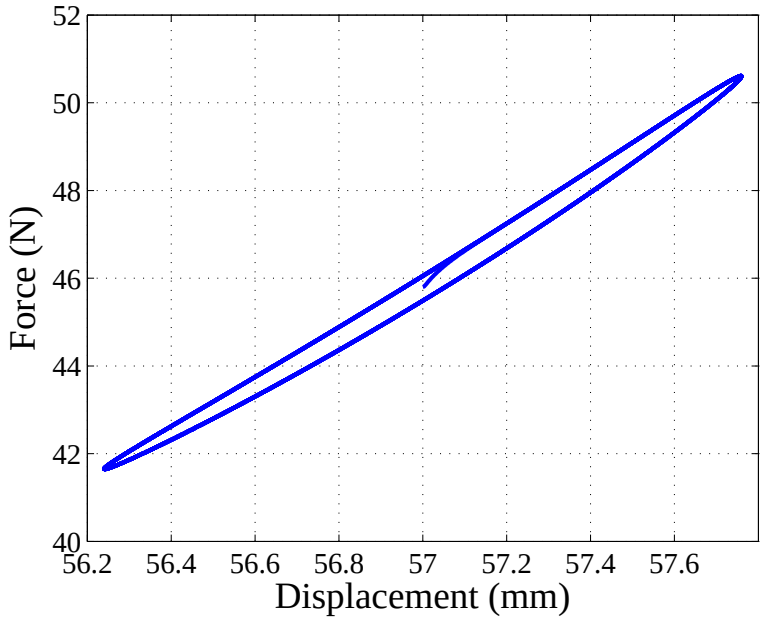

Figure J.1. Force-displacement response when CONFOR Foam 1 is subjected to harmonic input in Equation (J.1).

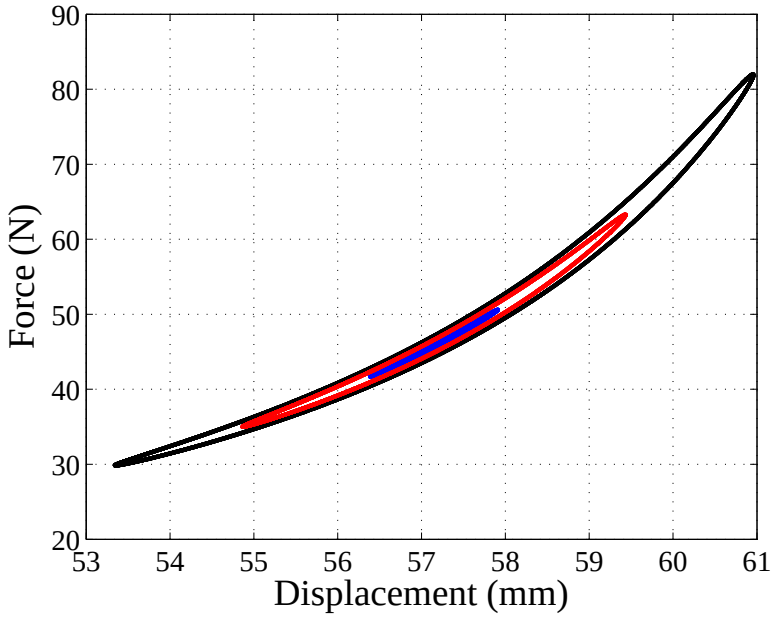

Figure J.2. Force-displacement response when CONFOR Foam 1 is subjected to harmonic input with different amplitude ΔE. Blue: $\Delta S = 0.76\ mm$ (corresponding to 1% of the foam thickness), red: $\Delta S = 2.28\ mm$ (corresponding to 3% of the foam thickness) and black: $\Delta S = 3.80\ mm$ (corresponding to 5% of the foam thickness). $S_{average} = 57\ mm$ (corresponding to 75% precompression in foam).

where T is the period. A common quantity which is used to characterize the damping properties of materials is the loss angle δ. This parameter can be interpreted as the phase shift between the input displacement and the corresponding measured force. The measured force can be expressed as

$$F = F_{average} + \Delta F sin(2\pi ft + \delta), \tag{J.4}$$

where $F_{average}$ and ΔF are shown in Figure J.3(b). Substituting Equations (J.1) and (J.4) into Equation (J.2) and integrating over a period gives,

$$A_{loss} = \pi \Delta S \Delta F sin(\delta). \tag{J.5}$$

Then the loss angle δ is

$$\delta = sin^{-1}\left(\frac{A_{loss}}{\pi \Delta S \Delta F}\right). \tag{J.6}$$

Another important parameter which is often used to characterize the local behavior of foam materials is the dynamic stiffness $K_{dynamic}$. For nonlinear materials, this parameter is calculated by linearizing the elastic component about the operating point. Alternatively, if the response is close to linear, the local stiffness can be defined as

$$K_{dynamic} = \frac{\Delta S}{\Delta F}, \tag{J.7}$$

where ΔS and ΔF are shown in Figure J.3(b).

The estimated loss angles for CONFOR Foam 1, Foam 2 and Foam 3 are shown in Figures J.4. In Figure J.4(a), the estimated loss angles are shown as functions of the precompression level. Here the amplitude of excitation is small $\Delta S = 0.76\ mm$ (corresponding to 1% of the foam thickness) to keep the response close to linear. The input frequency is $f = 0.01\ Hz$. It is clear from Figure J.4(a) that for Foam 1 the loss angle is maximum when the precompression is 15% and 28%. Comparing the estimated loss angle with the measured stress-strain curves from compression tests shown in section 3, it is observed that, in general, the damping property of all three foams is maximum when the foam is operating in the middle region, known as collapse region. Also, the estimated loss angle is the largest for Foam 3. Although for

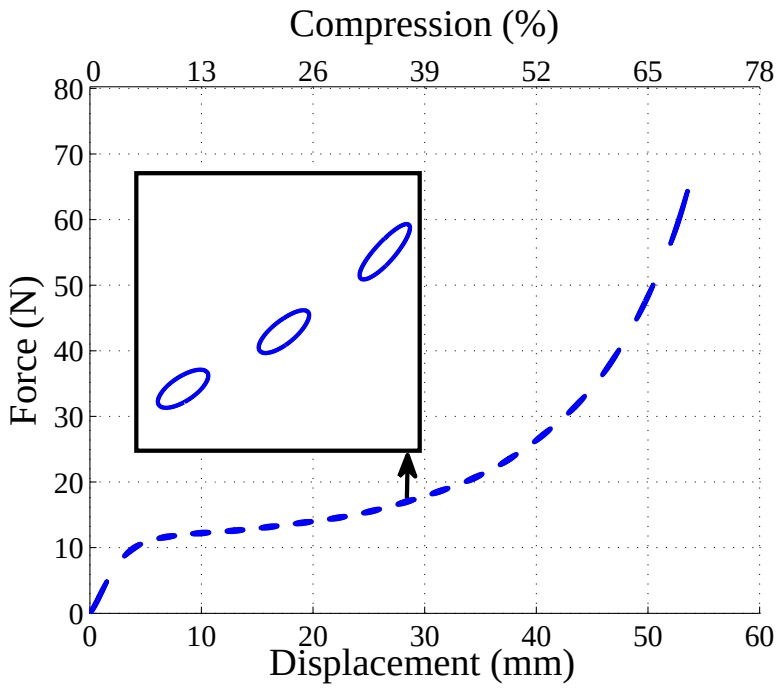

(a)

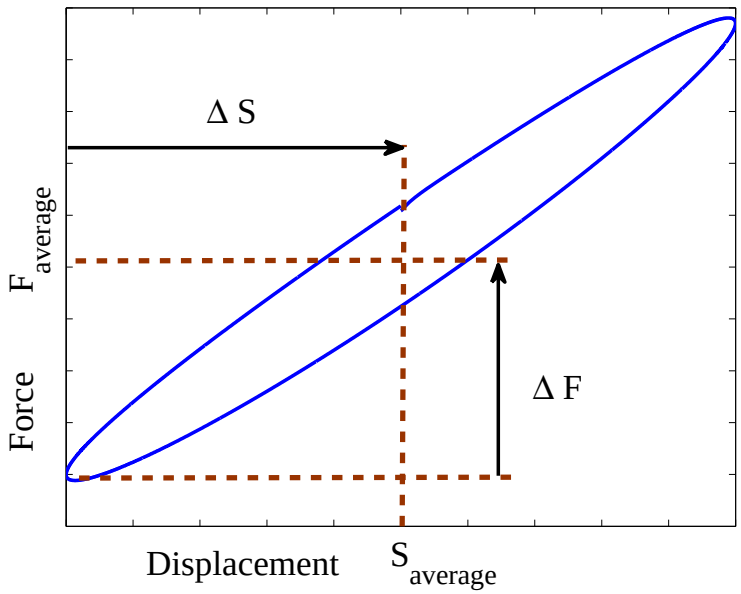

(b)

Figure J.3. Force-displacement response when foam is subjected to harmonic displacement input. (a) estimated response for different precompression levels, (b) the estimated force-displacement response.

higher operating levels, Foam 1 has a stronger damping property. The estimated loss angles as functions of the input frequency is shown in Figure J.4(b). Here, foam was precompressed by 30% and the operating level $\Delta S = 0.76\ mm$. It is observed that by increasing the excitation frequency, the estimated loss angle increases. However, if the excitation frequency is beyond 0.2 Hz, the variations in the estimated loss angles become very small. For higher frequencies, the damping property of Foam 2 is stronger than the damping properties of Foam 1 and Foam 3. Note that for lower frequencies, i.e. $f = 0.01\ Hz$, the damping property of Foam 3 is stronger than the damping properties of Foam 1 and Foam 2.

The estimated dynamic stiffness coefficients for CONFOR Foam 1, Foam 2 and Foam 3 are shown in Figures J.5. In Figure J.5(a), the estimated dynamic stiffness coefficients are shown as functions of the precompression level. Here the amplitude of excitation is small $\Delta S = 0.76\ mm$ (corresponding to 1% of the foam thickness) and the input frequency is $f = 0.01\ Hz$. The estimated dynamic stiffness coefficients are minimum when the precompression level is in the range of 10% and 40% which corresponds to the collapse region in the experimentally measured stress-strain responses of CONFOR foams. The estimated dynamic stiffness coefficients as functions of the input frequency are shown in FigureJ.5(b). Here, foam was precompressed by 30% and the operating level $\Delta S = 0.76\ mm$. It is observed that the estimated dynamic stiffness coefficients are almost linear functions of the frequency and monotonically increase as the frequency is increased. Also it is observed that when the excitation frequency is low Foam 2 is the stiffest foam while for higher frequencies Foam 3 is the stiffest among the three foams.

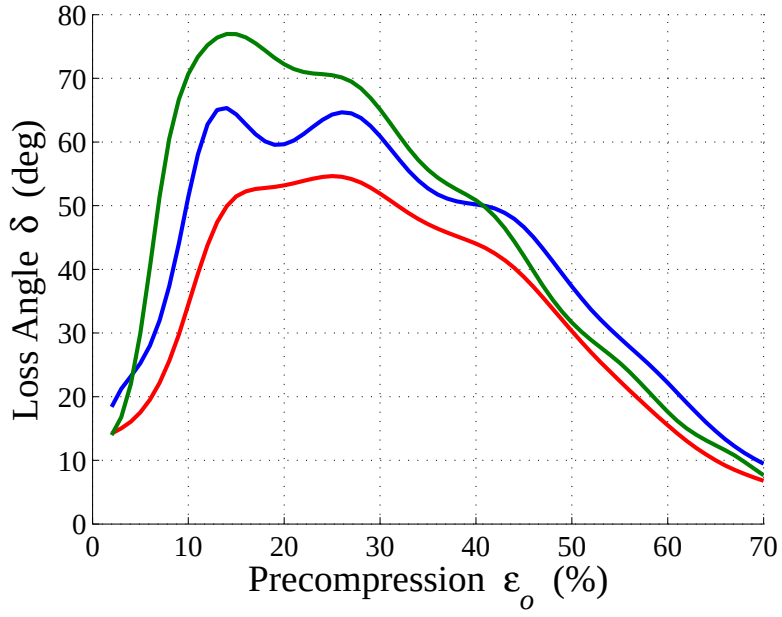

(a)

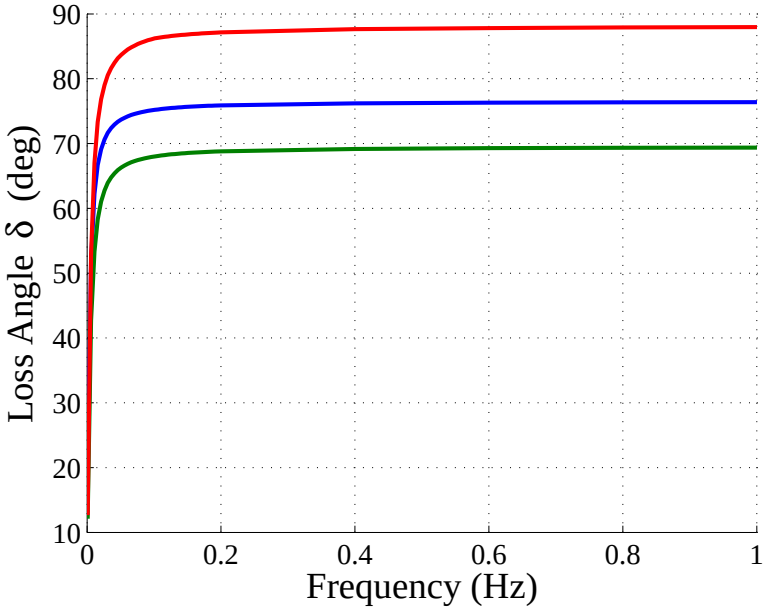

(b)

Figure J.4. Estimated Loss angle δ as a function of (a) precompression level when $\Delta S = 0.76\ mm$ and $f = 0.01\ Hz$ and (b) excitation frequency when $\Delta S = 0.76\ mm$ and precompression level is 30%. Blue: Foam 1, red: Foam 2, green: Foam 3.

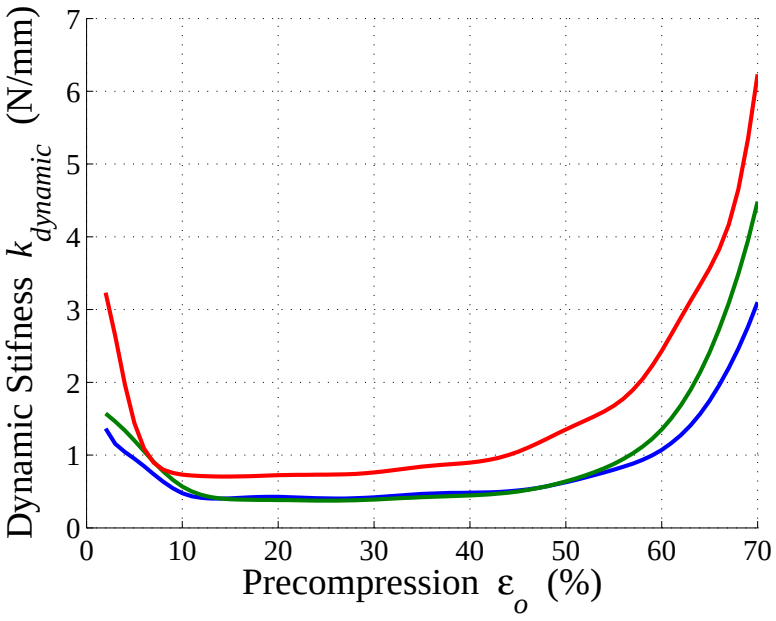

(a)

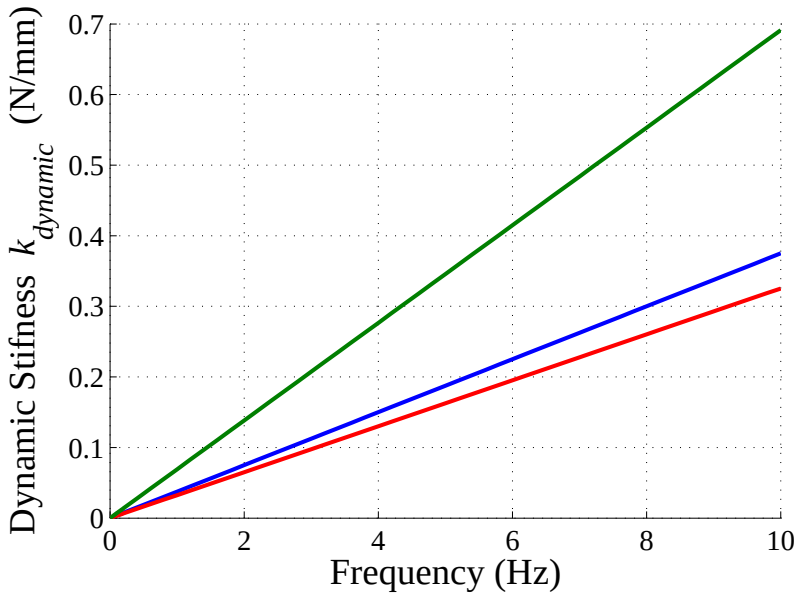

(b)

Figure J.5. Estimated dynamic stiffness K_{dynmic} as a function of (a) precompression level $\Delta S = 0.76\ mm$ and $f = 0.01\ Hz$ and (b) excitation frequency when $\Delta S = 0.76\ mm$ and precompression level is 30%. Blue: Foam 1, red: Foam 2, green: Foam 3.

Appendix K. Facilitating the Computation Process for Large Systems

The methodology discussed in Section 7.2 is similar to the method explained earlier in Chapter 4. Although, the methodology introduced in Section 7.2 is more efficient when it is applied to solve large nonlinear systems such as the multi-body seat-occupant system.

In order to estimate the system response, i.e. the generalized coordinates, Equations (7.17) and (7.19) are solved. Here, in Equation (7.17), $[\Pi]$, $[\Phi]$ and $[\Psi]$ are matrices that need to be determined. The elements of these matrices are functions of the elements of matrices $[A]$, $[D]$ and their derivatives such as $\frac{\partial A}{\partial q}$, $\frac{\partial A}{\partial q'}$, $\frac{\partial D}{\partial q}$ and etc. If the system is large, it is very difficult to differentiate the matrices parametrically as this involves differentiating many complex terms. To facilitate this process an alternative approach was developed.

Consider the damping matrix c in Equation (7.8). This matrix is defined as,

$$c(q, q') = -\frac{\partial D}{\partial q'}, \tag{K.1}$$

where matrix $[D]$ is given by Equation (5.54) by,

$$[D] = \begin{bmatrix} [S][Q] \\ -\omega^2[B'][q'] \end{bmatrix}. \tag{K.2}$$

Note that $[D]$ is a 6×6 matrix and its elements are complex functions of the generalized coordinates and given by Equations (5.27)-(5.29). Here, instead of differentiating the elements of the matrix parametrically, the derivatives of matrix $[D]$ are computed numerically. First, the assumed steady-state solutions for the generalized coordinates (see Equation (7.8)) are substituted into Equation (K.2) and used to evaluate each element of matrix $[D]$. Each element of matrix $[D]$ can be expressed by a Fourier series. That is,

$$\begin{aligned} q_j &= a_{j,0} + \sum_{l=1}^{NT}[a_{j,l}cos(l\tau) + b_{j,l}sin(l\tau)], \\ D_{j,i} &= m_{j,i,0} + \sum_{l=1}^{MT}[m_{j,i,l}cos(l\tau) + n_{j,i,l}sin(l\tau)], \end{aligned} \tag{K.3}$$

where q_j is the j^{th} generalized coordinate and $D_{j,i}$ is an element of matrix $[D]$. Also note that MT is chosen based on NT and the function describing $D_{j,i}$. To estimate the coefficients of the harmonic series given by Equation (K.3), the elements of matrix [D] are discretized (choosing a high enough sampling frequency so as to not alias the highest frequency that will result after nonlinear operations) and the coefficients are estimated by taking the discrete Fourier transform of the results. Here it is important to sample terms at high rates so that any effects of aliasing due to sampling of the harmonic functions over one period are very small. Next, differentiating q_j and $D_{j,i}$ with respect to τ gives,

$$\begin{aligned} \frac{\partial q_j}{\partial \tau} &= \sum_{l=1}^{NT}[-a_{j,l}lsin(l\tau) + b_{j,l}lcos(l\tau)], \\ \frac{\partial D_{j,i}}{\partial \tau} &= \sum_{l=1}^{MT}[-m_{j,i,l}lsin(l\tau) + n_{j,i,l}lcos(l\tau)]. \end{aligned} \tag{K.4}$$

The derivative of $D_{j,i}$ with respect to q_j is given by,

$$\frac{\partial D_{j,i}}{\partial q_j} = \frac{\frac{\partial D_{j,i}}{\partial \tau}}{\frac{\partial q_j}{\partial \tau}}. \tag{K.5}$$

Note that it is possible that the denominator of Equation (K.5) becomes zero. In that case the numerator of Equation (K.5) is also zero. To avoid any computational issue cased by dividing zero by zero, the equation is multiplied by a Heaviside function. Then Equation (K.5) can be expressed as,

$$\frac{\partial D_{j,i}}{\partial q_j} = \frac{\sum_{l=1}^{MT}[-m_{j,i,l}lsin(l\tau) + n_{j,i,l}lcos(l\tau)]}{\sum_{l=1}^{NT}[-a_{j,l}lsin(l\tau) + b_{j,l}lcos(l\tau)]}|Heaviside(-\frac{\partial q_j}{\partial \tau}) - Heaviside(\frac{\partial q_j}{\partial \tau})|. \tag{K.6}$$

Here $Heaviside$ represents the Heaviside function and is defined as,

$$Heaviside(x) = \begin{cases} -1, & \text{if } x < 0 \\ 0.5, & \text{if } x = 0 \\ +1, & \text{if } x > 0. \end{cases} \tag{K.7}$$

Note that since the coefficients of both harmonic series in Equation (K.6) are known, the right hand side of Equation (K.6) can be evaluated and expressed by a Fourier series as,

$$\frac{\partial D_{j,i}}{\partial q_j} = e_{j,i,0} + \sum_{l=1}^{MT} [e_{j,i,l} cos(l\tau) + f_{j,i,l} sin(l\tau)]. \tag{K.8}$$

Note that the procedure explained above can easily be coded in MATLAB and the process can be used to estimate the derivatives of matrices $[A]$ and $[D]$ (see Equation (7.7)), which then can be used to estimate matrices $[M]$, $[c]$, $[K]$ and $[\Omega]$ in Equation (7.8).

Appendix L. Estimation of Nonlinear Viscoelastic Parameters from Estimated Linear Models of Behavior Around Multiple Settling Points of a Foam-Mass System

In this section, a method is described to estimate the parameters of a global model of the foam behavior from data gathered in a series of impulse tests at different settling points. The estimated model is capable of describing the responses gathered from all the impulse tests using a unique set of parameters. The global model structure includes a nonlinear elastic term and a hereditary viscoelastic term. The model can be used to predict the settling point for each mass used and, by expanding the model about that settling point, local linear models of the response to impulsive excitation can be derived. From this analysis the relationship between the local linear model parameters and the global model parameters is defined. The parameters of the global model can be estimated using the data from conducting a series of impulse tests on a foam-mass system using different sized masses. The experimental foam-mass system is shown in Figure L.1. In this section, the parameters estimation process is described.

A schematic model of the foam-mass system shown in Figure L.1 is presented in Figure L.2. As discussed earlier in chapter 3, foam is modeled with three components: an elastic component represented by K(x) where x is the displacement of the top plate (can be converted to compression in foam if the initial length to foam is known), a viscoelastic component represented by V, and a viscous damper with coefficient c. Here the viscoelastic Model 2 is used to model the foam behavior. The equation of motion of this system can be expressed as:

$$\begin{aligned} m\ddot{x} + c\dot{x} + K(x) - V &= -mg - f(t), \qquad \text{(L.1)} \\ m\ddot{x} + c\dot{x} + \sum_{n=1}^{N} K_n x^n - \int_{-\infty}^{t} \sum_{i=0}^{M} g_i e^{-\alpha_i (t-\tau)} \dot{x}(\tau) d\tau &= -mg - f(t), \end{aligned}$$

where m is the riding mass, c is the viscous damping coefficient, K_n are the elastic parameters, g_i and α_i are the viscoelastic parameters, $f(t)$ is the external force provided by the impulse hammer in the experiments, M is the number of viscoelastic terms, and N is the order of the nonlinear elastic polynomial.

The global model given in Equation (L.2) can be linearized about the static settling point x_0 by setting $x = x_0 + y$. This yields equations of the form,

$$m\ddot{y} + c\dot{y} + k_L y - \int_{-\infty}^{t} \sum_{i=0}^{M} g_i e^{-\alpha_i (t-\tau)} \dot{y}(\tau) d\tau = -f(t), \tag{L.2}$$

where

$$k_L = \sum_{n=0}^{N} n K_n x_0^{n-1}. \tag{L.3}$$

Following the procedures discussed in chapter 4, the integral viscoelastic term in Equation (L.2) can be expressed as an M^{th} order differential equation. Here in this study it is assumed that $M = 2$. The viscoelastic term is represented by a linear differential equation as,

$$\ddot{V} + a_1 \dot{V} + a_2 V = b_1 \ddot{x} + b_2 \dot{x}, \tag{L.4}$$

where,

$$\begin{aligned} a_1 &= \alpha_1 + \alpha_2, \\ a_2 &= \alpha_1 \alpha_2, \\ b_1 &= g_1 + g_2, \\ b_2 &= g_1 \alpha_2 + g_2 \alpha_1. \end{aligned} \tag{L.5}$$

Combining Equations (L.2) and (L.4) gives,

$$\begin{aligned} m y^{iv} &+ (a_1 m + c) y^{iii} + (a_2 m + a_1 c + k_L - b_1) \ddot{y} \\ &+ (a_1 k_L + a_2 c - b_2) \dot{y} + k_L a_2 y = -f(t). \end{aligned} \tag{L.6}$$

For each settling point associated with a particular mass, the coefficients of this differential equation can be determined. The free response, after $f(t)$ is no longer acting, can be found by setting the right hand side of Equation (L.7) to zero. The free response is a sum of $(M + 2)$ exponentials, i.e., a Prony Series:

$$y(t) = \sum_{j=1}^{J} C_j e^{p_j t}, \tag{L.7}$$

where $J = M + 2$. Substituting Equation (L.7) into Equation (L.6),

$$\begin{aligned} m_l p_j^4 &+ (a_1 m_l + c)p_j^3 + (a_2 m_l + a_1 c + k_{L,l} - b_1)p_j^2 \\ &+ (a_1 k_L + a_2 c - b_2)p_j + k_{L,l} a_2 = 0. \end{aligned} \tag{L.8}$$

Note that subscript $_l$ denotes the l^{th} riding mass. Denoting the coefficients of the polynomial in Equation (L.9) by:

$$Q_{1,l} = (a_1 m_l + c), \tag{L.9}$$

$$Q_{2,l} = (a_2 m_l + a_1 c + k_{L,l} - b_1), \tag{L.10}$$

$$Q_{3,l} = (a_1 k_{L,l} + a_2 c - b_2), \tag{L.11}$$

$$Q_{4,l} = (k_{L,l} a_2). \tag{L.12}$$

Equation (L.9) can be rewritten as:

$$-m_l p_j^4 = (Q_{1,l})p_j^3 + (Q_{2,l})p_j^2 + (Q_{3,l})p_j + (Q_{4,l})2 = 0. \tag{L.13}$$

For each riding mass m_l the $p_{l,j}$ $(j = 1, 2, 3, 4)$ are known and Equation (L.13) gives four equations for four unknowns $Q_{1,l}$, $Q_{2,l}$, $Q_{3,l}$ and $Q_{4,l}$. These four unknowns can be identified by solving the four Equation (L.13) for each riding masses m_l. By following the same procedure for all 5 riding masses, a total of 20 $Q_{r,l}$ ($r = 1,\ 2,\ 3,\ 4$ and $l = 1,\ 2,\ 3,\ 4,\ 5$) are obtained. Knowing the $Q_{r,l}$ the unknown system parameters can be estimated by using the relationship defined in Equations (L.10) to (L.12). However, this leads to a problem because there are 20 equations but only 10 unknowns (a_1, a_2, b_1, b_2, c, $k_{L,1}$, $k_{L,2}$, $k_{L,3}$, $k_{L,4}$, $k_{L,5}$) and these equations are nonlinear functions of the unknown variables. However, Equation (L.10) yields 5 equations by setting $l = 1,\ 2, \cdots,\ 5$. There are only 2 unknowns, a_1 and c and the equations are linear because the masses are known. The least squares solution yields estimates for a_1 and c. From Equation (L.12), it can be linearized stiffness coefficients are related to one another by:

$$k_{L,l} = k_{L,1} \frac{Q_{4,l}}{Q_{4,1}}, \tag{L.14}$$

where $l = 2, \cdots, 5$. These relationships and Equation (L.12) for $l = 1,\ 2, \cdots, 5$ are used to estimate $k_{L,1}$. This can be done by eliminating $(a_2 c - b_2)$ term from each equation, e.g. subtracting the $l = 2$ equation from the $l = 1$ equation, the $l = 4$ equation from the $l = 3$ equation, and the $l = 5$ equation from the $l = 1$ equation. This results in three linear equations in $k_{L,1}$:

$$a_1 \left(1 - \frac{Q_{4,2}}{Q_{4,1}}\right) k_{L,1} = Q_{3,1} - Q_{3,2}, \tag{L.15}$$

$$a_1 \left(\frac{Q_{4,3}}{Q_{4,1}} - \frac{Q_{4,4}}{Q_{4,1}}\right) k_{L,1} = Q_{3,1} - Q_{3,4}, \tag{L.16}$$

$$a_1 \left(1 - \frac{Q_{5,4}}{Q_{4,1}}\right) k_{L,1} = Q_{3,1} - Q_{3,5}. \tag{L.17}$$

The only unknown in the above three equations is $k_{L,1}$ which can be estimated using the least squares method. The estimate of $k_{L,1}$ is then used in Equation (L.18) to determine the remaining unknown linearized stiffness coefficients $k_{L,l}$. Also Equation (L.12) are used to estimate a_2, the only remaining unknown in this equation. Then, Equation (L.11) and (L.12) are used to estimate the remaining two unknown variables b_1 and b_2, respectively. Finally, given the estimated linear stiffness parameters $k_{L,l}$, and the settling points $x_{0,l}$, Equation (L.3) is used to estimate the nonlinear elastic coefficients K_n:

$$[1 2x_{0,l} 3x_{0,l}^2 4x_{0,l}^3 5x_{0,l}^4] K_l = k_{L,l}. \tag{L.18}$$

This set of 5 equations is solved to yield estimates of K_1, K_2, K_3, K_4 and K_5. A summary of the parameter estimation process is shown in Figure L.3. Also for more details refer to [80].

Figure L.1. The experimental foam-mass system.

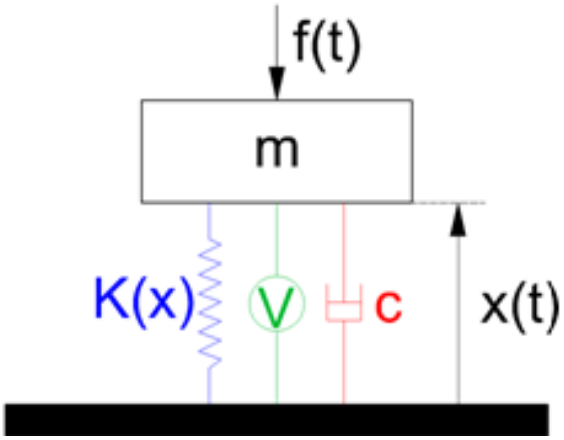

Figure L.2. Schematic of the foam-mass system.

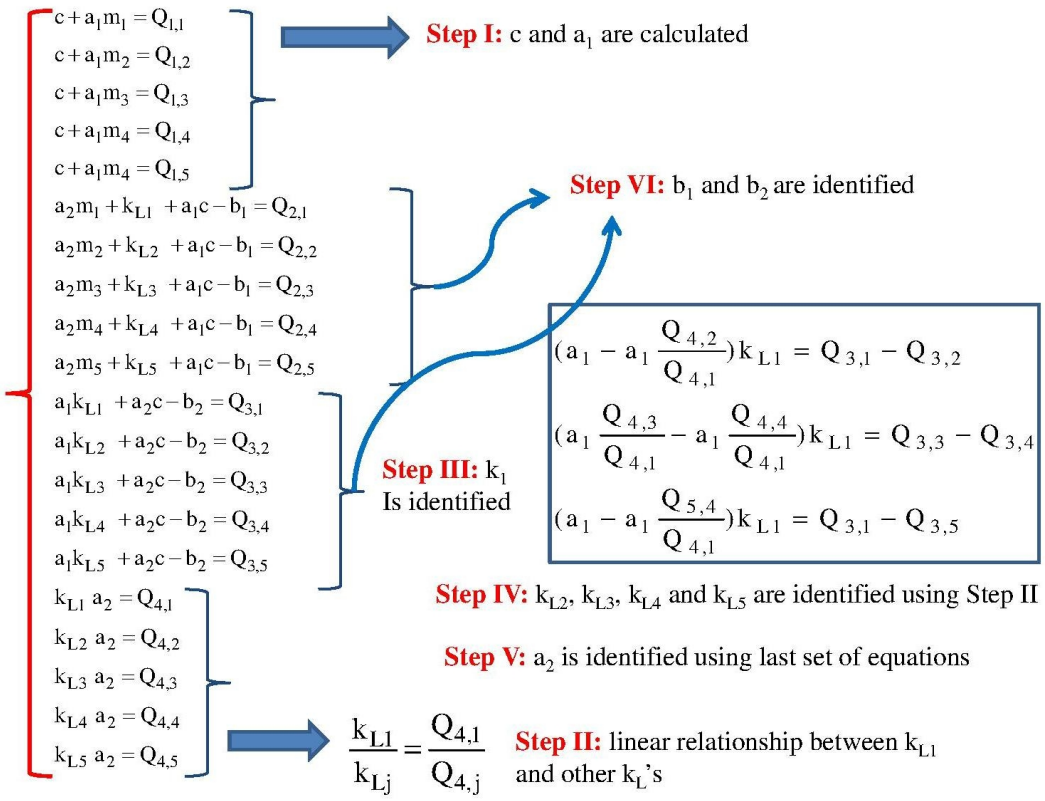

Figure L.3. The parameter estimation process.

VITA

VITA

Yousof Azizi is a Ph.D. candidate in school of Mechanical Engineering, Purdue University. In his research, he has studied nonlinear dynamics and vibration, system identification, modeling and signal processing. He has developed dynamic models of nonlinear viscoelastic materials and incorporated them into more complex multibody dynamical systems, developing computationally efficient methodologies that can be used in car seat design. Over the last few years, he has also gained experience as a teaching assistant in the undergraduate mechanism design classes in the School of Mechanical Engineering at Purdue.

Yousof Azizi received his B.S. in Mechanical Engineering from Isfahan University of Technology in 2006, and his M.S. in Electrical Engineering from Clarkson University in 2009. Also between 2005 and 2006, he represented Iran in the IASTE international program held in Pontifcia Universidade Catlica de Minas Gerais; this program was funded by Brazil government.

During his masters and doctoral graduate studies, he has published more than 20 peer reviewed conference and journal papers.